De Simon, Lia (2017) New mathematical approaches to the quantification of uncertainty affecting the measurement of U-value. PhD thesis, University of Nottingham.

# New mathematical approaches to the quantification of uncertainty affecting the measurement of U-value

Lia De Simon, MSc

Thesis submitted to the University of Nottingham
for the degree of Doctor of Philosophy

2017

# Abstract

This thesis describes the development and validation of a new computational procedure for the calculation of thermal transmittance (U-value) of existing building elements from the measurement of surface heat flux, and surface and nearby air temperatures.

The U-value plays a key role in the determination of the final energy consumption of a dwelling, and, as in the current political scenario reducing carbon emissions is a growing concern, obtaining accurate and quick measurements of thermal transmittance is of particular relevance to the precise representation of the energy performance of the building sector.

The calculation method developed is an extension of the RC network, a model based on the discretisation of building elements in resistors and capacitors in analogy with electrical circuits.

The advances proposed in this work extend the discrete RC networks to a model based on the full heat equation, with continuous, spatially varying thermal properties. The solution algorithm is inserted in a Bayesian framework that allows the reformulation of the problem in terms of probability distributions.

Two solution schemes have been confronted: Markov Chain Monte Carlo and Ensemble Kalman Filters approximation.

The model proposed has been validated on synthetic data, laboratory data collected in an environmental chamber on a solid and cavity wall, and in-situ data collected in 3 different locations (2 solid walls and 1 insulated steel frame construction).

The results show that the model offers an improved characterisation of the heat transfer through the building elements, furthermore, the algorithm can be used to analyse different wall constructions without the necessity of changing the structure of the model, as opposed to the standard RC networks, and, finally, it offers the practical advantages of the uncertainty reduction on thermal transmittance (from 14-25% to 7-10%) and a diminution of the necessary monitoring period from a minimum of 3 days to 1 day or less.

These advantages, in turn, benefit the building performance evaluation on different levels: in first instance, the practicality of measuring thermal transmittance in-situ is improved, thus making it easier to monitor the actual envelope performance and, secondly, the uncertainty reduction on the U-value leads to important reductions on the uncertainty surrounding the energy consumption predictions associated with a dwelling.

# List of Publications

- Lia De Simon, Marco Iglesias, Benjamin Jones, and Christopher J. Wood, **Quantifying the uncertainty in thermal properties of walls by means of Bayesian inversion**, *Submitted to Applied Energy.*

- Lia De Simon, Marco Iglesias, David Tetlow, Edward Cooper and Christopher J. Wood, **Deterministic and Bayesian approach to U-value measurements**, *Sustainable Energy Technologies Conference. Nottingham (UK). September 2015*

# Acknowledgments

I am extremely grateful to my first supervisor Dr. Christopher J. Wood for the unwavering support received during the last four years. In particular, I appreciate the energy and effort that you invested in this project since the very beginning, even if this was not part of your tasks at the time. You have always given me precious guidance, pushing me to achieve the best and improving my skills both on an academic and personal level.

Similarly, I want to thank my second supervisor Dr. Marco A. Iglesias for the invaluable advice received and the in depth discussions about maths, physics and life. In particular, I want to acknowledge the fundamental contributions that you gave for the development of the codes of the Markov Chain Monte Carlo algorithm, and, together with Chris, for the management of this collaborative project.

I'd like to take this occasion to thank my third supervisor, Dr. David Tetlow, for setting up the funding necessary for this PhD project and Kingspan Ltd. for partially funding my research at the University of Nottingham.

I cannot leave out of this section my fellow PhD students (and now researchers), postdocs and staff in the MGH. In particular to Vasilis, Sean, Alan and Ken: it was a pleasure to share this journey with you guys! I really enjoyed the time that we spent together inside and outside the office, and this experience would have not been the

same without you.

Likewise I want to thank “The Family”: Pietro, Isha, Giulia and Marco for being next to me all this time and sharing together (alongside the joys and pains of PhDs) TV series, adventures and Food. There is not enough space to thank all the inspiring and wonderful people I met in Nottingham but I would still like to thank Emily and Piers for sharing their house with me for the past two years, Vale, Benito, Rowan, Kai, Giannis, Luis and Patricia for all the good times spent together.

To old friends Elisa, Sara and Maria I’d like to say thank you for being there every time I come back, and a special thanks to Stefi, for keeping in touch during all these years independently of wherever we are.

A special thanks goes to my family in Italy for all the support received during my whole university career, in particular to Anna for being a friend as well as a sister. In the same way, I want to say thanks to my new Dutch family and friends.

Finally, I am particularly grateful to Sid Visser for the constant support that I received during the past years. Thanks for all the unconditional help that you gave me in the course of this research project, especially at the beginning, and for being at my side through the tough times that I encountered.

# Contents

# List of Figures

# List of Tables

# List of Acronyms and nomenclature

| | |
|---|---|
| $C$ | Heat capacity per unit area [J/m$^2$K] |
| $c$ | Volumetric heat capacity [J/m$^3$K] |
| $d$ | Thickness of a construction/construction layer [m] |
| $\mathbf{E}(u)$ | Expected value of u |
| $\mathcal{G}(u)$ | Forward model |
| $h_c$ | Convective heat transfer coefficient |
| $h_{ext}$ | External convective heat transfer coefficient |
| $h_{int}$ | Internal convective heat transfer coefficient |
| $I(x)$ | Initial temperature |
| $k$ | Thermal conductivity [W/mK] |
| $K$ | Thermal conductance [W/m$^2$K] |
| $L$ | Total thickness of a construction element [m] |
| $\mathbb{P}(u\|y)$ | Likelihood |
| $\mathbb{P}(u)$ | Prior probability distribution |
| $\mathbb{P}(y\|u)$ | Posterior probability distribution |
| $q$ | Heat flux [W/m$^2$] |
| $R$ | Resistance [m$^2$K/W] |
| $R_{se}$ | External surface resistance [m$^2$K/W] |
| $R_{si}$ | Internal surface resistance [m$^2$K/W] |
| $t$ | Time [s] |
| $T_{air}$ | Air temperature [°C] |
| $T_{ext}$ | External air temperature [°C] |
| $T_{int}$ | Internal air temperature [°C] |
| $T_{out}$ | Outdoor air temperature [°C] |
| $T_{ref}$ | Reflected ambient temperature [°C] |
| $T_s$ | Surface temperature [°C] |
| $T_{se}$ | External surface temperature [°C] |
| $T_{si}$ | Internal surface temperature [°C] |
| $T_\infty$ | Temperature of surrounding fluid [°C] |
| $u$ | Unknown parameters |
| $U$ | Thermal transmittance [W/m$^2$K] |
| $y$ | Experimental data |
| $\mathbf{V}(u)$ | Variance of u |

*Greek symbols*
$\Gamma$ Variance
$\Delta t$ Time discretisation element
$\Delta x$ Space discretisation element
$\varepsilon$ Emissivity
$\eta$ Gaussian noise
$\lambda_k, \sigma_k$ Parameters of the gaussian random field
$\nu$ Random realisation of a gaussian random field
$\xi_k$ Vector of random numbers
$\pi(x)$ Stationary distribution
$\rho$ Density [kg/m$^3$]
$\psi_k$ Gaussian random field
$\sigma$ Stephan-Boltzmann constant [W/$m^2K^4$]

*Acronyms*
BRE Building Research Establishment
BSRIA Building Services Research and Information Association
CERT Carbon Emissions Reduction Target
CESP Community Energy Saving Programme
CHM Cambridge Housing Model
DER Dwelling $CO_2$ Emission Rate [kg$CO_2$/m$^2$]
DFEE Dwelling Fabric Energy Efficiency [kWh/m$^2$]
DUKES Digest of UK Energy Statistics
ECO Energy Company Obligation
ESS Effective Sample Size
GHG Green house Gasses
HDM Heat Diffusion Model
ISO International Organisation for Standardisation
IR Infrared
KF Kalman Filter
mtoe million tonnes of oil equivalent
MCMC Markov Chain Monte Carlo
RdSAP Reduced data Standard Assessment Procedure
RH Relative Humidity [%]
SAP Standard Assessment Procedure
STM Single Thermal Mass

TER Target $CO_2$ Emission Rate [$kgCO_2/m^2$]
TFEE Target Fabric Energy Efficiency [$kWh/m^2$]

# Introduction

Climate change is a growing concern in the current international political agenda as it could represent the biggest challenge, so far, that humanity has had, and will have to face.

Rising of sea levels, expansion of the deserts and an increased number of extreme weather events such as heat waves, droughts, heavy rainfalls and floods that are being witnessed in the last two decades [9] can all be connected to the effects of global warming.

Global warming has been related to the increasing emissions of green house gases (GHG) generated by the combustion of fossil fuels and the activities characterising the development of the industrial era [9].

Since this connection has been ascertained, there has been evidence of international efforts to reduce $CO_2$ and green house gas emissions from all fronts of human activities, such as the Kyoto protocol, [10], promoted by the United Nations Framework Convention on Climate Change.

Under the protocol, the subscribing countries have to monitor their carbon emis-

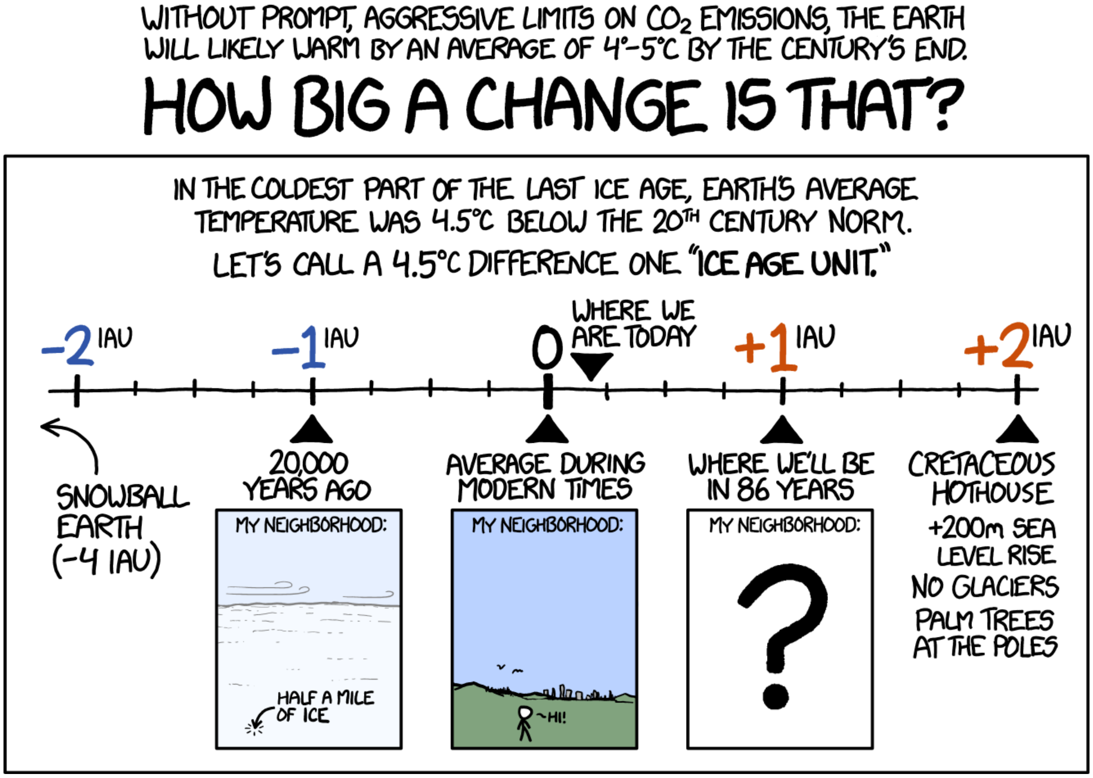

Figure 0.0.1: A light-hearted representation of the consequences of global warming. Source Data: 4.5 Degree, xkcd.com [1]

sions and reduce them, aiming to reach an agreed target: for most European countries, the second commitment period of the Kyoto protocol (2013-2020) requires a 20% reduction of the emissions of the 1990 baseline year [11].

Countries that ratified the Kyoto protocol, must meet their targets mainly through national measures, and, in this context, the UK promoted the climate change act, [12], binding the UK to achieve 80% emissions reduction by 2050.

In line with the climate change act, the UK has promoted the production and transmission of electricity obtained from renewable sources (such as solar, wind, hydro and tidal), bioenergy, the generation of heat through low carbon technologies such as air source and ground source heat pumps, and more efficient energy usage [13].

## UK National Energy Consumption

According to the latest UK national statistics, [2], the energy supply sector is the largest contributor to the national carbon emissions (29%) followed by the transport sector (24%). Business and Residential sectors occupy the third and fourth place with 17% and 13% of the national emissions respectively, see Figure 0.0.2 for more details.

Carbon and GHG emissions from the business sector primarily relate to the combustion of fossil fuels required for the operation of machinery, refrigeration and air conditioning, while the main emission sources in the residential sector relate to the combustion of natural gas for heating and cooking. In this case, the emissions related to residential electricity consumption (also for heating purposes) were counted in the energy supply sector.

According to the latest Digest of UK Energy Statistics (DUKES), the current UK national energy consumption amounts to 145.7 mtoe (million tonnes oil equivalent) [14], and the domestic sector contributes approximately 27% of this figure [14]. As can be seen from the energy flow chart published by the Department for Business, Energy & Industrial Strategy [3], figure 0.0.3, this amounts to 39.6 mtoe, 63% of which are attributed to natural gas consumption.

The last figure can be explained looking at the energy usage breakdown in a

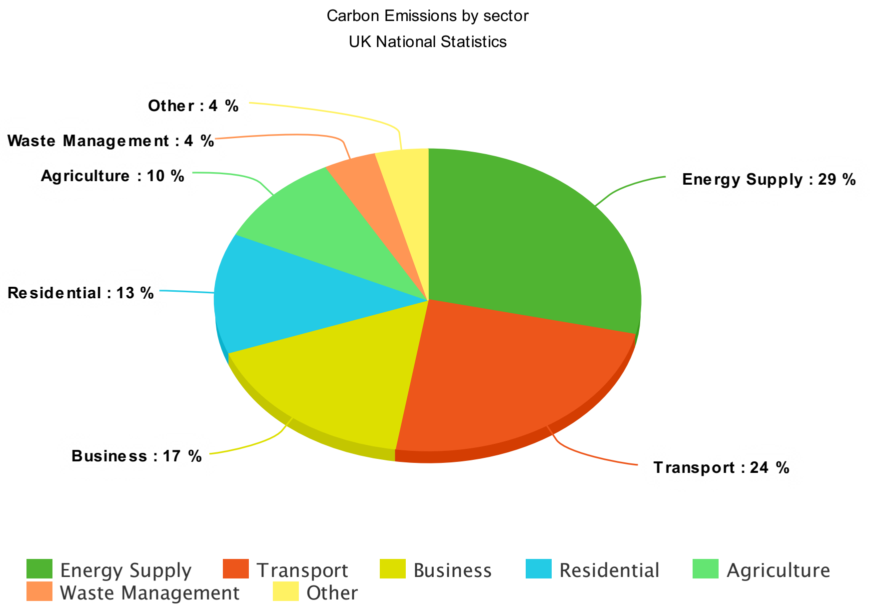

Figure 0.0.2: Breakdown of carbon emissions by sector in the UK [2]

household. According to the data tables published by the Department for Business, Energy & Industrial Strategy, relative to the latest Energy Consumption in the UK Report, [4], space heating accounts for 57.5% of the domestic energy consumption, mostly obtained by natural gas consumption. Figure 0.0.4 displays a pie chart of the data relative to the energy consumption by end use published in the 2016 Energy Consumption in the UK Report tables.

It is estimated that in a traditional dwelling construction up to 45% of the energy necessary to maintain a comfortable indoor environment is lost to the outdoor environment [15]. In a traditional house, the most prominent heat loss mechanisms are infiltration, ventilation and conduction via the building envelope. The largest share of envelope heat losses occurs through the external walls, 35%, and roof, 25%. This means that, excluding doors and windows, the majority of heat losses occurs through

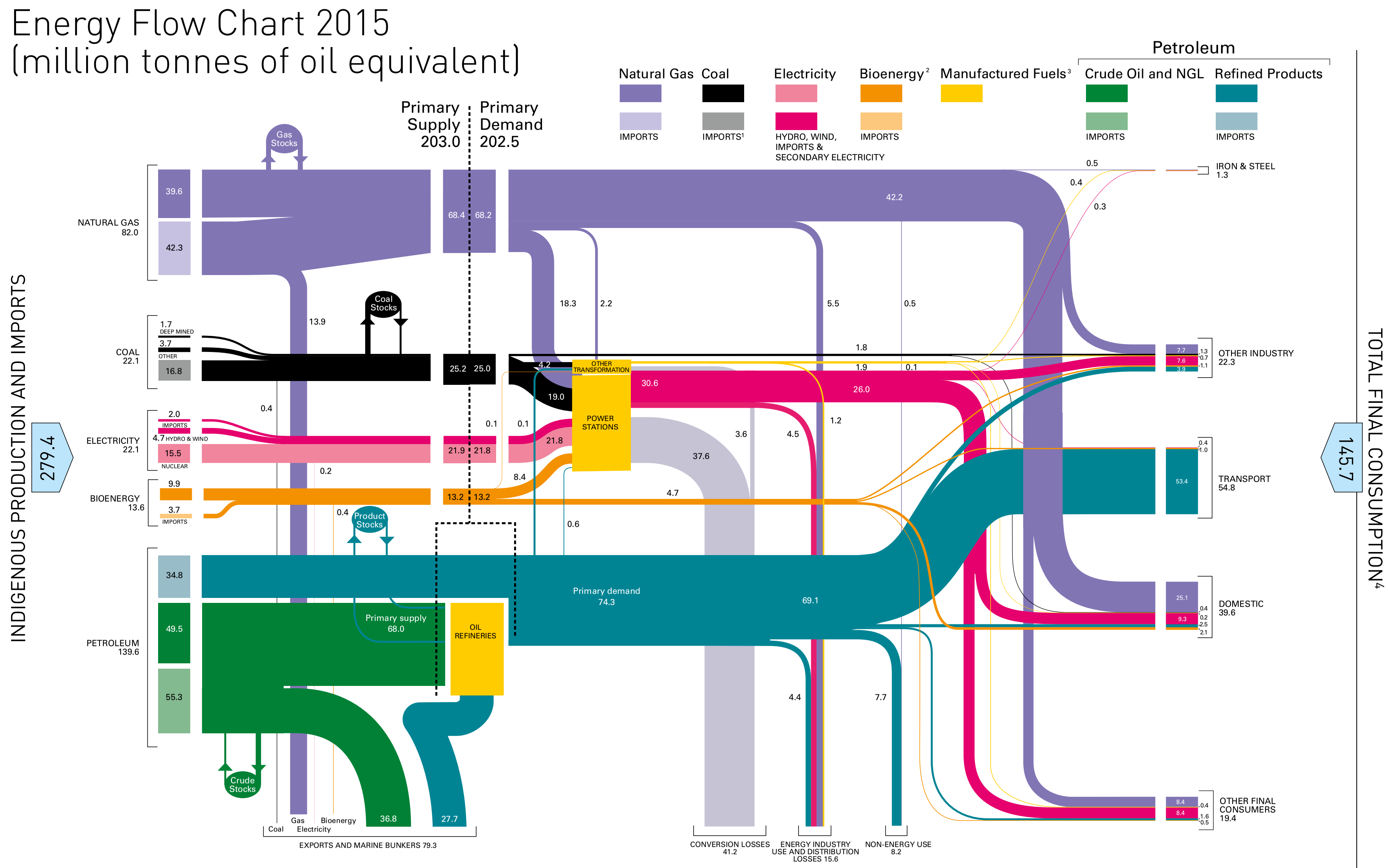

FOOTNOTES:
1. Coal imports and exports include manufactured fuels.
2. Bioenergy is renewable energy made from material of recent biological origin derived from plant or animal matter, known as biomass.
3. Includes heat sold.
4. Includes non-energy use.

This flowchart has been produced using the style of balance and figures in the 2016 Digest of UK Energy Statistics, Table 1.1.

Department for
Business, Energy
& Industrial Strategy

Figure 0.0.3: Breakdown of energy consumption by sector in the UK [3]

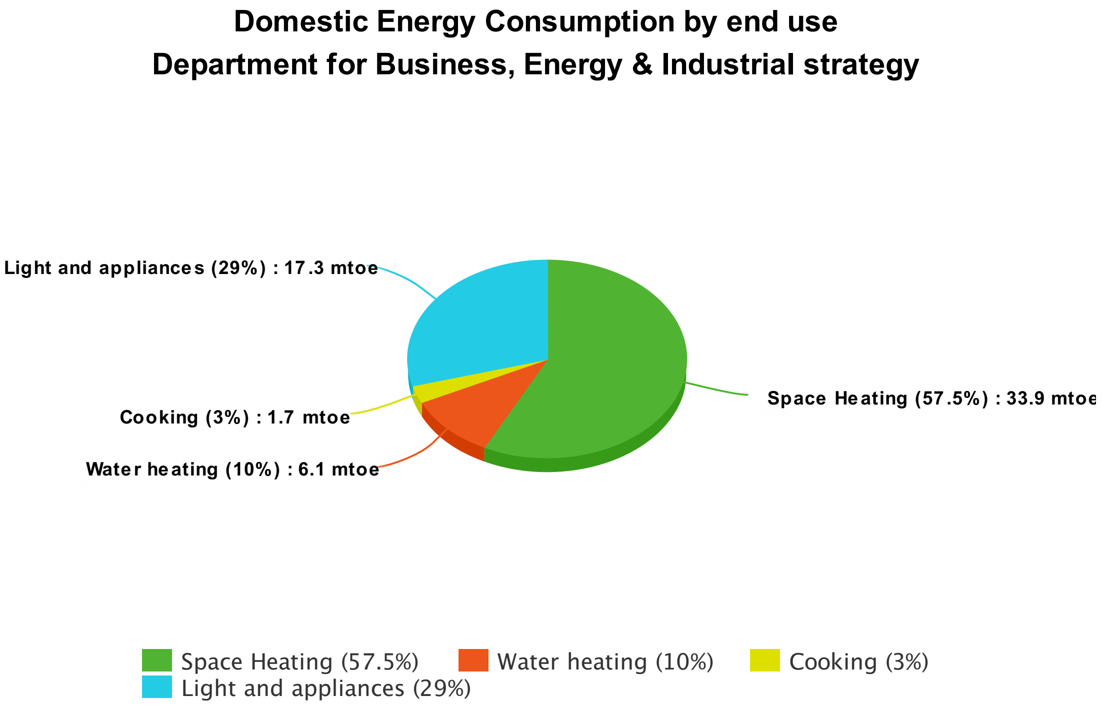

Figure 0.0.4: Breakdown of domestic energy consumption by end use, [4]

the building fabric. Figure 0.0.5 shows a schematic diagram of the heat losses and heat gains in a typical dwelling. The parameter that characterises the thermal performance of the building fabric, is the thermal transmittance or U-value. In the light of the figures presented above, it can be seen that this represents a crucial parameter for building performance and building performance evaluation. An explanation of the role of the U-value on the heat losses mechanism is given in section 1.1. The impact of the U-value on whole building energy performance is explained in detail in the literature review, sections 1.4 - 1.5.

From the figures presented above, it is clear that improving the building stock energy performance must be a priority in the carbon savings strategy, and, in line with these data several support policies and incentive schemes targeting building per-

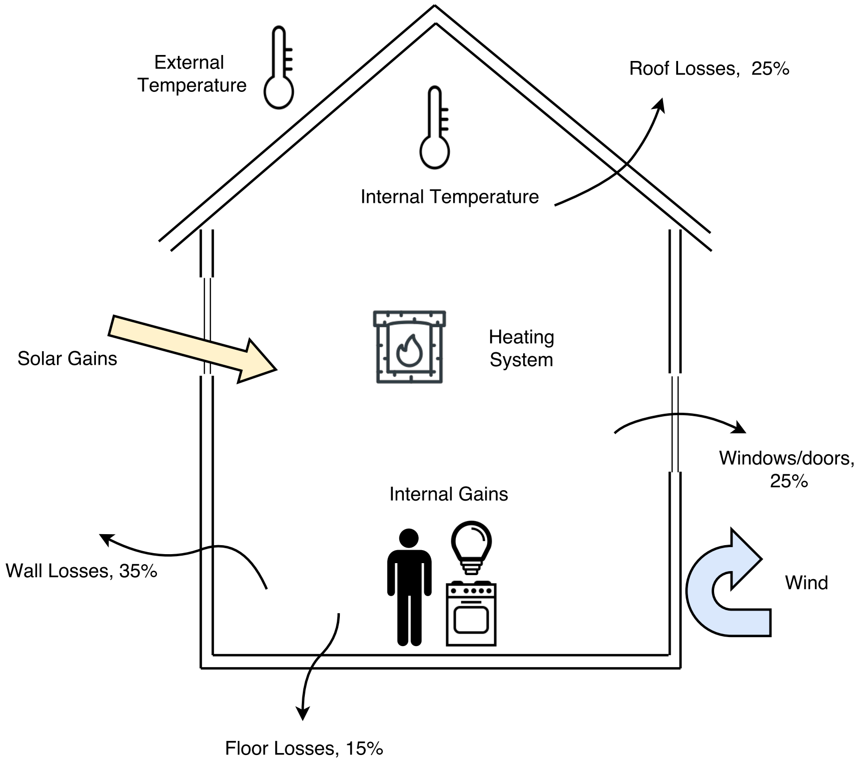

Figure 0.0.5: Diagram explaining the fabric heat losses in typical dwelling

formance are currently operating in the UK such as the Energy Company Obligation (ECO), Minimum Energy Performance Standards, Renewable Energy Feed in Tariff and Renewable Heat incentive, [16].

Among these, the ECO and the Minimum Energy Performance Standards are the policies that focus mostly on the improvement of the building fabric. The first aims in particular to provide energy efficient measures to low income population via their energy provider [17]. The latter targets the private rented sector, which presents the highest proportion of homes with low energy efficiency ratings, as from April 2018 it will be illegal to rent properties in the two lowest energy performance bands [18].

Several policies promoting energy efficiency have been scrapped by the 2015 government such as the Green Deal, providing pay-as-you-save loan schemes and the Zero Carbon Homes Policy, requiring all new buildings built after 2016 to be highly energy efficient. Still, energy efficiency policies remain part of the UK political agenda as recently a POSTnote on the future of energy efficiency policies was published amongst the parliament research briefings [19]. The briefing outlines options for future energy efficiency policies and summarises analysis of the effectiveness of different policy options.

Perhaps the most important and continuous drive ensuring minimum energy efficiency standards of domestic buildings are the building regulations, a set of laws ensuring that the environmental policies proposed in the Kyoto protocol and climate change act are respected. Part L of the building regulations is the most relevant to this research, as it regulates the conservation of fuel and power in existing and newly built dwellings. This part of the regulations will be discussed further in Chapter 1, section 1.2, where details of the current building regulations are explained.

To ensure that the standards outlined in the building regulations are met, the government promoted the development of the Standard Assessment Procedure (SAP), a tool to evaluate the actual and predicted energy performance of domestic buildings. Still, as discussed in sections 1.3 - 1.4, a wide discrepancy between the predicted and actual thermal performance of dwellings exists. This is commonly referred to as “performance gap” and, as explained in section 1.4, it can lead to important misestimations of the energy consumption and carbon emissions attributed to the built environment.

## Aims and objectives

The previous sections illustrated the role of the residential sector in the national energy consumption and carbon emissions. From the heat transfer mechanisms occurring in a dwelling, it is clear that the role played by the building fabric has an important effect on the energy efficiency performance of the building, thus determining the amount of energy consumed in guaranteeing the thermal comfort of the occupants. As mentioned in the previous paragraphs, this can be summarised in the U-value, and, therefore, it is clear that a good characterisation of this parameter is essential for the characterisation of the building energy performance that, in turn, will determine the amount of energy consumed and the carbon emissions generated by the building.

In particular, the thermal transmittance measurement is of particular relevance in this context as it characterises the actual performance of the building envelope as built, and, therefore, it is reasonable to assume that energy performance assessments based on a measured value of the thermal transmittance will offer the most accurate energy consumption and carbon emissions predictions.

This study aims to develop a new computational approach for the calculation of the U-value that will improve the current measurement methodology, allowing for shorter monitoring periods and, at the same time, providing an estimation of the uncertainty of the value found. This, in turn, will enable researcher to estimate the confidence level of a building performance assessment thus contributing to the reliability of the carbon saving estimates obtained.

This aim is pursued by fulfilling the following objectives:

i. Investigation of the most recent publications in the field of thermal transmittance measurements and building performance assessment, aiming to understand the work already published in this area and the current research trends.

ii. Numerical solution of the heat transfer equation with space varying thermal properties across the wall thickness, as opposed to constant (or piecewise constant) thermal properties.

iii. Introduction of a statistical framework to solve the inverse heat transfer problem of determining building element thermal properties from measurements of surface temperature (or near-by air temperature) and heat flux.

iv. Definition of probability distributions, modelling the prior knowledge of the researcher concerning the wall structure under examination. This includes the adaptation of a mathematical framework allowing the generation of continuous, spatially dependent, thermal properties.

v. Implementation of sampling algorithms for the solution of the inverse problem, including Markov Chain Monte Carlo and Ensemble Kalman filter techniques.

vi. Experimental data collection for the validation of the model proposed, including data collected in controlled environment (such as an environmental chamber), unoccupied and occupied properties, for different construction types.

vii. Assessment of the results obtained, including an evaluation of the impact of U-value uncertainty on the whole building energy efficiency.

The rest of the thesis has been organised as follows:

I. Chapter 1 offers a description of the context justifying the research carried out, posing particular attention to the work available on the performance gap and in particular to the role of the U-value calculation on the whole building energy performance.

   Moreover this chapter offers a review of the methodologies available to the measurement of U-values, dividing the techniques in direct and indirect methods, stressing advantages and disadvantages of each procedure. Later, an overview of the efforts made in the advancement of RC network models and inverse heat transfer problems is presented and finally the aims and contributions of this study are explained in further detail.

II. Chapter 2 offers a description of the mathematical background necessary to understand and develop the models proposed. This includes a formulation of the heat transfer problem in one dimension and an explanation of the Bayesian framework adopted. Here, the sampling techniques employed are explained along with the Markov Chain Monte Carlo procedure and Metropolis within Gibbs algorithms used.

III. Chapter 3 describes the experimental methodology followed for the collection of different data sets employed for the validation of the models proposed. This includes data collected in an environmental chamber, monitoring of an unoccupied solid wall property, including a thermographic survey, and monitoring of an occupied office space. Finally, a section is reserved for the description of a set of data collected by the Building Services Research and Innovation Association (BSRIA). The model was also validated using this data set to compare its results with studies available in literature.

IV. Chapter 4 demonstrates the performance of the Markov Chain Monte Carlo model developed. Here the model is trialled on synthetic data and on the data collected in the environmental chamber.

Synthetic data experiments permit the validation of the model in an optimal situation, where the researcher has absolute knowledge of the problem considered. This allows for exploration of the limitations and the potentials of the model developed that can be later tested on experimental data.

Secondly, the results obtained from the environmental chamber data are presented and discussed.

V. Chapter 5 presents the validation of the model developed on different data sets collected under more realistic conditions to demonstrate to what extent the findings and conclusions obtained from the synthetic data trials and climatic chamber tests can be expected to hold in reality. This chapter includes an explanation of the model limitations and computational costs.

VI. Chapter 6 Introduces the Ensemble Kalman Filter algorithm and discusses how this technique can overcome the limitations experienced with the Markov Chain Monte Carlo method. Secondly it presents the results obtained implementing the Ensemble Kalman filtering technique. These are compared with the figures obtained with the Markov Chain Monte Carlo, advantages and disadvantages of both techniques are discussed.

VII. Chapter 7 Draws the conclusions from the results obtained and includes a discussion of the relevance of the outcomes in relation to the existing body of work, stressing the improvements that the model can achieve as compared with current standards. In particular it is shown how the uncertainty impacts on the final energy consumption predictions and how the error reduction achievable with the model proposed offers significant improvements on this prediction.

    This chapter also includes proposals for future research to improve the model developed and suggests other sectors in the built environment that can benefit from the type of analysis proposed.

# Chapter 1

# Literature Review

This chapter introduces the context in which this research is inserted. Initially some general building physics concepts necessary to understand the importance of the U-value in determining the amount of heat lost through the building fabric is given in section 1.1. Following this, a panoramic on Part L of the current building regulations is given, section 1.2 followed by an explanation of the Standard Assessment Procedure, section 1.3. Section 1.4 illustrates the current research on the performance gap and enlightens the impact of U-value on the final building energy consumption predictions. Section 1.5 explains the current practices on inferring U-values from assumed thermal properties values and "in-situ" measurements of temperature and surface heat flux. Finally, section 1.6 provides a detailed outline of the contributions of this thesis in light of the literature investigated, showing how this research extends the works reviewed so far.

## 1.1 Heat transfer through building walls

Heat losses through single layer walls mainly occur by conduction, convection and radiation. In a cold climate, the indoor temperature, most of the time, is higher than the external temperature, and therefore the heat will naturally flow from the internal environment to the external environment, following the temperature gradient.

If the building element can be considered an isotropic material, (i.e. constant thermal conductivity) and the temperatures across the internal and external facades are uniform across the surface, it is reasonable to assume that the heat transfer process across the wall thickness is unidimensional. Figure 1.1.1 shows a diagram representing this situation.

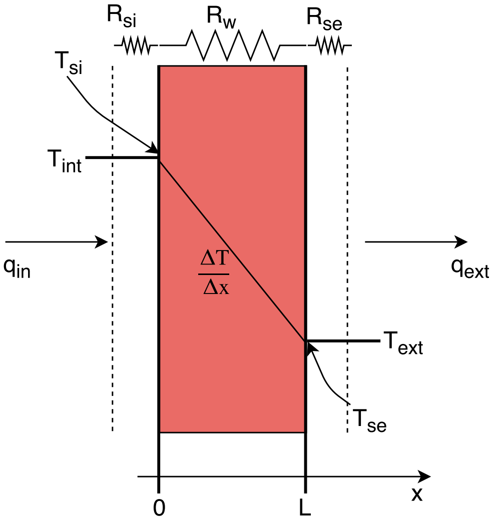

Figure 1.1.1: Diagram explaining the heat conduction process across a planar wall

If the temperature inside the wall remains constant, i.e. no change in energy stored inside the wall, the heat flux entering the wall equals the heat flux leaving the wall, in other words the rate of heat transfer through the wall is constant. Under such conditions the heat flux through the wall can be expressed by the Fourier's law, equation (1.1), [20]:

$$q(t) = -k\frac{\partial T}{\partial x} \qquad [W/m^2] \tag{1.1}$$

Note that in equation (1.1) the left hand side $q(t)$ represents the heat flux, $[W/m^2]$, this explains the absence of the area on the right hand side. Separating the variables in equation (1.1) and integrating from $x = 0$ where $T(0) = T_{si}$ to $x = L$ where $T(L) = T_{se}$, it can be seen that

$$\int_0^L q(t)dx = -\int_{T_{si}}^{T_{se}} kdT \tag{1.2}$$

leading to

$$q(t) = \frac{k}{L}(T_{si} - T_{se}) \tag{1.3}$$

From equation (1.3), it is clear that the heat flux through the wall depends linearly on the temperature gradient across the wall and it is inversely proportional to the thermal conductivity $k$. Defining the thermal resistance as

$$R = \frac{L}{k} \qquad [m^2K/W] \tag{1.4}$$

The heat flux through a homogeneous planar element can be calculated as

$$q(t) = \frac{(T_{si} - T_{se})}{R} \tag{1.5}$$

### 1.1.1 Surface Resistance

Convection heat transfer from a surface at temperature $T_s$ to a fluid at temperature $T_\infty$, is given by Newton's cooling law, [20]:

$$q_{conv}(t) = h_c(T_s - T_\infty) \tag{1.6}$$

where $h_c$ [W/m$^2$K] is the convective heat transfer coefficient. Using an approach similar to the conduction case, the convective resistance $R_{conv}$ can be defined as

$$R_{conv} = \frac{1}{h_c} \tag{1.7}$$

Radiation effects also contribute to the overall wall heat transfer, and depend upon the surface temperature of the body in consideration and the temperature of the surrounding surfaces at average temperature $T_{surr}$, [20]. The flux deriving from the radiative component can be written as

$$q_{rad}(t) = \varepsilon\sigma(T_s^4 - T_{surr}^4) = h_{rad}(T_s - T_{surr}) = \frac{T_s - T_{surr}}{R_{rad}} \tag{1.8}$$

where

$$h_{rad} = \varepsilon\sigma(T_s^2 + T_{surr}^2)(T_s + T_{surr}) \tag{1.9}$$

The notation adopted in equation (1.8), is very convenient as it makes it possible to express the contribution of radiative heat transfer in the same format as the convective and conductive contribution. Still, looking at equation (1.9), it must be remarked that the radiative heat transfer coefficient depends on the temperature, as opposed to the convective heat transfer coefficient.

When $T_\infty \approx T_{surr}$, as it is often the case for the heat transfer problem in building elements, the radiation effect can be properly accounted for by replacing the convective heat transfer coefficient with

$$h_{combined} = h_c + h_{rad} \tag{1.10}$$

and the contribution to the heat flux can be calculated as

$$q(t)_{conv,rad} = h_{combined}(T_s - T_\infty) \tag{1.11}$$

The combined heat transfer coefficient in equation (1.11) represents a convective heat transfer coefficient modified to account for radiation effects, reassuming the heat transfer effects occurring at the surface, [20]. As it was done for conduction and pure convection, a surface resistance can be connected to this coefficient and here $R_{si}$ is used for the internal surface and $R_{se}$ for the external surface. This reflects the different conditions occurring in the indoor and outdoor environment, as the convective coefficient depends on the surface roughness and the air velocity (different indoors and outdoors), [8], and the radiative coefficient depends on the temperature difference.

In practice, these values are tabulated for different wall structures and environmental conditions and can be found in the CIBSE Guide A [8].

### 1.1.2 Multilayered walls

In practice, building elements are often composed of a series of layers, each with different resistances, such as a cavity wall that includes an air gap sandwiched between two layers of bricks, or an insulated solid wall, that comprises a double layer of bricks and an insulation layer. Figure 1.1.2 shows a schematic representation of these constructions. In this case, in analogy with the electrical case, the total resistance of the whole building element is given by the sum of the resistances of the single elements.

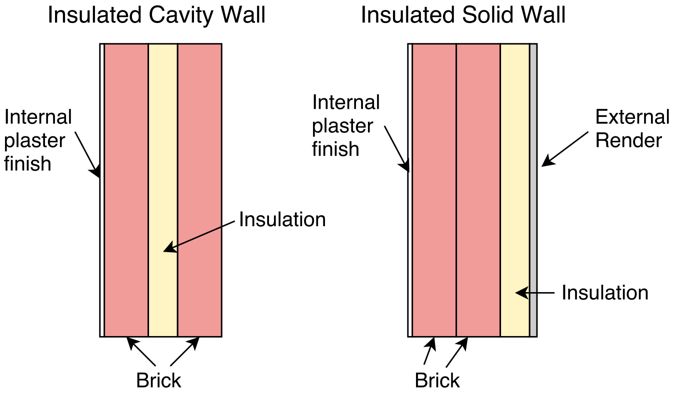

Figure 1.1.2: Schematic representation of an insulated cavity wall construction and insulated solid wall construction

$$R_w = R_1 + R_2 + ... + R_N \tag{1.12}$$

Considering the concepts of surface resistance introduced in the previous paragraphs, the total resistance of the wall can be calculated by combining the surface resistance values with the resistance of the construction:

$$R_{tot} = R_{si} + R_w + R_{se} \tag{1.13}$$

In practice, it is more convenient to consider the reciprocal of the resistance. If considering the resistance of the building element alone, this is called thermal conductance, $K$, and, if considering also the effect of the surface resistances this is called thermal transmittance or U-value, $U$,

$$K = \frac{1}{R_w}[W/m^2K] \qquad U = \frac{1}{R_{tot}}[W/m^2K] \tag{1.14}$$

so that the total heat flux through the building element can be given by

$$q_{tot}(t) = U(T_{int} - T_{out}) \tag{1.15}$$

From equation (1.15), it is clear that the U-value ultimately determines the amount of heat transferred through a construction element and, as this applies to all the external surfaces of a building, it is clear that it has a large role in determining the amount of heat losses through the building envelope, thus dictating to a large extent the building energy consumption.

## 1.2 Building Regulations

In line with the results of the UK energy consumption analysis and of the role played by the domestic sector in this scenario, it is essential to promote the construction of new low energy buildings, and, as it is estimated that 70% of the existing buildings will still be standing as of 2050 [21], it is imperative to improve the current building stock energy performance.

In order to guarantee the energy efficiency of new built constructions and effective retrofit measures, the UK government issued specific building regulations is support of the policies to achieve the carbon reduction targets.

Part L1a and Part L1b of the 2016 building regulations, [7], are the parts specifically relevant to this study, as they concern the conservation of fuel and power in new built (Part L1a) and existing dwellings (Part L1b).

Part L1a, Schedule 1 L1(a) - (b) establishes five criteria to be met to demonstrate compliance with the energy efficiency requirements [7]:

**Criteria 1:** Achieving Dwelling $CO_2$ Emission Rates [kg/m$^2$] (DER) and Dwelling Fabric Energy Efficiency [kWh/m$^2$] (DFEE) no greater than the Target $CO_2$ Emission Rates [kg/m$^2$] (TER) and Target Fabric Energy Efficiency [kWh/m$^2$] (TFEE) calculated with the Standard Assessment Procedure SAP2012 (see paragraph 1.3.1).

**Criteria 2:** "The performance of each individual fabric element and the fixed building services should achieve reasonable overall standards of energy efficiency", including meeting the prescribed U-value thresholds indicated in table 1.2.1.

**Criteria 3:** The dwelling should have passive control measures to limit the effect of heat gains in the summer.

**Criteria 4:** The performance of the dwelling as built should be consistent with the DER and DFEE.

Table 1.2.1: U-values imposed by the building regulations for new and retrofitted elements [7]

| Building element | New Built $[W/m^2K]$ | Retrofit $[W/m^2K]$ |
|---|---|---|
| Wall (cavity insulation) | 0.28 | 0.55 |
| Wall (internal or external insulation) | 0.28 | 0.30 |
| Floor | 0.22 | 0.25 |
| Roof (insulated at ceiling level) | 0.16 | 0.16 |
| Roof (insulated between the rafters) | 0.18 | 0.18 |
| Flat Roof | 0.18 | 0.18 |

**Criteria 5:** Provisions for enabling the energy efficiency of the dwelling should be put in place, such as provide the owner with sufficient information about the building.

Part L1b establishes that "[...] the renovation of an individual thermal element [...] must be carried out as to ensure that the whole element complies with paragraph L1(a)(i) of Schedule 1 as far it is technically, functionally and economically feasible", and prescribes new target U-values for the improved building elements set out in table 1.2.1, [7].

As can be seen from this brief overview of Part L, the building regulations approach building efficiency from different angles by regulating the upgrade of energy efficient systems and building envelope, avoiding overheating and achieving an overall higher dwelling efficiency.

Indeed, in the literature investigated, there is evidence of efforts to improve building performance across multiple disciplines, such as improved fabric performance by increased envelope air tightness [22], more efficient windows and glazing [23], whole building performance [24, 25] and improved building services [26].

In the past, to facilitate the take up of domestic energy efficiency measures, the government pressed larger gas and electricity suppliers to achieve carbon reduction targets from domestic premises in Britain via the Carbon Emissions Reduction Target (CERT 2008-2012) and the Community Energy Saving Programme (CESP 2009 - 2012)[27]. Furthermore the Warm Front scheme (2000-2013) was designed to provide economic assistance to low-income households with the installation of insulation and energy efficient heating measures in their homes. All these schemes have been substituted by the Green Deal from 2013 - 2015 [28].

Besides these practical interventions, other aspects of improving the building performance include the modelling of the building behaviour (criteria 1), and the post-intervention assessment (criteria 4). As will be shown in the following paragraphs, 1.3-1.4, these steps play a crucial role in the quantification of the dwelling energy consumption.

## 1.3 Building Performance Assessment

A key step to the improvement of building energy efficiency, is the understanding of the current building performance, in order to maximise the energy savings achievable with a retrofit intervention. This will lead to a sound and realistic national carbon saving policy.

The simulation of building performance and energy demand can be accomplished with the aid of commercial software (such as DesignBuilder [29], EnergyPlus [30] and Tas [31] amongst others) based on numerical models of the heat dynamics in the building elements. These software tools allow for the specification of single wall constructions, efficiency of heating systems, building-tailored geometry specifications, producing design days and annual simulations based on actual weather data.

Still, they are impractical to use on wide scale as they are time consuming, weather data are not easily available and they require advanced skills to setup and run the models.

### 1.3.1 Standard Assessment Procedure

To overcome these issues, the Building Research Establishment (BRE), on behalf of the former Department of the Environment (1992), developed the Standard Assessment Procedure (SAP), a methodology to assess and compare the energy and environmental performance of dwellings.

SAP assesses how much energy a dwelling will consume when delivering a defined level of comfort and service provision. This is based on standardised assumptions for occupancy and behaviour thus enabling a like for like comparison of dwelling performance [32]. The calculation methodology is set out in a form of worksheets, accompanied by tables, specifying standard values for the parameters taken in consideration. Once the worksheets are completed, the data can be used to perform the calculation. The following entries are requested as inputs:

**Dwelling Dimensions:** The geometry of the building envelope is defined, disregarding the internal dwelling partitions, defining the size of the elements, type of roof, floor area and glazing surfaces, leaving out unheated spaces clearly divided from the dwelling.

**Ventilation:** The ventilation air change rate and infiltration rate are specified. If its not possible to carry out a pressurisation test, these can be calculated from the information available on chimneys, fans and passive vents. Mechanical ventilation systems are detailed in this section

**Heat Transmission:** U-values of windows, walls, roofs and floors are specified based on the design construction. Allowance is made for thermal bridging based on the total exposed surface area.

**Domestic Hot Water:** The demand for hot water is based on the floor area. Heat gains from the hot water storage and distribution are estimated in this section.

**Internal Gains:** Gains from lights, appliances, cooking and occupants are estimated from the floor area.

**Solar Gains:** Calculated based on the area of glazed surfaces.

**Mean Internal Temperature:** Calculated monthly based on the average heating requirement of a typical household, taking account of the extent to which the dwelling is insulated and how well the heating can be controlled.

**Climatic Data:** Solar radiation, wind speed and external temperature of the location selected.

**Space Heating Requirements:** Calculated from the internal and external temperatures, allowing for internal and solar gains. This calculation includes the heating system efficiency and type of fuel.

**Space Cooling Requirements:** Should always be calculated as it is included in the DER. It is based on a standardised 6 hour/day cooling schedule to cool the spaces to 24°.

**Fabric Energy Efficiency:** Calculated as the heating and cooling requirements per floor square meter.

**Total Energy Use:** Including total annual heating and cooling requirements and electricity for pumps, fans and lighting.

**Energy Cost Rating:** Cost rating related to the energy consumption, also including the energy generating on site by technologies like micro-CHP and photovoltaics.

**Carbon Dioxide Emissions and Primary Energy:** $CO_2$ emissions related to space and water heating, ventilation and lighting less the emissions saved by energy generation technologies.

The SAP will then elaborate the data inputed to generate the Energy Efficiency Rating Band of the dwelling (on a scale from 1 to 100), the Dwelling Emission Rate, in compliance with the building regulations presented in the previous section.

When the complete data set for the SAP calculation is not available, it is possible to assess the performance of a dwelling by applying the Reduced data SAP (RdSAP). This is based on a site survey and it can be used only for existing dwellings. The calculation takes part in two stages: first the data available are expanded to the full data set, based on default assumptions and inference procedure, and then the SAP calculation is performed on the extended data set, as explained in appendix S of the Standard Assessment Procedure for the energy rating of dwellings [32].

## 1.4 Performance Gap

Unfortunately, in spite of the best efforts at characterising and predicting building energy performance, experimental evidence based on post occupancy monitoring has shown that a large gap exists between the design performance and as built performance. This, besides leading to unreliable carbon savings predictions [33], directly affects home owners, since nowadays, retrofit interventions are advised on economical grounds, based on the payback period that energy savings and capital costs will generate [34].

The performance gap has been widely investigated and several factors have been indicated as potential contributors to the discrepancy.

Hong et al., [35], in a study of the effectiveness of the Warm Front retrofit actions involving more than 3000 dwellings, found that the combination of loft and cavity insulation could reduce the space heating gas consumption by 11-17%. Still this is a wide discrepancy with the predicted savings obtained from SAP modelling, that were indicating a 45-49% reduction from the pre-retrofit energy consumption level.

It was found that in several of the monitored dwellings, cavity insulation was not uniform, leaving uninsulated approximately 20% of the area that theoretically was expected to be filled. Similarly, loft insulation was covering approximately 13% less loft area, especially close to the edges where the installation of the insulation is more difficult.

The same authors found that, draft stripping interventions, undertaken as part of Warm Front scheme, failed to achieve the theoretical reduction of air infiltration. Furthermore, it was found that the installation of gas central heating systems contributed to increases in air infiltration of up to 13% [36].

These findings show that the construction/installation phase can be detrimental to the expected performance of the energy saving measures if not carried out accurately and that the combination of multiple interventions, such as draft stripping and fitting a gas central heating system, could show counterproductive effects.

Still, these are not the only factors affecting the performance gap.

Hong et al., [35], in their study cite the “take back” or “Comfort factor” i.e. energy efficiency benefits are taken through maintaining higher indoor temperatures, thus improving the thermal comfort of the occupants rather than in fuel savings. Furthermore, it has been shown that occupancy behavioural parameters have significant influence on the results of building energy models, confirming the impact of occupant’s actions on energy use [37].

Rajat Gupta and Matt Gregg, [38], studied a pre and post retrofit energy performance of two occupied properties: a solid wall victorian house and a modern 1990s cavity wall house. Both dwellings were monitored pre and post retrofit through site visits, energy bills, in-situ measurements and occupant interviews. Furthermore, a pre retrofit building assessment was carried out through the Standard Assessment Procedure (SAP 2005). The pre-retrofit monitoring and evaluation highlighted that, in the Victorian house, the indoor temperatures were considerably lower than those assumed in the SAP methodology, leading to an actual gas consumption 50% lower than the expected values. In the modern house it was found that the electricity demand was significantly higher than SAP estimates.

Such discrepancies could be attributed to occupancy patterns and behaviours, especially in the second case, due to the full time high occupancy. The pre-retrofit monitoring informed the retrofit actions that, in both cases, followed the fabric-first approach allowing some specific interventions, such as the increase of natural daylighting in the first case and the re-organisation of the internal space in the second case. Neither dwelling reached the 80% reduction target: the Victorian property achieved 75% emission reductions while the modern house achieved 55%. When comparing with the actual pre retrofit performance, the reduction was around 40% in both cases.

This work highlights other difficulties and limitations of the building assessment procedure, emissions reductions achieved in practice do not always correspond to the modelled reduction as, as this case shows, the original actual performance of both dwellings might be quite different from the assumed base line.

On the other hand some improvements included in the retrofit, such as the passive clothes drying space and the installation of energy efficient appliances, give an important contribution to the reduction of $CO_2$ emissions and energy savings but do not have an effect on the SAP rating, thus not contributing to the 80% reduction target.

These findings suggest that the models adopted for the prediction of building performance do not fully capture the impact of human behaviour and cannot cope with unforeseen construction issues that lead to suboptimal constructions. In other words, they are not flexible, providing a guideline only whereas an accurate model should be able to be tailored case by case.

Other sources of uncertainty in building performance modelling that contribute to the performance gap, are related to the definition of the material constructions in the model. Indeed, many building performance software tools, including SAP, rely on the specification of the structure of the building elements, such as order, number of layers and specific thermal properties of different construction materials, for the calculation of the construction thermal transmittance, or allow the user to specify directly the U-value of the building element assumed from the building design.

The U-value of the construction elements plays a key role in the final energy performance of the building, as it is an essential parameter for the determination of the heat losses through the fabric.

The values input to building simulation software are often sourced from the literature, such as tabled values in the CIBSE guides, where a wide range of values is available. This increases the difficulty in selecting the appropriate material for the case taken under consideration, or calculated via the calculation method proposed by ISO6946, (see section 1.5.1 for further details).

Furthermore, it is often assumed that the wall is formed of layers each with homogeneous thermal properties (i.e. conductivity and capacitance) without accounting for defects and inhomogeneities. Parameters such as the number of constitutive layers, their material, their thickness and heterogeneities, such as cavities, are typically assessed by visual inspection. All together, these assumptions lead to an inaccurate characterisation of the wall and to a misleading evaluation of its thermal transmittance.

Indeed, it has been reported that assumed U-values of solid walls might not be sufficient to produce reliable carbon saving estimates.

Li et al. [33], for example, analysed the thermal transmittance of 40 solid wall constructions and 18 stone walls. Their findings showed that the assumed U-value (2.1 $W/m^2K$) underestimates the actual performance of these constructions, that, in both cases, showed mean U-values of 1.3 $W/m^2K$. Propagating this finding across the whole English housing stock by means of the Cambridge Housing Model (CHM [39]), the authors showed that the U-value from standard assumptions leads to an overestimated mean predicted annual heating demand of 16% from the solid wall housing stock, corresponding to a 2% change in the mean English heat demand.

Cesaratto and De Carli, [40], carried out a monitoring campaign over the winters 2006 - 2010 on 29 buildings in the North-East of Italy, collecting in-situ measurements of heat flux and surface temperature. Following the measurement campaign the data were analysed with different methodologies: according to the “Average Method” and calculation method described in the iso standards ISO9869 and ISO6946, through the software package LORD, [41], and other techniques.

The authors found that LORD was the most reliable tool for the inference of the thermal conductance.

In most of the cases considered, the measured thermal conductance was higher than the design conductance, showing differences from 6% (for constructions with higher conductance) to 20% (for constructions with lower conductance). Following the analysis of the experimental results, the authors carried out building performance simulations by means of the software TRNSYS [42] comparing the net energy demand when using the design conductance and the measured conductance. It was found that this could lead to differences of between 11 and 14%.

These studies show the impact of the U-value alone on the assessment of building energy performance. It is considered that in-situ measurements of thermal transmittance are able to provide more realistic observations of the actual performance of the building envelope and thus contribute to a more faithful characterisation of the energy requirements of a dwelling.

Sean Doran, on behalf of the Building Research Establishment, carried out an investigation of the thermal transmittance of “as built” construction elements, [43], monitoring 29 cavity walls and timber frame walls across Great Britain. This study focussed especially on modern constructions complying with the 1995 Edition of the Approved Document L, (Building Regulations Part L). The results of the project indicated that the measured U-values are greater than the U-values obtained by calculation, and therefore the calculation method might underestimate the heat losses for walls by more than 30%.

With similar results, Asdrubali et al [44], presented the outcomes of a monitoring campaign in Central Italy in six study case buildings of new construction with expected thermal transmittance between 0.25 $W/m^2K$ and 0.33 $W/m^2K$. The authors showed how the calculated U-values are often lower than the measured ones, thus leading to an overestimation of the performance of the building fabric.

Later on, Baker, carried out a study on behalf on Historic Scotland to assess the suitability of modern U-value calculation methods, such as the BRE U-value calculator, for predicting the properties of traditional constructions [45]. The study considered 67 in-situ U-value measurements carried out from 2007 to 2010. As opposed Doran’s findings, this study found that modern calculation methods tend to overestimate the U-value of traditional constructions thus underestimating their thermal performance.

Both studies demonstrate the importance of the in situ measurement, as a simple calculation based on assumed values is found to be unreliable on a diverse number of construction techniques. This, coupled with the results presented in [33, 35, 40] stressing the impact of U-values on the whole building performance, shows how it is necessary to use in-situ U-value measurements as opposed to assumed figures.

Furthermore, the large number of elements investigated in both studies allows some observations on the shortcomings of the experimental procedure to the measurement of the U-value to be made. For instance, both studies were limited by the fact that the measurements are season bound, as, in order to minimise solar radiation impact, the monitoring can be carried out only during the winter season. This meant that the monitoring campaigns were carried on over several years to monitor all the elements accurately.

Another important drawback is the length of the monitoring period for a single element, that, as reported by Baker, [45], takes at least two weeks foe accounting the inertia of the wall, therefore contributing to the length of the experimental data collection.

Finally, the quantification of uncertainty surrounding the U-value measurement cannot be easily determined as stated by Baker [45] due to the model adopted in the calculation of the U-value from experimental measurements and parameters that are outside the control of the experimenter. This will be discussed further in section 1.5.1.2.

As previously mentioned, the lack of uncertainty in relation to single parameters propagates in the building performance models, thus leaving the researchers without an estimate of the reliability of the results obtained.

Based on these conclusions, the aim of the work carried out in this study is to produce a mathematical model that will be able to infer the thermal transmittance from a short measurement period, possibly non season bound, and that, most importantly, will be able to offer an estimate of the uncertainty of the U-value measured.

Having stated the clear aim of this research, the following sections of this literature review will cover the current U-value calculation standards, both in-situ and from literature values, and other methodologies developed to infer the U-values from experimental measurements of heat flux and surface temperatures.

## 1.5 Current U-value calculation methodologies

This section describes the current methodologies for the measurement of U-value. It starts by presenting the direct procedures to obtain the thermal transmittance via predefined formulas, from design specifications or experimental measurements. These correspond to the procedures promoted by the ISO standards and, more recently, to the calculation of the U-value from surface temperature measurements taken with the employment of infrared cameras. These techniques have been classified as “direct methods" as in each case the U-value can be obtained from the application of a pre-defined formula.

The second section instead is concerned with techniques where the U-value is inferred by producing a best fit to collected data. In this case, there is not a formula that can be applied to calculate the U-value, for this reason these techniques are referred to as "indirect methods".

## 1.5.1 Direct Methods

### 1.5.1.1 ISO 6946, calculation method

ISO 6946:2007 regulates the calculation procedure based on the construction design.

According to the ISO 6946:2007, the U-value can be calculated from the total resistance of a building element. This, in turn, can be obtained by combining the thermal resistances of each of its thermally homogeneous components and, where appropriate, the effects of the surface resistance due to the air layers in proximity of the element surface.

The single component resistance can be obtained by dividing its thickness $d$ by its thermal conductivity $k$, as shown in equation (1.16) where the index $i$ indicates the component taken in consideration.

$$R_i = \frac{d_i}{k_i} \qquad [m^2K/W] \tag{1.16}$$

The surface resistances have to be chosen according to the situation considered, and in the case of vertical surfaces with horizontal heat flow these can be considered as $R_{si} = 0.13 m^2K/W$ for the internal surface and $R_{se} = 0.04 m^2K/W$ for external surfaces [46]. The components thermal resistances are then summed to obtain the total resistance of the building element, $R$, and the U-value, $U$, is the reciprocal of the resistance (equation (1.17))

$$R = R_{si} + R_1 + R_2 + ... + R_N + R_{se}, \qquad U = \frac{1}{R}, \qquad [W/m^2K] \tag{1.17}$$

#### 1.5.1.2 ISO 9869, measurement method

ISO 9869 describes the standard measurement procedure to calculate the U-value in-situ, thus obtaining the evaluation of the performance of the actual building element. This calculation is based on measurements of surface heat flux and temperature. This procedure necessitates the installation of several instruments on the location of interest. The equipment necessary comprises, heat flux sensors, also called heat flux plates, (in this study Hukseflux HFP01 sensors are used,[5]), temperature measurement equipment (in this study PT100 and thermocouples are used) and a data logging system (this study used a DataTaker DT85 with CEM20 expansion [47]).

A description of the working principles of the instrumentation necessary for the data collection can be found in the explanation of the experimental methodology, Chapter 3.

According to the ISO 9869:2014 [48], the U-value can be inferred from in-situ measurements of temperature and heat flux. The calculation should be performed using the "Average Method", as shown in equations 1.18

$$R = \frac{\sum(T^i_{si} - T^i_{se})}{\sum q_i}, \qquad K = \frac{\sum q_i}{\sum(T^i_{si} - T^i_{se})}, \qquad U = \frac{\sum q_i}{\sum(T^i_{air,I} - T^i_{air,E})} \tag{1.18}$$

where R is the wall resistance $[m^2K/W]$, K is the thermal conductance $[W/m^2K]$, U is the thermal transmittance$[W/m^2K]$, $T_{si}, T_{se}$, $T_{air,I}, T_{air,E}$ are the internal and external surface and air temperatures, and $q_i$ is heat flux through the building element considered at regular time intervals $i$.

The "Average Method" is based on the assumption that the energy stored in the wall during the measurement is not changing. This in reality will occur only if the temperature profile through the element is the same at the beginning and the end of the test. As this situation is quite unlikely, the final result might be affected by storage effects. In order to reduce these, it is recommended that the test period is continued for an integer multiple of 24h periods, (at least 72h), and to verify the following two stability criteria, [48]:

**Criteria 1:** The resistance value R obtained at the end of the test does not deviate by more than ±5% from the value obtained 24h before.

**Criteria 2:** The R value obtained by analysing the initial 2/3 of data does not deviate by more than ± 5% from the values obtained from the data collected during the last time period of the same duration.

#### 1.5.1.3 Limitations of the ISO standard calculations

ISO6946 relies on the ready availability of design thermal conductivity or thermal resistance of all the layers comprising a building element. In practice, these are not easily available and the ISO does not account for scenarios where the actual construction differs from the design due to unavailability of prescribed materials or substitutions of design materials during the construction phase.

It often happens that the assessment of the building element construction is done visually and therefore the detailed layering of the wall might be misunderstood or misrepresented.

Furthermore, design values of thermal properties might not correspond to the actual thermal properties of the element taken in consideration, due to their large variability for the same building material: for instance the thermal conductivity of brick ranges between 0.3 $W/mK$ and 1.30 $W/mK$, according to the values listed in Appendix 3.A7 of CIBSE Guide A [8]. Besides, these values are derived from measurements taken under controlled test conditions, that might not be representative of the environment conditions where the wall is located (e.g. they might not account for the amount of moisture absorbed) nor for the presence of impurities or inhomogeneities in the material itself.

All the observations detailed above underline the limitations of calculating the U-value a priori, just relying on literature values as the end result might be unrepresentative of the actual specimen taken in consideration.

Due to the concerns given above, and the findings obtained from the literature survey, measuring the U-value in-situ is preferable as it will be a more faithful representation of the thermal performance of the actual element under consideration. The measurement procedure is detailed in the ISO9869 as explained in the section above. Still, the methodology and the calculations promoted by ISO 9869:2014 present some practical difficulties that prevent a quick and reliable estimate of the element thermal transmittance.

The assumption that the energy stored in the wall will not change during the measurement period is unlikely to be true in practice, as the weather conditions are unpredictable and can lead to important fluctuations of the mean external temperature, thus increasing or decreasing the energy stored in the wall. In order to ascertain that the heat storage effects are not affecting the measurement result, the standard introduced two stability criteria and the test shall continue until the duration exceeds 72h and both criteria are met. In practice, as reported by Baker, [45], monitoring periods of above 10 days are common.

Even if these monitoring conditions are fulfilled, ISO 9869:2014 introduces a 10% uncertainty on the measured value due to the variations over time of temperatures and heat flow [48]. This error is a direct consequence of the model adopted for the calculation and it is the largest contributor to the total uncertainty in the measured U-value.

Furthermore, the sensors should be placed in an area of the wall far from thermal bridges and joints, that is uniform and without defects so that it is representative of the whole wall. In practice, this can be difficult to find and it has been shown that the sensor location has an important effect on the U-value measurement [49]. Externally the location should be shielded from solar radiation, snow and rain, therefore, very often, this restricts the monitoring periods to the winter season, as this offers the advantage of a reduced solar radiation, which can have a minor impact on the energy stored in the wall, and produce a steep temperature gradient between the indoor and outdoor environment [50]. As a drawback, this impacts on the flexibility of the measuring technique since it can only be applied during a small fraction of the year.

All the observations listed above, underline the impracticalities of the "Average Method" and contribute to the difficulty of realising frequent monitoring campaigns thus limiting the supervision of the "as built" performance and impeding the narrowing of the so called "Performance gap".

#### 1.5.1.4 Thermography

In the built environment thermal imaging is widely used, to investigate the presence of defects in the building envelope thanks to its quick, portable and non destructive nature, [51]. Fox et al. [52] presented a review of the existing literature, covering well-established and emerging building thermography methodologies. Thermal imaging has been used for production aerial surveys, offering the advantage of screening several buildings in a single session but presenting the drawback of being expensive and a qualitative tool only. Two more traditional surveying techniques are the walk around (external) and walk through methodologies, where the researchers monitor the external perimeter (walk around) and the external and internal surfaces (walk through) of a building. These traditional techniques are still the most common for building survey as they have proved to be more effective in defect detection [53].

More recently, some research studies presented quantitative applications of thermography, especially in relation to the measurement of the thermal transmittance.

Albatici et al. described the "Infrared Thermovision Technique (ITT)" [54] to compute the U-value of a building element from measurements taken with an IR camera. In the calculation procedure adopted in the "Infrared Thermovision Technique", the thermal transmittance is given by the ratio between the rate of heat transfer per unit area through the element and the difference between the inner and outer temperature:

$$U = \frac{P}{T_{int} - T_{out}} \qquad [W/m^2K] \tag{1.19}$$

Where P is the thermal power passing through the building element, dissipated in the form of radiation and convection:

$$P = \varepsilon \sigma T_s^4 + h_c(T_s - T_{air}) \tag{1.20}$$

Here $T_s$ is the surface temperature expressed in Kelvin [K], $\varepsilon$ is the surface emissivity and $\sigma$ is the Stephan-Boltzmann constant.

Later on, the same authors presented the results of a 3 year research study on the calculation of the U-value of heavy and light constructions via the ITT explained above[55]. The authors compared the U-values obtained with the ITT against the thermal transmittance obtained with the “Average Method”, (see section 1.5.1.2), finding good agreement for heavyweight structures with an absolute deviation between 8-20% between the two methodologies, but poor repeatability on lightweight structures.

Fokaides et Kalogirou [56] calculated the U-value from thermograms via equation (1.21) based on the same principle of the ITT :

$$U = \frac{4\varepsilon\sigma T_s^3(T_s - T_{ref}) + h_c(T_s - T_{int})}{(T_{int} - T_{out})} \tag{1.21}$$

The authors compared the results obtained via equation (1.21) with the values obtained employing a thermohygrometer and the nominal values obtained via the ISO6946. They found that the discrepancy between the nominal values and the values found via equation (1.21) showed an absolute deviation between 10-20%.

Giuliano Dall’O et al. [57] used IR thermography to survey 14 residential buildings of different construction in Milan during January 2013. The U-values were calculated via equation (1.22), where $T_{se}$ is the external surface temperature, and $T_{int}$ and $T_{out}$ are the internal and outdoor temperature respectively:

$$U = h_c \frac{T_{se} - T_{out}}{T_{int} - T_{out}} \tag{1.22}$$

The results of the research showed that the method does not allow the determination of a precise U-value but rather a range within the value is likely to lie. This is attributed to the large number of critical parameters that influence the temperature reading with an IR camera in an external environment: difficulty in obtaining precise emissivity and reflected temperature, accurate determination of the convective heat transfer coefficient $h_c$ and variability of the weather conditions.

Minkina et Dudzik [58] presented a thorough review of the factors affecting the temperature measurements with an IR camera.

From this analysis the authors concluded that the parameter that produces the largest error is the incorrect evaluation of the object emissivity, where a 30% uncertainty on the object emissivity led to 7% uncertainty on the temperature value, followed by the reflected ambient temperature, where a 3% uncertainty on ambient temperature can lead up to 5% uncertainty in the temperature.

In a similar way, Fokaides et Kalogiru, [56], carried out a sensitivity analysis varying the average reflected temperature, emissivity of the surface, ambient temperature and relative humidity and the distance between the thermographer and the target. Their findings agree with the conclusions drawn by Minkina et Dudzik [58], indicating the average reflected temperature and the surface emissivity as the factors with major impact on the measured temperature.

Due to the large number of parameters that require monitoring, the difficulties in ascertaining the final uncertainty of the U-value obtained with this methodology and the strong dependence on external weather conditions at the time of measurements, quantitative thermography was not pursued in this study for the determination of the thermal transmittance.

### 1.5.2 Indirect methods

Besides the calculations proposed in the ISO standards and IR methodology, many examples from the literature show approaches for estimating thermal transmittance and thermal capacitance based on reduced/simplified models of building structures. For the purpose of this thesis, these have been classified as indirect methods since there is not a ready-made formula to calculate the U-value directly, instead they require the fitting of the experimental data on a case by case scenario. Indeed, reduced models such as neural networks, autoregressive models and resistance-capacitance RC networks (or lumped capacitance models) are very common for building thermal modelling because (i) they often have a small number of input parameters that are easy to calibrate with an inverse modelling approach and (ii) are computationally inexpensive [59].

Neural networks are computational methods based on the same functioning principles of the human brains. In this setup networks can be trained to recognise patterns in data and, later, make predictions on new data sets. In building simulations, neural networks have been used to predict building indoor temperatures and relative humidity [59]. The advantage of neural networks is that no knowledge is needed about the physical properties of the building, but, as a drawback, the building cannot be characterised by its parameters. For this reason neural network models are often referred to as black box models .

Autoregressive models can approximate the current state of a system as a linear combination of past measurements with the addition of noise. In these models, the parameters that need to be identified are the coefficients of the linear combination. Similar to the case of neural network models, these have been used for the prediction of indoor temperature, thermal comfort and optimisation of the building energy demand [60, 59] and they are also referred to as black box or grey box models, since the parameters of the model are not directly connected to the physical properties of the problem studied. For this reason, neural networks and autoregressive models have not been chosen as computational methods for this work.

#### 1.5.2.1 RC Networks

Perhaps one of the most common simplified models to describe heat dynamics through the walls of buildings is the RC network in which a building element is discretised in a specified number of nodes associated with a capacitor, where, ideally, the heat capacity of the building element is concentrated. The capacitors are then connected by thermal resistances. A diagram of an RC thermal network with two resistors and one capacitor, is displayed in Figure 1.5.1.

The heat equation can be discretised in the nodes forming the RC Network and, the case of the RC network represented in figure 1.5.1, the discretized equation be-

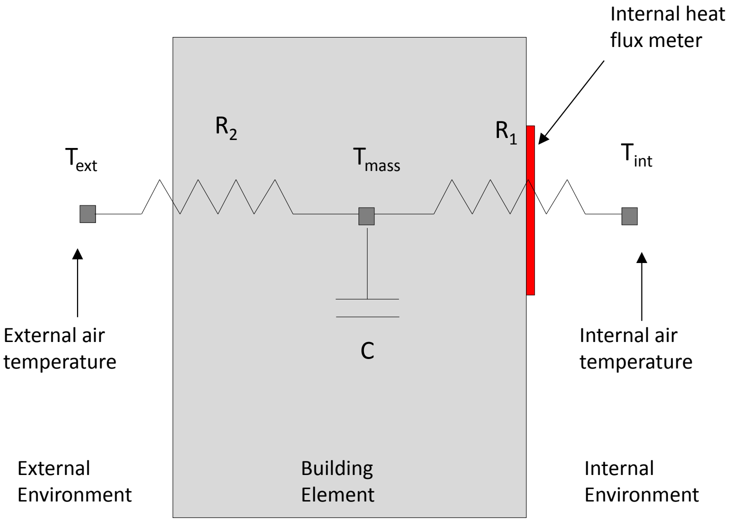

Figure 1.5.1: RC network and measurement configuration.

comes:

$$C\frac{T_{mass}^{i+1}-T_{mass}^{i}}{\Delta t}=\frac{T_{int}^{i+1}-T_{mass}^{i+1}}{R_1}+\frac{T_{ext}^{i+1}-T_{mass}^{i+1}}{R_2} \tag{1.23}$$

where $C$ is the heat capacity per unit of area (or thermal mass per unit of area), $\Delta t$ is the time step and $R_1$ and $R_2$ are the resistances of the first and second element of the discretized domain. $T_{int}^{i}$ and $T_{ext}^{i}$ corresponds to the internal and external temperatures at the $i^{th}$ time step.

Possibly, one of the most remarkable contributions in the implementations of the RC network models was the introduction of the software package LORD LOgical R-Determination [41, 61], developed under the PASLINK project [62]. LORD is a software tool for the modelling and calculation of thermal systems. It infers the thermal resistance of building elements from measures of temperature and heat flux. As mentioned earlier, the wall (or more complex structure) is divided into a series of resistances and capacitors and to each node a heat balance equation similar to equation (2.40) is assigned. At this point, an objective function is defined as the difference between the model output and the measured data. It is assumed that the combination of resistances and capacities that minimises the objective function will give the best estimate of the thermal parameters and from this point onward, the problem is treated as a minimisation problem.

In the software LORD, two different approaches are adopted for the minimisation of the objective function: the Downhill Simplex Method and a Monte Carlo procedure. The software LORD has been used in by different research groups in their data analysis: as already mentioned Cesaratto and De Carli found it to be the most reliable tool for the inference of thermal conductance [40], Wakili et al. [63], used LORD to measure in situ U-values, finding it was able to characterise appropriately storage effects.

Still, the implementation of the analysis with the software package LORD requires the user to trial different configurations of the RC network, trying a variable number of resistors and capacitors according to what type of element is under observation.

A wide range of literature is available concerning model topology (number of resistor and capacitors) and optimal parameter identification in RC models. Xu and Wang, [64], for example, have shown that RC models with 3 resistances and 2 capacitors produce very accurate results for lightweight constructions but their performance worsens for heavier constructions and in general, higher order network models produce more accurate results.

In a different study, Kircher and Zhang [65], investigated the limitations of RC network models in building application, finding that these models may not be suitable for walls that are thick or well insulated or have large convection coefficients at the indoor surface.

While RC models have been shown to provide an accurate representation of building structures, the applicability has some limitations, such as the fact that RC models still need to be tailored on a case by case basis and without knowing in advance the suitable number of resistors and capacitors for different wall constructions.

In many cases, the RC network models are combined with an inverse modelling optimisation scheme, where the model parameters are determined by minimising an objective function matching the output of the model to measured data.

As mentioned before, the LORD software adopted two strategies, Downhill Simplex Method and Monte Carlo procedure [41]. In many examples, parameter identification has been carried out in the frequency domain, based on the assumption that the simplified model should reproduce the principal harmonics of the complete ideal model [64, 66, 67].

A large variety of optimisation approaches has been adopted such as Genetic Algorithms [68, 69] and Gauss-Newton. Still these methods offer a most likely estimate of the model parameters obtained in a deterministic fashion from the best fit of the experimental data but do not offer a characterisation of the uncertainty surrounding those parameters. There are many examples of the application of Bayesian inference used for handling and quantifying uncertainty [70, 71]. For this reason a Bayesian approach has been adopted that, as explained in the following paragraph, 1.5.2.2, provides a good characterisation of the uncertainty surrounding the model parameters.

#### 1.5.2.2 Bayesian Inference

The Bayesian framework involves in the definition of probability distributions that can be interpreted as the dispersion of the prior knowledge that the researcher has about the problem studied. In the case of the measurement of thermal transmittance, this corresponds to the knowledge about the possible spread of thermal properties of the building element considered.

The optimisation of the choice of the parameters, in this case, is obtained by maximising the likelihood function. The likelihood can be interpreted as an evaluation of the probability of the observed data given a determined parameter.

A recent publication by Biddulph et al, [72], has showcased the potential application of Bayesian techniques to infer thermal properties of walls given temperatures and heat flux measurements. In this work, the authors are interested in inferring the thermal transmittance of solid walls based on the collection of heat flux and air temperature measurements. The data set used was collected by the Building Services Research and Information Association (BSRIA) during the 2010 winter. The heat transfer through the wall is described with an RC model with 2 resistances and 1 capacitor, as the model represented in figure 2.4.1. The four unknown parameters associated with the model are inferred with a standard Bayesian framework.

This approach suggests that an evaluation of the U-value could be possible within 3 days of monitored data but, as it will be shown in the following chapters it does not offer an accurate characterisation of the uncertainty surrounding the heat flux predictions, due to the coarse approximation of the heat diffusion equation provided by the RC model with a single capacity (corresponding to the discretisation of the heat equation in three points).

Gori et al. [73], compared the performance of an RC Network with a single thermal mass to the performance of a model with two capacitors. Both models have been implemented within a Bayesian framework, using measured surface temperatures as boundary conditions and internal and external surface heat flux predictions as outputs (measurements of the heat flux at both surfaces were available for comparison with the model outputs).

The authors found that both methods provide an evaluation of the U-values within the expected margins but the estimates of the thermal mass are lower than the estimates obtained from literature values based on the expected wall structure. Furthermore, the authors demonstrate that the model with a single thermal mass is not able to accurately predict the internal and external surface heat fluxes simultaneously, while this is possible for the model with two capacitors.

These findings suggest that increasing the number of capacitors in an RC network might provide a better characterisation of the heat transfer process through the wall, ultimately leading to improved models of energy transfer through the building fabric.

In the work published by Berger et al [74], the authors used a Metropolis-Hasings Markov Chain Monte Carlo (MCMC) algorithm for the investigation of the thermal properties of a three layered building wall, using surface temperatures and inner structure temperature measurements. In this case, the model adopted was the 1D heat equation discretised in 6 nodes.

Wang et Zabaras in [75] discuss the solution of two inverse heat conduction problems through a Bayesian inference approach, aiming to reconstruct the unknown heat flux on part of the boundary from temperature measurements. The authors show that the Bayesian approach is effective in producing smoother inverse solutions when compared to deterministic approaches and it is able to provide quantification of system uncertainties.

Orlande, [76], proposes a review of the current mathematical approaches to the solution of the inverse heat transfer problems, reviewing both classical techniques based on the minimisation of an objective function and techniques based on Bayesian framework that make use of sampling methods.

In contrast to deterministic approaches, such as the Gauss Newton method and Down hill simplex method, probabilistic approaches such as Bayesian inference provide a statistical framework that enables the quantification of uncertainty in the inferred parameters, thanks to the formulation of the problem in terms of probability distributions. As mentioned in the previous section, the quantification of uncertainty associated with the determination of U-value is still an open issue in the context of the built environment that is fundamental to overcome due to the impact of U-value on the prediction of building energy performance.

## 1.6 Contributions of this work

The literature reviewed shows that the heat transfer inverse problems are of growing interest and, thanks to the increased computational power available to researchers, sampling methods such as Markov Chain Monte Carlo are increasingly more common.

In this framework, the research carried out during this study, aims to extend the flexibility of the RC networks presented in the previous section. In order to avoid the limitations deriving from discretising the heat equation across only 2 or 3 nodes. A continuous model was developed as an alternative so that, in principle, the same tool can be applied to different types of walls without the necessity of modifying its governing equations.

Besides the achievement of a "universal" tool applicable to diverse building elements, the solution of the heat equation with continuous thermal properties will provide a better characterisation of the heat transfer problem, thus providing a solid basis for the improvement of whole building simulations.

It has been shown that RC Networks could be capable to infer the thermal transmittance within three days of experimental measurements [72]. The present work aims to expand from this result and individuate the shortest time window over which the inference of thermal properties is possible, thus providing an important improvement over the current in situ measurement practice.

Finally, this study aims to obtain a full characterisation of the uncertainty surrounding the measurement of the U-value as well as a quantification of the impact that this uncertainty has on the final energy consumption predictions made by current modelling tools. As mentioned in the previous section, a probabilistic approach, such as Bayesian inference, offers the framework necessary to the uncertainty evaluation, therefore this will be the structure adopted for the parameter optimisation.

In order to achieve the goals proposed, several alterations to the approaches found in literature have to be carried out.

The choice of modelling the thermal properties as continuous functions gives rise, upon discretisation, to a large number of parameters to be inferred. This cannot be carried out in the classical Bayesian framework, as it generates instabilities and convergence problems.

For instance, considering a fine discretisation grid where the wall thermal properties are discretised in 100 nodes, will give rise to 200 unknown parameters (100 for the discretisation of the thermal conductivity and 100 for the discretisation of the volumetric heat capacity). In the case of a simple RC network with 1 capacitor and 2 resistances the number of parameters to be inferred is 4 (2 resistances, 1 capacity and the initial internal temperature), 50 times smaller.

Furthermore, as the thermal properties are assumed to be spatially varying across the wall thickness, the parameters to be inferred cannot be totally independent but are subject to correlation i.e. it is expected that in a (supposedly) homogeneous layer, the thermal conductivity and volumetric heat capacity vary slowly and that the thermal properties of a node do not differ dramatically from its neighbours.

In other words, the problem corresponds to choosing functions with a suitable "profile" across the wall thickness rather than choosing independent scalars.

To overcome this issue there was the need to resort to new sampling techniques that extend the classic Bayesian framework to the case where it is required to sample from a high dimensional domain. The details of this mathematical framework are described in the following chapter.

Still, the large amount of parameters inferred allows for an accurate exploration of the initial domain, thus providing a reliable method to characterise the uncertainty on the parameters obtained. This will be discussed in Chapters 4 and 5, where the results obtained with the model researched are presented.

The exploration of the domain is done by constructing a Markov Chain Monte Carlo (MCMC). This can be seen as a succession of draws that will eventually converge to samples of the posterior probability distribution sought. The advantage of using MCMC methods is that, by construction, the chain is converging to the correct distribution, but, as a drawback, this system is computationally expensive due to the large number of iterations required to ascertain that the chain has converged.

Chapter 6 presents a possible answer to avoid this issue, by reformulating the problem using more efficient methodologies for the characterisation of the posterior probability. The solution proposed in this study is a novel implementation of Ensemble Kalman filters as explained by Iglesias et al. [77]. Ensemble Kalman filters have already been used in the context of inverse heat transfer problems, [76], but have not yet been applied to the specific field of U-value inference. Ensemble Kalman filters, as opposed to Markov Chain Monte Carlo, are an approximation technique that represents a probability distribution with a finite number of samples. The advantage of this method is that it will reduce the number of iterations necessary to characterise the posterior distribution, thus reducing the computational costs attached to the MCMC method.

The implementation of the Ensemble Kalman filter for the inference of the U-value from heat flux and temperature measurements is illustrated in chapter 6 (paragraph 6.1).

# Chapter 2

# Mathematical Background

In this chapter, a detailed description of the physical models adopted to analyse data from heat transfer measures is given in section 2.1, followed by a thorough explanation of the mathematical tools that have been employed to elaborate the experimental data, section 2.2. In section 2.4, the Single Thermal Mass (STM) model is presented and its implementation within this research project, for providing data for comparison with the available literature, is described.

## 2.1 Heat conduction equation

Consider the situation of one dimensional heat transfer across a wall, and denote the direction where the heat transfer occurs by $x$. Assuming that the wall thickness is denoted by L, let $x = 0$ and $x = L$ correspond to the internal and external surfaces, respectively. Assuming that there are no internal sources/sinks of heat, the temperature distribution within the wall, denoted by $T(x, t)$ ($x \in [0, L]$), on a given time window $(0, t_f]$ is the solution of the heat equation

$$c(x)\frac{\partial T}{\partial t} = \frac{\partial}{\partial x}\left[\kappa(x)\frac{\partial T}{\partial x}\right], \qquad (x,t) \in [0, L] \times (0, t_f] \tag{2.1}$$

where $\kappa(x)$ $[W/m^2]$ is the thermal conductivity of the wall $c(x)$ $[J/m^3K]$ and the heat capacity per unit of volume at each point within the wall (i.e. $x \in [0, L]$). Equation (2.1) is supplied with the following initial condition

$$T(x, 0) = I(x), \qquad x \in [0, L] \tag{2.2}$$

where $I(x)$ is the initial temperature inside the wall. In addition, there is the need to specify appropriate boundary conditions, that, in the case of fixed temperature boundary conditions can be specified as Equations 2.3 - 2.4

$$T(0, t) = T_{int}(t) \qquad x \in [0, t_f] \tag{2.3}$$

$$T(L, t) = T_{ext}(t), \qquad x \in [0, t_f] \tag{2.4}$$

In the previous expressions, $T_{int}(t)$ and $T_{ext}(t)$ represent internal and external surface temperature measurements at every time $t$. The heat flux at the internal and external surfaces of the wall is given by the Fourier equation:

$$q_{int}(t) = -\left[\kappa(x)\frac{\partial T}{\partial x}\right]\Bigg|_{x=0}, \qquad q_{ext}(t) = -\left[\kappa(x)\frac{\partial T}{\partial x}\right]\Bigg|_{x=L} \tag{2.5}$$

And the conductance and heat capacity can be calculated from the values of $\kappa(x)$

and $c(x)$ via equation (2.6):

$$\mathcal{K} = \left[\int_0^L \frac{1}{\kappa(x)} dx\right]^{-1} [W/m^2K], \qquad \mathcal{C} = \int_0^L c(x)dx \; [J/m^2K] \tag{2.6}$$

Note, from expressions (2.1)-(2.5), that the heat transfer model has the following set of parameters: $(T_{int}(t), T_{ext}(t), \kappa(x), c(x), I(x))$. As $T_{int}(t), T_{ext}(t)$ are observed measurements, once $k(x), c(x)$ and $I(x)$ are inferred, the U-value, as well as the heat capacity per unit area (or thermal capacity,) can be calculated in terms of $\kappa(x)$ and $c(x)$ via equations 2.6. As the surface measurements are considered, and according to what specified in Annex F of the ISO 9869:2014, [48], it is reasonable to assume that the initial temperature can be approximated as linear interpolation between the two surface temperatures, equation (2.7). Therefore the only unknown parameters in the problem described by equations (2.1)-(2.5) are the thermal conductivity $k(x)$ and the volumetric heat capacity $c(x)$.

$$T(x,0) \;=\; T_{ext}(0) + \frac{(L-x)}{L}(T_{int}(0) - T_{ext}(0)), \qquad x \in [0, L] \tag{2.7}$$

Equations (2.1)-(2.5), define a simple Heat Diffusion Model and, for brevity, they will be referred to as HDM in the remainder of this thesis. A diagram sketching the HDM, with notional values for the distribution of $\kappa(x)$ and $c(x)$ through the wall thickness, is displayed in figure 2.1.1

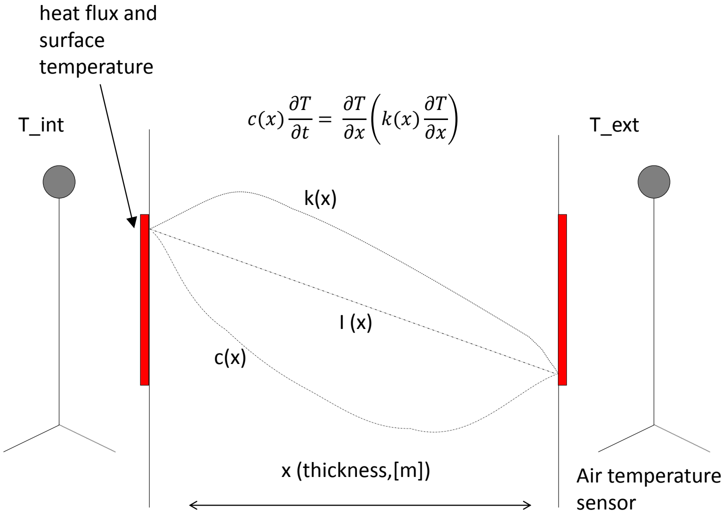

Figure 2.1.1: Diagram showing the setup of the HDM

### 2.1.1 Problem notation

The mathematical models detailed above, constitute a map that associates to the thermal properties of the building materials, the prediction of the heat flux profile at different times. In practice, the prediction times correspond to the sequence of measurement times at which the heat flux is observed. it is assumed that measurements of heat flux will be available at $2N$ time steps denoted by $(t_1, t_2, ..., t_{2N})$.

In the rest of this manuscript, the set of the unknown thermal properties characterising the models will be referred to as $u(x)$ and corresponds to

$$u(x) = (\kappa(x), c(x)) \tag{2.8}$$

The data sample will be divided in to parts: the first part $t_1, t_2, \cdots, t_N$ will be used for the calculation of the unknowns, $\kappa(x)$ and $c(x)$. In this context, the map that associates to every unknown $u$, the sequence of heat flux predictions will be called $\mathcal{G}(u)$. This will correspond to

$$\mathcal{G}(u) = (\mathcal{G}_{int}(u), \mathcal{G}_{ext}(u)) \tag{2.9}$$

where

$$\mathcal{G}_{int} = (q_{int}(t_1), q_{int}(t_2), ..., q_{int}(t_N)), \qquad \mathcal{G}_{ext} = (q_{ext}(t_1), q_{ext}(t_2), ..., q_{ext}(t_N)) \tag{2.10}$$

The second part of the data sample, $t_{N+1}, t_{N+2}, \cdots, t_{2N}$ will be used for validation. In this time window, the heat flux predictions obtained from the model described in the previous section, using the inferred values of $\kappa(x)$ and $c(x)$, will be compared against the real data. In this context, the map associating the heat flux predictions to the inferred thermal properties will be called $\hat{\mathcal{G}}(u)$ and is denoted by

$$\hat{\mathcal{G}}(u) = (\hat{\mathcal{G}}_{int}, \hat{\mathcal{G}}_{ext}) \tag{2.11}$$

where

$$\hat{\mathcal{G}}_{int} = (q_{int}(t_{N+1}), \cdots, q_{int}(t_{2N})), \qquad \hat{\mathcal{G}}_{ext} = (q_{ext}(t_{N+1}), \cdots, q_{ext}(t_{2N})) \tag{2.12}$$

A summary of the model notation is presented in figure 2.1.2

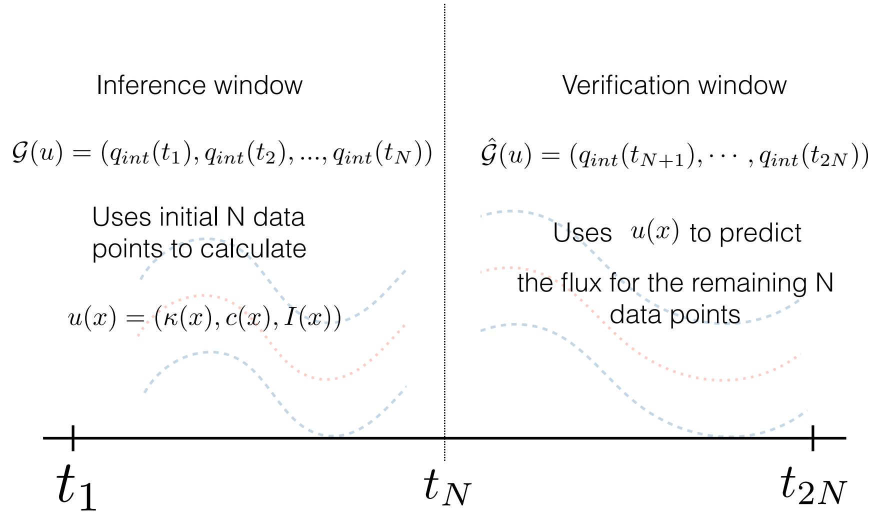

Figure 2.1.2: Diagram summarising the problem notation

#### 2.1.1.1 Convective boundary conditions

In case of modelling the heat equation (2.1) with nearby air temperature measurements denoted by $T_{int}^{air}(t)$ and $T_{ext}^{air}(t)$, the boundary condition equations have to be substituted by (2.13) -(2.14):

$$-\left[\kappa(x)\frac{\partial T(x,t)}{\partial x}\right]\Bigg|_{x=0} = -h_{int}[T(0,t) - T_{int}^{air}(t)] \qquad t \in [0, t_f] \tag{2.13}$$

$$-\left[\kappa(x)\frac{\partial T(x,t)}{\partial x}\right]\Bigg|_{x=L} = -h_{ext}[T_{ext}^{air}(t) - T(L,t)], \qquad t \in [0, t_f] \tag{2.14}$$

where $h_{int}$ and $h_{ext}$ are the combined convection and radiation heat transfer coefficients of the internal and external surfaces, respectively. In this case, in accordance to what is specified in CIBSE guide A,[8] it is assumed that

$$\frac{1}{h_{int}} = 0.13 \quad [m^2K/W] \qquad \frac{1}{h_{ext}} = 0.04 \quad [m^2K/W] \tag{2.15}$$

In a manner similar to the previous case, the heat flux can be obtained by the Fourier equation (2.16):

$$q_{int}(t) = -\left[\kappa(x)\frac{\partial T(x,t)}{\partial x}\right]\Bigg|_{x=0} \tag{2.16}$$

In contrast to the previous section where the internal temperature is known on the surface of the wall, in this case it is not appropriate to assume that the internal temperature is an interpolation between the nearby air temperatures, therefore $I(x)$ is an additional unknown in the problem considered. In a similar fashion to equation (2.6), once $\kappa(x), c(x), I(x))$ are inferred, the thermal transmittance and wall resistance can be calculated via (2.17).

$$\mathcal{U} = \left[h_{int}^{-1} + h_{ext}^{-1} + \int_0^L \frac{1}{\kappa(x)}dx\right]^{-1}, \qquad \mathcal{C} = \int_0^L c(x)dx, \tag{2.17}$$

The rest of the problem notation will be modified accordingly to include the initial temperature amongst the unknown variables:

$$u(x) = (\kappa(x), c(x), I(x), h_{int}, h_{ext}) \tag{2.18}$$

The forward maps denoted by $\mathcal{G}(u)$ and $\hat{\mathcal{G}}(u)$ will correspond to

$$\mathcal{G}(u) = (q_{int}(t_1), q_{int}(t_2), ..., q_{int}(t_N)) \tag{2.19}$$

and

$$\hat{\mathcal{G}}(u) = (q_{int}(t_{N+1}), \cdots, q_{int}(t_{2N})) \tag{2.20}$$

## 2.2 The Bayesian framework

This section provides a description of the mathematical framework adopted in this research that enabled the implementation of the heat transfer model described in subsection 2.1. The algorithm is based on *Bayesian inference*, and the problem considered here is treated as an *inverse problem.*

An *inverse problem* refers to the calculation, from a set of observations, of the causal factors that produced them. A simple example of an inverse problem is the calculation of a car speed from its breaking distance. These problems are called *inverse problems* because they start from the results (i.e. the breaking distance) and try to infer the causes that led to such results (i.e. the car speed). These problems are the inverse of the *forward problems*, which proceed from the causes to the results [78].

Within this framework, the heat transfer process can be seen as an inverse problem where the heat flux is the consequence of the particular thermal properties of the wall considered under prescribed temperature conditions.

The problem of determining the thermal properties from heat flux measurements was approached with a Bayesian inference scheme. Bayesian inference is a branch of probability that finds application in different subjects, often unusual for classical statistics, due to its ability to redefine the probability of a hypothesis once some sort of evidence is given, whereas this is not so common for other statistical approaches [79].

Bayesian inference is used to combine *prior* experience about an event with observed data to generate a *posterior* probability distribution that can then be interpreted [80].

Prior and posterior are linked by the *likelihood*. In common speech, likelihood and probability are considered synonyms, but in statistical context, in particular when solving an inverse problem, they refer to two different things. Probability is used to indicate the possible future outcomes of a result, before any observations are available, under determined hypothesises. Likelihood, instead, is used to indicate the "credibility" of an hypothesis once experimental observations of the results are available.

### 2.2.1 Problem Notation

Applying intuitively the framework described above to the heat transfer problem, the prior probability is a distribution that summarises all the a priori knowledge regarding the wall under observation: possible ranges of thermal conductivity and volumetric heat capacity, (for this study the ranges assumed are those found in literature), and initial temperature that in this work has been assumed similar to the possible range of initial temperatures specified in Annex F of ISO9869:2014 [48]. The prior is indicated by $\mathbb{P}(u)$.

The posterior probability is the result of the inference process: it is a distribution that describes the most probable values of $u$, (the thermal properties of the wall), given the data collected [81]. The posterior is denoted by $\mathbb{P}(u|y)$.

The likelihood is denoted by $\mathbb{P}(y|u)$ and in this problem it represents the probability of the observed data $y$ given a particular realisation of the unknown parameter $u$ [81].

In the case considered, it is assumed that the data ($y$) are corrupted by Gaussian random noise ($\eta$) and are related to the model described in subsection 2.1 by equation 2.21.

$$y = \mathcal{G}(u) + \eta, \qquad \eta \sim N(0, \Gamma) \tag{2.21}$$

As $\eta$ is normally distributed with mean zero and variance $\Gamma$, it gives rise to a Gaussian likelihood given by

$$\mathbb{P}(y|u) \propto exp(-\phi(y, u)) \tag{2.22}$$

where $\phi(y, u)$ represents the residuals between the model output and the data measured

$$\phi(y,u) = \Big[ -\frac{1}{2}\|\Gamma^{-1/2}(y-\mathcal{G}(u))\|^2 \Big] \tag{2.23}$$

and $\|\|$ refers to the euclidean norm between $y$ and $\mathcal{G}(u)$. The *prior* and *posterior* distributions and the likelihood are related via the Bayes' rule:

$$\mathbb{P}(u|y) = \frac{1}{\mathbb{P}(y)}\mathbb{P}(y|u)\mathbb{P}(u) \tag{2.24}$$

From equation 2.24 it can be seen that the *posterior* $\mathbb{P}(u|y)$ is known up to the normalisation constant $\mathbb{P}(y)$, as the likelihood and the prior can be defined mathematically as explained in the paragraph above and further detailed in section 2.2.2. $\mathbb{P}(y)$ is a normalisation constant, guaranteeing that the integral of the posterior probability over the whole event space equals one. From equation (2.24), it can be seen that

$$\mathbb{P}(y) = \int \mathbb{P}(y|u)\mathbb{P}(u)du \tag{2.25}$$

but, as the likelihood is defined in (2.22) - (2.23), this integral cannot be computed as in the case considered here, $u$ is a function and, upon discretisation, it will require that the likelihood is integrated over a high dimensional space. This implies that the *posterior* $\mathbb{P}(u|y)$ needs to be approximated by sampling methods such as the *Markov Chain Monte Carlo* (MCMC), since it cannot be represented in a closed form.

Values for $u$ are proposed randomly and are accepted directly when they minimise equation (2.23). After an initial burn in period, the accepted values form a reliable sample of the posterior distribution, from which we can compute mean values $\mathbf{E}(u)$ and standard deviations $\mathbf{V}(u)$. Figure 2.2.1 summarises the algorithm followed for the inference process.

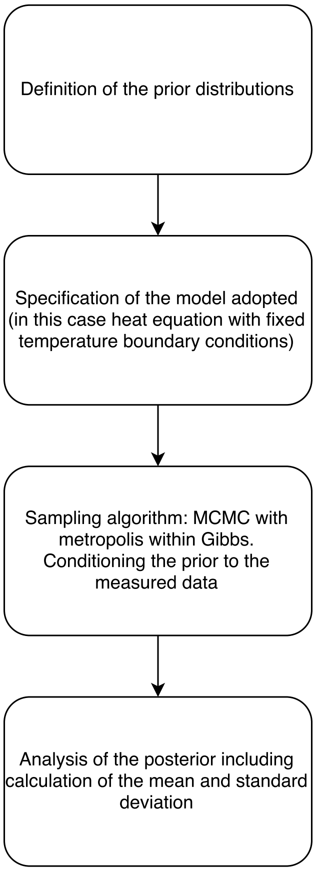

Figure 2.2.1: Flowchart summarising the inference scheme

It is important to note that the standard finite-dimensional Bayesian formalism that leads to expression (2.24) does not apply in the case considered since, as it can be seen from equations (2.1) -(2.6), the thermal properties are continuous functions varying across the wall thickness and not scalars. Still, it is applicable in the case of an RC Network with a small number of resistors and capacitors as described in section 2.4.

In practice, the heat conduction model (2.1)-(2.6) is discretized and so $u(x)$ results in a finite dimensional vector that contains nodal values of $\kappa(x)$, $c(x)$ and $I(x)$ (in the case of the model with convective boundary conditions). However, discretising gives rise to a posterior distribution $\mathbb{P}(u|y)$ defined on a high dimensional space, leading to stability problems in the scheme considered. The aforementioned issue is overcome by adopting the functional analytical Bayesian framework for inverse problems introduced in [82]. This framework provides a rigorous mathematical interpretation of expression (2.24) in the case where the unknown $u$ is a function. Moreover, within this framework it is possible to use a state-of-the-art MCMC algorithm that has been recently developed to sample posteriors defined on functional spaces [82]. The main advantage of this method is that, upon discretisation, their efficiency is independent of the dimension of the discretisation of $u(x)$. A thorough review of the Bayesian framework for functions and the corresponding MCMC methods can be found in [82, 80]

In subsection 2.2.2, a detailed mathematical description of the definition of the prior distribution and sampling algorithm adopted is given. In subsection 2.3 the details of the numerical scheme implemented to solve equation (2.1) is explained.

### 2.2.2 Mathematical description of the Prior distributions

In this section the prior distribution $\mathbb{P}(u)$ for the unknown $u(x) = (\kappa(x), c(x))$ is defined. The objective is to define priors that provide enough variability to reflect the lack of prior knowledge of the values assumed by $\kappa(x)$ and $c(x)$. First the priors for each of the components of $u(x)$ are defined. For the prior of $\kappa(x)$ a lognormal Gaussian distribution is considered. More precisely, it is assumed that

$$\kappa(x) = \kappa_0 \exp(\psi_\kappa(x)) \tag{2.26}$$

where $\kappa_0$ is a positive constants and $\psi_k$ is a Gaussian random field with zero mean and correlation function $\mathcal{C}_k$. It must be stated here, that the choice of prior modelling distributions is arbitrary, as the investigation of the literature provided only an interval of plausible values suitable to describe $\kappa(x)$ and $c(x)$, rather than a description of how these values are distributed. The selection of lognormal distributions ensures that the function $\kappa(x)$ is always positive. Biddulph et al. in [72] adopted uniform distributions as priors for the thermal properties. Both approaches are equally acceptable, as the "real" or "true" distribution of $\kappa(x)$ and $c(x)$ is not known.

The specification of the prior covariance function has an important effect on the regularity of the functions characterised by the prior. As mentioned in the previous section, appropriate specification of the prior covariance form is important to help guaranteeing the physical representation of the thermal properties (i.e. ensuring that the thermal properties vary smoothly, without presenting abrupt changes between neighbouring nodes). For the present work, a Mattern correlation function is considered given by:

$$\mathcal{C}_k(x) = \sigma_k^2 \left( 1 + \sqrt{3}\frac{|x|}{\lambda_k} \right) \exp\left( -\sqrt{3}\frac{|x|}{\lambda_k} \right) \tag{2.27}$$

where the constants $\sigma_k^2$ and $\lambda_k$ are the variance and the correlation length of the Gaussian random field $\psi_k$. The correlation length, $\lambda_k$ represents the characteristic length of the material. It reflects the distance up to which the values of the resistivity have a high correlation with each other. This implies that the change in conductivity for points close to each other will be smaller than for points further apart. In equation (2.27) this is modelled with a decaying exponential. From (2.26)-(2.27) it follows, [77], that the resulting log-normal prior distribution of $\kappa$ has constant mean and constant variance given by

$$\mathbf{E}(\kappa) = \kappa_0 \exp\left(\frac{1}{2}\sigma_k^2\right), \qquad \mathbf{V}(\kappa) = \kappa_0^2 \exp(\sigma_k^2)(\exp(\sigma_k^2) - 1) \tag{2.28}$$

In a similar fashion, an analogous log-normal distribution with mean $\overline{c}$ and variance $\sigma_c$ is defined for the prior of the unknown function $c(x)$. Figure 2.2.2 shows some samples drawn from the prior distributions of the thermal conductivity and volumetric heat capacity for different values of the correlation distance. From the three panels presented, it can be seen that for larger correlation lengths, the samples generated are smoother.

Assuming that the variables $\kappa$ and $c$ are independent, the prior on the joint variable $u(x)$ is then

$$\mathbb{P}(u) = \mathbb{P}(\kappa, c) \equiv \kappa_0 \exp(N(0, \hat{\mathcal{C}}_\kappa)) \times c_0 \exp(N(0, \hat{\mathcal{C}}_c)) \tag{2.29}$$

where $\hat{\mathcal{C}}_\kappa$, $\hat{\mathcal{C}}_c$ and $\hat{\mathcal{C}}_I$ are covariance operators that arise from the selection of our

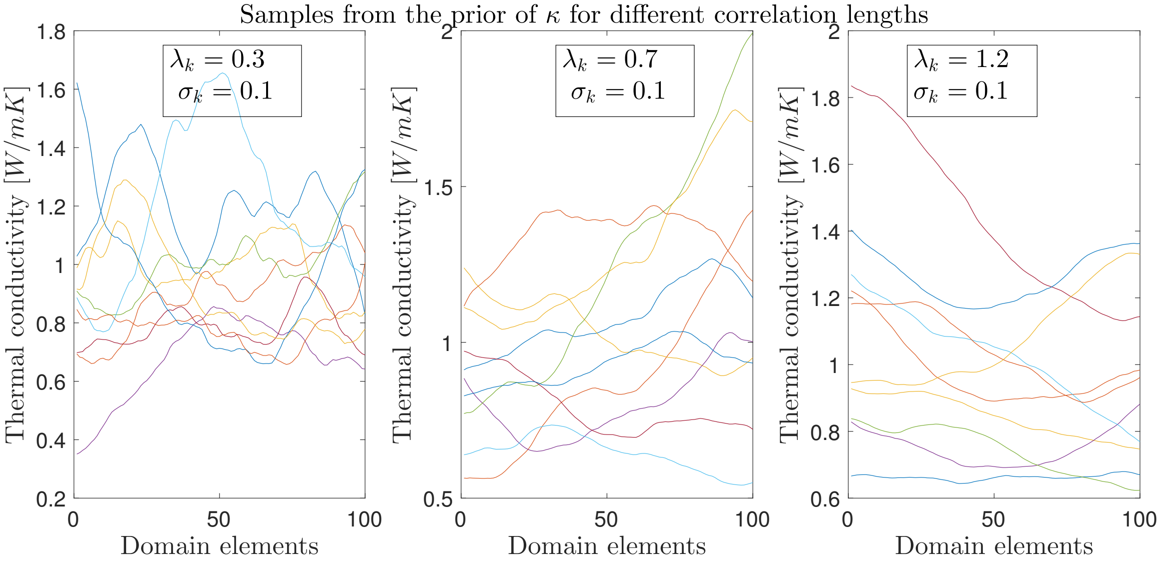

Figure 2.2.2: Samples from the priors of thermal conductivity with different correlation lengths. The $x$ axis represents the discretisation elements across the domain thickness, the $y$ axis represents the value of the thermal conductivity $\kappa(x)$

.

correlation functions $\mathcal{C}_r$, $\mathcal{C}_c$ and $\mathcal{C}_I$ respectively. The prior mean and prior variance on the joint variable $u$ are then given by

$$\mathbf{E}(u) = (\mathbf{E}(\kappa), \mathbf{E}(c)), \qquad \mathbf{V}(u) = (\mathbf{V}(\kappa), \mathbf{V}(c)) \tag{2.30}$$

To better understand the the prior distributions described above in mathematical terms, the following figures illustrate some of the concepts expressed in the previous paragraphs. In Figure 2.2.3 the mean and the standard deviation of the *prior* distribution of $k(x)$ and $c(x)$ are shown; it can be seen that these values are constant, in agreement with equation (2.28). The uncertainty band of two standard deviations around the prior mean for each of the components of the unknown $u$ are displayed. The left panel of this figure, for example, shows the prior mean $\mathbf{E}(\kappa)$ alongside with the plots of $\mathbf{E}(\kappa) + [\mathbf{V}(\kappa)]^{1/2}$ and $\mathbf{E}(\kappa) - [\mathbf{V}(\kappa)]^{1/2}$.

Figure 2.2.4, displays 100 random samples from the prior for each of the components of $u(x)$. Even if, for the selection of the prior for $\kappa$ and $c$, both the prior mean and variance are constant functions (see expression (2.28) and figure 2.2.3), samples of these prior distributions display a significant variability as a function of the wall thickness, (showing diverse possible "profiles" of how the thermal properties may vary through the wall thickness), thus incorporating a significant amount of variability within the wall. The aim is to reduce such variability by means of conditioning the prior to heat flux measurements.

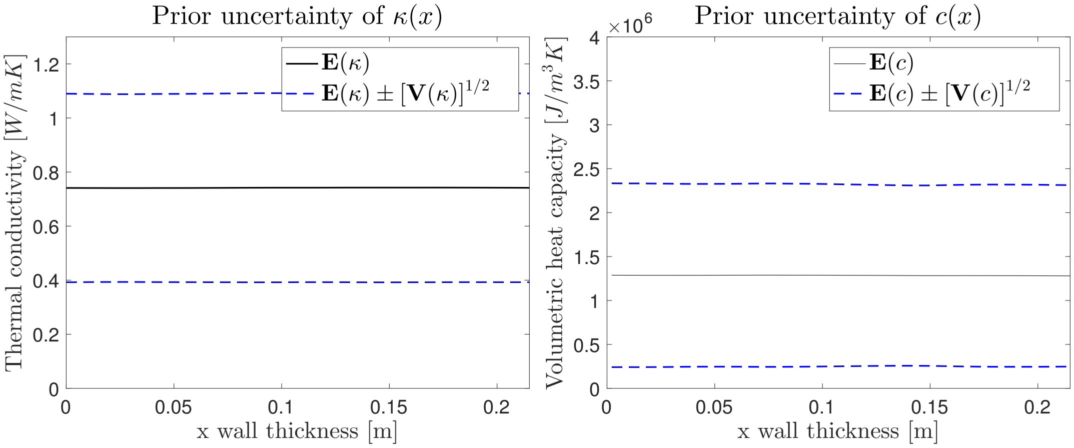

Figure 2.2.3: Mean and mean ± standard deviations of (from left to right)of $\kappa(x)$ and $c(x)$ for the prior. The figures refer to the analysis of the data collected in an environmental chamber (discussed in the next chapters) and are used here to illustrate the concepts explained in this section.

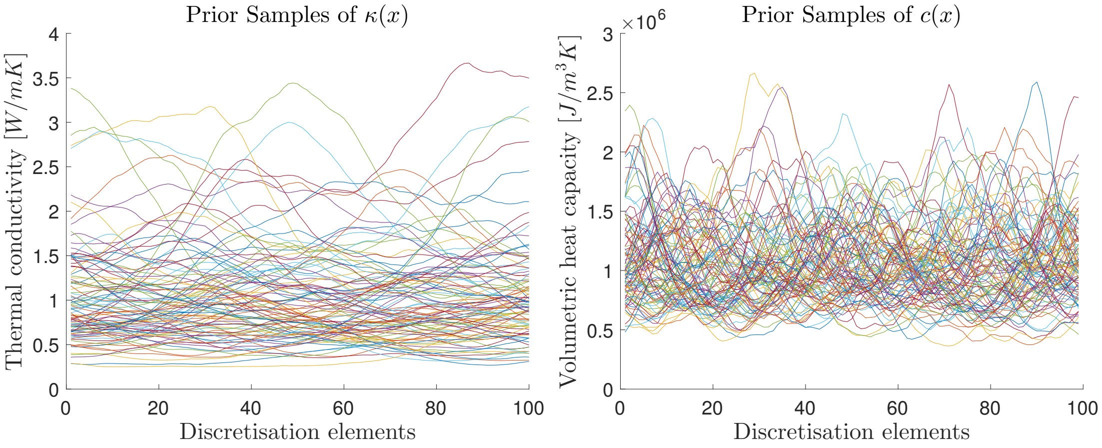

Figure 2.2.4: Left: samples from the prior of $\kappa(x)$, right: samples from the prior of $c(x)$. The figures refer to the analysis of the data collected in an environmental chamber (discussed in the next chapters) and are used here to illustrate the concepts explained in this section.

#### 2.2.2.1 Prior samples and Sampling algorithms

Drawing random numbers from a normal or uniform distribution is an easy and established practice and many routine functions such as *randn(n)* or *rand(n)* are available in nearly all software programming packages.

In the case considered here, there is the necessity to generate a random sample for a function that is normally distributed with covariance $C$. This is not a common procedure and there are no library functions available to perform the task requested. For the present work, random samples from the prior can be produced by means of Karhunen-Loeve expansion. This section introduces the algorithm implemented, and more detailed technical descriptions of the generation of Gaussian (or log-normal) random functions with a specified mean and correlation function can be found in [82].

Suppose that, as in the case of the thermal conductivity, the function $\kappa(x)$ depends on a particular realisation of the Gaussian random field $\psi_\kappa$ with mean zero and correlation $C_\kappa$, (equations (2.26)-(2.27)). From the correlation function, equation (2.27), the covariance matrix C can be constructed depending on the variance and correlation length of the Gaussian random field. If the covariance matrix C can be decomposed as

$$C = VDV^T, \tag{2.31}$$

then a random realisation $\nu$ of the Gaussian random field $\psi_\kappa$ can be constructed from the decomposition of the covariance matrix C

$$\nu = V\sqrt{D}\xi_k \tag{2.32}$$

Here $\xi_k$ is a random vector drawn from a normal distribution N(0,1), V in the matrix containing the eigenvectors of the covariance matrix, and D is the diagonal matrix containing the eigenvalues of the covariance matrix.

To carry out the simulations in the Bayesian framework described in section 2.2, several sampling schemes have been adopted. This section offers a brief description of the algorithms employed: Markov Chain Monte Carlo (MCMC) and Metropolis within Gibbs. The algorithm described above for drawing proposals from the priors was integrated in the sampling schemes as illustrated in the flowchart in figure 2.2.5.

*Markov Chain Monte Carlo, MCMC*

A Markov Chain is a stochastic process where, given the present state, past and future states are independent [83]. An example of a Markov Chain sequence is the succession of steps of a *random walk*. In the case of the random walk, a particle can move left or right on a line with equal probability, independently of the previous steps. Markov Chains are used to build a sequence of random draws with a prescribed transition probability $P$. Under certain conditions, it can be shown that, for a large number of steps, a Markov chain will approach a *stationary distribution*, or *equilibrium distribution* [83] denoted by $\pi(x)$. Once the stationary distribution has been reached, the chain retains this distribution for all the subsequent stages[83]. Stationary distributions have finite variance and constant mean.

A Markov Chain Monte Carlo is a sampling algorithm that exploits this property: the aim is to design a Markov Chain that has the desired equilibrium distribution. After an initial number of steps, called *burn in* period, the MCMC outcomes are samples of the desired distribution, in the case considered here, this is the posterior distribution of the thermal properties of the wall under consideration.

The MCMC presents some limitations and leaves some open questions, such as “How many iterations are necessary to explore the posterior appropriately?” or “How is it possible to determine whether convergence has been reached?”, “Are the samples chosen an appropriate representation of the posterior?”. These problems are addressed by convergence diagnostics procedures. Convergence diagnostics is a wide branch of research and a thorough review of MCMC convergence diagnostics has been presented in [84]. Ultimately, convergence diagnostics cannot indicate whether the chain has converged but can clearly demonstrate if it has not.

For the purpose of the work carried out for this PhD research, convergence of the chain has been assumed after $10^6$ iterations. The strategy employed to verify the convergence was the monitoring of the decay of residuals (2.33) as the iterations increased: if the residuals stabilise on a constant value, it is assumed that the chain has converged and the samples drawn after residual stabilisation are samples from the target distribution.

$$|y - \mathcal{G}(u_j)|^2 \tag{2.33}$$

The appropriate characterisation of the posterior distribution is assessed by means of trace plots. Trace plots are constructed by plotting the value of the sample draw versus the iteration number. If the samples explore accurately the posterior distribution (often referred to as the mixing of the chain), trace plots will tend towards a constant mean and variance (i.e. it will resemble white noise) [84]. In the work considered here, the trace plots given by the values of the thermal conductance and heat capacity are considered to assess convergence. The assessment of the trace plots is done visually and no further mathematical calculations are employed.

*Metropolis within Gibbs*

Metropolis within Gibbs indicates an algorithm to propose new samples. It stems from the combination of the Gibbs scheme and the Metropolis-Hastings scheme. The Gibbs algorithm can be applied when the unknown sought can be divided into components and the distribution of the individual components are available. This is the example considered in this research, the unknown $u(x)$ comprises two components $(\kappa(x), c(x))$ and, as mentioned in section 2.2 and detailed further in 2.2.2, each component is drawn from a separate distribution. The Gibbs sampler allows a single component to be updated, for instance the thermal conductivity $\kappa(x)$, while fixing the remaining variables. Once the first component has been updated, the algorithm proceeds to updating the remaining parameters, using the latest values of the previous components.

The Metropolis-Hastings scheme is an algorithm to design a Markov chain that converges to a desired stationary distribution, $\pi(x)$. The scheme involves designing a symmetric transition probability from a given state $x$ to a new state $y$, i.e. $P(x|y)\pi(y) = P(y|x)\pi(x)$. This takes place in two sub-steps: the proposal step and the acceptance/rejection step. Suppose that the chain is the state $x$. A new state $y$ is proposed from a chosen proposal distribution $r(y|x)$ and accepted with a probability $\alpha(y|x)$ so that $P(y|x) = r(y|x)\alpha(y|x)$, and similarly $P(x|y) = r(x|y)\alpha(x|y)$ . Inserting theses expressions in the above transition probability yields the following expression:

$$r(y|x)\alpha(y|x)\pi(x) = r(x|y)\alpha(x|y)\pi(y) \tag{2.34}$$

The probability $\alpha$ is chosen to favour transitions to more probable states: if the number of moves from $x$ to $y$ doesn't have to be reduced, $\alpha(y|x) = 1$ and similarly $\alpha(x|y) = 1$ if the number of transitions from $y$ to $x$ does not have to be reduced. In the case where the number of transitions from $x$ to $y$ needs to be reduced then,

$\alpha(y|x) = 1$ as the transitions from $y$ to $x$ do not need to be reduced, and $\alpha(y|x)$ is chosen as $\frac{r(x|y)\pi(y)}{r(y|x)\pi(x)}$. A similar argument can be made for $\alpha(x|y)$. In this way the general formula for $\alpha$ is [79]:

$$\alpha(y|x) = min\left[\frac{r(x|y)\pi(y)}{r(y|x)\pi(x)}, 1\right] \tag{2.35}$$

In practice, the Metropolis-Hastings scheme can be summarised as follows [79]:

1. Propose a candidate $y$ from $r(y|x)$
2. Calculate
$$\alpha(y|x) = min\left[\frac{r(x|y)\pi(y)}{r(y|x)\pi(x)}, 1\right] \tag{2.36}$$
3. Generate a random number $v$ $U(0,1)$ from a uniform distribution on $(0,1)$
4. If $v \leqslant \alpha(y|x)$, $y$ becomes the next element in the chain, otherwise retain the previous state $x$.

In the case considered in this work the proposal distribution $r(y|x)$ is chosen as equation (2.37) and the acceptance distribution is equation (2.38)

$$r(y|x) = \sqrt{1-\beta^2}x + \beta\xi \tag{2.37}$$

$$\alpha(y|x) = exp\left[\frac{1}{2}(\phi(x) - \phi(y))\right] \tag{2.38}$$

In equation (2.37), $x$ is the current state of the chain and $\xi$ is a random draw from the prior distribution, obtained following the procedure described an the beginning of this section and $\beta$ is a positive value, $0 \leq \beta \leq 1$ that determines the acceptance rate of the new proposals.

In equation (2.38) the function $\phi$ is the residual function denoted by equation (2.23).

Looking at equation (2.37), it can be seen that if $\beta = 0$, then the new proposal is identical to the current state, and the chain does not evolve. If $\beta = 1$, the new proposal is just a random sample from the prior, thus making it more difficult for the chain to converge. In the work produced, $\beta$ has been calibrated to maintain a healthy acceptance rate of the new proposals of approximately 30% [77].

A direct consequence of generating new samples via equation (2.37), is the correlation of nearby samples. This means that a set of outcomes close to each other do not reflect the correct target distribution. In order to obtain a set of samples representative of the target distribution, it is necessary to select outcomes that are sufficiently apart for each other to be considered uncorrelated. Such minimum distance is given by the sample's autocorrelation. This is further discussed in chapter 4, where the MCMC results obtained are presented and analysed. A copy of the MCMC scheme used for the data analysis described in chapters 4 and 5 is included in appendix A.

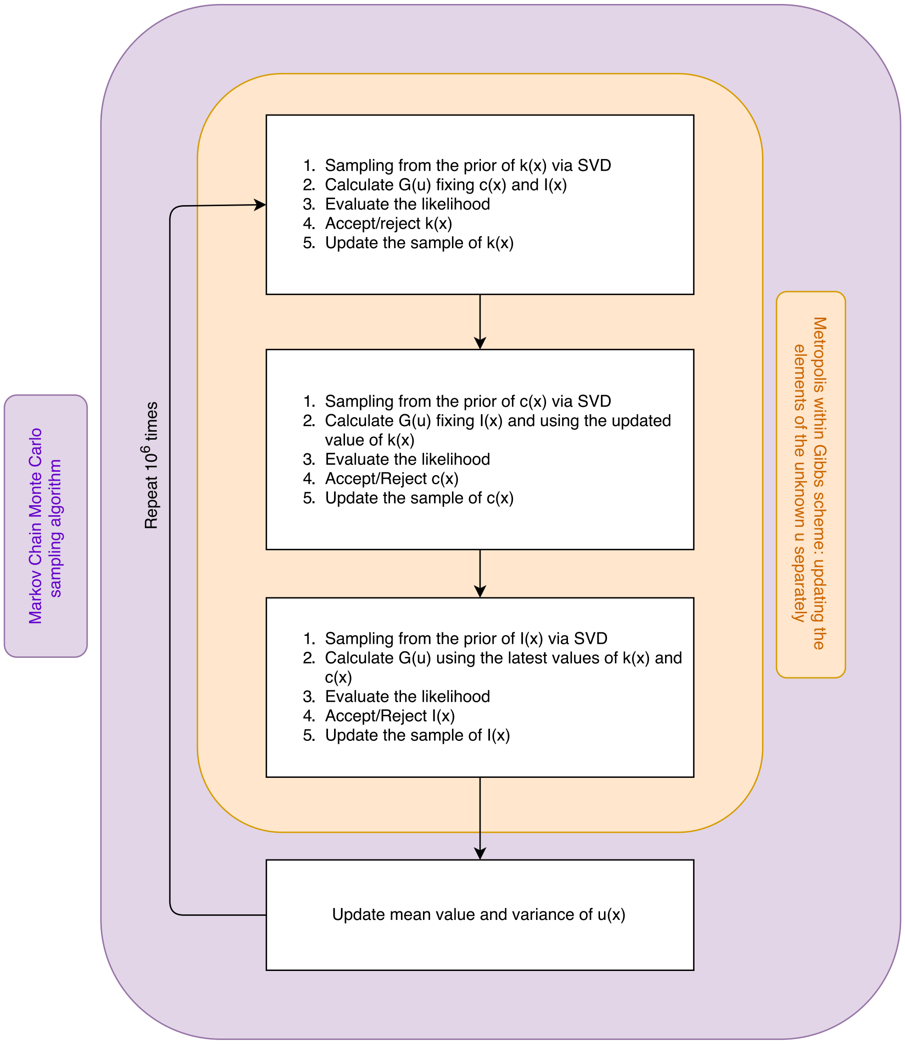

Figure 2.2.5: Flowchart detailing the sampling schemes structure adopted in the calculations

## 2.3 Numerical scheme

This section describes how the model presented in sections 2.1, 2.2 and 2.2 was implemented numerically. All the simulations were carried out using MATLAB. For the present example the domain (thickness of the wall) was discretized with $10^2$ nodes and cell-centred finite differences. This gives rise to the discretised heat equation form (2.39):

$$T_{m-1}^{i+1} - 2T_m^{i+1} + T_{m+1}^{i+1} = \frac{c\Delta x^2}{\kappa \Delta t}(T_m^{i+1} - T_m^{i+1}) \tag{2.39}$$

where $m$ represents the $m^{th}$ spatial element, the script $i$ the time step taken in consideration, $\Delta x$ is the spatial element and $\Delta t$ the time step.

## 2.4 Single Thermal Mass model

The Single Thermal Mass model, from hereon defined STM, was named so by Biddulph et al. [72]. It represents an RC network model with two resistors and one capacitor, as sketched in Figure 2.4, with a single internal temperature node $T_{mass}^i$.

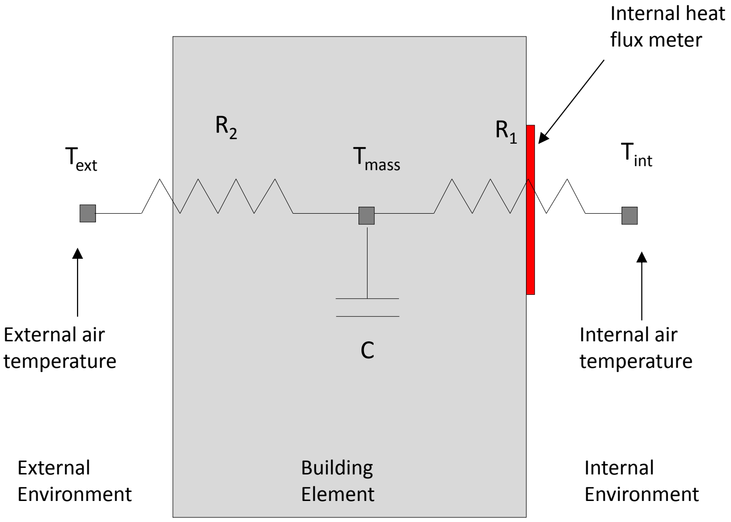

Figure 2.4.1: RC network and measurement configuration.

The discretised equation that describe the STM is

$$C\frac{T_{mass}^{i+1} - T_{mass}^{i}}{\Delta t} = \frac{T_{int}^{i+1} - T_{mass}^{i+1}}{R_1} + \frac{T_{ext}^{i+1} - T_{mass}^{i+1}}{R_2} \tag{2.40}$$

where $C$ is the heat capacity per unit of area (or thermal mass per unit of area), $\Delta t$ is the time step and $R_1$ and $R_2$ are the resistances per unit of area for the first and second cell of the discretized domain. $T^n_{int}$ and $T^n_{ext}$ corresponds to the internal and external temperatures. Note that for this model, the unknown/uncertain parameters are represented by 4 scalar values:

$$u = (R_1, R_2, T^0_{mass}, C) \tag{2.41}$$

If $u$ is known $T^n_{mass}$ can be computed via (2.21) and then heat fluxes can be obtained using

$$q^n_{int} = \frac{T^n_{int} - T^n_{mass}}{R_1}, \qquad q^n_{ext} = \frac{T^n_{mass} - T^n_{ext}}{R_2} \tag{2.42}$$

Thus, for the STM model, the forward map is given in terms of the following expression

$$\mathcal{G}_{STM}(u) = (q^1_{int}, \cdots, q^n_{int}, q^1_{ext}, \cdots, q^n_{ext}) \tag{2.43}$$

Similar to the previous subsection, the inverse problem is to find $u$ given noisy measurements of $\mathcal{G}_{STM}(u)$. Note that once $u$ is obtained, the thermal mass $C$ is automatically known, while the resistance can be simply computed by means of $R = R_1 + R_2$ and then the U-value by finding the reciprocal of the resistance, $U = 1/R$. Also in this case, it was assumed that the data $y$ and the unknown $u$ are related by means of

$$y = \mathcal{G}_{STM}(u) + \eta \qquad \eta \sim N(0, \Gamma) \tag{2.44}$$

where $\eta$, as before, is random noise and $\mathcal{G}_{STM}$ is the forward map defined by the STM model from 2.40. Note that, in this case, $u$ is a four dimensional vector rather than a function, thus the computational problem arising from the need to compute a large number of variables does not occur. This means that the priors describing $u = (R_1, R_2, C, T^0_{mass})$ are represented by probability distributions on real intervals, rather than by functional spaces. This implies that the sampling of the priors can be performed using routine functions that generate random numbers such as *randn*.

The posterior is $\mathbb{P}(u|y)$ is characterised by conditioning the unknown parameter $u = (R_1, R_2, C, T^0_{mass})$ to heat flux observations. This means that a new sample for $u = (R_1, R_2, T^0_{mass}, C)$ is accepted if it reduces the residuals between the model output (2.42) and the heat flux data measured.

# Chapter 3

# Experimental data collection

This chapter describes the method followed to collect the data necessary for the validation of the HDM. Three sets of data were collected: one set was collected under laboratory conditions in an environmental chamber (§3.2) available at the University of Nottingham Innovation Park, one set was collected in a unoccupied solid walled house (§3.3) and the last set in an inhabited office space (§3.4). For each study, details of the construction and the experimental procedure is given.

In addition, the model was tested on a data set collected by BSRIA. This dataset was previously employed by Biddulph et al, [72] to validate their RC network model with a single capacitor. Their data are used here to trial the proposed model against already published results that have been subject to an independent process of validation.

## 3.1 Methodology

The method adopted in this research for the verification and validation of the model was to utilise data collected in different environments, where the researcher has different levels of control on the experimental setup.

The data set collected in the environmental chamber offers ideal conditions for the verification of the model, as the chamber allows to control the temperature profiles of the internal and external environment and to exclude random effects dictated by the weather conditions, thus outside the researcher's control, such as solar radiation and wind. In other words, in the environmental chamber it is possible to collect a set of experimental data in a setting as close as possible to the physical model described by equations (2.1) - (2.5).

In a second moment four other datasets have been collected in locations that offer only the possibility of a partially controlled environment. These sets were necessary for the validation of the model and to assess whether the model proposed is able to reach the targets outlined in the aims and objectives in a realistic scenario, where the researcher cannot exclude the influence of unexpected weather changes.

In the data collection, different wall constructions have been monitored, as one of the aims of the model proposed is to be able to characterise different constructions without prior knowledge of the construction details.

## 3.2 Environmental chamber tests

Due to the nature of the problems investigated in the built environment, often focussing on the behaviour of building elements or whole building assessment, experimental campaigns are often conducted in real buildings and thus affected by weather dependent phenomena like wind, sunshine and rain. The purpose of conducting tests in an environmental chamber, is to collect data from a controlled environment, thus excluding the influence of parameters outside the researcher's control that could affect the experimental observations.

Environmental chambers permit the control of parameters affecting the performance of building elements (temperature difference, relative humidity, radiation) and therefore offer an ideal scenario to test the behaviour of specific construction materials.

The aim of the tests carried out in this environment were to study the behaviour of solid wall and cavity wall construction (two extremely common building constructions) under ideal conditions, thus producing a data set as close as possible to the theoretical heat transfer model described in the previous chapter.

Two different tests were carried out with this setup: one simulating steady state conditions and one replicating "real" temperature conditions. In the latter, the external temperature profile was modelled on data collected from a local weather station and the internal temperature was maintained constant.

### 3.2.1 Environmental chamber preparation

The chamber available in Nottingham University is composed of two rooms separated by a partition wall, with one room able to slide on a set of rails in order to modify the composition of the partition wall, as indicated in Figure 3.2.1. The internal dimensions of the two rooms were 3.70 x 3.50 on plan with a height of 2.38m.

The partition wall was divided in two parts: the upper part comprised a timber frame lined with mounted plasterboard, the lower part comprised four sections of brickwork: three of a solid wall construction and one of cavity wall construction. Figures 3.2.2-3.2.4 show the wall sections monitored and the measuring equipment used.

The timber frame was filled with three layers of 7cm thick phenolic foam board insulation. In order to encourage unidirectional heat flow through the individual samples of brick wall, each was thermally isolated from its neighbour and the chamber using a 20 cm layer of insulation.

The face dimensions of each brick wall sample were 970x600x210 mm and each section was separated from its neighbour by a layer of insulation material. The cavity wall was filled with EPS, the insulating layer was 5 cm thick.

Figure 3.2.1: Environmental Chamber

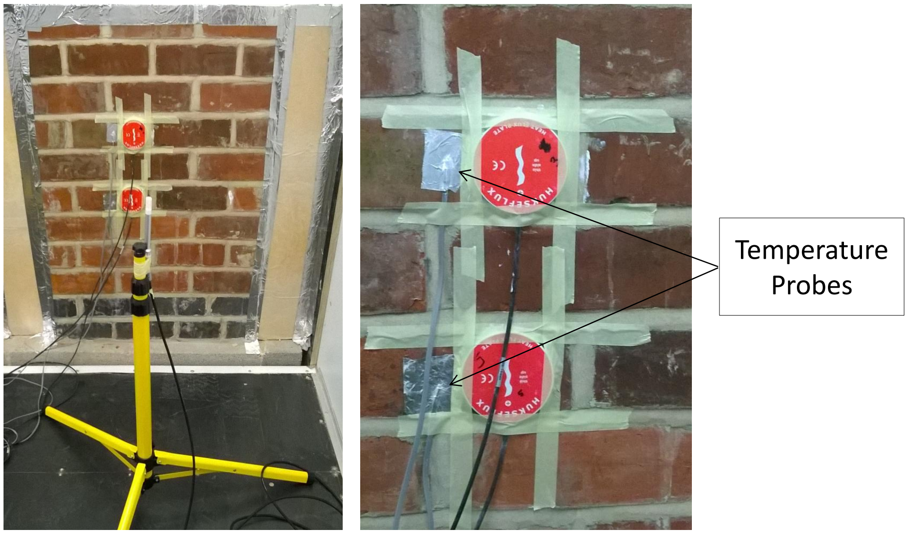

Figure 3.2.2: Experimental equipment placed in front of each wall, details

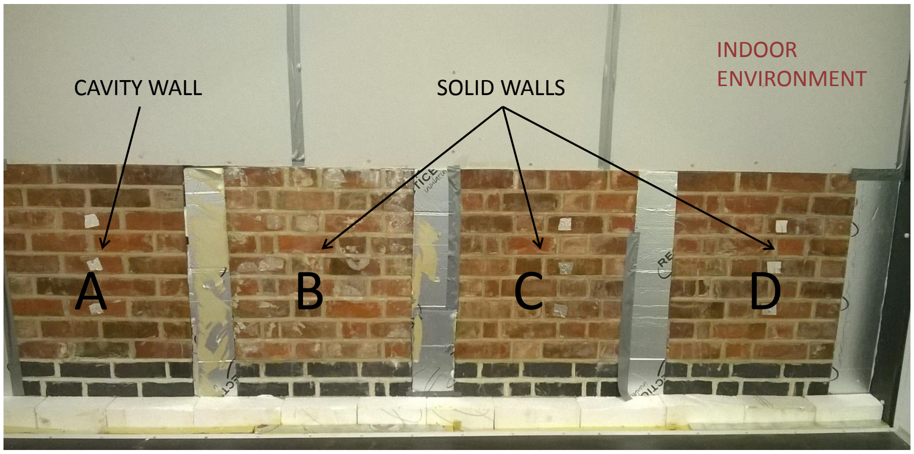

Figure 3.2.3: Brick walls in left room

Figure 3.2.4: First layer of insulation fitted into the cavity of the timber frame wall

### 3.2.2 Experimental instrumentation

For the purpose of this experiment, the air temperature, surface temperature and heat flux were monitored continuously during the observation period. This has been carried out employing heat flux sensors, temperature probes, and temperature and relative humidity sensors. This sections offers a description of the working principles of the instruments used.

*Platinum Resistance Thermometers*

Platinum resistance thermometers are a common temperature sensor belonging to the family of resistance temperature detectors (RTDs). Their working principle is based on the measurement of the resistance of a platinum element. The relationship between temperature and resistance is almost linear for small temperature variations.

*Heat flux sensor*

The heat flux plates used in this study are flat discs of ceramic-plastic composite material of known thermal conductivity encasing the sensing element in the centre. The sensing element comprises in a thermophile generating a voltage output proportional to the temperature difference across the body of the heat flux sensor.

The heat flux through the sensor is proportional to the temperature difference across the sensor divided by the effective thermal conductivity of the body [5]. Figure 3.2.5 shows an image of the Hukseflux HFP01 heat flux sensors used in the experimental setup.

Figure 3.2.5: Pictures of the heat flux sensors used in this study. Left: face in thermal contact with the element studied, right: side in contact with the environment [5]

#### *Temperature and Relative humidity sensors*

The CS215 [6], is a Campbell Scientific temperature and relative humidity probe uses a digital humidity and temperature sensor produced by Sensirion (SHT75)[85]. The sensor integrates sensor elements and signal processing to provide directly a fully calibrated digital output. A picture of the probe and the sensor are displayed in figure 3.2.6

#### *Thermocouples, T-type*

Thermocouples are widely used temperature sensors based on the thermoelectric principle, i.e. the generation of a voltage differential in a metal subject to a temperature gradient.

In practice, thermocouples consist of a junction of two dissimilar conductors that have a different response to the temperature gradient. In this way, at the opposite

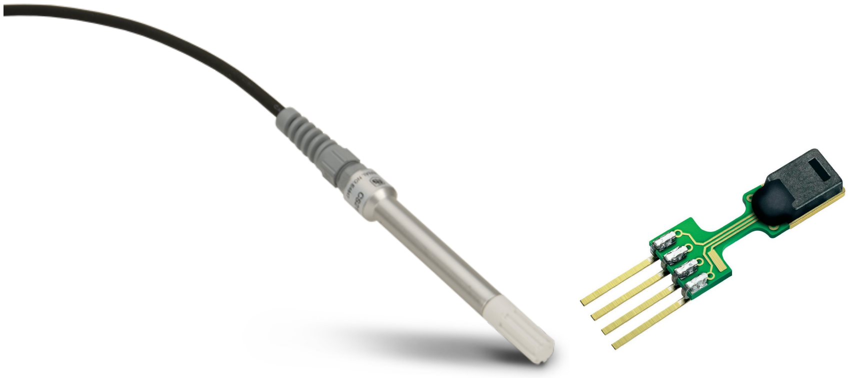

Figure 3.2.6: Pictures of the Temperature and Relative Humidity probe and its digital sensor, [6]

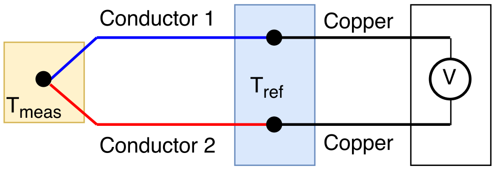

Figure 3.2.7: Diagram explaining the configuration of a thermocouple

ends of the junction, a voltage difference can be measured and this is proportional to the temperature differential experienced by the single metals.

From the voltage measured it is then possible to obtain the temperature of the body observed. Figure 3.2.7 explains the functioning of a thermocouple.

Table 3.2.1: Summary of the measuring equipment, by function and accuracy

| Name | Function | Accuracy |
|---|---|---|
| HFP01 | Heat Flux measurement | ± 5% |
| CS215 | Relative humidity and temperature probe | RH ± 1.8%, °C ± 0.3 |
| PT100 | Temperature measurement | °C ± 0.1 |
| T-type | Temperature measurement | °C ± 0.5 |

### 3.2.3 Instrumentation set-up

The instrumentation employed in this experiment amounts to 16 heat flux sensors (Hukseflux, HFP01 [5]) 18 temperature probes (PT100), 8 Temperature and relative humidity sensors (CS215 temperature and relative humidity probe, [6]) one data logger and expansion module (DataTaker, DT85 and CEM20, [47]).

For each brick section, two heat flux sensors (HFP01) were positioned vertically at the centre of the wall, and next to each heat flux sensor a temperature probe (PT100) was installed to measure the local surface temperature. The air temperature and relative humidity sensors (CS215) were supported on a tripod situated 50 cm from the surface of each wall sample and 70cm from the floor. This instrumental setup was replicated on each side of the wall.

Figure 3.2.8 shows a schematic diagram of the positioning of the sensors on both rooms and details on one of the wall samples are shown in Figure 3.2.2.

The room on the left, Room 1, was designated as the internal environment and the room on the right, Room 2, designated as the external environment. All the measuring equipment was numbered and connected to the data logger (DT85, CEM20). The data were recorded once per minute. The wall sections were denoted using the letters A,B,C,D, wall A being the cavity wall and B,C and D solid walls as indicated in Figure 3.2.3.

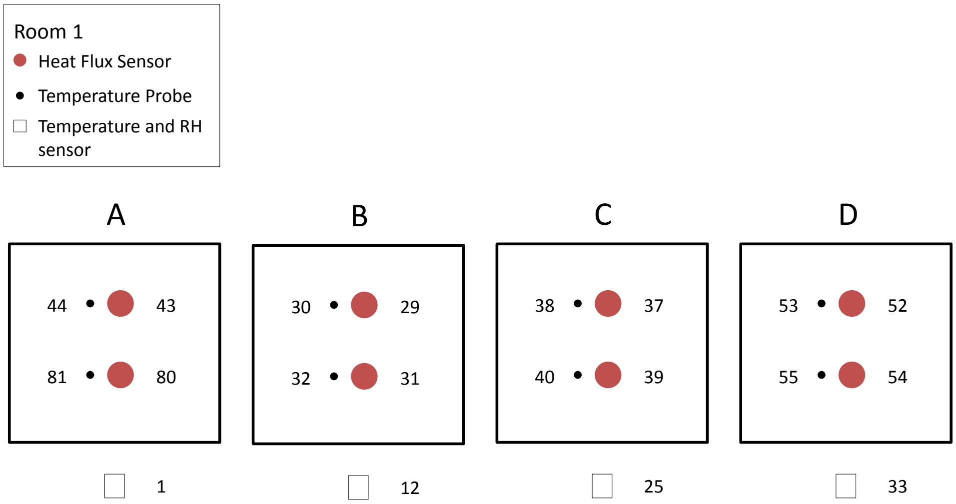

Figure 3.2.8: Diagram explaining the position of the sensors in Room 1

### 3.2.4 Steady state

The first test measured the heat flux through the wall samples under steady state conditions. This was necessary to obtain reference values for the U-value of the specimens tested.

The indoor temperature was set at 25°C while the external temperature was set at 5°C. The RH in Room 1 was fixed at 60 % and in Room 2 at 80% to represent notional values found in practice, however it is assumed that RH does not influence measured and predicted heat flux. The chamber was operated continuously for four days under these conditions.

### 3.2.5 Non steady state

For the second test, the temperature in the indoor environment was kept constant at 22 °C, with 50% relative humidity. The temperature of the outdoor environment was modelled on hourly weather data collected from the weather station in the in the

Department of Architecture and Built Environment. The data recorded were relative to the week 8-15th February 2014. The minimum temperature was 1.4°C, registered at 9am on 10th of February and the maximum temperature was 10.8 °C, registered at 6pm on 12th of February. The relative humidity in this test was kept constant at 55% in each room.

In order to generate suitable figures to program the environmental chamber, the hourly data were fitted using a spline and the values of the fit were interpolated for every minute of the week. The temperature profile was modified and smoothened in order to achieve a variable but representative profile that excludes the peaks and sharp variations that can be observed in hourly data. These data were fed into the chamber, the temperature profile produced being displayed in Figure 3.2.9

The aim of this experiment was to study the specimen under more realistic conditions, excluding the effect of solar radiation and unpredictable weather phenomena. The data were recorded every minute for 7 days. Table 3.2.2 summarises the nature and length of each test.

Table 3.2.2: Summary of all the tests carried out in the environmental chamber in Jubilee

| Test | Length | Description |
|---|---|---|
| Test 1 | 4 Days | steady state 25-5 °C |
| Test 2 | 7 Days | real outdoor data |

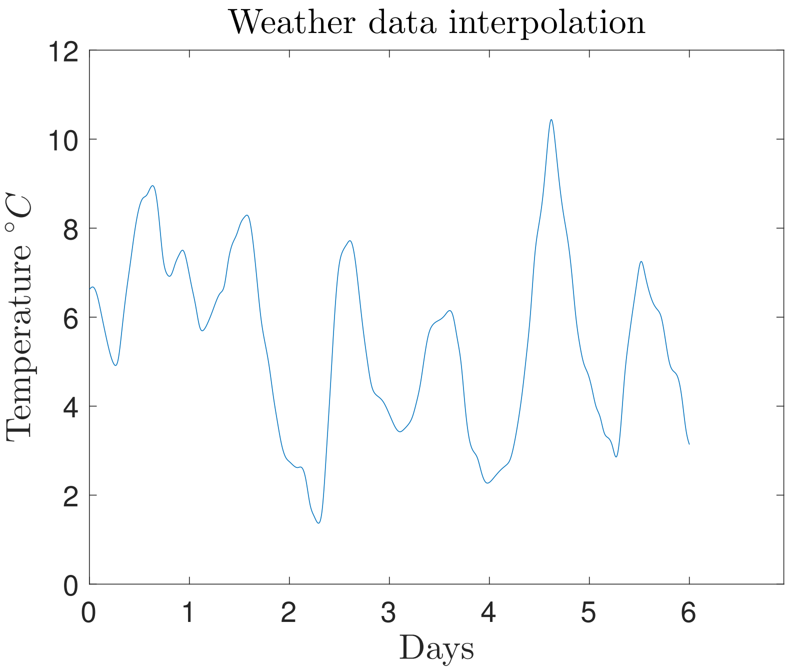

Figure 3.2.9: Final temperature profile obtained from the interpolation of the weather data

## 3.3 Unoccupied solid wall property

This section describes the experimental set up followed to monitor 5 Wortley Hall Close, a solid wall unoccupied property located in the University Park of the University of Nottingham. The data were collected during the period 12-19 March 2016.

The four bedroom property is a two floor, solid wall, detached house, representative of the UK hard to treat stock and it can be seen in the top of figure 3.3.1. The room monitored was located on the ground floor, facing north east, with windows facing north and south, see the bottom of figure 3.3.1.

The wall investigated in this experiment is the east facing wall as the north facing wall was not suitable due to the small dimensions combined with the presence of a window. Thermal images of the wall are presented in figures 3.3.1 - 3.3.2.

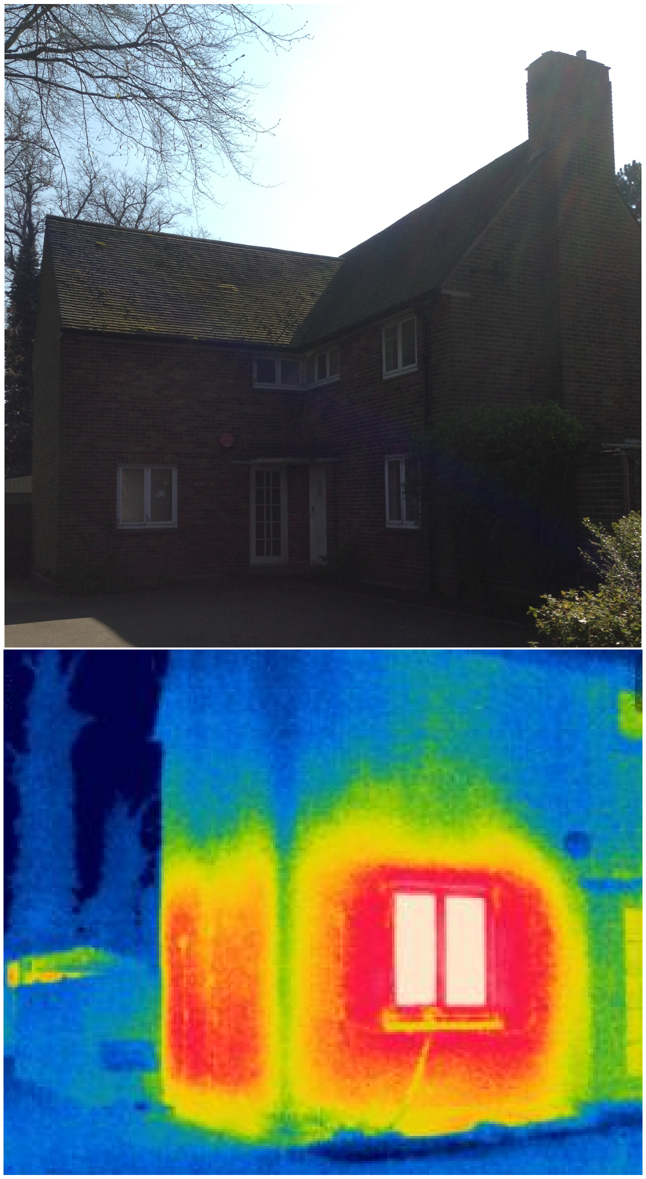

Figure 3.3.1: A picture of the property studied taken during the day and an infrared picture of the room under investigation

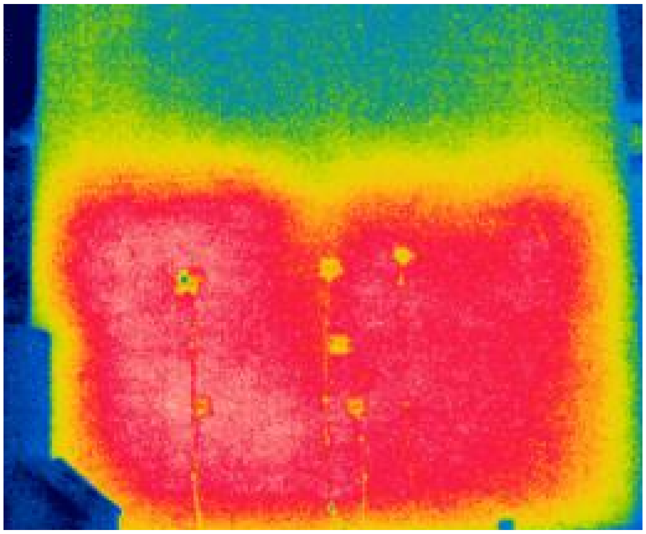

Figure 3.3.2: Figure showing the external thermal image of the monitored wall.

Internally, the east wall presents a large central thermal non-uniformity that could be attributed to a non-uniformity in the wall construction, such as a chimney or flue. This inhomogeneity was identified with the infrared camera and the information was used to obtain a clear image of the boundaries of the defect and optimise the position of the sensors.

The infrared mapping of the internal wall was not as straightforward as in the external case, as the small dimensions of the room did not allow the capture of the whole wall in a single shot. To address this the wall was divided into six portions and the final image was obtained by stitching together the six images.

As the cables and the equipment attached to the wall have a different emissivity than the plaster finish, they reflect radiation differently, thus disturbing the final image. In order to obtain a clean image of the wall by itself, as a first step, the brightest pixels have been substituted by a random pixel in their neighbourhood. This first step was called dampening. Following this, the image has been filtered with a median filter and finally with a gaussian filter. Figure 3.3.3 shows the different stages of image elaboration: dampening, median filtering and gaussian filtering.

The presence of a non-visible defect in the wall, provides an opportunity to explore whether the model developed is able to provide some insightful information that could inform the experimenter about the non-standard construction lying under the surface without having prior knowledge of it.

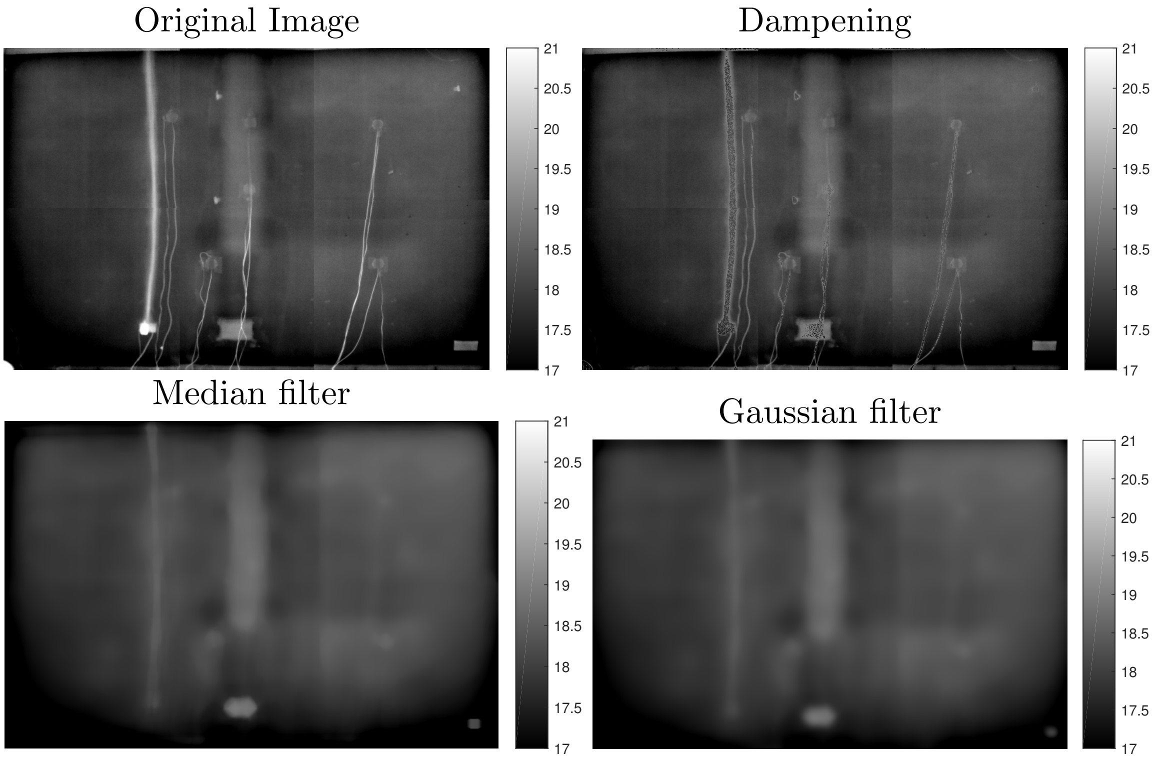

Figure 3.3.3: Different stages of the thermal image elaboration. Top left: original image. Top right: Dampening. Bottom left: Median Filter. Bottom right: Gaussian filter

### 3.3.1 Experimental setup

In a similar fashion to the monitoring setup carried out in the environmental chamber, the east wall was monitored in 6 locations with 6 hukseflux heat flux plates (HFP01) [5] and 6 platinum RTDs (PT100). The locations were chosen to be representative of the wall, therefore 4 heat flux plates were placed on a uniform defect free part of the wall and the other 2 heat flux meters were placed on the non uniformity. Figure 3.3.4 shows a diagram with the internal dimensions of the room and the position of the equipment, and figure 3.3.5 shows the location of the heat flux sensors and temperature sensors on the internal wall.

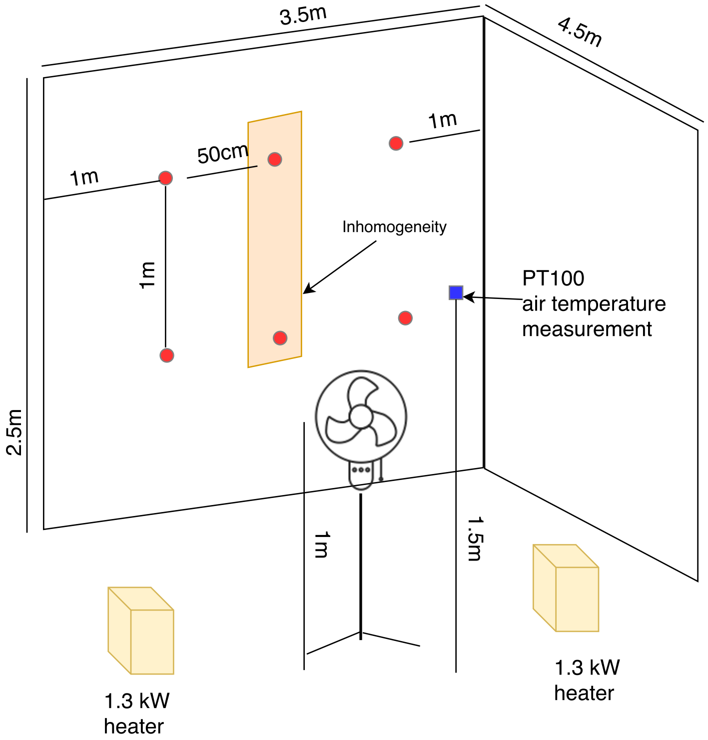

Figure 3.3.4: Diagram showing the dimensions of the room and the position of the equipment.

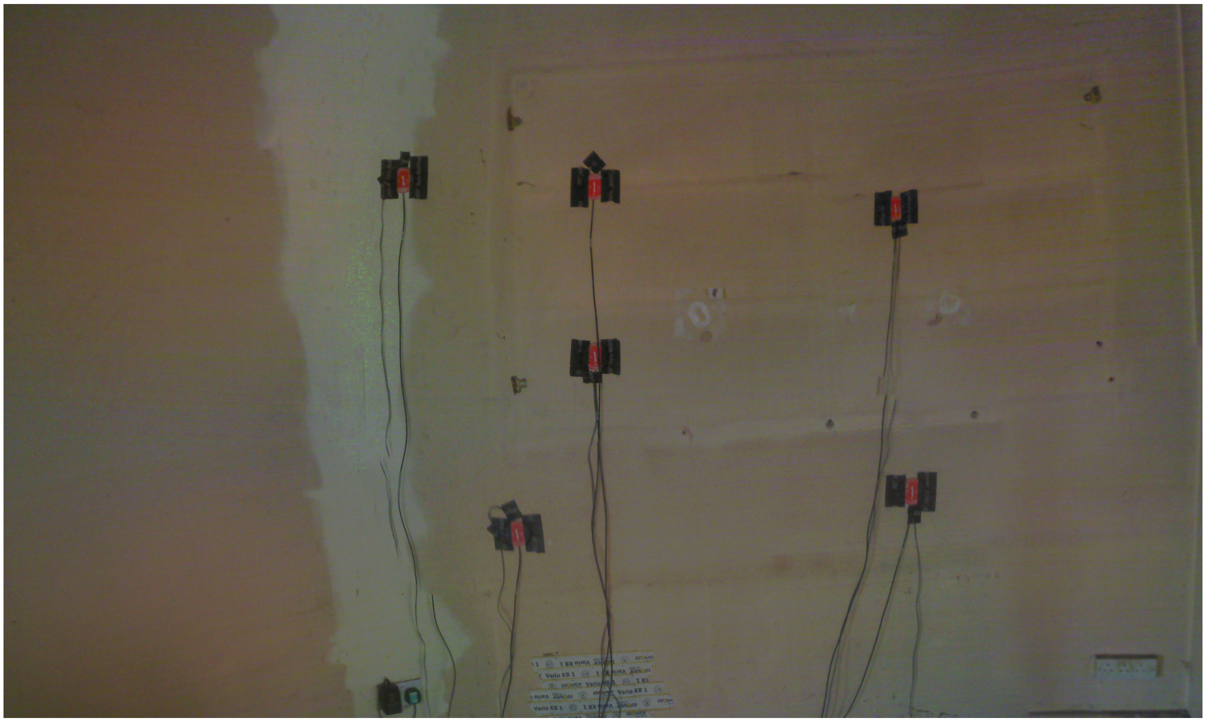

Figure 3.3.5: Figure showing the equipment setup on the north-east facing wall.

The internal room temperature was conditioned by means of electric heaters [86] and thermostats, while the external temperature was determined by the weather conditions. The internal air temperature was monitored with a separate RTD hanging from the centre of the room at approximately 1.4 m from the floor.

Two electric heaters (1.3 kW each) were connected to a thermostat that was placed in the centre of the room. The thermostat was bespoke and comprised a PT100 temperature sensor connected to a chiller stat. The system thus set up constrained the indoor temperature within $0.5°C$ of the desired set point. An electric fan was employed to distribute the warm air uniformly through the space. A pyranometer was added on the external side of north east facing wall to monitor the solar radiation incident on the surface.

The external surface of the wall was equipped with 6 RTDs (PT100) approximately coinciding with the internal RTDs. The external air temperature was monitored with an RTD placed in the porch in front of the front door, (see top part of figure 3.3.1), a location shaded from the sun and reasonably well protected from wind and rain. All the sensors were connected to a DT85 data logger with a CEM20 expansion. The data were collected once per minute. The test started in the evening of 12/03/16. For the first two days the temperature was set at 25.5 °C and it was then reduced to 21°C. At the end of the experiment the heaters were switched off and the internal temperature was left to decay.

## 3.4 Occupied office space

Throughout the duration of this research, an external wall of an occupied office has been subject to a monitoring process. The construction of the building element monitored is a steel frame infilled with 75mm Polyisocyanurate (PIR) insulation boards and covered with 120mm external cladding of graphite enhanced expanded polystyrene (EPS) with white silicone render finish. The internal finish is plasterboard.

A preliminary investigation with an infrared camera revealed the position of the steel-frame structure. Three heat flux meters (Hukseflux, [5]) were distributed horizontally between two metal studs. Next to each heat flux meter a PT100 surface temperature sensor was positioned. The external surface temperature was measured by means of a single RTD and the external heat flux was measured at the centre of insulation (between the rafters of the steel frame structure) by means of a single heat flux meter. External air temperature and internal air temperature were monitored using two RTDs. A data logger DT85 was programmed to collect the data once per minute. The installation and the monitoring were setup in accordance with the method suggested by the standard ISO: 9869:2014.

The wall monitored faces north and it is heavily shaded by surrounding vegetation.

The office was occupied during the whole monitoring period with the exception of the vacation periods. The internal temperature, therefore, was determined by the heating pattern of the building and the preferences of the occupant, thus the office room was subjected to natural ventilation, equipment and occupant gains and solar gains. The data set used for the validation of the HDM correspond to the period 17 December 2015 to 14 January 2016. This period coincides with a vacation period, when the occupant was not in the office and the building showed a low occupancy profile. The data clearly show the impact of the ventilation due to the opening and closing of the window and entrance door during the rest of the year, therefore this particular period had been chosen since the temperature and heat flux profiles were relatively smooth.

## 3.5 BSRIA data

A 7-day data set comprising measurements of heat flux and near-wall air temperatures, collected by the Building Services Research and Information Association

(BSRIA) as part of an investigation into the U-values of solid walls of occupied UK dwellings, was used to test the HDM model. The measurements were made at 5 minutes intervals over a 14 day period during the winter of 2010. The estimated thickness of the building element investigated is L=0.310m, which includes a 0.01m layer of plaster on its internal surface. Full details of the measurement methods and outputs may be found in [72]. This set of data was initially used to compare the results obtained by the HDM with the results of the STM proposed by Biddulph et al. [72]. A full account of the results obtained is outlined in chapter 5.

## 3.6 Data analysis structure

The following two chapters will present the analysis of the experimental data collected.

Chapter 4 focusses on the verification of the model proposed, thus focussing on synthetic data generated for this purpose, (further details on the generation process and rationale of synthetic data are given in section 4.1), and the data collected in the environmental chamber. At first, the experimental data are studied by means of the "Average Method" and compared with the values found in literature, to provide a benchmark against which comparing the results obtained with the model proposed. Following this initial step, the experimental data are analysed by means of the HDM with the MCMC sampling algorithm (the model described in sections 2.1 - 2.3) and by means of the STM (described in section 2.4). The data analysis presented relates to the data collected on one solid wall section and on the cavity wall.

Chapter 5 focusses on the validation of the model proposed, thus aiming to verify to which extent the conclusions based on the analysis of the synthetic data and the experimental data collected in the chamber can be extended to a more realistic scenario. For this purpose, this chapter focusses on the analysis of the data collected by BSRIA, comparing the results obtained with the model proposed against the STM, and on the data collected on the solid wall unoccupied property and the insulated steel frame office. In total, beside the BSRIA data, four other experimental data sets have been analysed to maximise the diversity of constructions monitored: two datasets collected on the solid wall property (one in correspondence of the inhomogeneity and one in correspondence of the defect free area) and two data sets collected on the insulated steel frame construction (one in correspondence of the insulation and one in correspondence of the steel frame).

# Chapter 4

# Analysis of the MCMC results

In this chapter, the results obtained by applying the MCMC to the solution of the Heat Diffusion Model (HDM) described in sections 2.1-2.2 are presented and discussed. At first, the MCMC is trialled on synthetic data, to quickly assess its strengths in an ideal scenario. Secondly, the algorithm is validated on the data collected in the experiments described in chapter 3.

Initially the standard calculations with the "Average Method" and the relevant literature values are introduced to act as a benchmark for the model proposed (Section 4.2.1). Later on, the HDM and STM are tested and compared on the data set collected in the environmental chamber, Sections 4.2 - 4.4.

## 4.1 Synthetic Experiments

The purpose of trialling a model on synthetic data is to verify its performance in an ideal case scenario, where the experimenter has absolute knowledge of the system under investigation. In the case studied, this corresponds to the knowledge of the "true values" of the functions describing the thermal conductivity and volumetric heat capacity.

Furthermore, as the choice of such functions is completely arbitrary, it is possible to test the performance of the MCMC technique in the case of a known discontinuous function and explore whether the thermal properties inferred may be used to indicate the presence of a non uniformity in a real case scenario.

The case proposed as a synthetic experiment corresponds to a wall construction with 5 layers. The profile of the "true" thermal conductivity and of the "true" specific heat capacity are displayed in figure 4.1.1. The thickness of the wall was considered to be 0.3m and it was discretised in 100 elements for the numerical solution of the heat equation. With such profiles for thermal conductivity and volumetric heat capacity, the "true" $\mathcal{K}$-value and $\mathcal{C}$-value, calculated via equations (2.6), were

$$\mathcal{K}_{true} = 3.62[W/m^2K] \qquad \mathcal{C}_{true} = 3.19 \times 10^5[J/m^2K] \tag{4.1}$$

The model adopted to solve the forward problem is the heat equation with fixed temperature boundary conditions, described by equations (2.1) - (2.5). The boundary conditions are based on sinusoidal variations in surface temperature and are shown in the left panel of figure 4.1.2. The length of the synthetic test is equivalent to a week of data with a 5 minute timestep. The heat flux is obtained via equation (2.5), and for the purpose of the analysis it was corrupted with Gaussian noise $\eta \sim N(0, 0.5)$.

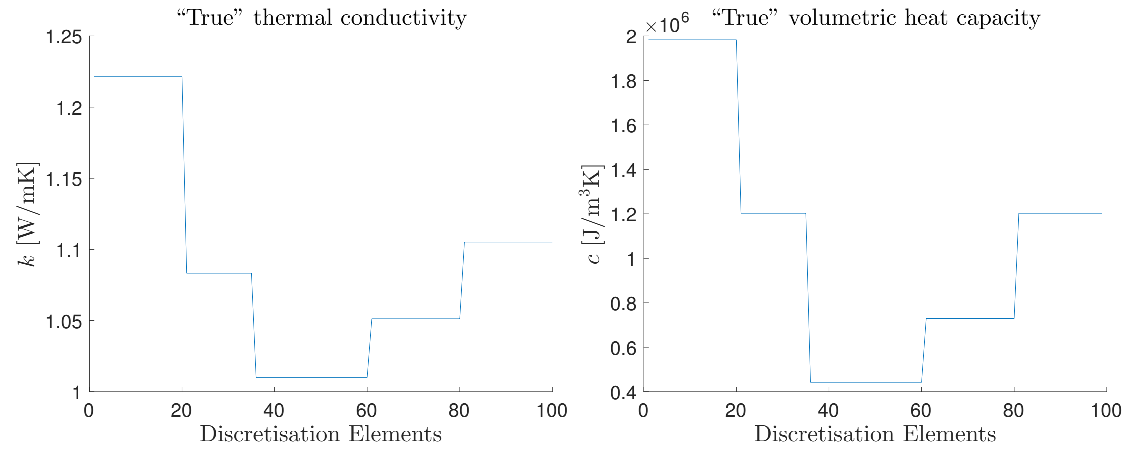

Figure 4.1.1: Discontinuous thermal properties assumes as "true" profiles for the synthetic experiments. Left: thermal conductivity. Right: volumetric heat capacity.

The heat flux thus obtained is displayed in the right panel of figure 4.1.2.

The priors were modelled to be representative of the uncertainty surrounding the thermal properties. Referring to equations (2.26) - (2.27), the parameters defining the prior of the thermal conductivity are $\lambda_k = 0.5$ and $\sigma_k = 0.25$ and, in a similar fashion, the parameters for the volumetric heat capacity are $\lambda_c = 0.1$ and $\sigma_c = 0.1$. Such distributions give rise, via equation (2.6) to the distributions of conductance and heat capacity: the mean value of the conductance is $\mathcal{K}_{prior}^{mean} = 2.92$ $[W/m^2K]$, with the distribution taking values from 0.44 $[W/m^2K]$ to 13.22 $[W/m^2K]$ and the mean value of the heat capacity is $\mathcal{C}_{prior}^{mean} = 3.12 \times 10^5$, $[J/m^2K]$ with the distribution taking values from $1.71 \times 10^5$ $[J/m^2K]$ to $5.47 \times 10^5$ $[J/m^2K]$. Figure 4.1.3 shows 100 draws from the prior distributions of $\kappa(x)$ and $c(x)$, and figure 4.1.4 displays the prior distributions of the conductance and heat capacity.

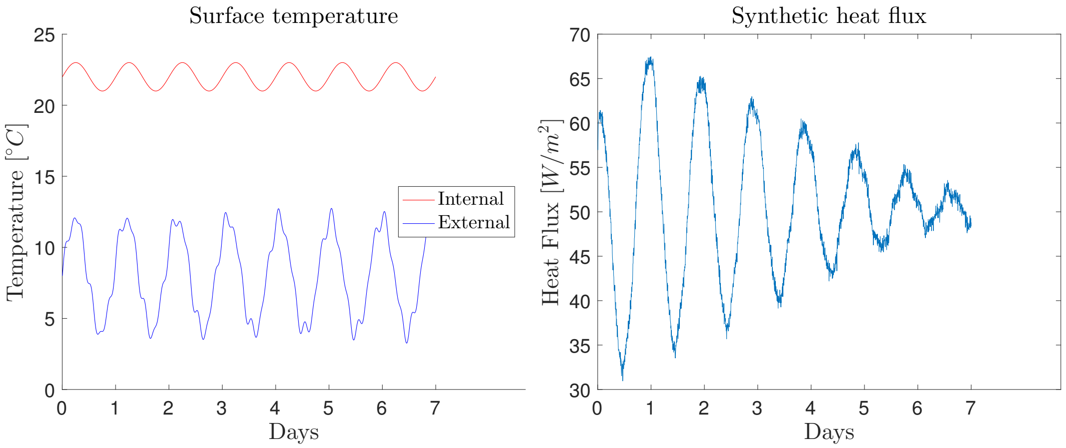

Figure 4.1.2: Left: Surface temperature boundary conditions employed for the solution of the forward problem. Right: Heat flux, obtained from the solution of the forward problem, corrupted by Gaussian noise.

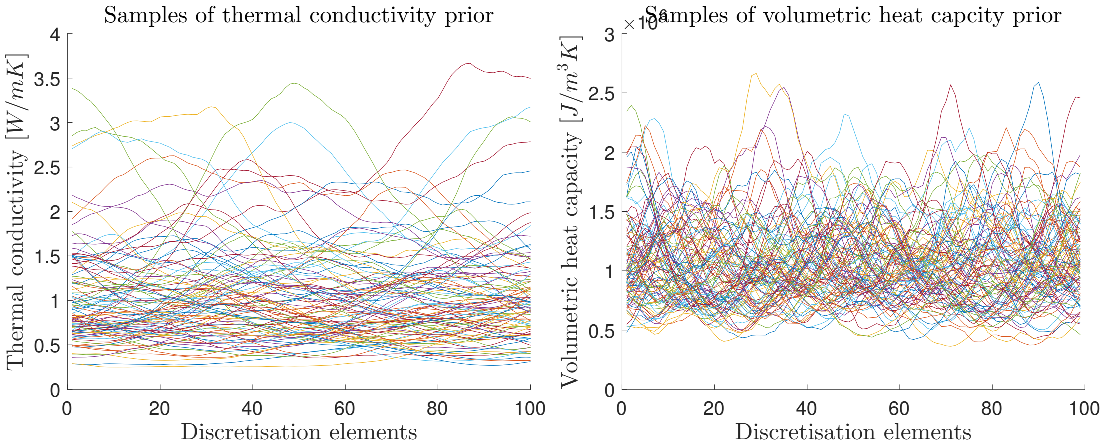

Figure 4.1.3: Left panel: 100 samples from the thermal conductivity prior distribution, right panel: 100 samples from the volumetric heat capacity distribution

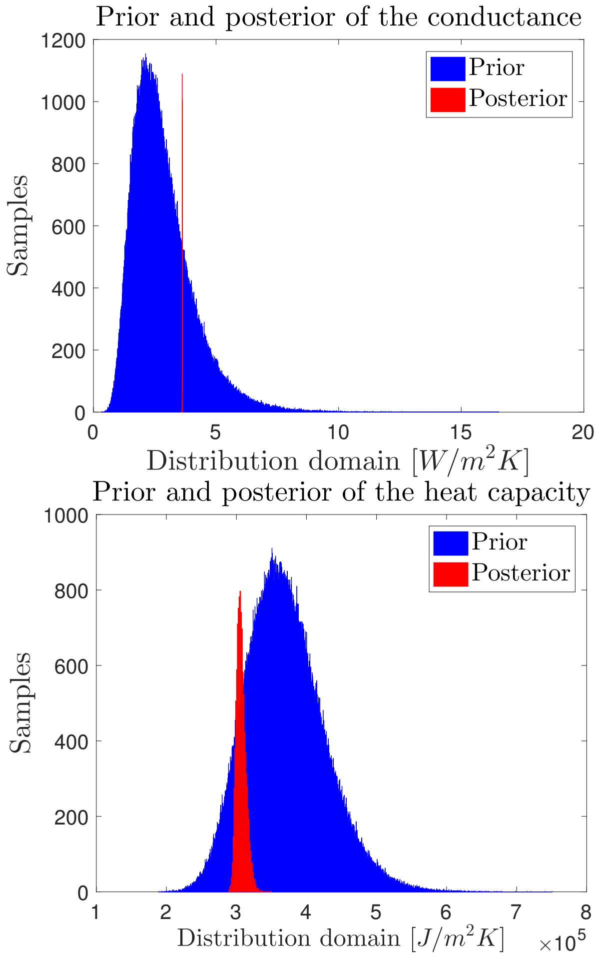

Figure 4.1.4: Comparison between the prior ($10^6$ samples) and posterior ($10^4$ samples) distributions for the values of conductance and heat capacity.

It is now possible to evaluate how effectively the MCMC algorithm described in chapter 2 is able to infer the thermal properties of the synthetic problem studied and quantify the uncertainty surrounding these results. As explained in the previous chapter, half of the time window available was employed for the inference process while the second half was used for validating the results obtained.

Figure 4.1.5 shows the inferred thermal conductivity and volumetric heat capacity against the true values. The prediction corresponds to the mean value of the posterior of the thermal conductivity and volumetric heat capacity, and the uncertainty band corresponds to one standard deviation from the mean value of each property. Given the samples produced by the MCMC the posterior mean and variance of the thermal conductivity can be calculated as

$$\begin{aligned} \mathbf{E}(\kappa|y)(x) &\approx \frac{1}{J}\sum_{j=1}^{J}\kappa^{(j)}(x) && (4.2)\\ \mathbf{V}(\kappa|y)(x) &\approx \frac{1}{J-1}\sum_{j=1}^{N}(\kappa^{(j)}(x)-\mathbf{E}(\kappa|y)(x))^2 && (4.3) \end{aligned}$$

and similarly for $c(x)$:

$$\begin{aligned} \mathbf{E}(c|y)(x) &\approx \frac{1}{J}\sum_{j=1}^{J}c^{(j)}(x) && (4.4)\\ \mathbf{V}(c|y)(x) &\approx \frac{1}{J-1}\sum_{j=1}^{N}(c^{(j)}(x)-\mathbf{E}(c|y)(x))^2 && (4.5) \end{aligned}$$

Figure 4.1.6 shows the data fit obtained during the first 3.5 days and the pre-

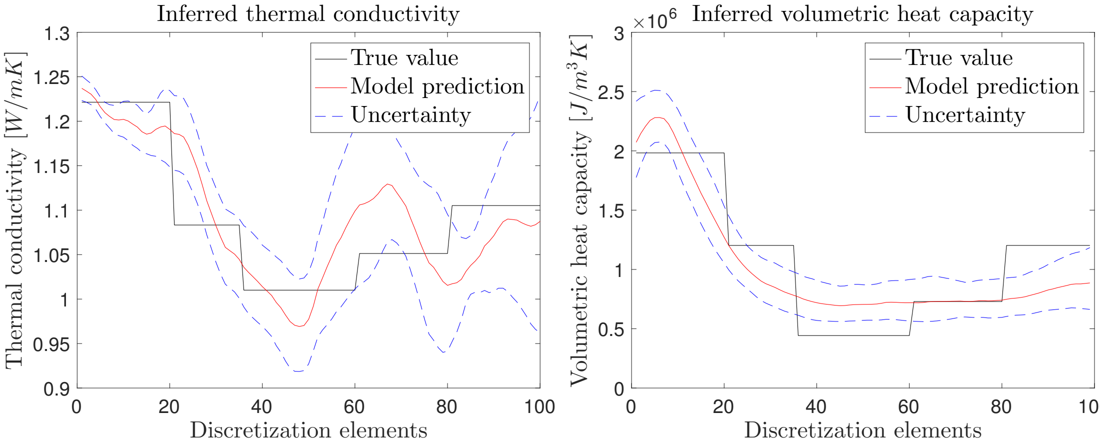

Figure 4.1.5: Comparison of the inferred thermal properties with the true values. Left: Thermal conductivity, Right: Volumetric heat capacity

dictions of the model compared with the latter half of data. The uncertainty band corresponds to the predictions obtained using, in the calculations of the heat flux, one standard deviation from the mean value of thermal conductivity and volumetric heat capacity displayed in figure 4.1.5.

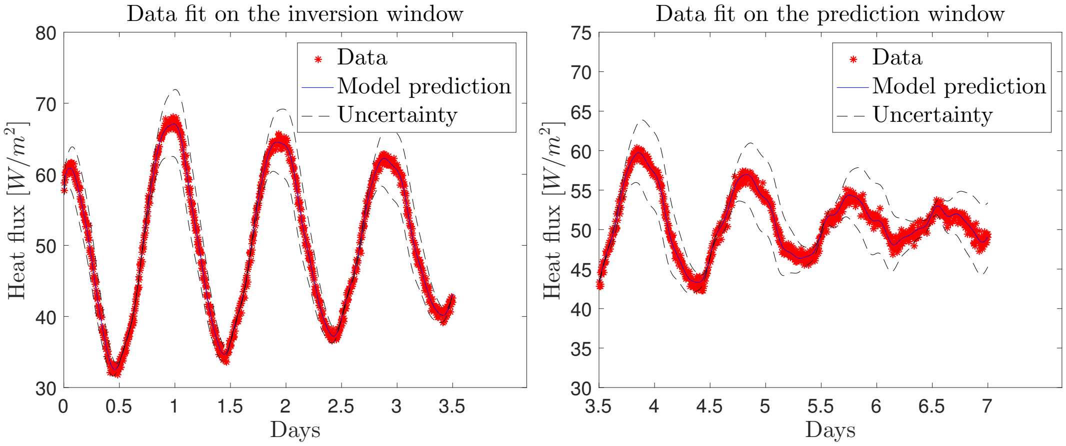

Figure 4.1.6: Predicted heat flux vs synthetic data. Left: inference window, Right: prediction window.

Looking at figure 4.1.6, it is clear that the MCMC technique is a powerful tool for the solution of the HDM as it is able to reproduce accurately the synthetic data. Furthermore, the uncertainty band encloses the data and the predictions through the whole validation window, offering a demonstration of the reliability of the results obtained.

Observing figure 4.1.5, it can be seen that the inferred thermal properties follow the pattern of the true values, recognising step downs and increments without prior information. Clearly, the inference of the thermal properties is not able to reconstruct the exact number of strata and interface locations of the layers present in the wall construction but it offers an indication of the presence of interfaces between different materials. These limitations can be attributed to the model itself, as amongst the postulates, it was chosen to assume continuous functions for the thermal properties, but, in the case considered here, the thermal properties are clearly discontinuous as in the case offered by a multi-layered construction.

Comparing the left and right panel of figure 4.1.5, the impact of the choice of the prior, defined in equations (2.26) - (2.27), can be seen. The prior of the volumetric heat capacity guarantees smoother functions due to the low values of $\sigma_c$ and $\lambda_c$. As a consequence, the inferred profile just shows the general trend of the volumetric heat capacity but does not present the abrupt changes visible in the case of the thermal conductivity. On the other hand, the inferred profile of the thermal conductivity presents small irregularities that are a by-product of choosing a prior that allows for sharper variations within the wall thickness.

### 4.1.1 Uncertainty quantification

The biggest advantage of approaching the solution of inverse heat transfer problem through probability distributions is the quantification of uncertainty around the values obtained.

Given the samples of the thermal properties obtained from the MCMC algorithm, the conductance and heat capacity can be calculated via equations (2.6) for each sample, giving rise to the posterior distributions of the $\mathcal{K}$-value and $\mathcal{C}$-value, from which the mean value and variance of both terms can be calculated.

As it may be seen from figure 4.1.4, the posterior distribution of the values of conductance and heat capacity are considerably sharper; for instance the posterior of the capacitance takes values from 2.96 $[W/m^2K]$ to 3.07 $[W/m^2K]$ while the posterior of the heat capacity takes values from $2.92 \times 10^5$ $[J/m^2K]$ to $3.52 \times 10^5$ $[J/m^2K]$. If we consider the mean value of the posterior as "best guess" and the spread of the distribution as maximum uncertainty, this gives rise to 3.6% and 19% relative error on the conductance and heat capacity respectively.

This is however a coarse estimation of uncertainty and it includes the extremes of the distribution, i.e. values at the margin of the distribution that have a low probability. A more representative way of characterising the uncertainty could be to calculate the variances of the distribution and use them to calculate the relative error.

The results of these calculations are shown in table 4.1.1.

Table 4.1.1: Mean, variance and relative error of the conductance and heat capacity distributions obtained for the synthetic experiment analysis

| | Mean value | Variance | Relative error |
|---|---|---|---|
| Conductance $[W/m^2K]$ | 3.62 | $2.82\times10^{-6}$ | 0.05% |
| Heat Capacity $[J/m^2K]$ | $3.07\ \times10^{5}$ | $4.46\ \times10^{7}$ | 2.17% |

Figure 4.1.7 shows 100 draws from the posteriors of $\kappa(x)$ and $c(x)$, and it can be seen how the samples obtained display a much smaller variability than that is seen in the prior (Figure 4.1.3)

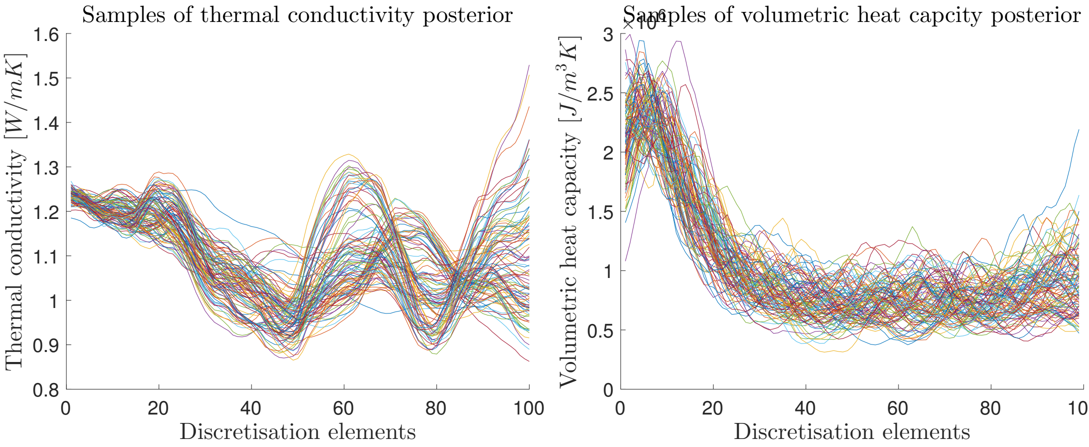

Figure 4.1.7: Left panel: 100 samples from the thermal conductivity posterior distribution, right panel: 100 samples from the volumetric heat capacity posterior distribution

In order to visualise the reduction of uncertainty around the inference of the thermal properties, the prior uncertainty (3 standard deviations) and the posterior uncertainty have been plotted against the true value of the thermal conductivity and volumetric heat capacity: this is displayed in figure 4.1.8. Observing the panel on the left, the prior of the thermal conductivity is completely uninformative with respect to the true value, and the prior of the volumetric heat capacity does not fully capture the profile of the true value. From this picture, the reduction in uncertainty obtained through the inference process can be clearly observed, as the posterior distributions are centred around the true values in both cases.

Further observations relative to the reduction of the uncertainty and the propagation of the prior and posterior uncertainties are given in the following paragraphs, in relation to the experimental data sets collected.

From the results presented in this section, it can be seen that the MCMC technique proposed looks like a promising tool for the investigation of the thermal properties of building elements using measurements of surface temperature and internal heat flux, which is the current standard measurement procedure for the thermal transmittance of building elements.

Furthermore, this analysis can be useful for providing general feedback on the internal composition of a wall structure without a priori knowledge, such as in the case where visual inspection fails to individuate a cavity construction or the presence of insulation.

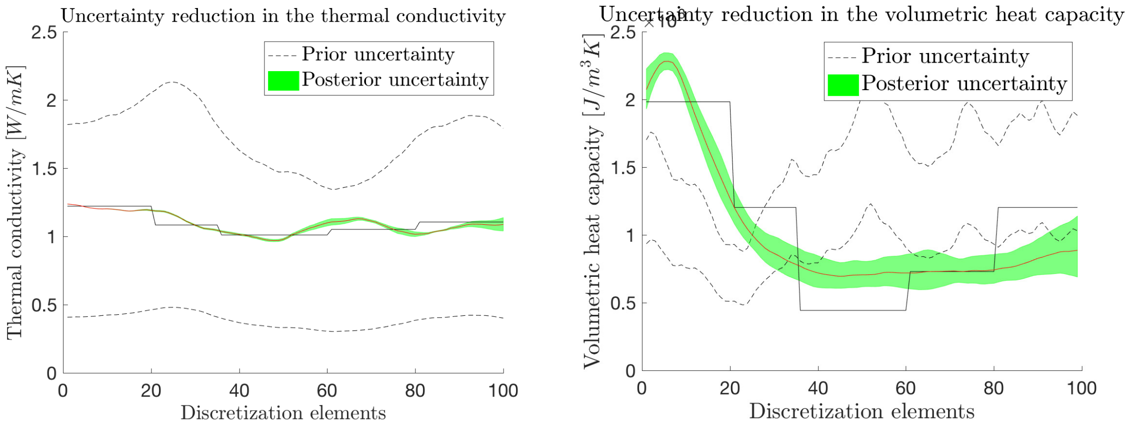

Figure 4.1.8: Reduction of the uncertainty in the distributions of thermal conductivity and volumetric heat capacity. Left: thermal conductivity, Right: volumetric heat capacity

## 4.2 Environmental Chamber Data

This section presents the analysis of the experimental data collected in the environmental chamber. Section 4.2.1 presents the benchmark results obtained by applying the standard methods described in chapter 1. Section 4.2.2 investigates the surface resistance in the environmental chamber. Section 4.2.3 applies the MCMC algorithm proposed to the experimental data relative to the solid wall. Section 4.3 analyses the performance on the STM on the same data set. Section 4.4 compares the performance of the HDM and STM model using data collected on the cavity wall and finally section 4.5 discusses the results obtained.

### 4.2.1 Benchmark results

Ballpark estimates of the conductance ($\mathcal{K}$-value) were calculated using two methods: the “Average Method”, equation (1.18), and, estimates made according to the values indicated in CIBSE Guide A. The values obtained from these procedures are shown in table 4.2.1 and are used as a reference for the results obtained by implementing the MCMC algorithm. The uncertainty shown on the "Average Method" value will correspond to ±25%, as indicated by the ISO9869.

Table 4.2.1: Conductance values calculated via "Average Method" and reported on the CIBSE Guide A [8]

| Wall type and method | Conductance $[W/m^2K]$ | Heat Capacity per unit area $[J/m^2K]$ |
|---|---|---|
| Solid wall (average method) | $3.17 \pm 0.63$ | NA |
| Solid wall (CIBSE) | 2.60 - 3.58 | 277200-440000 |
| Cavity wall (average method) | $0.79 \pm 0.16$ | NA |
| Cavity wall (CIBSE) | 0.60 - 0.65 | 277200-440000 |

### 4.2.2 Investigation of the Surface Resistance

As both air and surface temperature measurements were available from the data collected in the chamber, a brief investigation was conducted to estimate the values of surface resistance in the environmental chamber.

As the environmental chamber is mechanically ventilated to obtain a uniform temperature distribution within each room, it was considered that the standard values for surface resistance, indicated by the CIBSE guide A, 0.13 $m^2K/W$ and 0.04 $m^2K/W$, were not applicable for the conditions in the present chamber.

The values suggested by the CIBSE Guide A, represent a simplification of the heat transfer process occurring at the surface, where the internal and external surface resistances depend only on the convective heat transfer coefficient and the radiative heat transfer coefficient.

In literature, the convective heat transfer coefficients have been measured with the use of Mayer ladder [87] or calculated from the total heat flux and temperature by the fitting method [88] or by the difference between the heat flow through the building element and the long-wave radiation [89].

The purpose of this research is not the investigation of surface resistances, therefore only a superficial examination was carried out on the data collected under steady state conditions.

The method adopted consisted of comparing the difference between the resistance obtained using the air temperature measurements and the resistance obtained using the surface temperature measurements. The rationale behind this choice is that, when calculating the resistance using air temperature measurements, the value obtained contains also the contributions from surface resistances, while the resistance of the element alone can be calculated from surface temperatures.

The calculations were performed with the average method, equation (1.18), for the 4 walls monitored in the chamber. Several attempts have been made to maximise the information available from the data set.

At first, the wall resistance ($R_{wall}$) was calculated taking the mean between the resistance values obtained using the internal flux and external flux and surface temperature measurements, as the situation in the chamber is symmetric.

Secondly, the total resistance ($R_{tot}$) was calculated using the air temperature measurements and the mean surface resistance was calculated as $R_s = (R_{tot} - R_{wall})/2$.

In an effort to characterise the internal and external surface resistances individually, further configurations were tried.

To infer the internal surface resistance, the resistance of the wall plus the internal surface resistance ($R_{wall} + R_{si}$) was calculated by using the temperature difference between the internal air and external surface temperature. From this value, the internal surface resistance was obtained by subtracting the wall resistance.

A similar procedure was used for the external surface difference. A diagram explaining the calculation procedure is displayed in figure 4.2.1. The results are summarised in table 4.2.2.

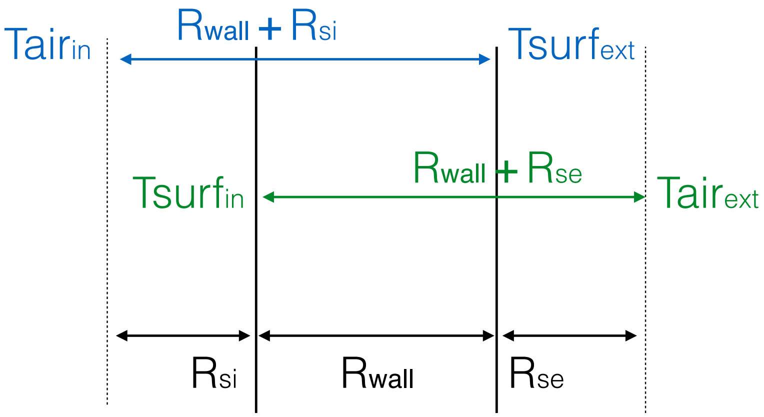

Figure 4.2.1: Diagram explaining the calculation procedure followed to obtain the internal and external surface resistances

.

In the cases of wall B, C, and D the internal and external surface resistances are

Table 4.2.2: Internal and external surface resistances calculated in the environmental chamber

| Wall type and method | Wall A | Wall B | Wall C | Wall D |
|---|---|---|---|---|
| Internal surface resistance $[m^2K/W]$ | 0.11 | 0.10 | 0.10 | 0.06 |
| External surface resistance $[m^2K/W]$ | 0.06 | 0.08 | 0.08 | 0.05 |
| Mean surface resistance $[m^2K/W]$ | 0.08 | 0.09 | 0.09 | 0.05 |

quite similar, thus corroborating the hypothesis that the convective coefficients are similar in both rooms of the chamber and supporting the hypothesis that the standard values are not applicable in the case considered. Still this analysis is not conclusive as this is not the case for wall A. At the same time, it can be observed that while the values found for wall B and C are the same, the values found for wall A and D are quite different. This could be seen as a consequence of the wall configuration in the chamber: walls A and D are at the sides, thus they will feel the effect of the chamber external walls, while for walls C and D this might not be the case as they are located in the centre.

Nevertheless, this analysis is not conclusive for the determination of the walls surface resistances. For this reason, a decision was made to continue the analysis of this data set using the surface temperature measurements and thus consider the thermal conductance rather than the thermal transmittance.

### 4.2.3 MCMC performance

This section investigates the performance of the MCMC algorithm on the experimental data collected in the environmental chamber. At first a detailed analysis of the prior distributions is presented, using the same process as shown previously with the synthetic data section 4.1. Later on, the performance of the MCMC algorithm in inferring the effective thermal properties and in reducing the uncertainty in the posterior distribution are discussed.

#### 4.2.3.1 Investigation of the priors

The prior distributions of $\kappa(x)$ and $c(x)$ give rise to priors on the $\mathcal{K}$-value and the heat capacity defined in equation (2.17). The top of Figure 4.2.2 displays the histogram of the resulting prior distributions of the $\mathcal{K}$-value (right) and the heat capacity (left) obtained from equation (2.17) by simple Monte Carlo sampling from the prior of $k(x)$ and $c(x)$ defined in chapter 3.

Note that the resulting priors for the $\mathcal{K}$-value and heat capacity of the wall show a wide spread of values. The prior for the heat capacity takes values between $2.4 \times 10^4$ $[J/m^2K]$ and $2 \times 10^6$ $[J/m^2K]$ while the prior for the $\mathcal{K}$-value takes values between 0.25 $[W/m^2K]$ and 8.0 $[W/m^2K]$.

In summary, the priors provide substantial variability in $\kappa(x)$ and $c(x)$, which, in turn, lead to a wide range of possible values for $\mathcal{K}$ and $\mathcal{C}$. These wide ranges and variability within the priors seek to characterise the large uncertainty associated with the prior knowledge of these properties, as, for example, is evident in values found in the literature. As stated before, the aim of the work implemented in this research is to reduce such variability by means of Bayesian inversion to generate a posterior distribution of values that are likely to be representative of the wall under examination. Figure 2.2.4 shows 100 draws from the prior distributions of thermal conductivity and volumetric heat capacity.

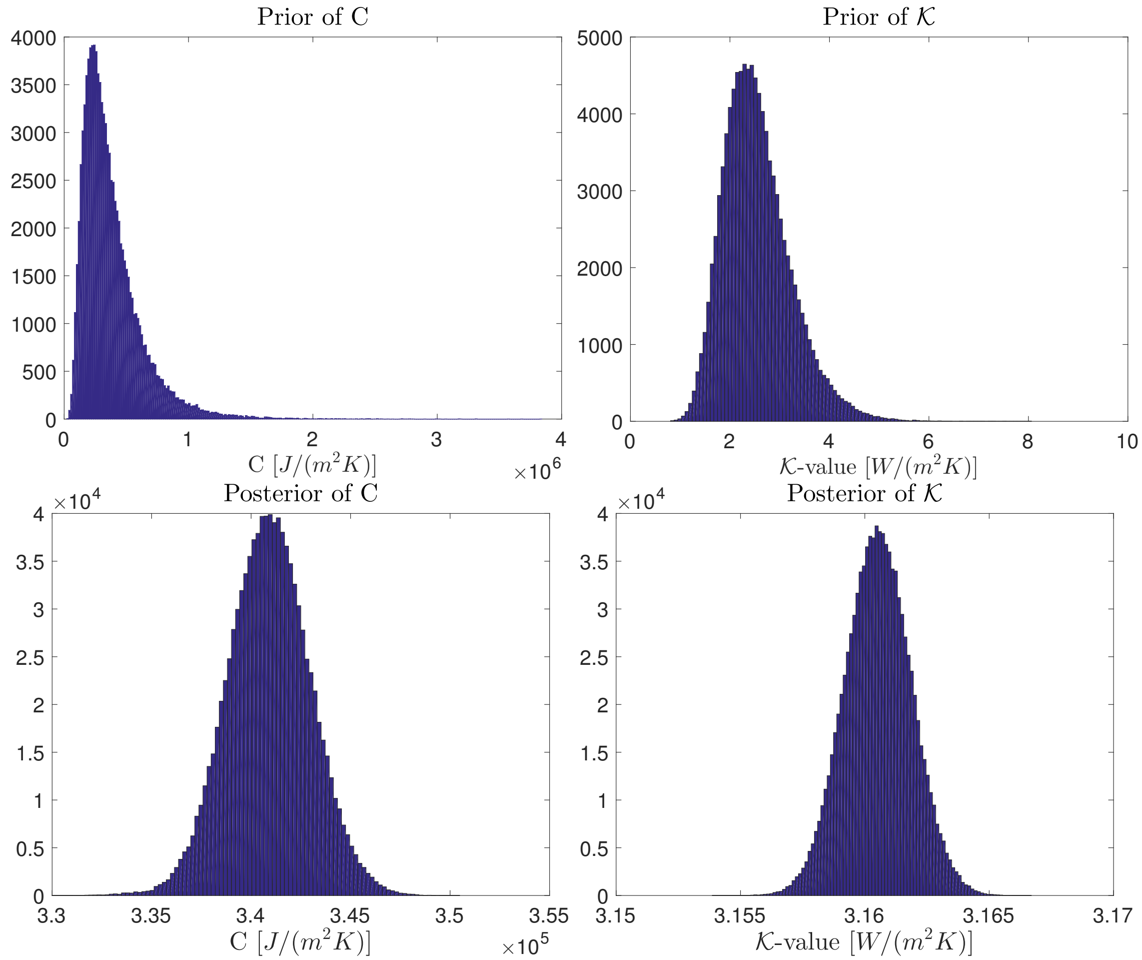

Figure 4.2.2: Top: Histogram of samples from the prior distribution of the heat capacity (left) and K-value (right). Bottom: Chamber data: Histogram of samples from the posterior distribution of the heat capacity (left) and K-value (right)

#### 4.2.3.2 Heat Diffusion Model performance on the chamber data

In this section the results obtained from applying the model described by equation (2.1), with fixed temperature boundary conditions, equations (2.3)-(2.4) to the data set collected in the environmental chamber are presented. The initial temperature was assumed to be the interpolation between the internal and external surface temperature given by equation (2.7). The heat flux obtained at the internal and external facade is given by equation (2.5).

Figure 4.2.3 shows the sample of data used to perform the inference and validate the results obtained. As mentioned in chapter 2, the first 3.5 days are used for the inference while the last 3.5 days are used for the validation of the results obtained. From this moment onward, only the data collected on wall C are analysed, for the sake of brevity and avoiding repetition. the results from the remaining solid walls, walls B and D, show similar trends.

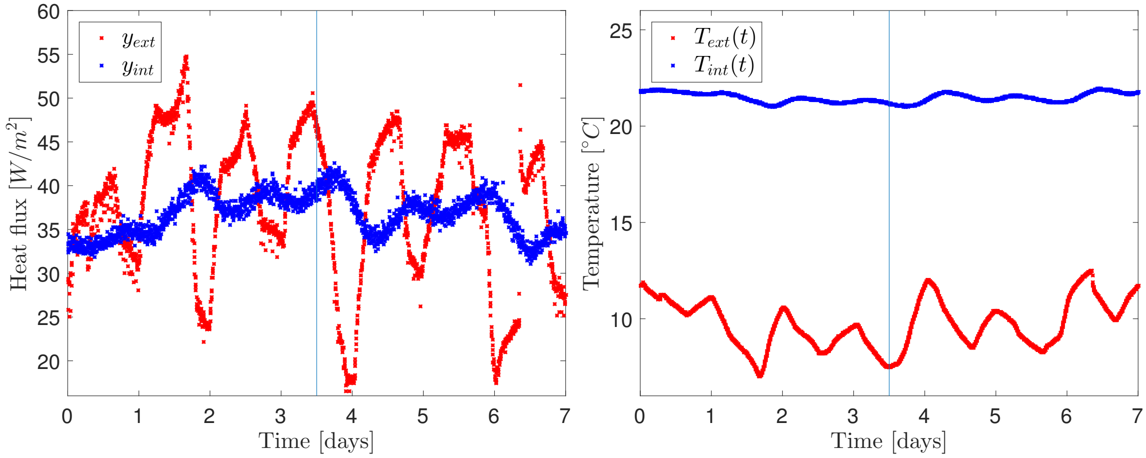

Figure 4.2.3: Chamber data set (Solid wall). Left: Internal and external heat flux. Right: Internal and external surface temperatures.

#### 4.2.3.3 Propagating the prior uncertainty

This subsection shows how the uncertainty in the prior knowledge affects the predictions of the model, without conditioning the results with the data collected. This procedure also offers an insight into how accurately the data published in the literature fit the case study considered here.

If the prior mean of the unknown, $\mathbf{E}(u)$, represents an accurate estimate of the thermal properties of the wall, the simulations of $\mathcal{G}_{int}(\mathbf{E}(u))$ and $\mathcal{G}_{ext}(\mathbf{E}(u))$would provide a close fit to the heat flux data $y$.

If, in addition, the prior uncertainty around $\mathbf{E}(u)$ (given by $\mathbf{E}(u) \pm [\mathbf{V}(u)]^{1/2}$) was small, the uncertainty band given by $\mathcal{G}_{int,ext}(\mathbf{E}(u) \pm [\mathbf{V}(u)]^{1/2})$ should enclose $\mathcal{G}_{int,ext}(\mathbf{E}(u))$ and thus contain the observations of the heat flux. Note that $\mathbf{E}(u)$ and $\mathbf{V}(u)$ refer to the mean and the variance of the functions of $\kappa(x)$ and $c(x)$, represented in figure 2.2.3 , whose distributions, via equation (2.6), give rise to the priors of $\mathcal{K}$ and $\mathcal{C}$ displayed in figure 4.2.2.

Figures 4.2.4 and 4.2.5 display the heat flux data alongside with the curves $\mathcal{G}_{int}(\mathbf{E}(u))$, $\mathcal{G}_{int}(\mathbf{E}(u) \pm [\mathbf{V}(u)]^{1/2})$ and $\mathcal{G}_{ext}(\mathbf{E}(u))$, $\mathcal{G}_{ext}(\mathbf{E}(u) \pm [\mathbf{V}(u)]^{1/2})$.

It may be seen that, $\mathcal{G}_{int,ext}(\mathbf{E}(u) \pm [\mathbf{V}(u)]^{1/2})$ defines an uncertainty band around $\mathcal{G}_{int,ext}(\mathbf{E}(u))$. However, it can be seen also that the predictions of the model (black line) do not capture the data (red dots) at all. This clearly indicates that the prior knowledge of $u(x)$ is very poor at capturing the data. This situation can be easily encountered in practice when, $\mathbf{E}(u)$ is based on values taken from the literature and where the inspection does not reveal internal structures within the wall.

The right panel of Figures 4.2.4 and 4.2.5 displays the curves given by $\hat{\mathcal{G}}_{int}(\mathbf{E}(u))$, $\hat{\mathcal{G}}_{int}(\mathbf{E}(u) \pm [\mathbf{V}(u)]^{1/2})$ and $\hat{\mathcal{G}}_{ext}(\mathbf{E}(u))$ $\hat{\mathcal{G}}_{ext}(\mathbf{E}(u) \pm [\mathbf{V}(u)]^{1/2})$. These curves represent the propagation of the prior uncertainty under the prediction map $\hat{\mathcal{G}}$, which corresponds to model predictions of heat flux within the subsequent time window $[3.5 \text{ days}, 7 \text{ days}]$. While some of the measured heat flux data fall within the uncertainty band determined by $\hat{\mathcal{G}}(\mathbf{E}(u) \pm [\mathbf{V}(u)]^{1/2})$, there is a large uncertainty around $\hat{\mathcal{G}}(\mathbf{E}(u)$. Bayesian inversion makes it possible to reduce such uncertainty as will be shown in the following subsection.

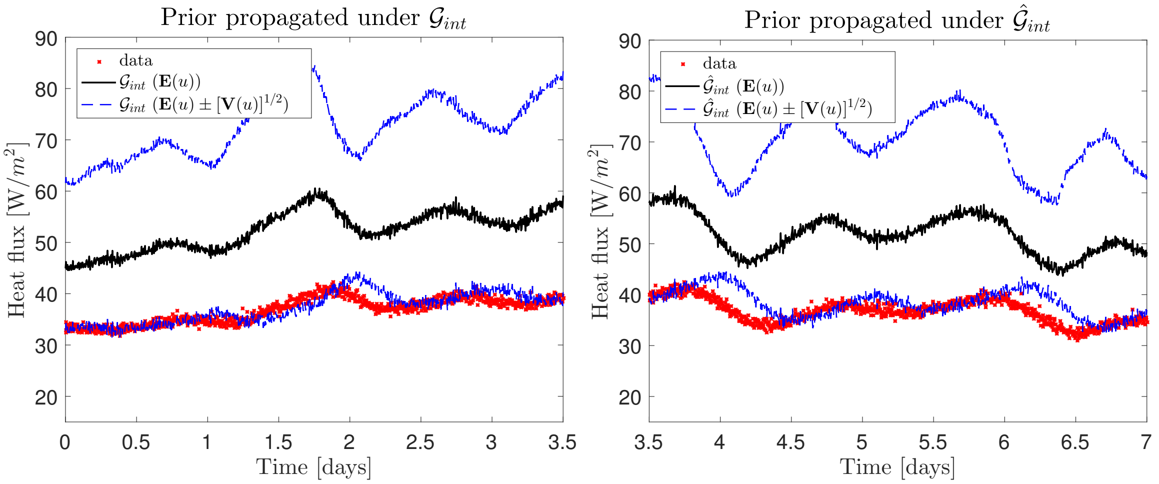

Figure 4.2.4: Analysis of chamber data (solid wall). Propagation of the uncertainty under $\mathcal{G}_{int}$ (left) and $\hat{\mathcal{G}}_{int}$ (right) under the prior.

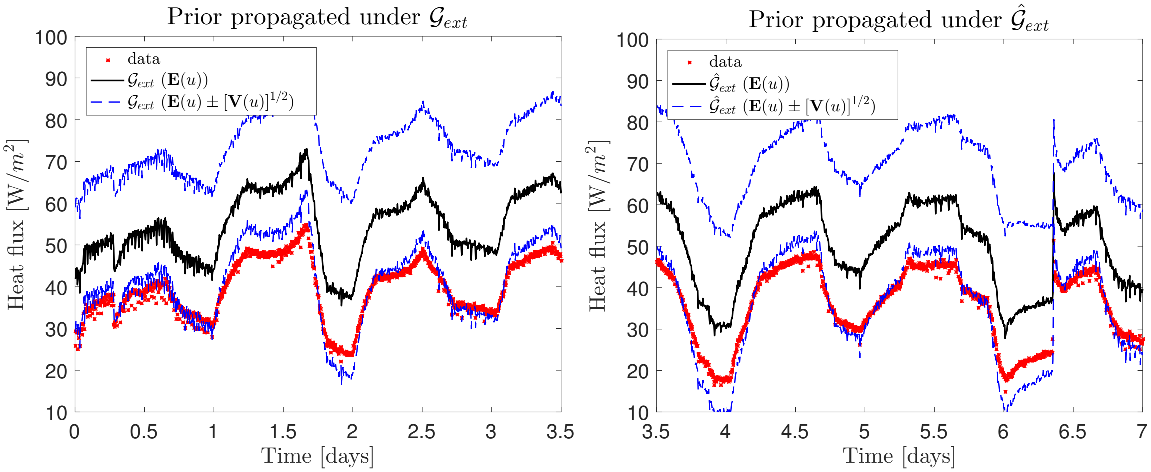

Figure 4.2.5: Analysis of chamber data (solid wall). Propagation of the uncertainty under $\mathcal{G}_{ext}$ (left) and $\hat{\mathcal{G}}_{ext}$ (right) under the prior.

#### 4.2.3.4 The posterior uncertainty

In this section, the results obtained from the analysis proposed for $\mathcal{K}$-value and heat capacity are compared with previous results and literature values. Furthermore it is shown how the uncertainty in the predictions is reduced once the information contained in the data has been included in the model, illustrating how the model output and the uncertainty band capture the experimental measurements.

The MCMC method applied to produce $J = 10^6$ samples of the posterior $\mathbb{P}(u|y)$ is described in section 2.2. These samples are denoted by $u^{(j)}(x) = (\kappa^{(j)}(x), c^{(j)}(x))$ ($j \in \{1, \ldots, J\}$). The Figure 4.2.6 displays 100 samples of the posterior for $\kappa(x)$ (left) and $c(x)$ (right) obtained from the MCMC method from section 2.2. It can be observed that the posterior samples exhibit a much smaller variability than the ones from the prior (see Figure 2.2.4).

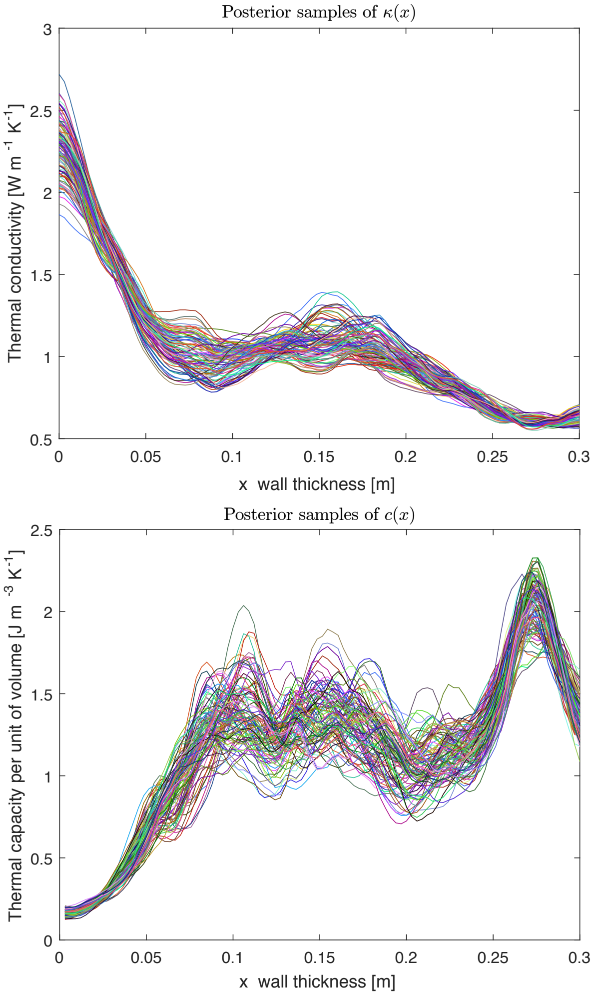

Figure 4.2.6: Analysis of chamber data (solid wall). Samples from the posterior distribution. Left: posterior samples of the thermal conductivity $\kappa(x)$. Right: posterior samples of the volumetric heat capacity $c(x)$

These posterior samples may be used to compute relevant information relating to the unknown parameters, such as any statistical moments. In particular, from these samples $u^{(j)}(x) = (\kappa^{(j)}(x), c^{(j)}(x))$, the posterior mean and variance of $\kappa(x)$ can be approximated by means of

$$\begin{aligned} \mathbf{E}(\kappa|y)(x) &\approx \frac{1}{J}\sum_{j=1}^{J}\kappa^{(j)}(x) && (4.6)\\ \mathbf{V}(\kappa|y)(x) &\approx \frac{1}{J-1}\sum_{j=1}^{N}(\kappa^{(j)}(x) - \mathbf{E}(\kappa|y)(x))^2 && (4.7) \end{aligned}$$

with analogous definitions for the posterior mean and variance of the variables $c(x)$:

$$\begin{aligned} \mathbf{E}(c|y)(x) &\approx \frac{1}{J}\sum_{j=1}^{J}c^{(j)}(x) && (4.8)\\ \mathbf{V}(c|y)(x) &\approx \frac{1}{J-1}\sum_{j=1}^{N}(c^{(j)}(x) - \mathbf{E}(c|y)(x))^2 && (4.9) \end{aligned}$$

Note that both the posterior mean and variance are spacial functions, i.e. dependent on the variable $x$.

For each component of the unknown, $u$, an uncertainty band of two standard deviations around the posterior mean is displayed in figure 4.2.7. comparing this figure with figure 2.2.3 the reduction of the prior uncertainty can be clearly appreciated.

The posterior distributions of the $\mathcal{K}$-value as well as heat capacity defined in equation (2.6) are investigated.

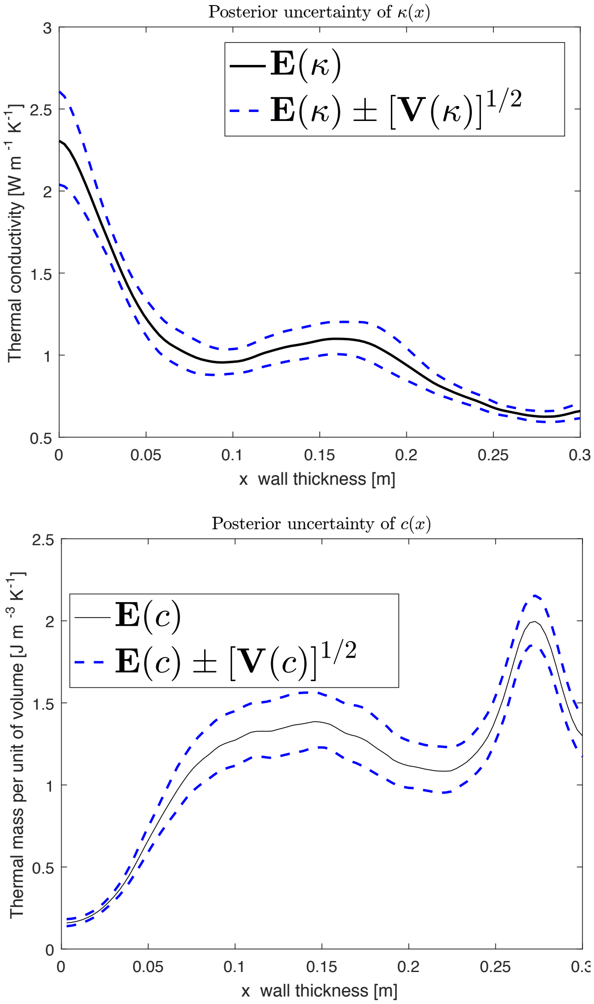

Figure 4.2.7: Analysis of chamber data (solid wall). Mean and variance of the posterior distributions. Left: posterior mean and variance of the thermal conductivity $\kappa(x)$. Right: posterior mean and variance of the volumetric heat capacity $c(x)$

Figure 4.2.2 (bottom) displays the histogram of posterior samples of $\mathcal{C}$ (left) and $\mathcal{K}$(right). For each of the MCMC samples of $\kappa(x)$ and $c(x)$, the corresponding values of $\mathcal{K}$ and $\mathcal{C}$ were computed via equation (2.6) and then the whole samples displayed in histogram form. Note that the reduction of the variability of the posterior distribution is further enlightened by the different scale on the abscissa of figure 4.2.2.

It can be observed, that the conditioning of $u(x)$ on the heat flux data reduces substantially the prior uncertainty in both the $\mathcal{K}$-value and the heat capacity. The posterior mean and posterior standard deviations determined from the results for $\mathcal{K}$ and $\mathcal{C}$ are displayed in Table 4.2.3.

Table 4.2.3: Posterior mean and posterior standard deviation of the conductance value $\mathcal{K}$ and the heat capacity $\mathcal{C}$ for the environmental chamber data.

| Chamber | $\mathbf{E}(\mathcal{K}\|y)$ $[W/m^2K]$ | $[\mathbf{V}(\mathcal{K}\|y)]^{1/2}$ $[W/m^2K]$ | $\mathbf{E}(\mathcal{C}\|y)$ $[J/m^2K]$ | $[\mathbf{V}(\mathcal{C}\|y)]^{1/2}$ $[J/m^2K]$ |
|---|---|---|---|---|
| HDM (solid wall) | 3.161 | $4.2 \times 10^{-3}$ | $3.41 \times 10^{5}$ | $1.99 \times 10^{3}$ |
| STM (solid wall) | 3.142 | $4.71 \times 10^{-4}$ | $1.81 \times 10^{5}$ | $1.18 \times 10^{3}$ |
| HDM (cavity wall) | 0.783 | $1.2 \times 10^{-3}$ | $3.75 \times 10^{5}$ | $6.73 \times 10^{3}$ |
| STM (cavity wall) | 0.768 | $4.1 \times 10^{-3}$ | $1.35 \times 10^{5}$ | $2.01 \times 10^{3}$ |

The propagation of the posterior uncertainty under the forward model $\mathcal{G}$ is now examined. At this point, it is important to introduce an observation on the uncertainty margin displayed in the following figures. It would be reasonable to assume that the variability of the model outputs, i.e. $\mathbf{V}[\mathcal{G}(\mathbb{P}(u|y))]$, is sufficient to capture the uncertainty surrounding the heat flux predictions. As may be seen from figure 4.2.8, this variance is very small, and does not capture the full variability observed in the data. For this reason, the propagation of the posterior expected value and variance are displayed instead, i.e. $\mathcal{G}(\mathbf{E}[\mathbb{P}(u|y)] \pm \mathbf{V}[\mathbb{P}(u|y)])$, rather than the variance of the propagation of the posterior, i.e. $\mathbf{E}[\mathcal{G}(\mathbb{P}(u|y))] \pm \mathbf{V}[\mathcal{G}(\mathbb{P}(u|y))]$.

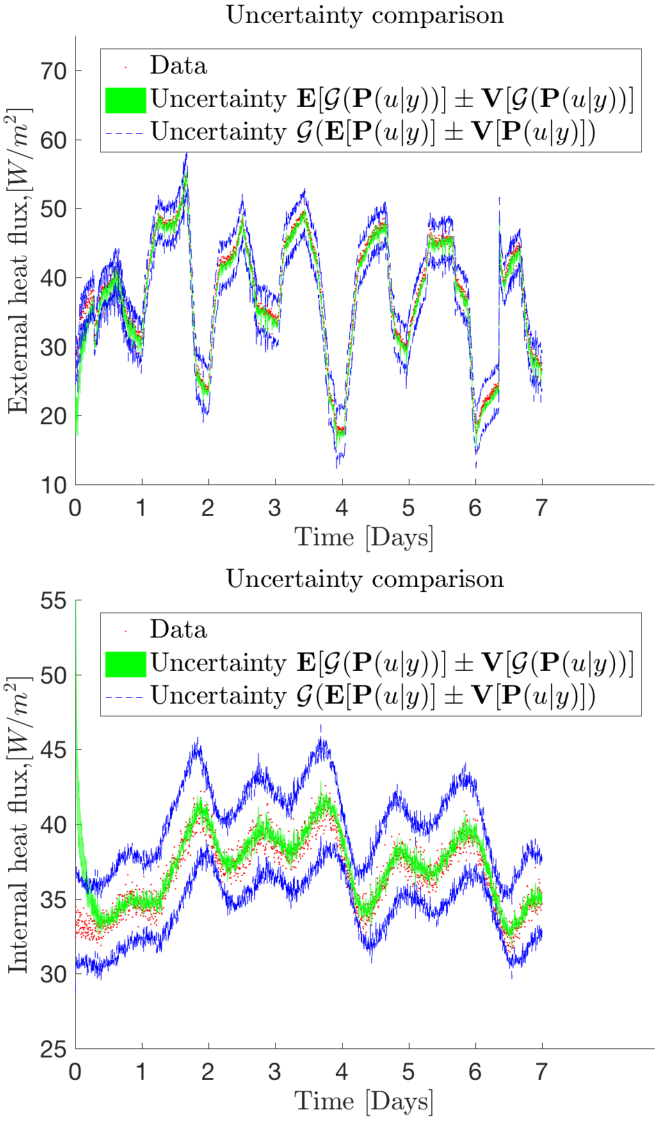

Figure 4.2.8: Figure showing the difference between the propagation of the posterior variance and the variance of the posterior propagation

As before, the propagation of the uncertainty band of two (posterior) standard deviations around the posterior mean $\mathbf{E}(u|y)(x)$ is shown. The posterior mean and variance of the joint variable $u(x) = (\kappa(x), c(x))$ are given by

$$\mathbf{E}(u|y) = (\mathbf{E}(\kappa|y), \mathbf{E}(c|y)) \tag{4.10}$$

$$\mathbf{V}(u|y) = (\mathbf{V}(\kappa|y), \mathbf{V}(c|y)) \tag{4.11}$$

with $\mathbf{E}(\kappa|y)$ and $\mathbf{V}(u|y)$ computed from (4.6)-(4.9) and with analogous definitions for $\mathbf{E}(c|y)$ and $\mathbf{V}(c|y)$. The curves given by $\mathcal{G}_{int,ext}(\mathbf{E}(u|y))$ and $\mathcal{G}_{int,ext}(\mathbf{E}(u|y) \pm [\mathbf{V}(u|y)]^{1/2})$ are displayed in figures 4.2.9 and 4.2.10. The posterior uncertainty under $\mathcal{G}$ results in a considerable reduction of the prior uncertainty in the model predictions of heat flux. In particular, at the beginning of the time window, the model prediction is more concentrated around the heat flux data. It can be seen that the uncertainty band encloses the data through the whole time window.

Similarly in Figures 4.2.9 and 4.2.10 data for the propagation of the posterior uncertainty under the prediction map $\hat{\mathcal{G}}_{int}$ and $\hat{\mathcal{G}}_{ext}$ are presented. It can be appreciated from these figures that the HDM outcome captures the data fully, including the observations in the posterior uncertainty band, thus providing a verification of the model and calculation method investigated.

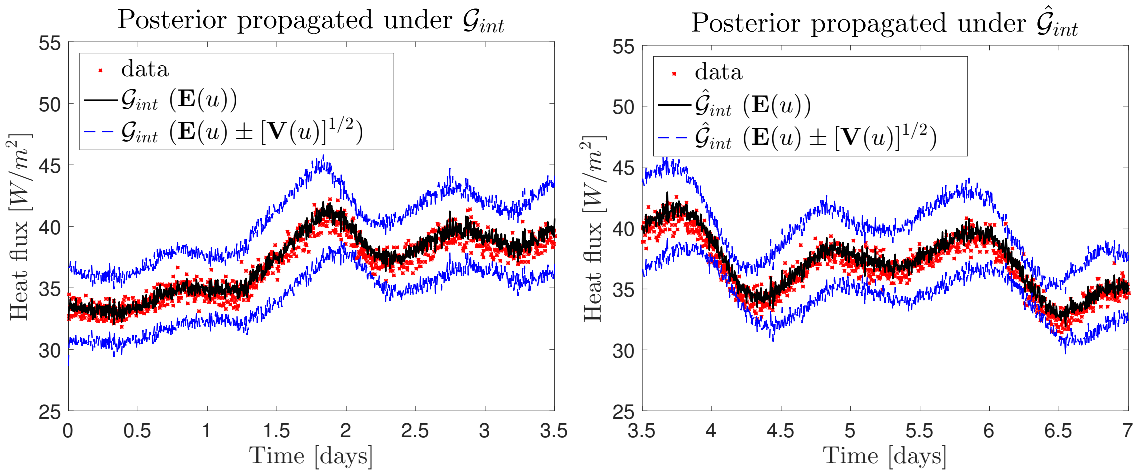

Figure 4.2.9: Analysis of chamber internal heat flux data (solid wall). Propagation of the uncertainty under $\mathcal{G}_{int}$ (left) and $\hat{\mathcal{G}}_{int}$ (right) under the posterior. (HDM)

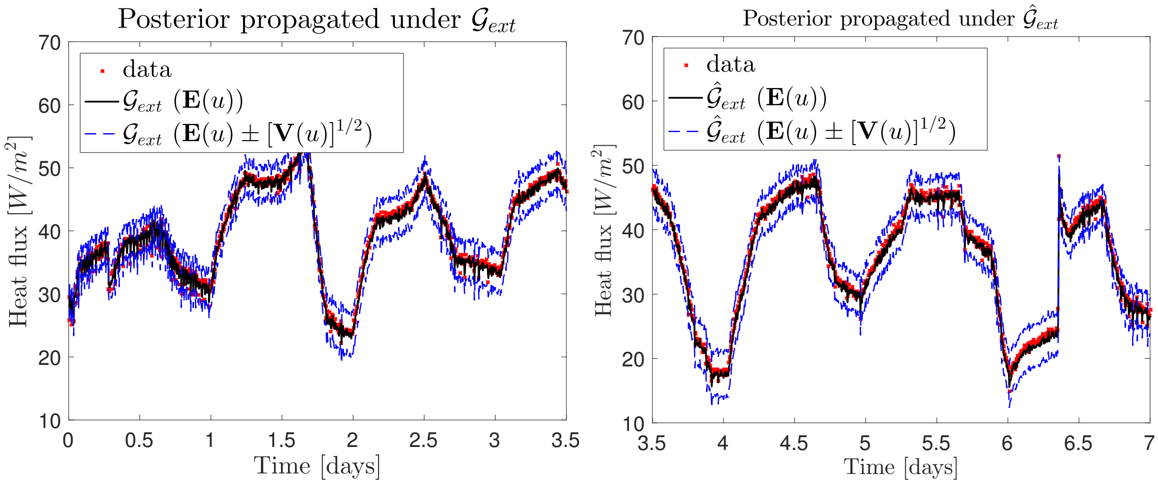

Figure 4.2.10: Analysis of chamber external heat flux data (solid wall). Propagation of the uncertainty under $\mathcal{G}_{ext}$ (left) and $\hat{\mathcal{G}}_{ext}$ (right) under the posterior. (HDM)

#### 4.2.3.5 Convergence

This section presents the analysis of the convergence of the Markov Chain, in relation to what was illustrated at the end of section 2.2.2.1.

Figure 4.2.11 shows the residuals calculated via equation 2.33 for the solid wall in the environmental chamber. Looking at the right panel of figure 4.2.11, it can be seen that the residuals drop sharply and stabilise within 500 iterations.

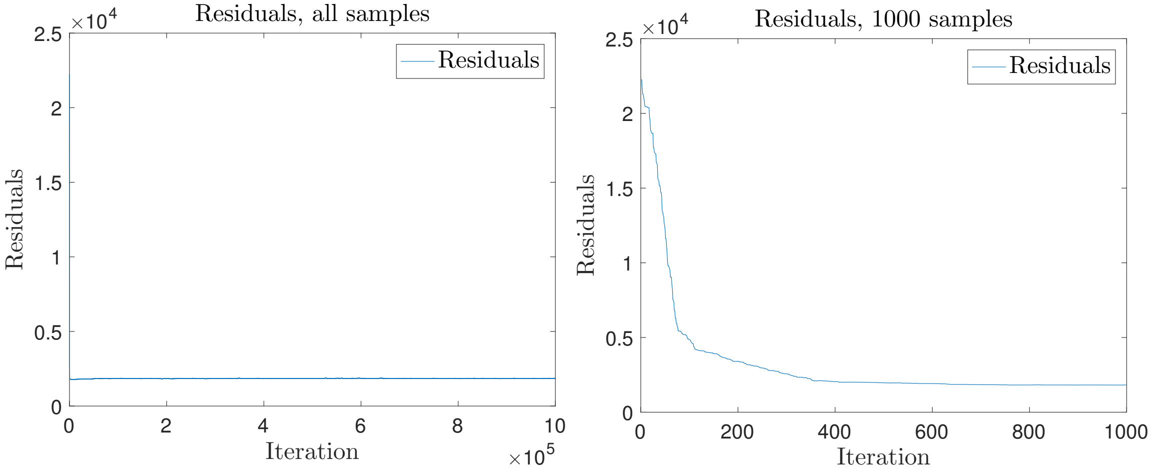

Figure 4.2.11: Samples residuals for the solid wall in the environmental chamber. Left panel: all samples. Right panel: first 1000 samples

This is in agreement with figures 4.2.12 and 4.2.13, which show the trace plots for the thermal conductance and heat capacity calculated from the samples produced with the MCMC algorithm. Looking at the right panels of figures 4.2.12 and 4.2.13, it can be seen that the trace shows a good mixing of the Markov Chain from roughly the $1500^{th}$ iteration. From these graphs it was deduced that the burn-in period (the number of the iterations that the Markov Chain needs to reach the stationary distribution, as explained in section 2.2.2.1) corresponds approximately to the initial 2000 iterations.

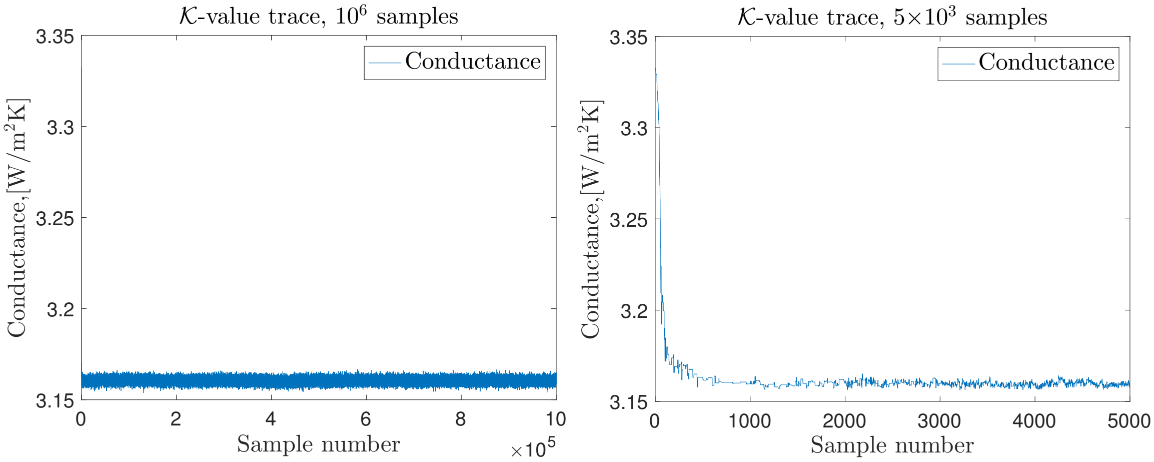

Figure 4.2.12: Trace plot of the thermal conductance values for the solid wall in the environmental chamber. Left panel: all samples. Right panel: first 5000 samples

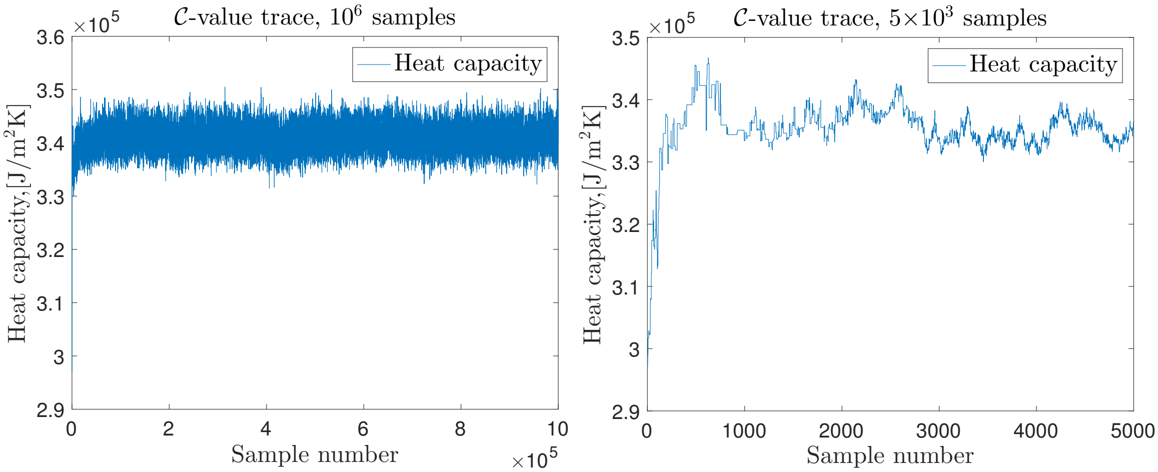

Figure 4.2.13: Trace plot of the heat capacity values for the solid wall in the environmental chamber. Left panel: all samples. Right panel: first 5000 samples

Figures 4.2.11-4.2.13 seem to suggest that the number of samples specified for use in the MCMC, i.e.$10^6$, is excessive given that within 2000 iterations the residuals have converged and the trace shows that the chain is mixing well. Still, these figures alone are not sufficient to understand the necessity of such a large number of iterations.

Figures 4.2.14-4.2.15, show the autocorrelation function of the values of the thermal conductance and heat capacity for different lags. The autocorrelation of a time series, in our case the sample series of the $\mathcal{K}$-value or $\mathcal{C}$-value, is the correlation of the time series with a delayed copy of itself, as a function of the delay. In practice, the autocorrelation is calculated via a number of computations. Initially the correlation between the chosen time series and an exact copy of itself is calculated; this value corresponds to the autocorrelation at lag 0 and yields an autocorrelation of 1. Following this, the copied vector is shifted by one timestep (lag 1) and a new correlation value is calculated. This procedure is repeated until a sufficient number of correlation values is produced, thus obtaining the autocorrelation function of the time series studied.

Looking at the right panel in these figures, it can be seen that the autocorrelation decays really quickly as the lag increases, and, in the case of the thermal conductance, it is nearly stable from the $100^{th}$ point forward. This means that only 1 in every 100 samples can be considered sufficiently uncorrelated and therefore the number of samples that can be considered for the characterisation of the posterior distribution is automatically reduced by 100. For this reason even if $10^6$ samples are produced, only $10^4$ can be considered for the calculation of the statistical moments of the posterior distributions.

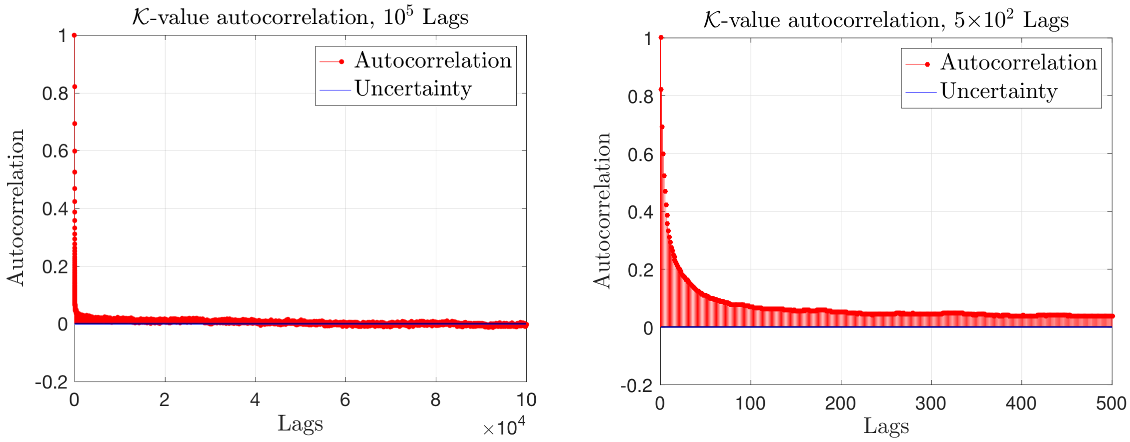

Figure 4.2.14: Autocorrelation of the samples of thermal conductance of the solid wall in the environmental chamber, excluding the first 1000 ("burn in") samples. Left panel: $10^6$ samples. Right panel: $10^3$ samples.

The left panel in figures 4.2.14-4.2.15 shows that the autocorrelation of the samples is always outside the uncertainty margin. This means that for the Markov Chain considered, it is nearly impossible to obtain samples that are completely uncorrelated. This is a consequence of the algorithm followed to construct the chain, equation (2.37), for which every new sample is calculated as a linear combination of the previous sample and a random element. In this way, every sample will bear some correlation with the other samples of the series that cannot be completely eliminated.

For this reason it is reasonable to accept samples every $100^{th}$ iteration, even if they still show a small autocorrelation.

For the analysis of the posterior distributions carried out in this and in the following chapters, one sample every 100 was kept (after the "burn-in" period), based on the autocorrelation function of the thermal conductance. This allows to make a clarification on figure 4.1.4: while it is possible to obtain as many samples as desired from the prior distribution, only $10^4$ posterior samples are available, this explains the

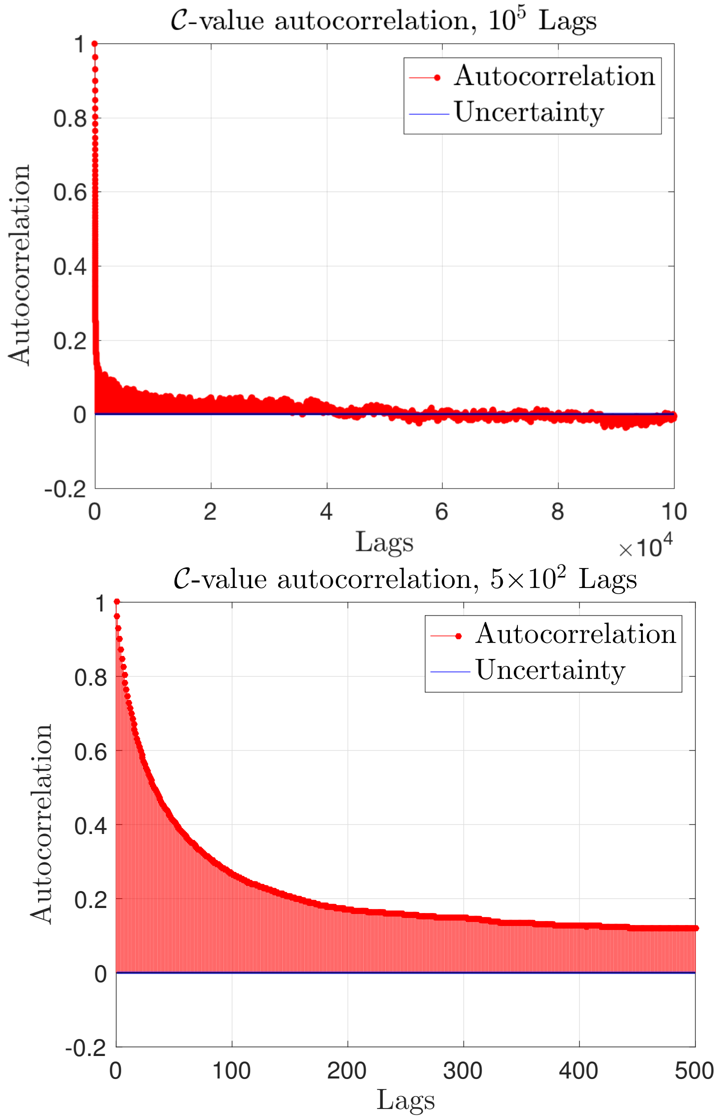

Figure 4.2.15: Autocorrelation of the samples of the heat capacity of the solid wall in the environmental chamber, excluding the first 1000 samples. Left panel: $10^6$ samples. Right panel: $10^3$ samples.

discrepancy between prior and posterior samples visible in figure 4.1.4.

## 4.3 STM performance

In this section, the STM described in Section 2.4 is implemented on the environmental chamber data set explored in section 4.2. The posterior distributions of the inferred thermal capacitance and heat capacity are shown in Figure 4.3.1, alongside the results of the HDM.

From figure 4.3.1, it can be seen that for both conductance and heat capacity the models produce different distributions. However, while in the case of the $\mathcal{K}$-value both results are acceptable when compared with values in the literature, the heat capacity suggested by the STM, is far too low to be representative of a solid wall construction (compare results in figure 4.3.1 with values inTable 4.2.1 and Table 4.2.3).

Figures 4.3.2 and 4.3.3 (left panel) show the propagation of the uncertainty in $G_{(int,STM)}$ and $G_{(ext,STM)}$. Figure 4.3.2 shows that the parameters inferred by the STM model poorly reproduce the measurements of the heat flux. In fact looking at the inference window of the internal heat flux it can be seen that the model predictions (black line) do not follow the data collected (red dots). Looking at figure 4.3.3 alone could be misleading, as the STM model seems to reproduce the external flux faithfully. However, looking more closely, it can be seen that, as well as for the internal flux, the uncertainty band collapses on the model predictions and excludes the experimental data from the error band. This suggests that the STM is overfitting the data and,

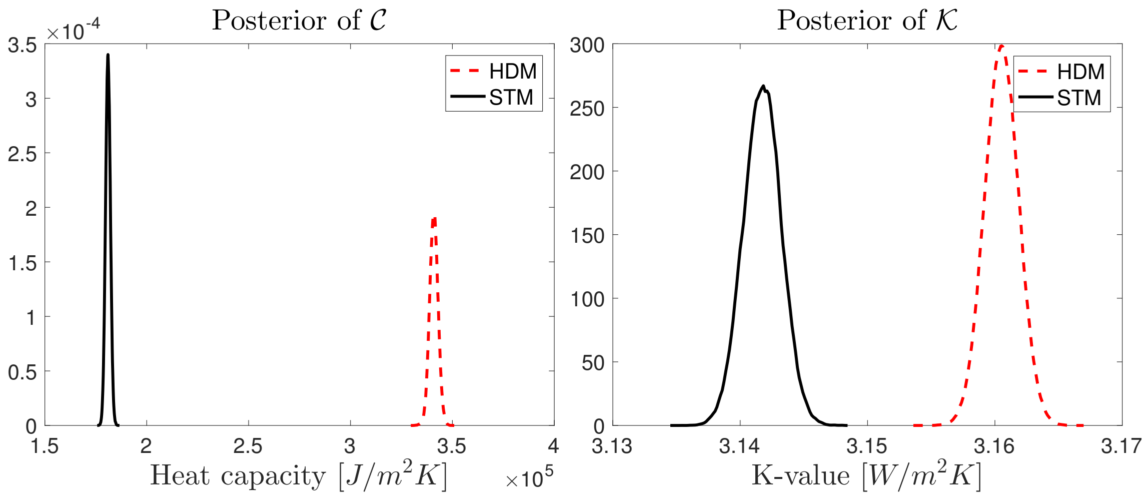

Figure 4.3.1: Analysis of chamber data (solid wall). Posterior densities of thermal mass (left) and K-value (right) obtained with the proposed methodology based on the Heat Equation and the STM model

.

consequently, its predictive capacities are poor, as can be seen from the right panel of figure 4.3.2. Conversely, if the model prediction was not presenting such a “good fit” to the data, but the uncertainty band was including the experimental data, it could have been concluded that the STM was capable of reproducing the heat flux profiles.

Summarising, it can be seen that the shortcomings of the STM, compared to the HDM, are the improper evaluation of the heat capacity, and consequent poorer ability at replicating the heat flux profiles, and the inappropriate characterisation of the uncertainty surrounding the model parameters.

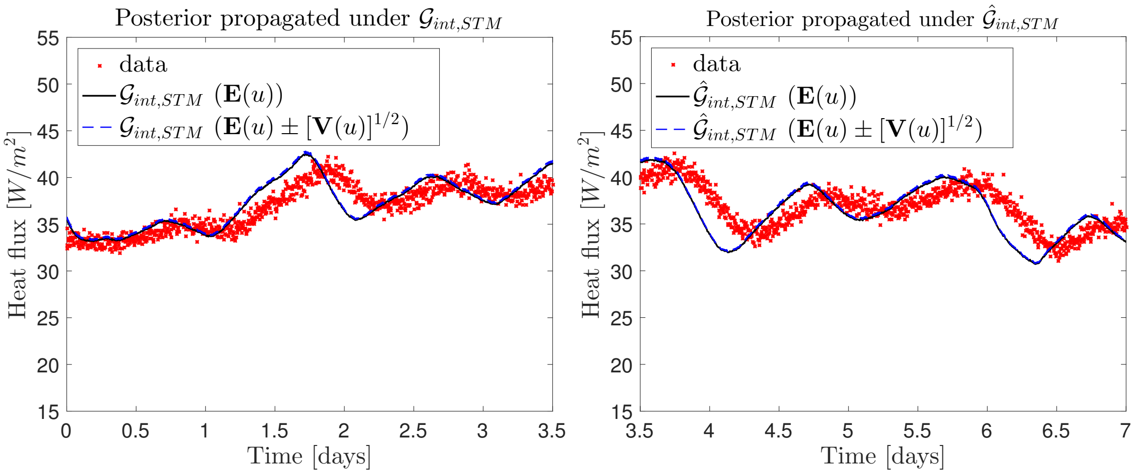

Figure 4.3.2: Analysis of chamber internal heat flux data (solid wall): Propagation of the uncertainty under $\mathcal{G}_{int,STM}$ (left) and $\hat{\mathcal{G}}_{int,STM}$ (right) under the posterior. (STM).

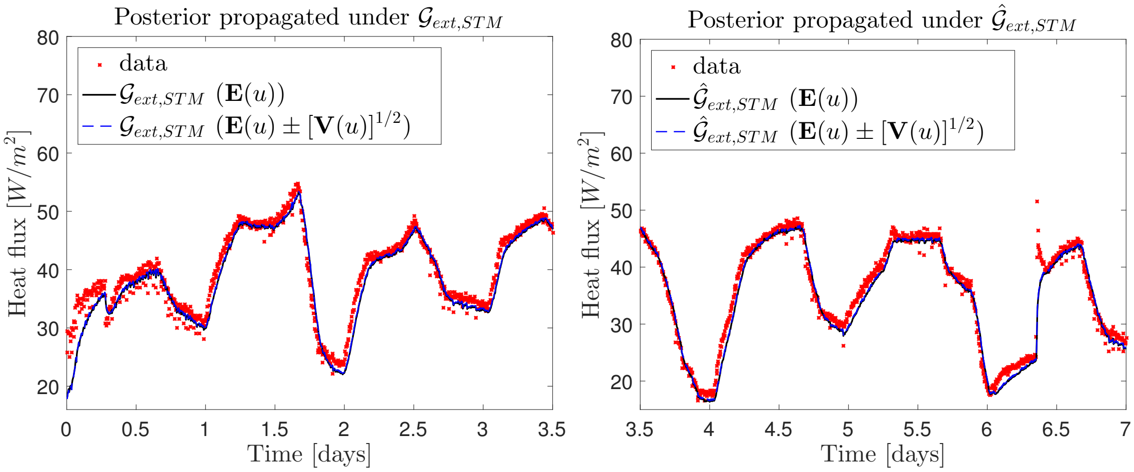

Figure 4.3.3: Analysis of chamber external heat flux data (solid wall): Propagation of the uncertainty under $\mathcal{G}_{ext,STM}$ (left) and $\hat{\mathcal{G}}_{ext,STM}$ (right) under the posterior. (STM).

## 4.4 Cavity wall

The HDM uses a Bayesian approach with a continuous heat transfer model of walls that has heterogeneous thermal properties. Section 1.6 proposes that a significant advantage of the HDM is that no a priori assumptions of the internal structure of the wall are needed to successfully infer the unknown parameters. To test this assertion, the HDM is used to infer $\kappa(x)$ and $c(x)$ for a cavity wall using internal and external heat flux measurements $y = (y_{ext}, y_{int})$. This corresponds to the data set collected on wall A in the environmental chamber. The prior distributions applied are the same as those used in the previous case, described in Section 2.2.2 and figures 2.2.3 - 2.2.4 and figure 4.2.2 (top). This tests the practical situation where the cavity within the wall is overlooked by a visual inspection and the internal heterogeneity is unknown.

Figures 4.4.1 and 4.4.2 show the propagation of prior uncertainty under the forward and predictive maps. They show that the uncertainty band does not capture the data and highlights how a lack of knowledge of wall structure can lead to poor model characterisation.

By applying the MCMC method discussed in Section 2.2, it is possible to sample from the posterior $u(x) = (\kappa(x), c(x))$. Figure 4.4.4 gives the posterior uncertainty bands for the cavity wall and shows that the thermal conductivity is considerably lower than the value assumed in the prior, as we would expect from a wall of this type, where the insulation in the cavity offers additional thermal resistance.

The inferred value of conductance ($0.78\ W/(m^2K)$) is very close to that estimated

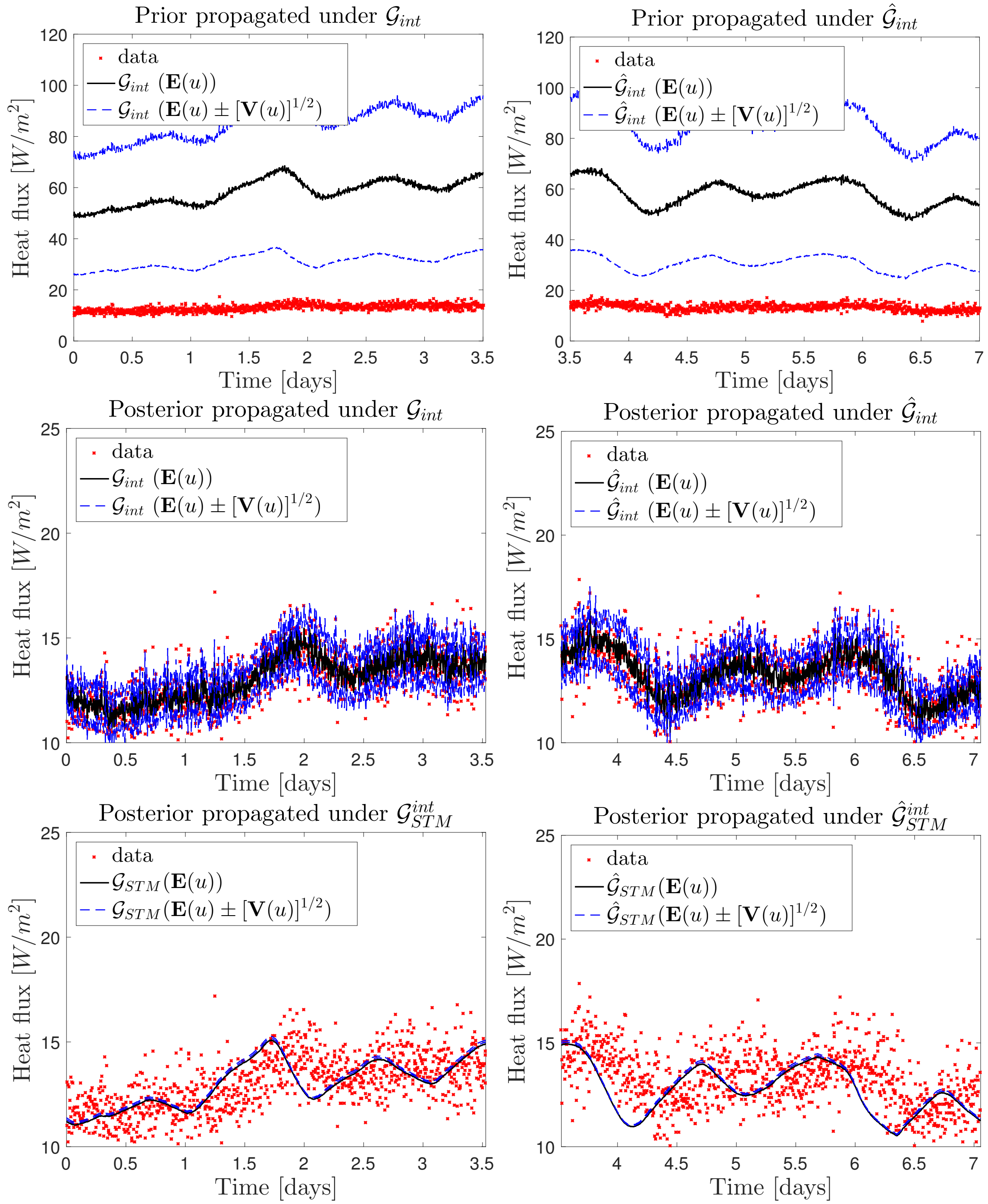

Prior propagated under $\mathcal{G}_{int}$

Prior propagated under $\hat{\mathcal{G}}_{int}$

Posterior propagated under $\mathcal{G}_{int}$

Posterior propagated under $\hat{\mathcal{G}}_{int}$

Posterior propagated under $\mathcal{G}_{STM}^{int}$

Posterior propagated under $\hat{\mathcal{G}}_{STM}^{int}$

Figure 4.4.1: Analysis of chamber internal heat flux data (cavity wall). Top and Middle: Propagation of the uncertainty under $\mathcal{G}_{int}$ (left) and $\hat{\mathcal{G}}_{int}$ (right) under the prior (top) and the posterior (middle). Bottom: Propagation of the uncertainty under $\mathcal{G}_{int,STM}$ (left) and $\hat{\mathcal{G}}_{int,STM}$ (right) under the posterior

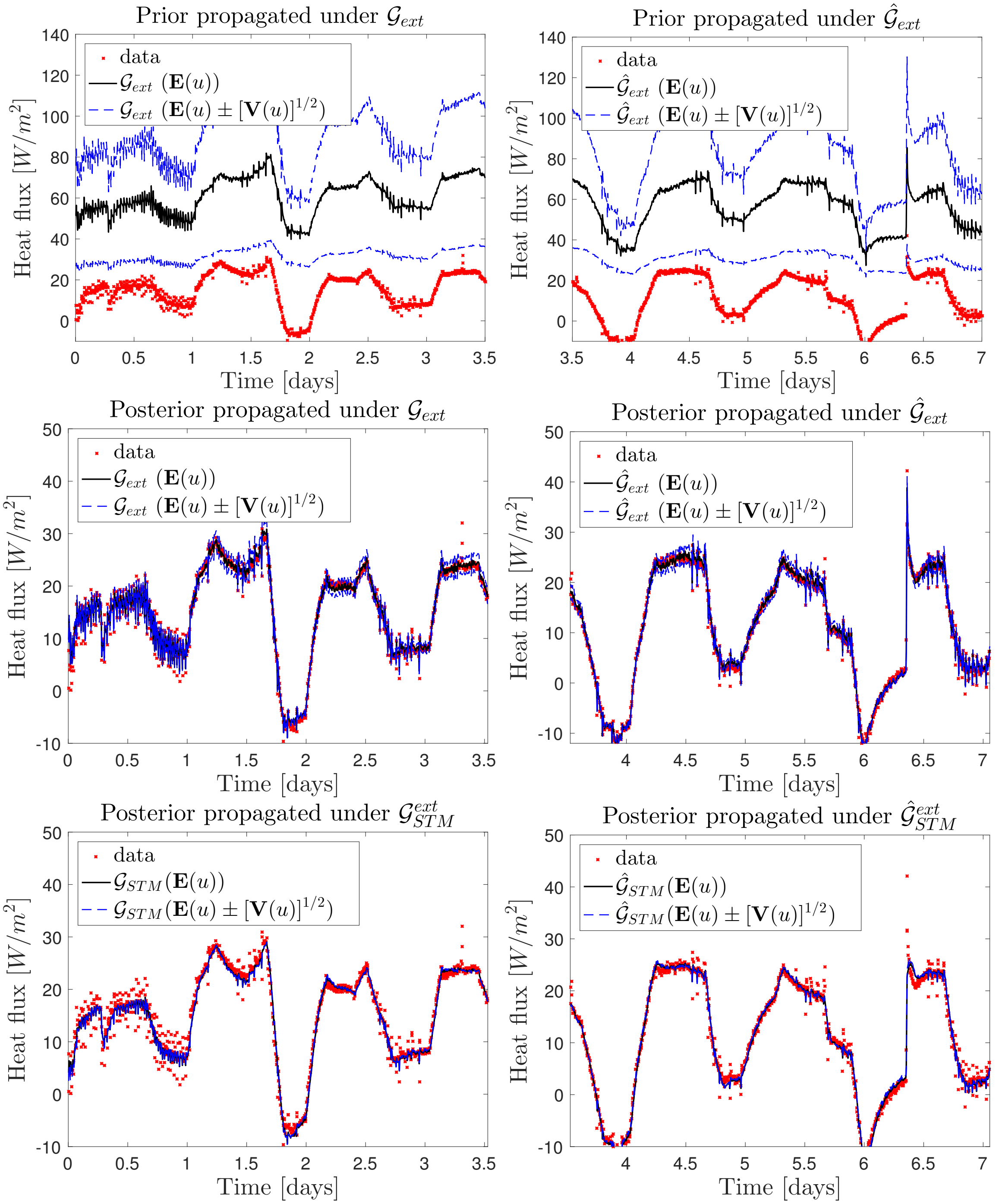

Figure 4.4.2: Analysis of chamber external heat flux data (cavity wall). Top and Middle: Propagation of the uncertainty under $\mathcal{G}_{ext}$ (left) and $\hat{\mathcal{G}}_{ext}$ (right) under the prior (top) and the posterior (middle). Bottom: Propagation of the uncertainty under $\mathcal{G}_{ext,STM}$ (left) and $\hat{\mathcal{G}}_{ext,STM}$ (right) under the posterior

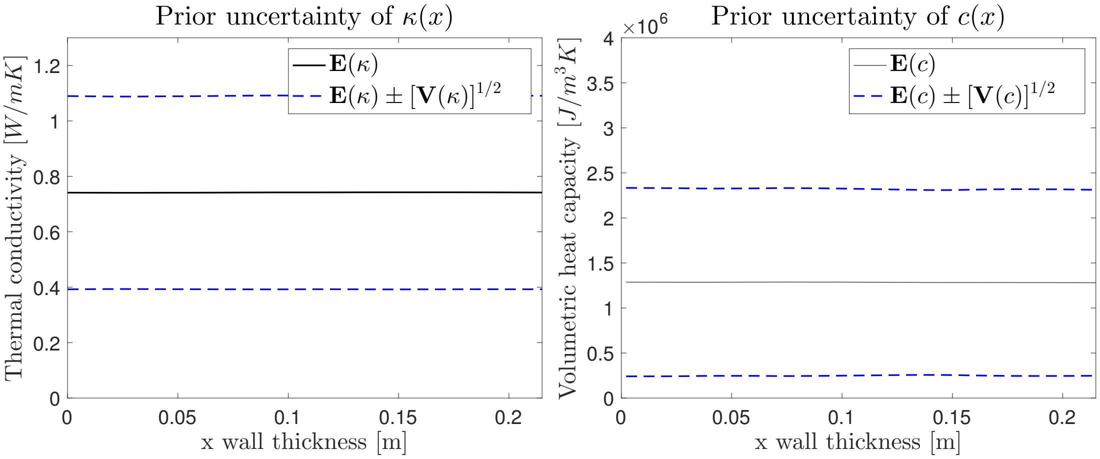

Figure 4.4.3: Analysis of chamber data (cavity wall). Prior uncertainty band of the thermal conductivity and volumetric heat capacity.

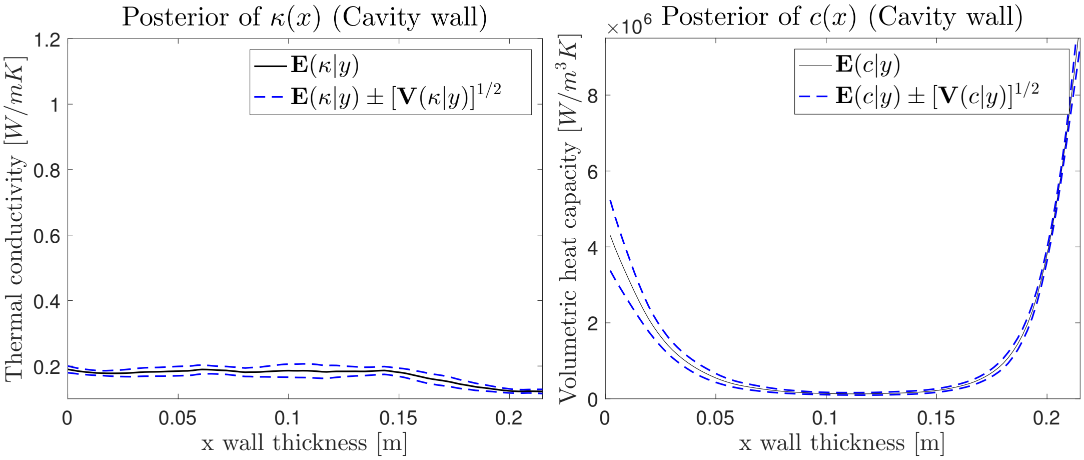

Figure 4.4.4: Analysis of chamber data (cavity wall). Posterior uncertainty band of the thermal conductivity and volumetric heat capacity.

using the “Average Method” (0.79 $W/(m^2K)$) , as it can be seen by comparing tables 4.2.3 and 4.2.1.

Looking at the results presented in the same tables, it can be seen that also in this case, the HDM is able to infer the heat capacity of the cavity wall and, furthermore, looking at figure 4.4.4, it can be seen that the heat capacity is considerably lower at the centre of the construction, as it is expected, since the capacity of insulation is considerably lower than the heat capacity of the brick layers. However, the spatial distribution of $\kappa(x)$, displayed on the left panel of figure 4.4.4, is quite constant through the wall thickness, as opposed to the expectations, as the thermal conductivity of the insulation layer is much lower than the thermal conductivity of the bricks, as in the case of the volumetric heat capacity.

From all the HDM results, summarised in table 4.2.3, it can be noted that the uncertainty in the heat capacity is always higher than the uncertainty in the conductance. This may be because, in order to obtain an appreciable change in the amount of energy stored in this wall, the construction should be subjected to large fluctuations in temperature. However, this is not possible by simulating realistic indoor and outdoor conditions, where temperature fluctuations are small.

Table 4.2.3 also displays the values for conductance and heat capacity obtained with the STM for the cavity wall. Comparing these values with those displayed in table 4.2.1, it can be seen that while the conductance value may be considered to sit within an acceptable range, the heat capacity calculated by the STM model is far too low to be indicative of a cavity wall. The inability of the STM to capture the dynamic thermal behaviour is further demonstrated by the heat flux prediction graphs as detailed in the next paragraphs.

Figures 4.4.1 and 4.4.2 (middle) give the propagation of posterior uncertainties for the HDM. They show an appreciable reduction in the uncertainty of the posterior mean, which provides a reasonable characterisation of the heat flux behaviour in the predictions of the HDM.

Figures 4.4.1 and 4.4.2 (bottom) give the propagation of the posterior for the STM. It can be seen that the uncertainty band collapses on the model prediction and does not capture the data. Looking at Figure 4.4.1 (bottom, right) in particular, (the internal heat flux profile for days 3.5 - 4.5), it can be observed that the behaviour predicted by the STM is quite different from the recorded measurements and it looks as if the prediction is “delayed” with respect to the data measured. This discrepancy in the internal environment is indicative of the fact that the STM is not able to accurately characterise the heat capacity of the wall considered.

Also in this case, the performance of the HDM in capturing the uncertainty around the heat flux predictions in the cavity wall is not optimal, as it may be seen from the middle parts in figures 4.4.1 and 4.4.2. This is because the prior distributions assumed were not representative of a cavity wall. Still, the model is able to determine realistic values of the thermal conductance and heat capacity of the construction. The uncertainty characterisation can be optimised by rearranging the priors, as will be shown in chapter 5.

## 4.5 Discussion of results

As may be seen from figures 4.2.4 - 4.2.5 the thermal properties values found in literature do not reproduce the heat flux profile measured experimentally for the wall samples used in this study. The wide range of values found in the literature, is reflected in the wide uncertainty band displayed in the analysis, that, as can be seen in figures 4.2.4 - 4.2.5 not always include the experimental data. This means that the assumptions made on the thermal properties based on values found in literature are completely unrepresentative of the actual wall constructions considered in this study.

This underlines the necessity of measuring the thermal properties experimentally and developing a reliable model to reduce the uncertainty on the thermal properties and obtain more accurate heat transfer predictions, able to match the data collected in situ. The HDM provides greater insight into the heat transfer process occurring in the building fabric, as may be seen by its ability to predict time varying behaviour, and to produce reasonable estimates of the thermal properties sought.

Comparing the results displayed in figures 4.2.9 and 4.2.10, against figures 4.3.2 and 4.3.3 it is clear that the HDM offers significant improvements over the STM for the characterisation of dynamic thermal behaviour. The posterior uncertainty for the forward map $\mathcal{G}_{STM}$ collapses into $\mathcal{G}_{STM}(\mathbf{E}(u|y))$, which is a sign that the STM is overfitting the data and consequently that it does not offer the ability to yield accurate predictions outside of the inference time window. This undermines the confidence in the results produced with this model.

Having investigated the performance of the STM and HDM using a 3.5 day window, under laboratory conditions, it is now interesting to verify the performance of the model under real life conditions and, possibly, determine the minimum amount of data necessary for the HDM to produce acceptable results in terms of conductance evaluation and heat transfer modelling. In the following chapter, the HDM is validated against the other data sets collected and described in chapter 3.

# Chapter 5

# Validation against other data sets

This chapter describes the validation of the HDM carried out on different experimental data sets.

Initially, in section 5.1, the HDM and STM are tested on the data collected by BSRIA and previously analysed by Biddulph et. al [72].

Following this, in section 5.2, the HDM is validated against the other data sets described in chapter 3, comprising different wall structures and experimental conditions.

Finally, the model is stress-tested in order to evaluate its limits and validate its strengths by exploring its performance using experimental data gathered over different time windows.

Section 5.3 discusses the results obtained, identifying the advantages of the HDM compared with the standard practice, and future work on this topic is suggested.

## 5.1 BSRIA data

In this section, the data set collected by the Building Services Research and Information Association (BSRIA) is considered. The sample of data used in this analysis is shown in Figure 5.1.1. The data are first analysed by implementing the MCMC algorithm with the HDM, section 5.1.1, and then the same data are analysed with the STM, section 5.1.2.

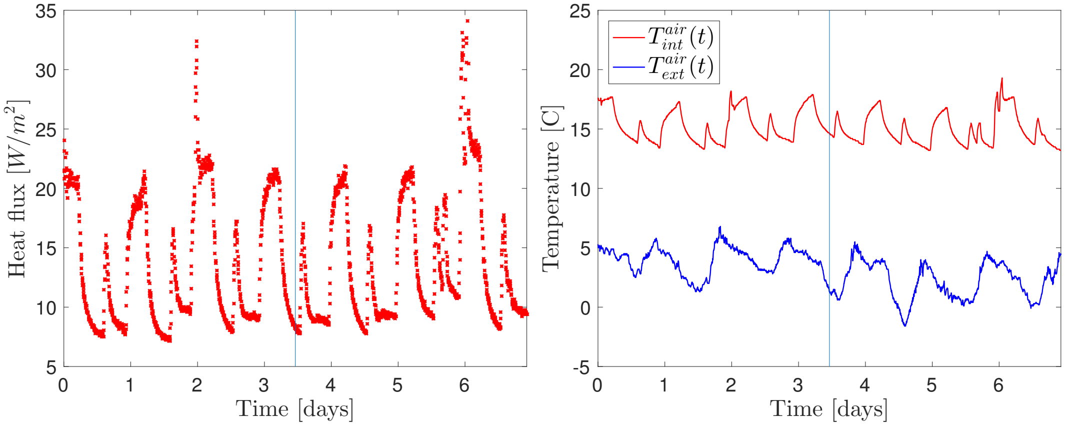

Figure 5.1.1: BSRIA data. Left: Heat flux measurements at the internal surface. Right: Internal and external nearby air measurements. The vertical line divides the inference time window $[0, 3.5 \text{ days}]$ from the validation time window $[3.5 \text{ days}, 7 \text{ days}]$

As adopted in chapter 4, the first 3.5 days are used for the inference of the thermal properties of the wall under consideration and a subsequent time window of the same length is used for validation purposes.

### 5.1.1 Analysis of BSRIA data by means of the HDM

For the analysis of this data set, the air temperatures, denoted by $T_{int}^{air}$ and $T_{ext}^{air}$, as opposed to the surface temperatures, are used in the boundary conditions of the heat transfer model introduced in subsection 2.1, equations (2.1), (2.13),(2.14) and (2.16).

This corresponds to the heat transfer problem with convective boundary conditions and, as illustrated in section 2.1.1.1, in this case the Bayesian formulation includes also the initial temperature amongst the unknown parameters.

As the boundary conditions include experimental measurements of the nearby air temperature, $T_{int}^{air}(t)$ and $T_{ext}^{air}(t)$, in this case the final values inferred relate to the thermal transmittance (as opposed to conductance) and heat capacity, calculated via equation (2.17).

The values of the scalars $h_{int}$ and $h_{ext}$ shown in equations (2.13) - (2.14) are given by $h_{int}^{-1} = 0.13\ [m^2K/W]$ and $h_{ext}^{-1} = 0.04\ [m^2K/W]$ as suggested in CIBSE guide A [8].

As the structure of the wall observed is of solid single leaf construction with plaster finish, the prior distributions of the thermal properties were based on the same literature values as used in the case of the environmental chamber analysis, in section 4.2.

Figure 5.1.2, top panel left, shows the predictions obtained from the prior knowledge, without conditioning the prior distribution with the experimental data. Again, it can be seen that prior knowledge based only on values of $\kappa$ and $c$ taken from the literature is insufficient to produce reliable estimates of heat flux predictions and, therefore, these are inappropriate estimators of the thermal properties of the wall considered. In particular, even if the uncertainty band contains the model predictions, it can be seen that during the first two days the prediction does not capture the measured data. Consequently, for the prediction window (top panel right in figure

5.1.2) there is a large uncertainty around the model predictions.

On the other hand, the bottom panels of figure 5.1.2 show that the HDM model fully captures the measured data in both in the inference and validation window. The uncertainty surrounding the model predictions is greatly reduced and it includes the experimental data thorougout the whole 7 day window. Figure 5.1.3 clearly shows the reduction in uncertainty between the prior and the posterior as already indicated for the previous data sets.

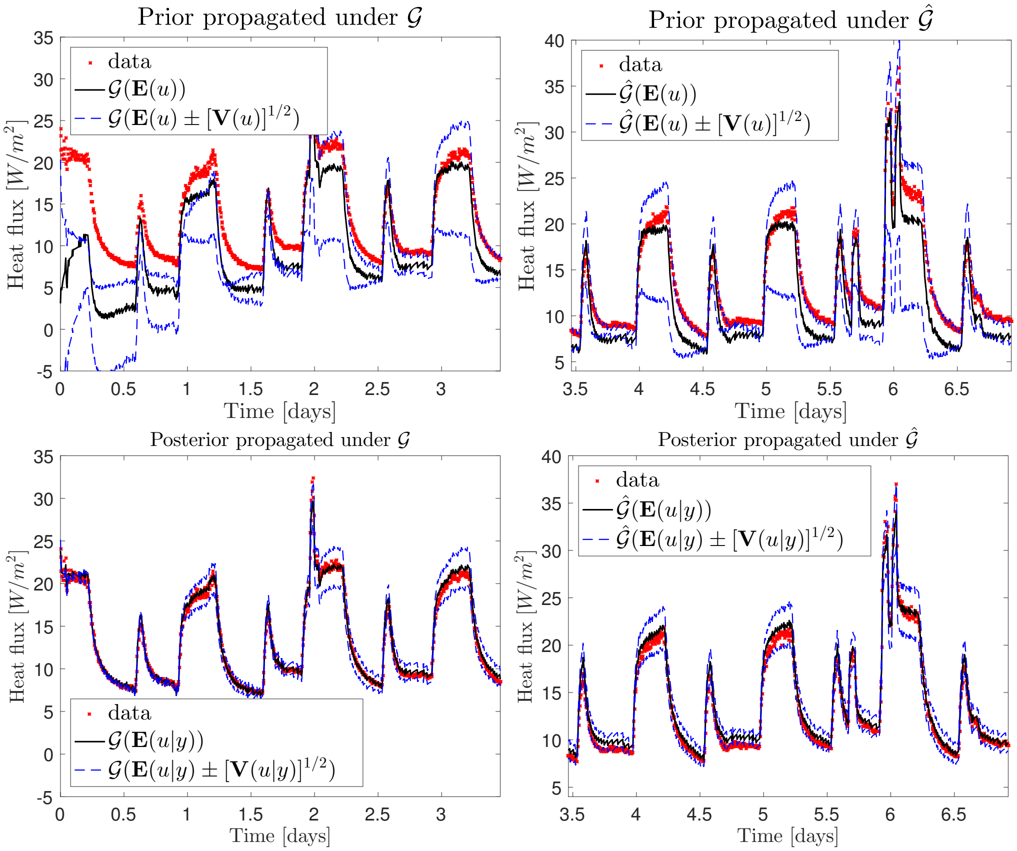

Figure 5.1.2: Analysis of BSRIA data. Propagation of the uncertainty under $\mathcal{G}$ (left) and $\hat{\mathcal{G}}$ (right) under the prior (top) and the posterior (bottom).

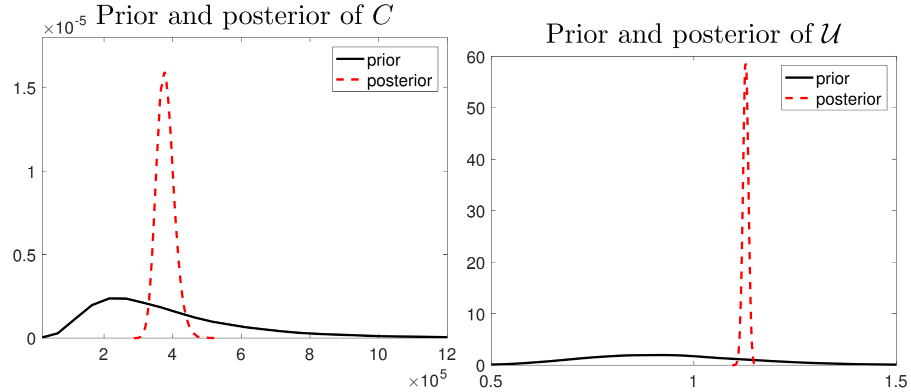

Figure 5.1.3: Analysis of BSRIA data. Comparison of prior and posterior for the probability densities of heat capacity (left) and U-value (right)

The results obtained for the $\mathcal{U}$-value and heat capacity per unit area are displayed in table 5.1.1. It might be seen that the $\mathcal{U}$-value obtained agrees with the results obtained by Biddulph et al. [72] (1.153 ± 0.002 $W/(m^2K)$), but the specific heat capacity obtained is considerably different than the value reported by [72] ($2.24 \times 10^5 \pm 0.19 \times 10^5$ $J/(m^2K)$). Considering that the value reported in [72] is quite low to be representative of the heat capacity of a solid wall, this might indicate that a simple RC network with one capacitor, such as the STM model, does not offer an appropriate characterisation of the thermal capacity of the construction investigated. The value obtained with the HDM instead is in agreement with the literature data on the heat capacity, as it can be seen from table 4.2.1 thus remarking how this model provides a better characterisation of the thermal properties of the wall studied.

Table 5.1.1: Posterior mean and posterior standard deviation of the U-value $\mathcal{U}$ and the heat capacity $\mathcal{C}$ for the BSRIA.

| BSRIA data | $\mathbf{E}(\mathcal{U}\|y)$ $[W/m^2K]$ | $[\mathbf{V}(\mathcal{U}\|y)]^{1/2}$ $[W/m^2K]$ | $\mathbf{E}(\mathcal{C}\|y)$ $[J/m^2K]$ | $[\mathbf{V}(\mathcal{C}\|y)]^{1/2}$ $[J/m^2K]$ |
|---|---|---|---|---|
| HDM | 1.128 | $6.8 \times 10^{-3}$ | $3.79 \times 10^5$ | $2.58 \times 10^4$ |
| STM | 1.17 | $4.4 \times 10^{-3}$ | $1.98 \times 10^5$ | $5.73 \times 10^3$ |

### 5.1.2 Analysis of BSRIA data by means of the STM

In this subsection the results obtained using the STM model, are presented.

While these results are similar to those presented by Biddulph et al. [72], some differences in the estimates presented in this work are expected because the time window used is shorter.

In Figure 5.1.4 the empirical posterior densities of the U-value (right) and heat capacity (left) obtained with the Bayesian inference for the STM are compared against the distributions obtained with the HDM from section 5.1.1.

While the distribution of the U-value obtained with the STM seems be slightly shifted to the left and have a small variance, the distribution of the heat capacity is substantially different. In this case, the value obtained with the STM, $1.98 \times 10^5 \pm 5.73 \times 10^3 [J/m^2K]$, is much closer to the value reported by Biddulph et al. i.e. $2.24 \times 10^5 J/m^2K$ [72], but again is too far from the literature values to be representative for a solid wall.

Figure 5.1.5 shows the propagation of uncertainty of two standard deviations with respect to the mean of the posterior distribution, $\mathbf{E}(u|y)$, under the forward map $\mathcal{G}_{STM}$ and the prediction map $\hat{\mathcal{G}}_{STM}$. The results from Figure 5.1.5 (left) agree with those from [72]. The STM model provides a good fit to the data; however, it can be observed that, under the map $\mathcal{G}_{STM}$, the posterior uncertainty collapses into $\mathcal{G}_{STM}(\mathbf{E}(u|y))$, which compromises the confidence in the uncertainty in model predictions. It is of course, clear that $\mathcal{G}_{STM}(\mathbf{E}(u|y))$ would provide a reasonable fit to the data since those very same observations were used for the inference of the unknown. However, inspecting Figure 5.1.5 (right) it can be appreciated that, in the prediction window, the data fit provided by the posterior mean $\mathbf{E}(u|y)$ propagated under $\hat{\mathcal{G}}_{STM}$ clearly deteriorates, (see the discrepancies between day 3.5 and 4 and between 4.5 and 5). Furthermore as noted in section 4.3, it can be seen that the uncertainty band collapses on the model predictions thus excluding the experimental data from the model posterior uncertainty. These facts are symptomatic that the STM might be overfitting the data and, therefore, it does not provide a reliable inference tool.

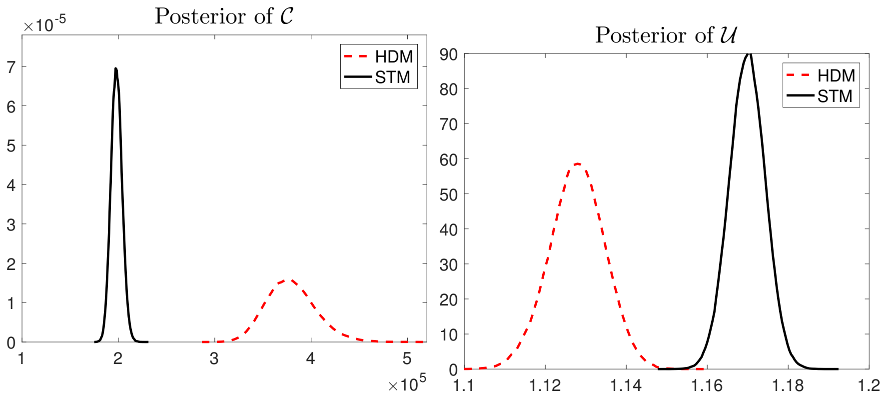

Figure 5.1.4: Analysis of BSRIA data. Posterior densities of heat capacity (left) and U-value (right) obtained with the HDM and STM model.

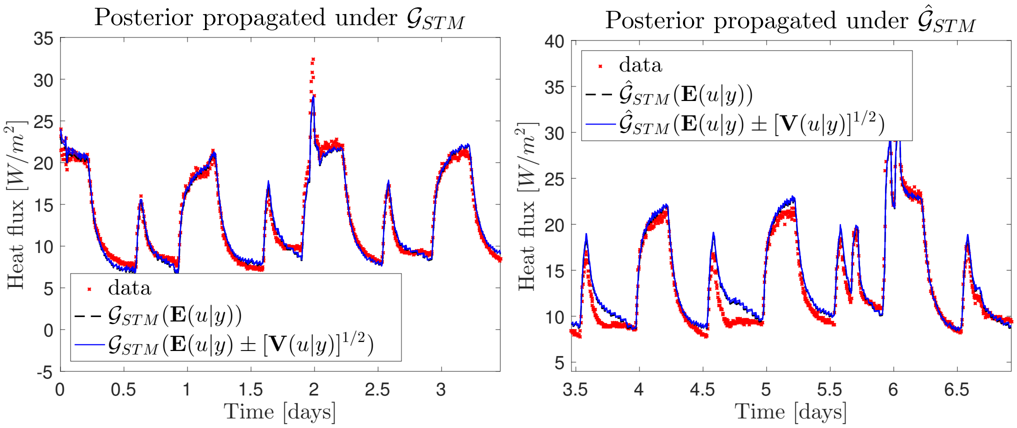

Figure 5.1.5: Analysis of BSRIA data. Propagation of the uncertainty under $\mathcal{G}_{STM}$ (left) and $\hat{\mathcal{G}}_{STM}$ (right) under the posterior.

## 5.2 Short time window performance

In this section, the model is tested to determine the shortest appropriate time window required to produce reliable results. Besides the BSRIA data set presented above, the HDM is also tested on the other data sets collected during this research and described in sections 3.3 and 3.4.

### 5.2.1 Different time windows performance

Having investigated the performance of the STM and HDM on a 3.5 day window, it is now interesting to determine the minimum amount of data necessary for the HDM to produce acceptable results in terms of conductance evaluation and heat transfer modelling. The data set utilized for the window length investigation is the one collected in the environmental chamber on the solid wall (wall C), which has been presented in section 4.2.1. A 7 day time window is considered in all cases, with different amounts of data used for the inference process (3.5 days, 2 days, 12 hours etc). The performance of the model was evaluated based on the residuals between the model prediction and measured data on the second part of the time window (3.5 days, 5 days, 6.5 days etc). The following definition of residuals is introduced:

$$Res = \sqrt{\frac{\sum (y - \hat{\mathcal{G}}(u))^2}{N}} \tag{5.1}$$

Where $y$ are the measured data and $\hat{\mathcal{G}}(u)$ are the model predictions and N is the number of data points in the prediction window. At this point, it is necessary to specify that for the shorter time windows (1 day and less) the sampling frequency was increased from 5 minutes to 3 minutes. It is worth noting that the residuals are independent of the number of data points used as the differences between model prediction and experimental data are divided by the total number of points used, as it may be seen in equation (5.1).

Table 5.2.1 shows the outcomes of the different inference processes with the relevant uncertainty. As was to be expected, the uncertainty in the thermal properties increases as the length of time window decreases, but all the values are found to be in good agreement with values found in the literature (Table 4.2.1). The algorithm developed cannot cope with time windows shorter that 1.5 hours: when the HDM was tested on a 45 min window it failed to produce any result. This may be attributed to the fact that 45 minutes are not sufficient to record the heat storage effects that naturally occur inside the wall and therefore the model does not have enough data to characterise the thermal properties of the construction investigated. Table 5.2.2 shows the residuals calculated via equation (5.1).

Table 5.2.1: Conductance and volumetric heat capacity and statistical uncertainty for different time windows

| | $\mathbf{E}(\mathcal{K}\|y)$ $[W/(m^2K)]$ | $[\mathbf{V}(\mathcal{K}\|y)]^{1/2}$ $[W/(m^2K)]$ | Relative uncertainty | $\mathbf{E}(\mathcal{C}\|y)$ $[J/(m^2K)]$ | $[\mathbf{V}(\mathcal{C}\|y)]^{1/2}$ $[J/(m^2K)]$ | Relative uncertainty |
|---|---|---|---|---|---|---|
| 3.5 days | 3.16 | $1.3 \times 10^{-3}$ | 0.04 % | $3.41 \times 10^5$ | $2.00 \times 10^3$ | 0.59 % |
| 2 days | 3.17 | $3.4 \times 10^{-3}$ | 0.11 % | $3.61 \times 10^5$ | $5.61 \times 10^3$ | 1.56 % |
| 12 hours | 3.17 | $9.5 \times 10^{-3}$ | 0.30 % | $3.72 \times 10^5$ | $2.16 \times 10^4$ | 5.80 % |
| 6 hours | 3.15 | $1.8 \times 10^{-2}$ | 0.58 % | $4.07 \times 10^5$ | $5.05 \times 10^4$ | 12.41% |
| 3 hours | 3.13 | $3.4 \times 10^{-2}$ | 1.08 % | $4.36 \times 10^5$ | $7.23 \times 10^4$ | 16.58% |
| 1.5 hours | 3.07 | $5.6 \times 10^{-2}$ | 1.81 % | $4.70 \times 10^5$ | $9.54 \times 10^4$ | 20.33% |
| 45 minutes | NA | NA | NA | NA | NA | NA |

Table 5.2.2: Residuals for internal and external heat flux for different time windows

| Time window | 3.5 Days | 2 Days | 0.5 Days | 6 hours | 3 hours | 1.5 hours | 45 minutes |
|---|---|---|---|---|---|---|---|
| Internal residual $[W/(m^2K)]$ | 0.74 | 1.42 | 1.40 | 1.39 | 1.40 | 1.61 | NA |
| External residual $[W/(m^2K)]$ | 0.69 | 0.76 | 0.93 | 1.37 | 1.44 | 2.00 | NA |

Figure 5.2.1 shows the variance in the $\mathcal{K}$-value, $\mathcal{C}$-value and the internal and external residuals against the time window length. In both graphs, especially for the $\mathcal{K}$-value variance and external residuals, it is clear that shortening the inference time window produces a larger uncertainty in the values obtained and larger residuals. All figures show that there is a sharp decrease in uncertainty and residuals when extending the time window to 0.5 days. This suggests therefore that 12 hours is the optimal window frame to minimise both the uncertainty and the data collection time.

The uncertainty in the heat capacity per unit area is larger than that in the $\mathcal{K}$-value, still, the estimates found appear to be in agreement when compared with values found in literature. Even if the data suggest that a 12 hour window is optimal for the calculation of the $\mathcal{K}$-value and heat flux predictions, the $\mathcal{K}$-value found using just 1.5 hours of observations is still in an acceptable range with the variance estimated with the MCMC algorithm being only 1.8%, (table 5.2.1). In light of this observation, if the focus of the research performed is simply to obtain an estimate of the $\mathcal{K}$-value and then $\mathcal{U}$-value of a construction, 1.5 hours of data, coupled with the HDM presented in this thesis, could be sufficient. This shows that the HDM is a powerful tool for large scale performance monitoring of building fabric.

These conclusions are drawn from the results obtained in the environmental chamber and might not be therefore representative of a real, in-situ application. For this reason, the same analysis was performed on the dataset collected in the unoccupied solid wall property described in section 3.3 and an insulated steel frame construction part of an office space described in section 3.4.

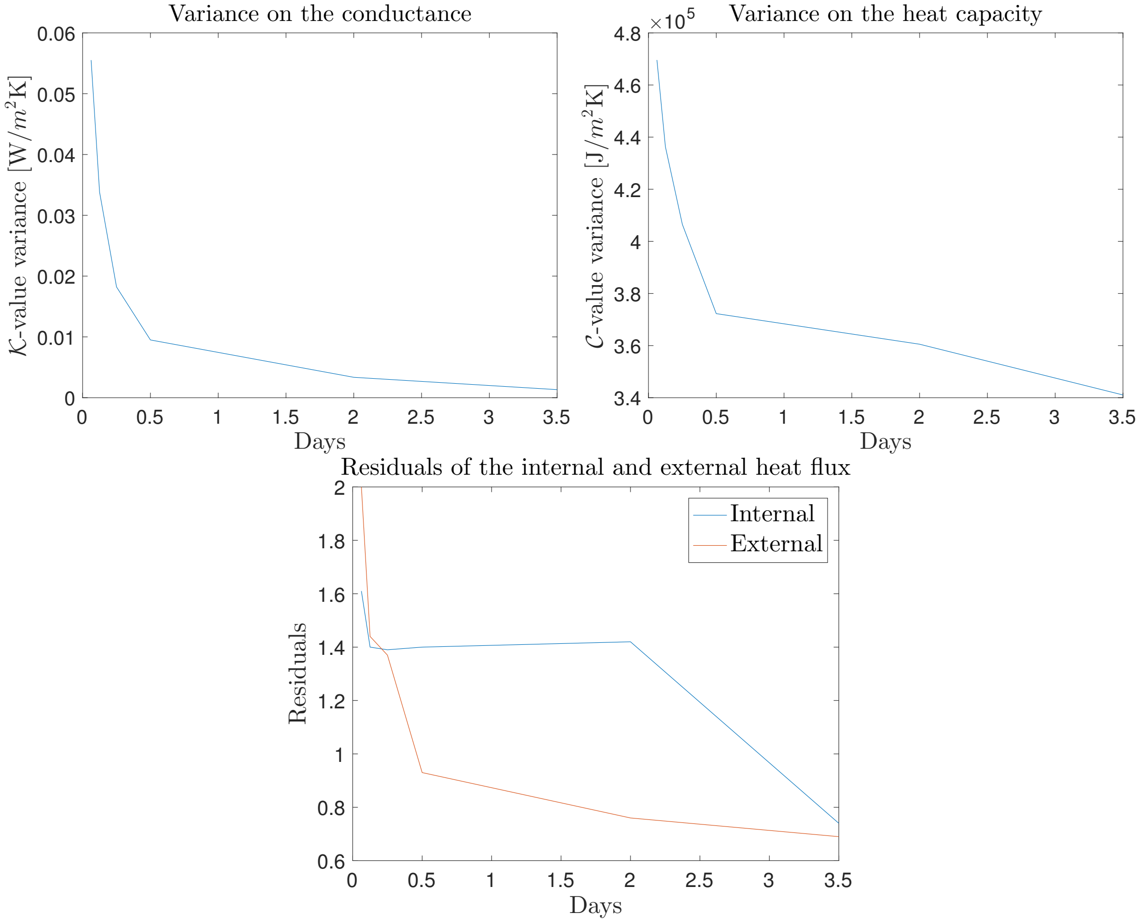

Figure 5.2.1: Analysis of the HDM on short time windows. Left: variance in the $\mathcal{K}$-value. Middle: variance in the heat capacity per unit area Right: Internal and External heat flux residuals

### 5.2.2 Analysis on the unoccupied solid wall property

The construction investigated in this case is an unoccupied solid wall property. The wall monitored appears to exhibit a defect area in the centre of the construction. As no other visual elements or design construction drawings were available, it was supposed that this could be the result of a chimney or flue present in the wall thickness.

This areas is included in the analysis as it represents a practical scenario where, from visual inspection only, the experimenter cannot distinguish the wall construction and the defect could be overlooked.

The air temperature profiles and heat flux data collected during the monitoring period are displayed in figure 5.2.2. Surface temperature measurements were also available for each location monitored, therefore the model adopted for the inversion is the heat equation with surface temperature boundary conditions, described by equations (2.1) - (2.5).

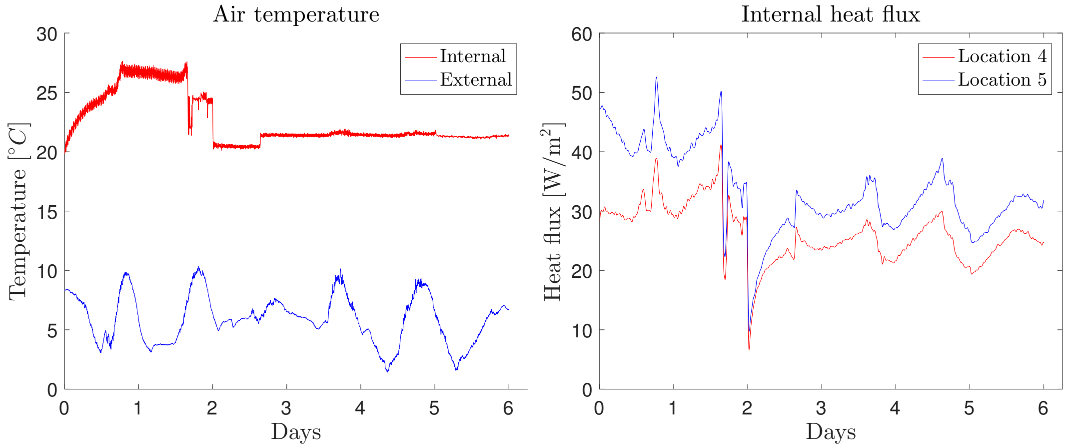

Figure 5.2.2: Air temperatures and heat flux profiles of the data collected in the unoccupied solid wall property

As in the case of the data collected in the environmental chamber, at first the data were analysed via the “Average Method”, equation (1.18) to provide a benchmark for future comparison. The $\mathcal{K}$-value/ resistance results are displayed in Figure 5.2.3, along with a schematic representation of the sensor locations. The full time window available for the calculations is 6 days, and, in the case of the calculation via the “Average Method”, the whole time window was necessary to meet the stability criteria described in ISO 9896:2014.

For this validation, the sensors in the locations bottom centre and top right of the wall were utilised (locations 4 and 5). Location 4 is representative of the defect within the wall whereas location 5 is a defect free area of the wall and is therefore expected to yield measured data that are representative of a solid wall. As the wall considered was supposedly a solid wall, the priors do not require adjustment and are the same as those used for the analysis of the data collected in the chamber as detailed in section 4.2.

#### 5.2.2.1 Location 5

From the results displayed in table 5.2.3, it can be seen that the HDM is able to produce reliable estimates of the conductance and heat capacity for the building structure considered, as the figures obtained (especially when using 3 and 2 days data windows) agree with the ““Average Method”” measurement (2.86 $[W/m^2K]$) and the values found in literature ($\mathcal{K}$-value 2.60 - 3.58 $W/m^2K$ and $\mathcal{C}$-value 2.77 $\times 10^5$-4.40 $\times 10^5$ $J/m^2K$, as displayed in table 4.2.1) as the uncertainty on the ““Average Method”” includes all the values obtained with the HDM.

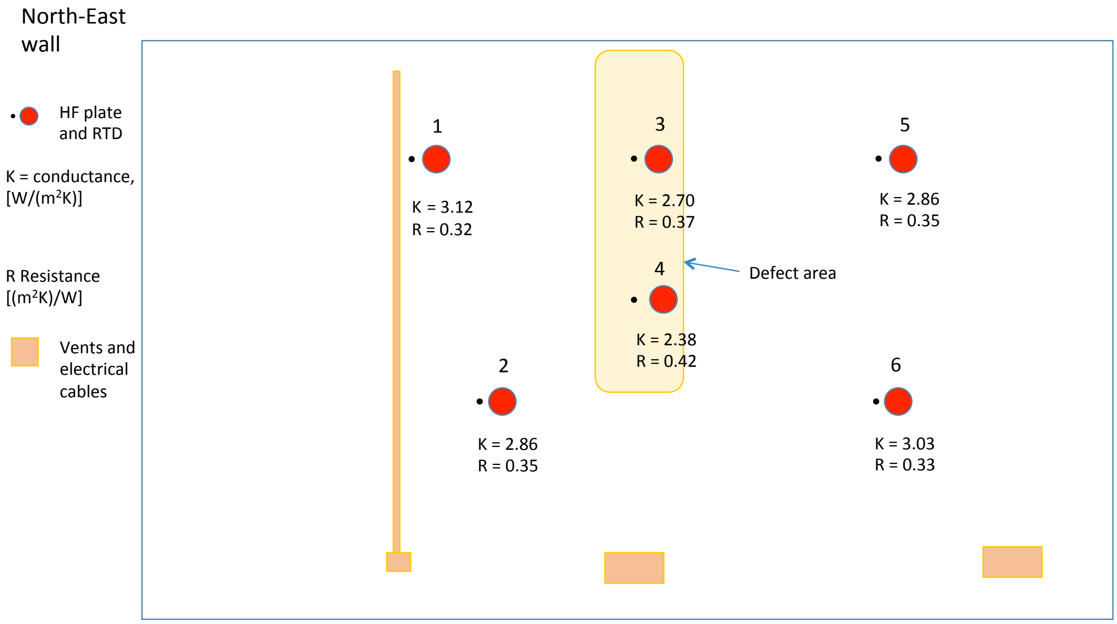

Figure 5.2.3: Wortley Hall Close data. Sensor location, resistance and U-value calculated with the "Average Method".

Table 5.2.3: Conductance, volumetric heat capacity and statistical uncertainty inferred for different time windows from data collected from Wortley Hall Close. Location 5

| | $\mathbf{E}(\mathcal{K}\|y)$ $[W/(m^2K)]$ | $[\mathbf{V}(\mathcal{K}\|y)]^{1/2}$ $[W/(m^2K)]$ | Relative uncertainty | $\mathbf{E}(\mathcal{C}\|y)$ $[J/(m^2K)]$ | $[\mathbf{V}(\mathcal{C}\|y)]^{1/2}$ $[J/(m^2K)]$ | Relative uncertainty |
|---|---|---|---|---|---|---|
| 3 days | 2.95 | $5.30 \times 10^{-3}$ | 0.18% | $3.87 \times 10^{5}$ | $1.07 \times 10^{4}$ | 2.77 % |
| 2 days | 2.94 | $7.40 \times 10^{-3}$ | 0.25 % | $3.94 \times 10^{5}$ | $1.33 \times 10^{4}$ | 3.39 % |
| 1 day | 2.65 | $4.62 \times 10^{-2}$ | 1.75 % | $5.47 \times 10^{5}$ | $4.65 \times 10^{4}$ | 8.50 % |
| 12 hours | 2.67 | $5.31 \times 10^{-2}$ | 1.98 % | $2.74 \times 10^{5}$ | $4.27 \times 10^{4}$ | 15.58 % |
| 6 hours | 3.19 | $1.84 \times 10^{-1}$ | 5.75 % | $2.10 \times 10^{5}$ | $3.17 \times 10^{4}$ | 15.12 % |

Table 5.2.4: Residuals for internal and external heat flux for different time windows, location 5

| Days used for the inference | 3 Days | 2 Days | 1Day | 0.5 Days | 6 hours |
|---|---|---|---|---|---|
| Residuals for internal flux $[W/(m^2K)]$ | 1.60 | 1.47 | 3.41 | 2.43 | 5.45 |

Looking at the residuals and uncertainty plots shown in figure 5.2.4, it can be seen that the general trend follows those for the data collected in the environmental chamber, figure 5.2.1: by decreasing the time window used for the inference, the confidence in the results obtained decreases. Still, in this specific case, looking at the residual plot and scrutinising the values displayed in table 5.2.3, it can be seen that the results obtained from the 12 hour window look more reliable that the results obtained using a whole day's worth of data, as the heat capacity inferred over 24 hours is too high to be representative of a solid wall.

This behaviour could be attributed to the fact that, for this peculiar data set, the indoor air temperature is highly unstable and, as can be seen from figure 5.2.2, the 1 day temperature profile includes a sharp jump in temperature, which is excluded from the 12 hour time window.

The prediction profiles obtained with the HDM model are displayed in figure 5.2.5. In this figure, also the predictions obtained from the inference on the 6 hour data have been included, to show that after the 12 hour window the quality of the fit deteriorates.

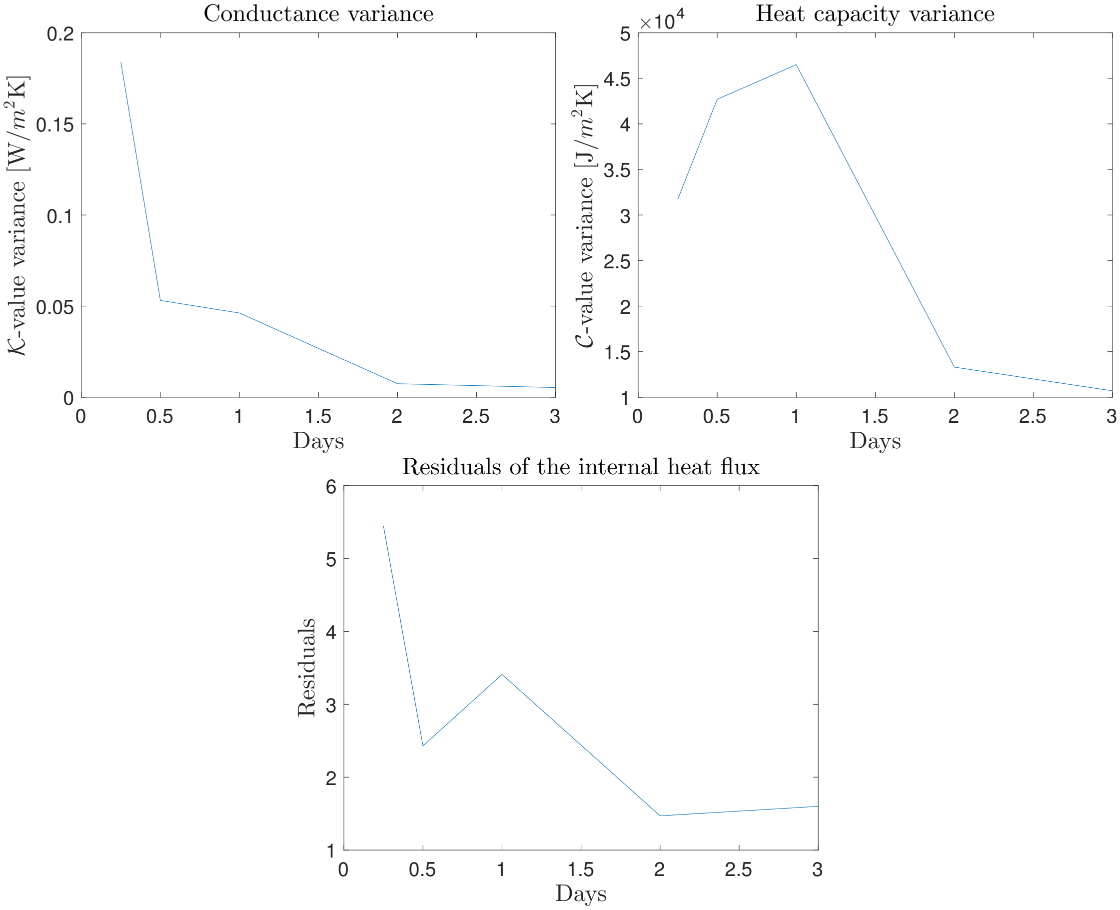

Figure 5.2.4: Analysis of the HDM performance on solid wall construction, unoccupied property, location 5. Left: variance on the conductance. Right: variance on the heat capacity. Bottom: Residuals.

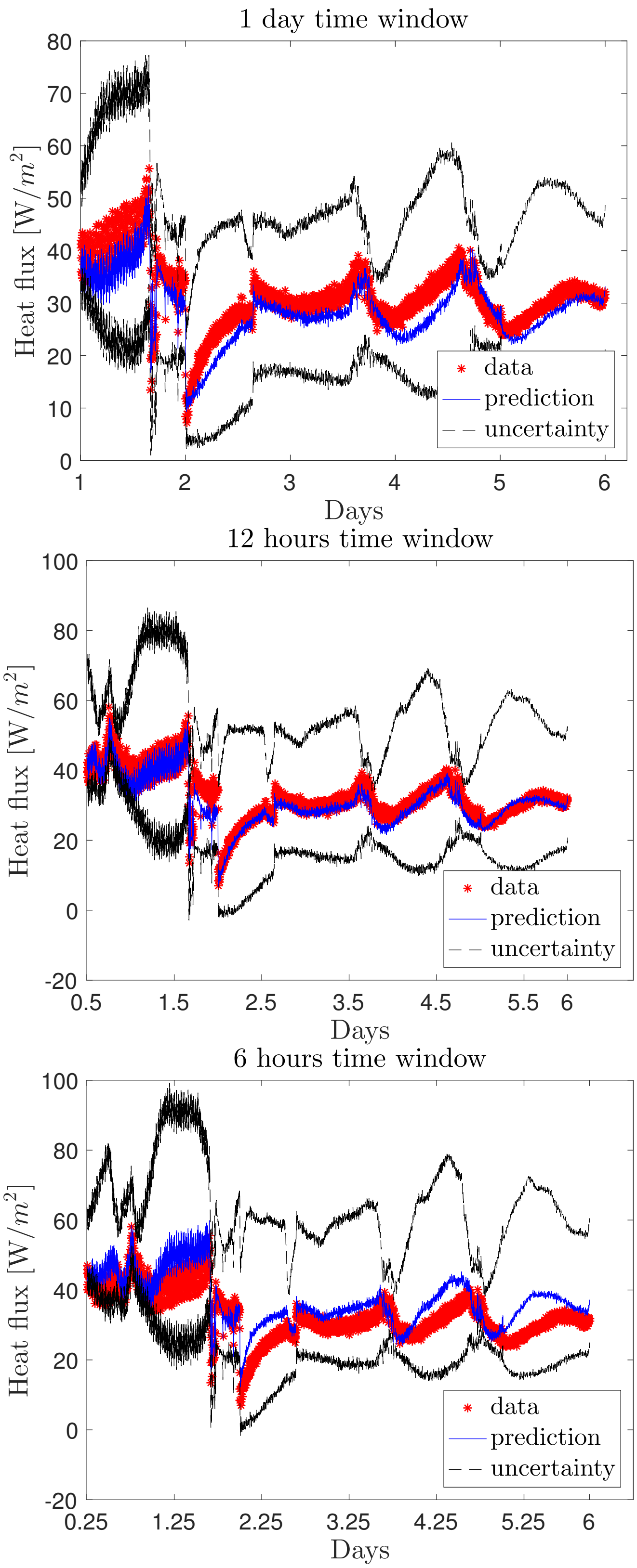

Figure 5.2.5: Heat flux predictions obtained from the HDM with different inference windows in location 5. Top: 1 day inference window, middle: 12 hours inference window, bottom: 6 hours inference window

#### 5.2.2.2 Location 4

The analysis carried out for location 5 was also carried out for location 4, investigating the performance of the HDM on different inference windows. The values of the conductance and heat capacity obtained are displayed in Figure 5.2.5 and the residuals, calculated via equation (5.1) are summarised in table 5.2.6.

Table 5.2.5: Conductance, volumetric heat capacity and statistical uncertainty for different time windows on Wortley Hall Close data, location 4

| | $\mathbf{E}(\mathcal{K}\|y)$ $[W/(m^2K)]$ | $[\mathbf{V}(\mathcal{K}\|y)]^{1/2}$ $[W/(m^2K)]$ | Relative uncertainty | $\mathbf{E}(\mathcal{C}\|y)$ $[J/(m^2K)]$ | $[\mathbf{V}(\mathcal{C}\|y)]^{1/2}$ $[J/(m^2K)]$ | Relative uncertainty |
|---|---|---|---|---|---|---|
| 3 days | 2.38 | $4.10\times10^{-3}$ | 0.17 % | $2.51\times10^{5}$ | $7.23\times10^{3}$ | 2.88 % |
| 2 days | 2.40 | $5.80\times10^{-3}$ | 0.24 % | $2.58\times10^{5}$ | $9.48\times10^{3}$ | 3.68 % |
| 1 day | 2.19 | $3.24\times10^{-2}$ | 1.48 % | $3.84\times10^{5}$ | $2.45\times10^{4}$ | 6.38 % |
| 12 hours | 2.23 | $2.95\times10^{-2}$ | 1.32 % | $2.31\times10^{5}$ | $4.49\times10^{4}$ | 19.43 % |
| 6 hours | 2.48 | $9.71\times10^{-2}$ | 3.91 % | $1.53\times10^{5}$ | $2.60\times10^{4}$ | 17.00 % |

Table 5.2.6: Residuals for internal and external heat flux for different time windows

| Days used for the inference | 3 Days | 2 Days | 1Day | 0.5 Days | 6 hours |
|---|---|---|---|---|---|
| Residuals for internal flux $[W/(m^2K)]$ | 1.35 | 1.54 | 2.61 | 1.67 | 3.28 |

Looking at the values shown in table 5.2.5, it can be seen that also in this case the HDM successfully characterises the value of the conductance, if the results obtained from the ““Average Method”” are used as a benchmark. The results obtained for the heat capacity are clearly different from those obtained in location 5, the lower value supporting the hypothesis that the construction in location 4 differs from a solid wall construction, possibly as the result of a void being present in the wall thickness.

This finding shows that, unless the researcher is aware of the presence of a defect

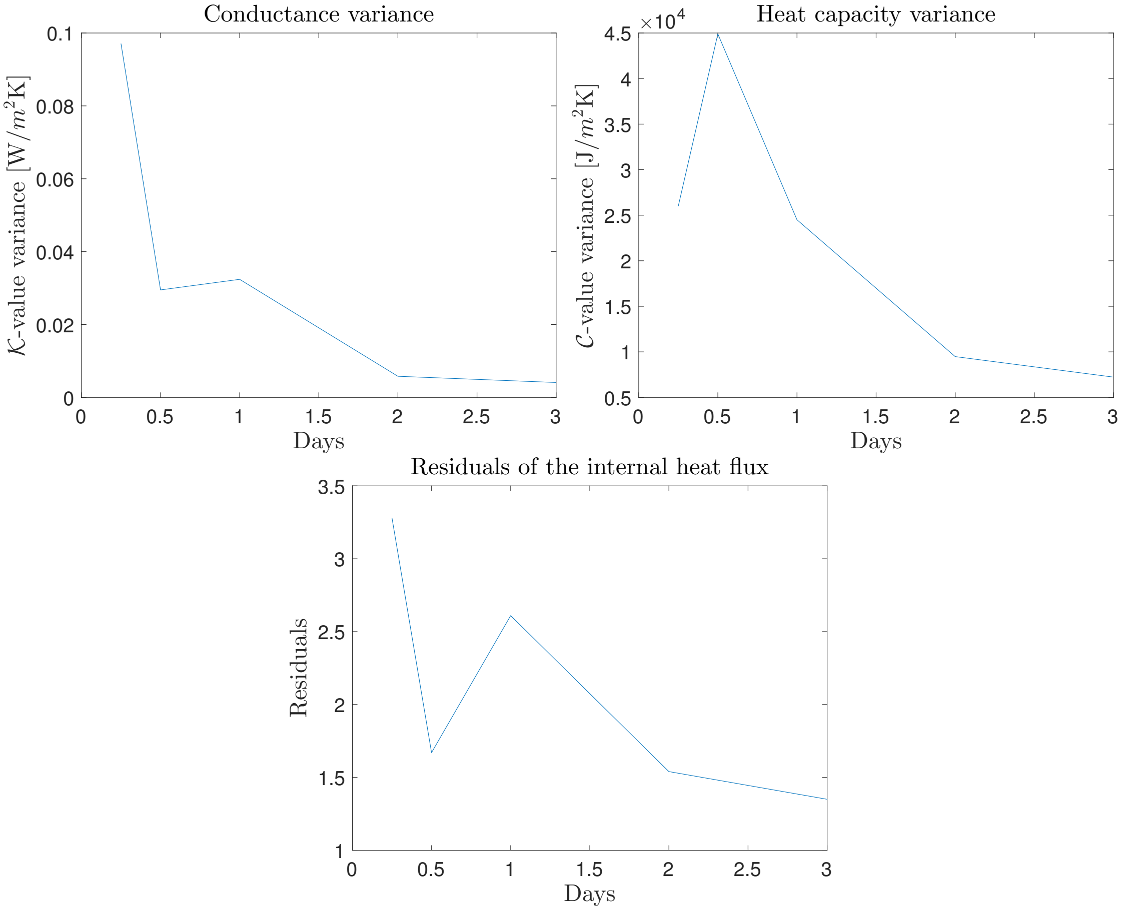

Figure 5.2.6: Analysis of the HDM performance on solid wall construction, unoccupied property, location 4. Left: Variance on the conductance. Right: Variance on the heat capacity. Bottom: Residuals.

in that particular area of the construction, an analysis that does not include sufficient variability in the thermal properties might lead to misleading results. In the case reported here, if location 4 was considered as representative of the whole wall construction in combination with the ““Average Method”” alone, the wall construction thermal performance would be overestimated, without further indicators that the construction might differ from the expectations.

Also in this case, the residuals and the uncertainty plots, displayed in figure 5.2.6, confirm the finding from the previous cases: reducing the inference time window increases the uncertainty and the residuals. Additionally, as was found in location 5, for location 4 too, the residual plot shows a worsening in the performance when the 1 day data window with the 12 hours inference window are compared. Again this behaviour could potentially be attributed to the fact that there is a jump in the indoor air temperature profile, as discussed in the previous subsection.

As well as in the previous case, it can be seen that the fit using 1 day's worth of data as an inference window worsens compared with the fit produced by inferring the thermal properties using 12 hours of data. Looking at the results displayed in table 5.2.5, it can be seen that this may be attributed to the inferred value of the heat capacity, which is considerably higher than the values inferred during the other time windows. In turn, this supports the hypothesis that the cause leading to the overestimation of the heat capacity may be the sudden jump in internal temperature observed in day 2 of the data set. As discussed in the previous sections, to measure the heat capacity of a building element, it may be necessary to expose the construction to large variations in heat flux to produce a change in the amount of heat stored in its body.

Looking at the results obtained from the data collected on the unoccupied solid wall property, it can be stated that 1.5 hour of inference data is insufficient for the characterisation of the building element behaviour as the heat capacity value obtained using 6 hour inference window presents approximately 15% uncertainty for the solid part of the wall tested (and nearly 17% for the test performed over an area of thermal

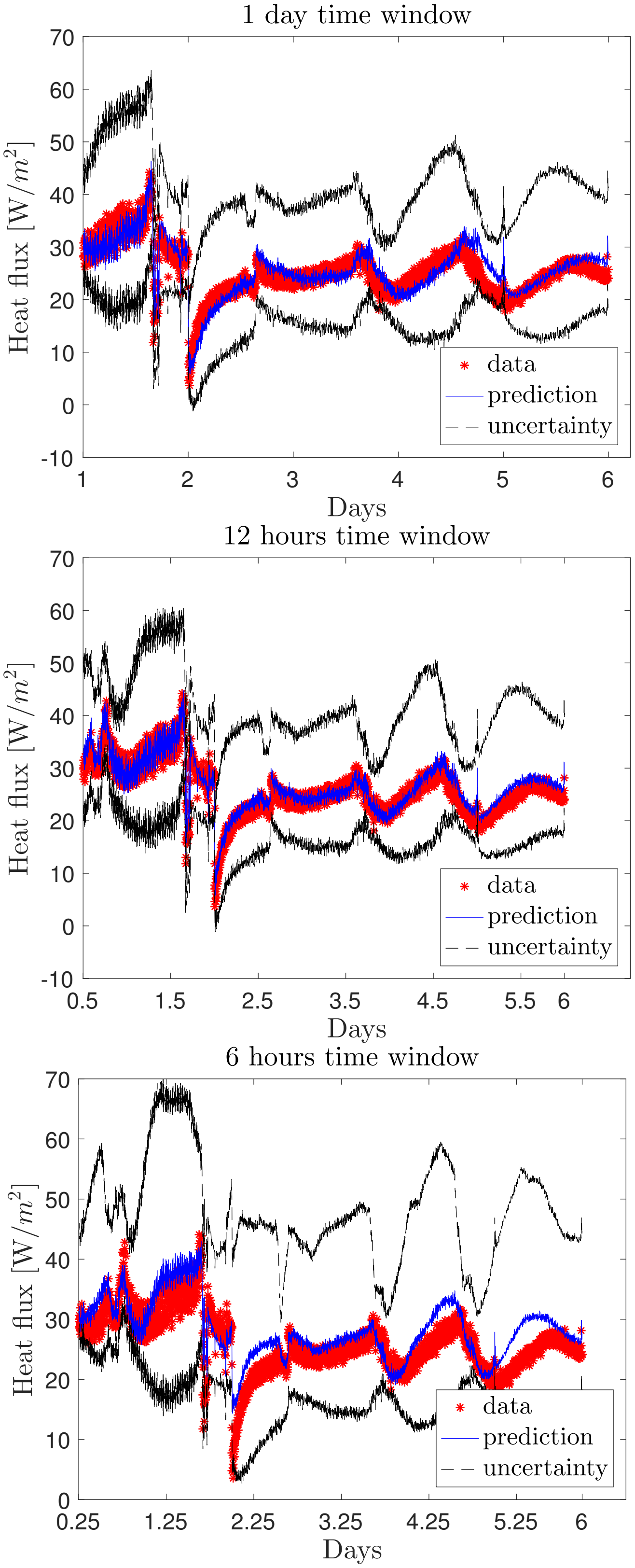

Figure 5.2.7: Heat flux predictions obtained from the HDM with different inference windows in location 4. Top: 1 day inference window, Middle: 12 hour inference window, Bottom: 6 hour inference window.

inhomogeneity). Despite uncertainty over the estimate in heat capacity, the expected conductance value, based on the ““Average Method”” estimate, is well within the uncertainty band found in both cases.

Based on the results presented, it is reasonable to assume that 2 day’s of data could be sufficient to characterise of the thermal properties of a wall of solid construction. In spite of the fact that in this case the 1 day predictions are suspicious, especially regarding the heat capacity, the properties inferred with 12 hours are reasonable and the data fit obtained is of good quality. Based on these grounds, it is reasonable to assume that the predictions based on 1 day’s worth of data are spoiled by the presence of a sudden discontinuity in the temperature boundary conditions, and that, under undisturbed boundary conditions, the 1 day window could be an optimal compromise between accuracy of the results obtained and measurement time.

In order to confirm this point, further investigations have been carried out on the insulated steel frame construction described in section 3.4, the findings for which are presented in section 5.2.3.

Looking at the profiles of the thermal properties found in location 4 and displayed in figure 5.2.9, it can be seen that both the thermal conductivity and the volumetric heat capacity profile suggest the presence of a strata with low thermal conductivity and low volumetric heat capacity in the centre of the construction. In contrast, this is not the case for the thermal properties profiles inferred for location 5, figure 5.2.8. As mentioned in section 4.1, this assessment can be only used as a qualitative tool as

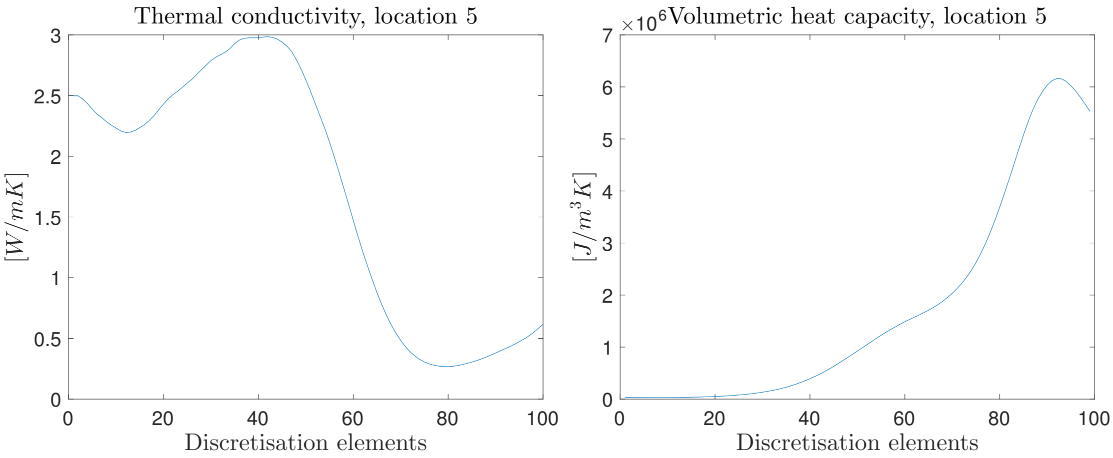

Figure 5.2.8: Thermal properties inferred from the 3 day inference window for location 5 in the unoccupied solid wall property.

the model is not able to give exact information on the location and number of layers comprising the wall structure. Still, the thermal properties profiles found corroborate the hypothesis of a chimney or a flue as an explanation to the defect area found in the solid wall construction.

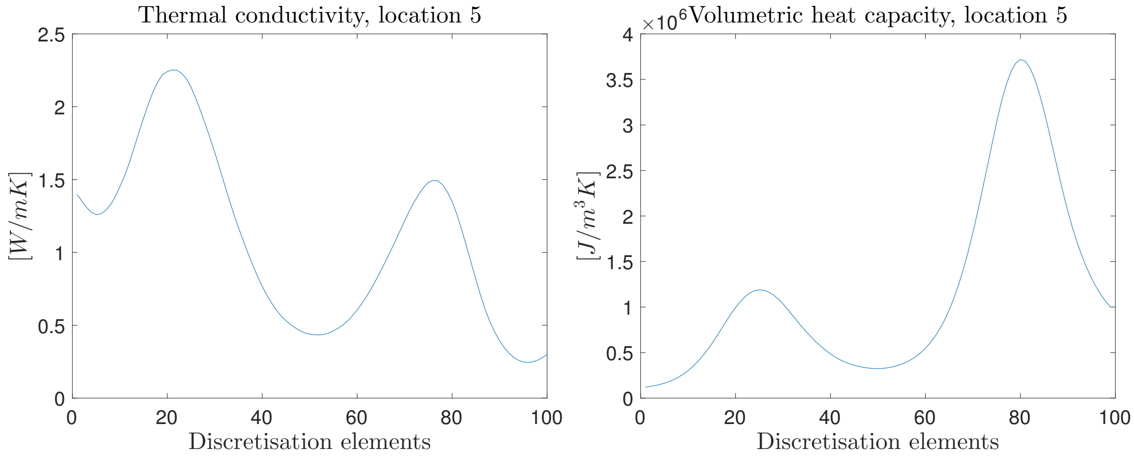

Figure 5.2.9: Thermal properties inferred from the 3 day inference window for location 4 in the unoccupied solid wall property.

### 5.2.3 Analysis of the insulated steel frame construction

The data collected from the insulated steel frame construction were initially analysed using the ““Average Method”” according to equation (1.18). Due to the nature of the wall construction, the heat flux sensors were distributed so as to capture the different thermal behaviour of the steel frame and the insulation. Therefore two sets of calculations are presented: one for the sensor placed between the structural studs i.e. over the insulation and one for the sensor placed on a stud i.e. over the steel frame. The data analysed correspond to the period $21^{st}$ December 2015 - $3^{rd}$ January 2016. Table 5.2.7 shows the values of conductance and wall resistance calculated with the “Average Method”. Figure 5.2.12 displays the air temperatures and surface heat fluxes during the monitoring period.

The heat capacity of the construction was estimated based on the design wall structure. The steel frame construction is filled by 75mm thick PIR board and covered with an external cladding of 120mm thick of graphite enhanced EPS as shown in figure

5.2.10. The internal finish comprises 10 mm plasterboard and approximately 2 mm of plaster. The thermal properties of the insulation, steel frame and plaster board were taken from CIBSE Guide A, appendix 3.A7 [8]. Still, due to the shape of the steel studs, some adjustment must be made to the calculation of the total heat capacity: the studs employed in the construction are an I section, and the cavities between neighbouring studs are filled with PIR insulation as indicated in figure 5.2.11. This is a highly inhomogeneous construction layer and considering only the steel heat capacity (or only the capacity of the insulation layers) displayed in table 5.2.8 as indicative heat capacity of the whole construction would disregard the inhomogeneity. The volume ratio between the steel and the insulation is approximately 20% to 80%, in favour of the latter therefore the effective heat capacity of such a construction is expected to be the weighted average of the steel and insulation heat capacity, in this case:

$$C_{eff} = 272550 \times 0.2 + 2208 \times 0.8 \simeq 56276 \qquad [J/m^2K] \tag{5.2}$$

The following subsections, will present the analysis carried out with the MCMC algorithm with the HDM on the data collected from the insulated steel frame construction. Section 5.2.3.1 describes the analysis of the data collected from the sensor located over the insulation and section 5.2.3.2 relates to the data collected from the position over the steel frame.

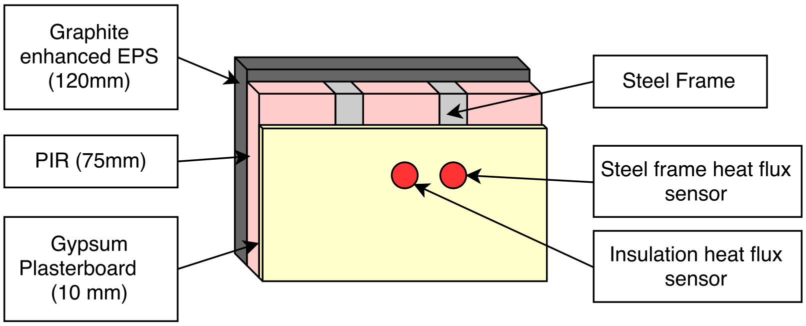

Figure 5.2.10: Diagram illustrating the insulated steel frame construction

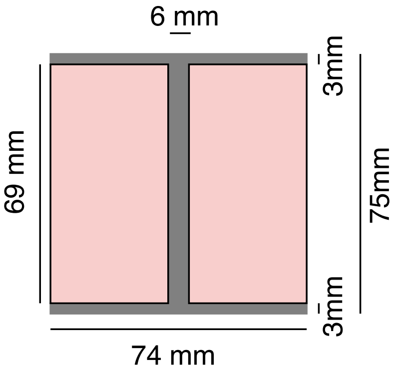

Figure 5.2.11: Diagram illustrating section of the steel beam filled with PIR

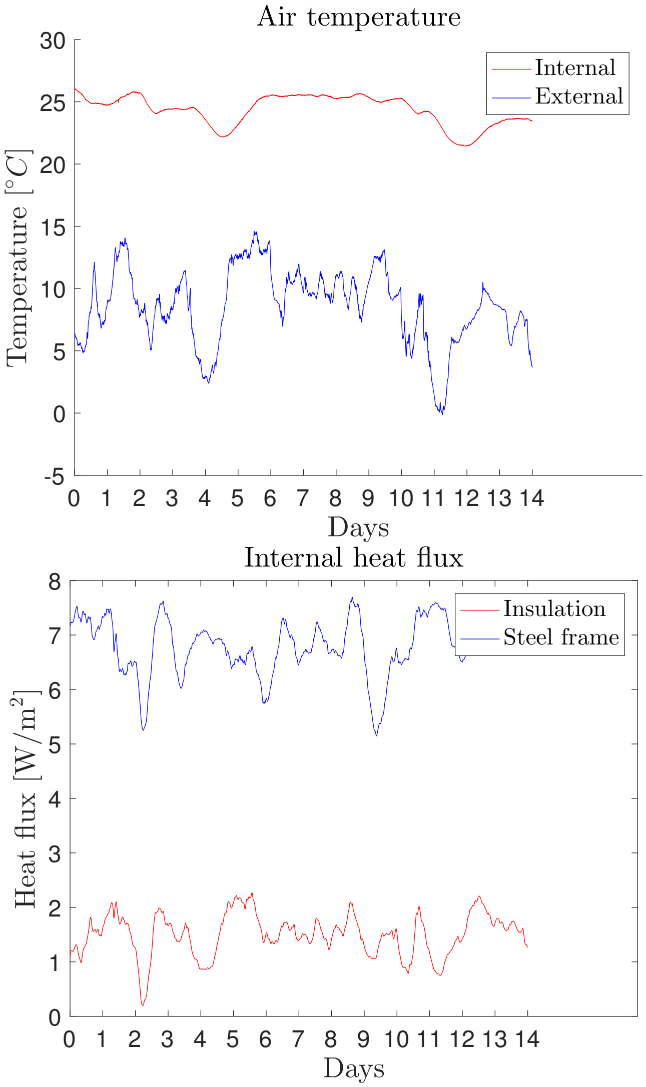

Figure 5.2.12: Air temperatures and heat flux profiles of the data collected in the insulated steel frame office

Table 5.2.7: Thermal characteristics of the insulated steel frame construction calculated with the "Average Method"

| | Resistance $[m^2K/W]$ | Conductance $[W/m^2K]$ |
|---|---|---|
| Insulation | 10.30 | 0.10 |
| Steel frame | 2.23 | 0.45 |

Table 5.2.8: Thermal properties of the construction materials according to CIBSE Guide A [8].

| | Specific heat capacity $[J/kgK]$ | Density $[kg/m^3]$ | Thermal conductivity $[W/mK]$ | Thickness $[m]$ | Heat Capacity per unit area$[J/m^2K]$ |
|---|---|---|---|---|---|
| PIR | 920 | 32 | 0.02 | 0.075 | 2208 |
| EPS | 1470 | 35 | 0.027 | 0.120 | 6174 |
| Gypsum Plaster | 960 | 1120 | 0.51 | 0.010 | 10752 |
| Steel frame | 460 | 7900 | 45 | 0.075 | 272550 |

#### 5.2.3.1 Insulation

To reflect the a priori knowledge relative to the wall construction, the priors were modified to account for the different expected values of thermal conductance and heat capacity of the insulated steel frame. The mean value of the prior of thermal conductance was set to 0.83 $[W/m^2K]$ and the mean value of the prior of the capacitance was set to 1.98x$10^4$ $[J/m^2K]$. The priors were wide enough to reflect the variability of the thermal properties of the construction taken in consideration, as in the previous cases.

As, surface temperature measurements were available in each of the locations monitored, the model adopted is the same as in section 5.2.2, namely equations (2.1) - (2.5). It is important to note that the model adopted for the calculation remains the same, independently of the wall construction investigated and that only the distributions of the priors are modified.

Table 5.2.9: Conductance, volumetric heat capacity and statistical uncertainty inferred for different time windows from the measurements made over the insulation

| | $\mathbf{E}(\mathcal{K}\|y)$ $[W/(m^2K)]$ | $[\mathbf{V}(\mathcal{K}\|y)]^{1/2}$ $[W/(m^2K)]$ | Relative uncertainty | $\mathbf{E}(\mathcal{C}\|y)$ $[J/(m^2K)]$ | $[\mathbf{V}(\mathcal{C}\|y)]^{1/2}$ $[J/(m^2K)]$ | Relative uncertainty |
|---|---|---|---|---|---|---|
| 3 days | 0.10 | 1.33 x $10^{-4}$ | 0.13 % | 4.18 x $10^4$ | 0.87 x $10^3$ | 2.08 % |
| 2 days | 0.10 | 2.14 x $10^{-4}$ | 0.21 % | 3.64 x $10^4$ | 0.70 x $10^3$ | 1.91 % |
| 1 day | 0.11 | 5.18 x $10^{-4}$ | 0.49 % | 3.74 x $10^4$ | 0.71 x $10^3$ | 1.91 % |
| 12 hours | 0.12 | 6.40 x $10^{-3}$ | 5.41 % | 5.42 x $10^4$ | 4.84 x $10^3$ | 8.94 % |
| 6 hours | 0.09 | 5.50 x $10^{-3}$ | 5.89 % | 2.87 x $10^4$ | 4.29 x $10^3$ | 14.94 % |

Table 5.2.10: Residuals for internal heat flux for different time windows, insulated steel frame construction for measurements made over the insulation

| Days used for the inference | 3 Days | 2 Days | 1 Day | 0.5 Days | 6 hours |
|---|---|---|---|---|---|
| Residuals for internal flux $[W/(m^2K)]$ | 0.07 | 0.12 | 0.13 | 0.30 | 0.34 |

Observing the values displayed in table 5.2.9, it can be seen that the conductance inferred with the HDM is extremely close to the value measured with the ““Average Method”” shown in table 5.2.7. The estimate of the heat capacity of the structure is approximately 4x$10^4$ $J/m^2K$. This value is considerably higher than the heat capacity of insulation only and considerably lower than the heat capacity of the steel beams, but it is similar to the effective heat capacity of the steel beam and insulation combined. This finding suggests that it is reasonable to suppose that the overall heat capacity of the insulated steel frame structure will be an average between the capacity of the insulation and the capacity of the steel, in favour of the former, due to the small volume of steel present in the construction compared with the volume of the insulation.

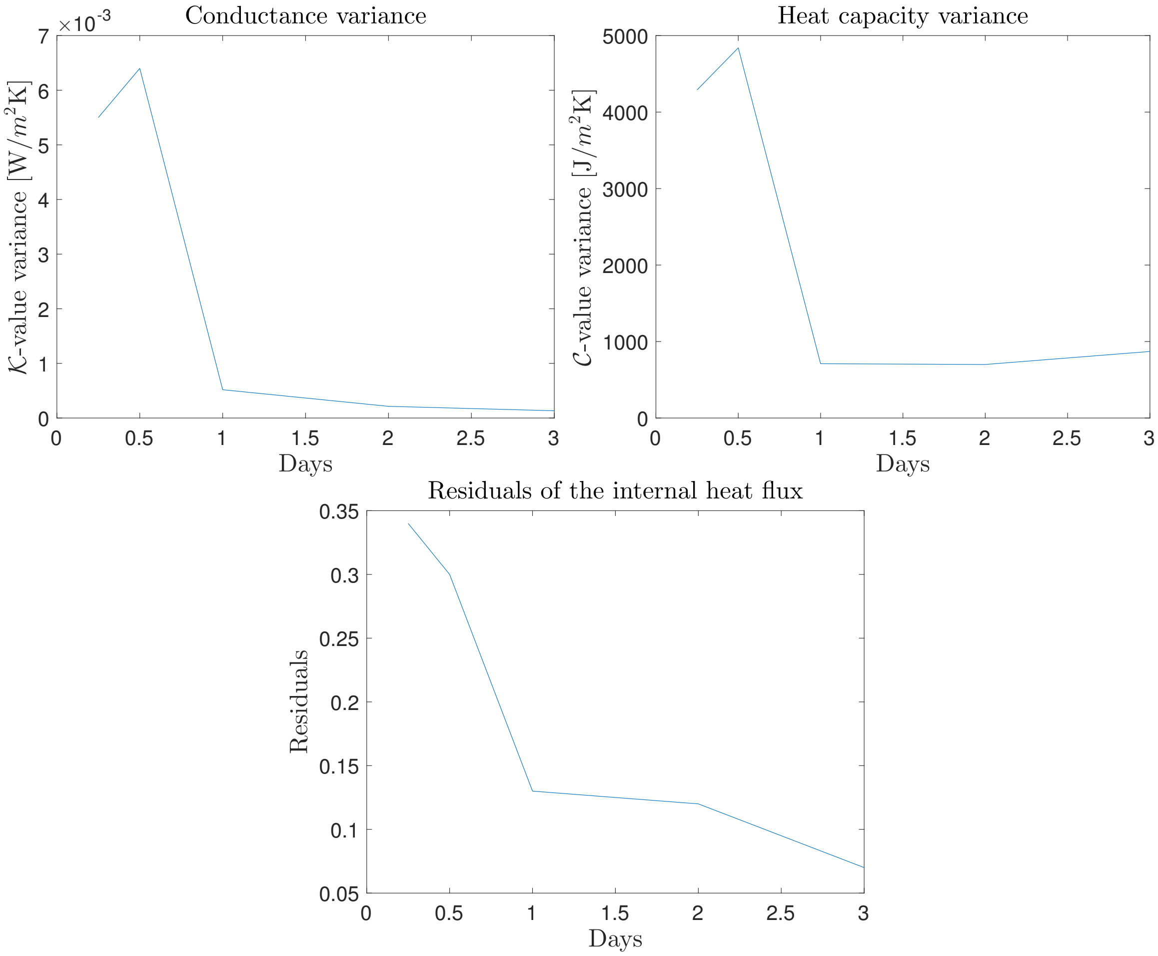

Figure 5.2.13: Analysis of the HDM performance on insulated steel frame construction: insulation. Left: Variance on the conductance. Right: Variance on the heat capacity. Bottom: Residuals

.

Analysing the results obtained as in the previous case (section 5.2.2), it can be seen that the residuals, (obtained using equation (5.1)), and the uncertainty follow a similar pattern to that observed in the environmental chamber data: as the length of the data window used for the inference decreases, the errors increase.

In this case, looking at figure 5.2.13, it can be seen that the point at which errors drop to a constant level occurs at 1 day and that time windows shorter that one day produce higher uncertainties and residuals.

Even if, in absolute values, the uncertainties and the residuals look small, the impact can be seen on the prediction of the heat flux behaviour. Figure 5.2.14 compares the heat flux predictions obtained with 1 day's worth of data and those obtained with 12 hour's worth of data. The black dashed lines represent two standard deviations from the mean value and, in the left panel, it can be seen that this contains the model prediction and wraps around the experimental data points. As it can be seen from the right panel of figure 5.2.14, the prediction produced by the inference window based on 12 hours of measurements deteriorates and the uncertainty band does not capture all of the data points.

#### 5.2.3.2 Steel frame

For this measurement position, the prior mean of the heat capacity was also modified to account for the different expected values and was increased to 1.58 x $10^5$

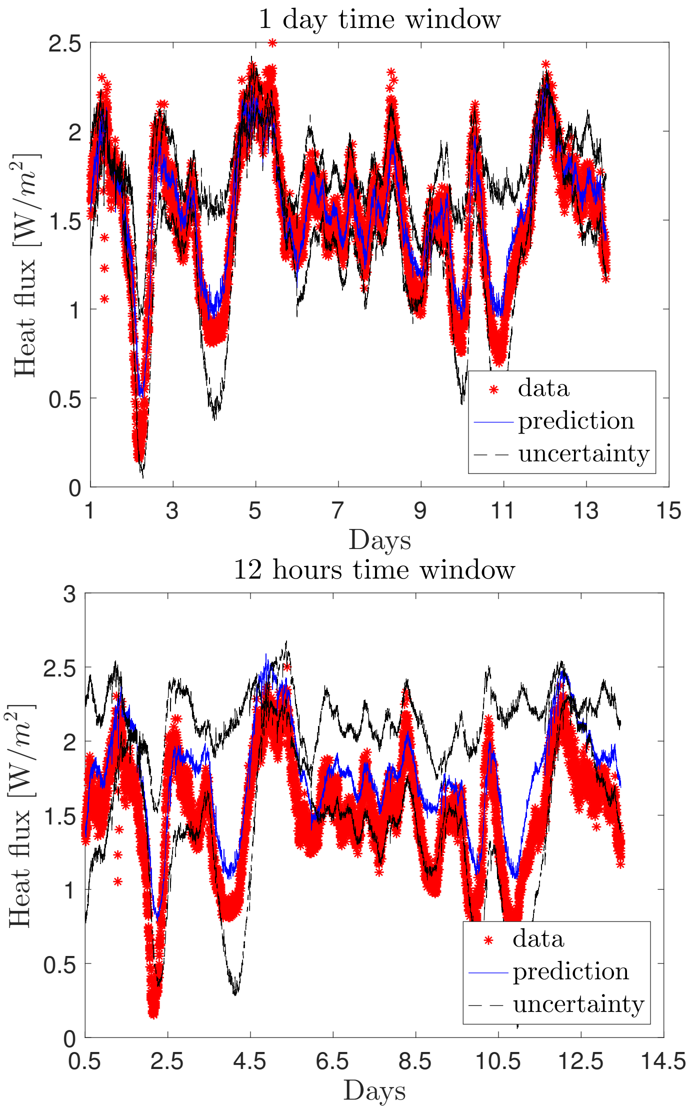

Figure 5.2.14: Comparison of model output and measured data, insulated steel frame: insulation. Top: calculations using 1 day inference time window, bottom: calculations using 12 hour inference time window

.

$[J/m^2K]$ to reflect the presence of the steel structure. Table 5.2.11 shows the results obtained with the HDM for the position located over the steel frame on the insulated steel frame construction. As may be seen by comparing these results with those displayed in table 5.2.7, the value of the conductance is compatible with the value calculated with the "Average Method". The heat capacity inferred, is of the order 7 x $10^4$ $J/m^2K$. In this case, it can be seen that the value is considerably higher than the estimate obtained from the measurements made over the insulation, reflecting the influence of the steel beam on the properties determined at this sensor location. Again, the value is not indicative of the heat capacity of the insulation alone or of the steel alone, but it is in agreement with the effective heat capacity calculated with the weighted average between the steel frame and insulation.

Once more, looking at the residuals and uncertainty plots, displayed in figure 5.2.15, it can be seen that the uncertainty and residuals increase when the time window for the data analysed decreases, showing the point at which errors stabilise occurring at 1 day. Observing figure 5.2.16, it can be seen that the model predictions made using 1 day of experimental measurements still produce a reliable data fit, while the fit deteriorates using just 12 hour of measured data.

The validation of the HDM model proposed in these sections is important because, here, the measurement conditions were not as controlled as in the case of the environmental chamber results from section 4.2, thus including the impact of external weather conditions. Furthermore, the availability of 14 day's of measured data makes it possible to understand the ability of the method to predict performance up to 13

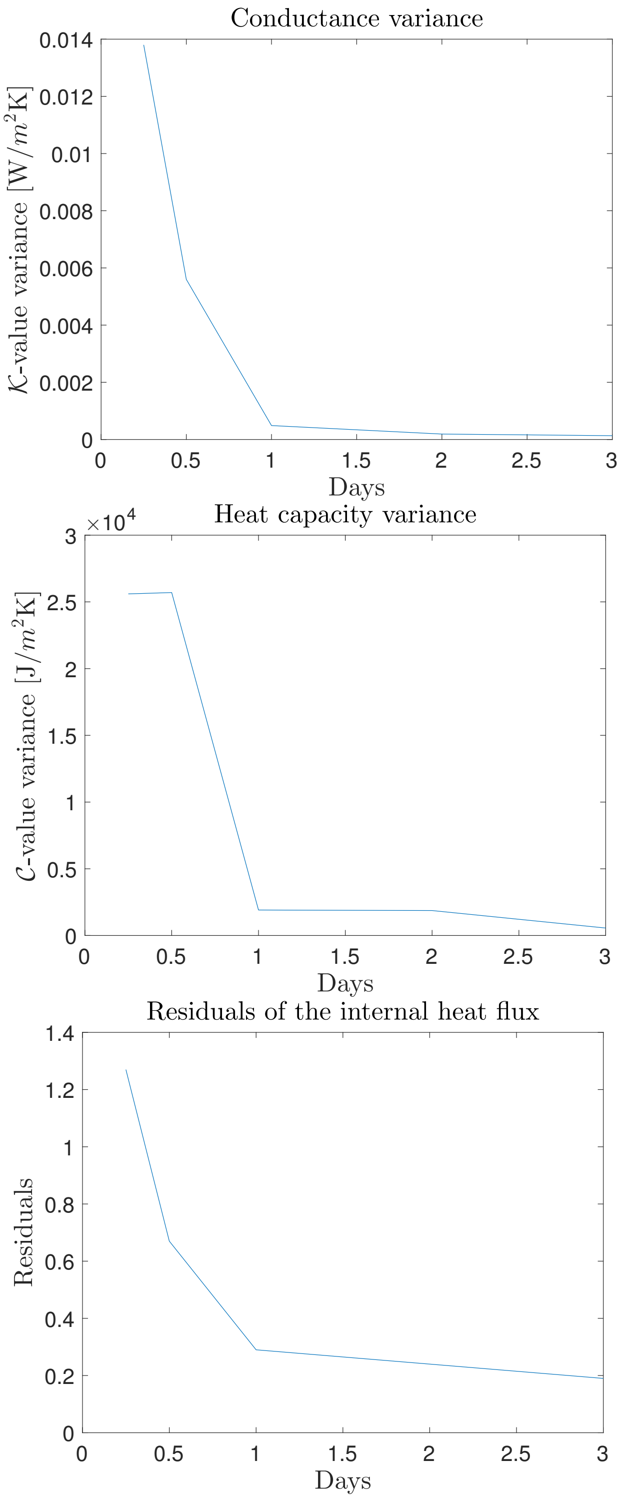

Figure 5.2.15: Analysis of the HDM performance for insulated steel frame construction for measurement position over steel frame. Left: Variance of the conductance. Middle: Variance of the heat capacity. Right: Residuals

.

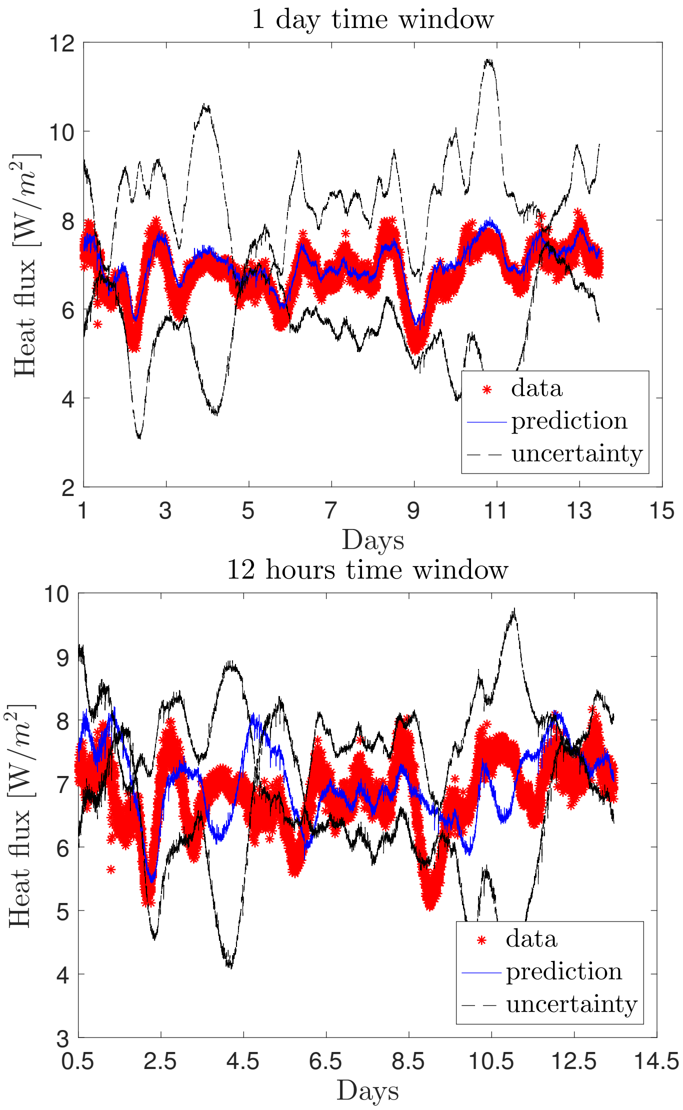

Figure 5.2.16: Comparison of model output and measured data, for measurement position over steel frame. Top: calculations using 1 day inference time window, bottom: calculations using 12 hour inference time window

.

Table 5.2.11: Conductance, volumetric heat capacity and statistical uncertainty inferred for different time windows from measurements made over the steel frame in the occupied office space.

| | $\mathbf{E}(\mathcal{K}\|y)$ $[W/(m^2K)]$ | $[\mathbf{V}(\mathcal{K}\|y)]^{1/2}$ $[W/(m^2K)]$ | Relative uncertainty | $\mathbf{E}(\mathcal{C}\|y)$ $[J/(m^3K)]$ | $[\mathbf{V}(\mathcal{C}\|y)]^{1/2}$ $[J/(m^3K)]$ | Relative uncertainty |
|---|---|---|---|---|---|---|
| 3 days | 0.46 | 1.33 x $10^{-4}$ | 0.03 % | 6.76 x $10^4$ | 0.56 x $10^3$ | 0.82 % |
| 2 days | 0.46 | 1.90 x $10^{-4}$ | 0.04 % | 7.18 x $10^4$ | 1.87 x $10^3$ | 2.60 % |
| 1 day | 0.47 | 4.87 x $10^{-4}$ | 0.10 % | 7.94 x $10^4$ | 1.91 x $10^3$ | 2.40 % |
| 12 hours | 0.47 | 5.60 x $10^{-3}$ | 1.20 % | 1.73 x $10^5$ | 2.57 x $10^4$ | 14.92 % |
| 6 hours | 0.53 | 1.38 x $10^{-2}$ | 2.58 % | 1.75 x $10^5$ | 2.56 x $10^4$ | 14.67 % |

Table 5.2.12: Residuals for internal heat flux for different time windows, for measurements made over the steel frame

| Days used for the inference | 3 Days | 2 Days | 1 Day | 0.5 Days | 6 hours |
|---|---|---|---|---|---|
| Residuals for internal flux $[W/(m^2K)]$ | 0.19 | 0.24 | 0.29 | 0.67 | 1.27 |

days in the future, thus providing stronger evidence in support of the reliability of the thermal properties inferred. Moreover, it proves the effectiveness of the model in modelling different structures: the case under investigation is a lightweight structure, as opposed to the previous cases consisting of heavyweight structures. The results obtained showed that the HDM can be applied in both cases, without the need to modify the governing model.

In addition, looking at the spatial variation in thermal properties inferred from the 3 day data window, displayed in figures 5.2.17 - 5.2.18, it can be seen that the model is able to infer the presence of a discontinuity in the construction. This may be seen from the panels on the right of each figure: in both, the thermal conductivity and in the heat capacity, there is a peak at approximately one third of the thickness of the wall. This is indicative of the presence of the steel stud in the construction, as it is known from the design that the steel studs are located towards the internal facade of the building.

In both cases, the heat capacity exhibits a sharp peak at the beginning, corresponding to the internal surface of the wall. This corresponds to the presence of the gypsum plasterboard, that, as may be seen from table 5.2.8, has a high heat capacity compared with the insulation materials themselves. As already explained in the synthetic experiment, section 4.1, this is not to be considered as a tool to infer the exact thermal properties of the separate layers, but it can still be useful to gain information about the structure of the wall and the presence of material layers with different thermal properties.

The thermal conductivity from the measurement made over the insulation (left panel in figure 5.2.17) exhibits a peak in the second half of the wall, corresponding to the external half of the construction. Looking at the thermal properties of the building materials in table 5.2.8, it can be seen that the external half of the wall is made of EPS which has a higher conductivity than the PIR used to fill the gaps between the steel studs.

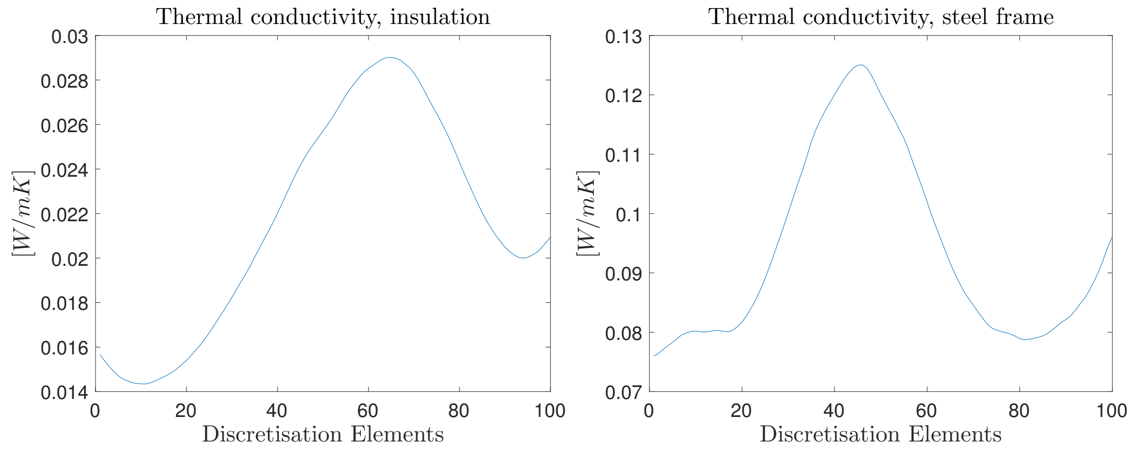

Figure 5.2.17: Inferred thermal properties for the steel frame construction, obtained from the 3 day data window inference. Left: thermal conductivity for the position over the insulation, right thermal conductivity for the position over the steel frame

.

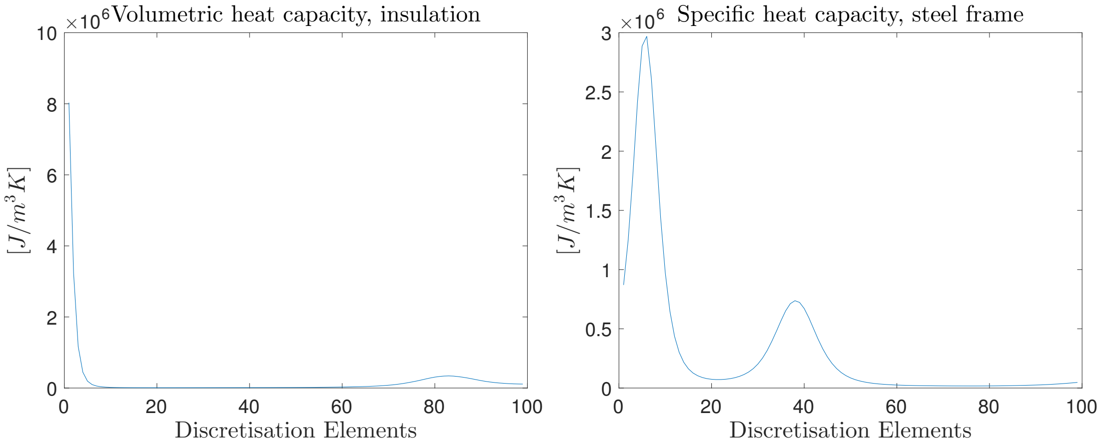

Figure 5.2.18: Inferred thermal properties for the steel frame construction, obtained from the 3 day data window inference. Left: heat capacity for the position over the insulation, right: heat capacity for the position over the steel frame

.

## 5.3 Discussion

The validation carried out in this chapter confirms the value of the MCMC as a tool for the inference of thermal properties on opaque building elements.

Section 5.1.2 replicates the analysis carried out by Biddulph et. al [72], analysing the BSRIA data set with a single capacitor RC network model (referred to as STM in this thesis). In this case, the results obtained for the thermal transmittance, heat capacity and heat flux predictions are in complete agreement with the values published in [72]. This comparison is extremely important for validating the results produced by this analysis and by the further development of the model, as it shows agreement with published material.

Section 5.1.1 evaluates the performance of the HDM on the same data set obtaining compatible values for the inference of thermal transmittance but different values for the evaluation of heat capacity.

Comparing the HDM and STM heat flux predictions, it can be seen that the HDM offers improved prediction abilities over the simple RC network model.

This, in addition to the fact that the heat capacity estimate lies in the range found in literature, indicates that the continuous model extends the capabilities of a discrete RC network and, looking at the results obtained on lightweight structures, also overcomes the limitations related to model topology, ([64, 65]), as the same model can be applied to different structures without need of changing the number of resistances and capacitances.

The results obtained on the unoccupied solid wall property indicate that a reliable estimate of the conductance can be obtained within two monitoring days. Shorter time windows suffer from the presence of sharp fluctuations in the boundary conditions, displaying a worsening in the predictions when a 1 day inference window is used. As shorter inference time windows seem to improve on the results obtained, it is reasonable to attribute this worsening to the boundary conditions particular to this experiment.

The results obtained from the analysis of the insulated steel frame construction, where there were no step changes in internal temperature, seem to indicate that 1 day of observations is sufficient to obtain a reliable estimate of the thermal properties sought.

Here, for measurements made over the insulation and over the steel frame, a sharp increase in the residuals and the uncertainty for windows shorter than 1 day is observed. As the results obtained using the 24 hour window are still in agreement with those found in the literature and with those obtained from the "Average Method" calculations, 1 day seems to be the optimal time window to minimise uncertainty and data collection time.

Summarising the results obtained from the analysis of short time windows, it can be stated that this MCMC method can, under moderately controlled conditions, infer the thermal properties based on only one day's data. Moderately controlled conditions are necessary, as, as shown in the unoccupied solid wall property data set, strong shocks in the internal temperatures lead to longer monitoring periods. Still, these conditions seem reasonably achievable in real life situations as it corresponds to a room with closed windows and doors and no occupants for 24 hours only.

Special attention should be dedicated to the question of the evaluation of the uncertainty on the U-value. The analysis performed with the MCMC offers the advantage of simultaneously evaluating the $\mathcal{K}$-value and its corresponding experimental error. The statistical error indicated in this body of work cannot be considered as the final uncertainty, as this is representative of the instrumentation uncertainty alone, still, the following observations can be made:

- The statistical error found shows that the effect of the accuracy of the instrumentation is well below the 5% error indicated by the ISO9869:2014
- The 10% error caused by the variations over time of the temperatures and heat flow, indicated by the ISO 9869:2014, does not apply in this case as the model used does not make any assumptions about the energy stored in the wall. Instead, as it uses the full 1D heat equation, it is able to simulate the change in energy storage.

The only other sources of error are due to the differences between air and radiant temperature (5% according to ISO 9869) and to random variations in the thermal contact between the sensors and the wall surface temperature (5% according to ISO 9869). ISO 9869:2014 states that “ If the heat flux meter is very thin and its thermal resistance low enough, [...] the corrections for the thermal resistance and finite dimensions of the heat flux meter are not required" [48]. Accordingly, the manual for the Hukseflux HFP01, the heat flux meter used during the experimental data collection, discourages corrections for the operational error as it relies on too many assumed values that lie outside the researcher's control [5]. For these reasons, in addition to the fact that the sensor resistance ($71\times10^{-3}m^2K/W$ [5]) is approximately 5 times smaller that the resistance of the solid wall constructions considered, the uncertainty related to the sensor resistance and operative error have been neglected.

Assuming the uncertainty values indicated by the ISO standard, the final uncertainty is expected to be less than the combined effect of instrumentation and air/radiant remperature differences, i.e. between 10% and $\sqrt{(5^2+5^2)}\% \approx 7\%$. Overall, using a more accurate model such as the HDM, the uncertainty was halved with respect to the value prescribed by the ISO 9869.

### 5.3.1 Limitations of the model

As indicated in sections 5.2.2 and 5.2.3 the HDM can be used to obtain an indication of the internal wall construction without detailed prior knowledge. This is only a qualitative tool as the model cannot predict the exact position and thickness of the various strata. This limitation is strictly connected to the definition of the prior distributions, as these were chosen to restrict the model to continuous functions. Furthermore, as shown in section 4.1 using synthetic data, the parameters adopted in the definition of the covariance (equation (2.27)) play a key role in dictating the flexibility allowed in the inference of thermal conductivity and volumetric heat capacity.

As a general guideline, it is not recommended to use this tool for the detection of internal layers. If this scope of detecting internal layers were to be pursued, further amendments to the model would have to be performed, such as developing priors that include discontinuous functions.

Currently the model is computationally expensive to run as, for the inversion based on the 3 days inference window it, takes more than 5 hours on on an Intel Core i3-4130 at 3.40 GHz. The computation based on a single day of monitored data reduces the computational time by 66%, but as it takes nearly 2 hours, it still yet carries high computational overheads. Table 5.3.1 shows the computation times required for different experiments and different time windows.

Table 5.3.1: Computation time needed for the inference of the thermal properties for different experiments

| Experiment | Computational time |
|---|---|
| Synthetic | 2.70 hours |
| Solid wall, 3.5 days | 5.24 hours |
| Solid wall, 1 Day | 1.75 hours |
| Solid wall, 12 hours | 1.43 hours |

This shows that even if the model developed introduces an improvement in the current U-value measurement procedure, reducing its monitoring time and producing a more accurate estimation of the uncertainty, the computational time necessary to implement the model is a drawback to the use of this model as a practical tool. It is therefore useful to explore methods by which its computational performance may be improved if the HDM is to be adopted in practice.

Based on the experience gained of implementing the model with fixed temperature boundary conditions and convective boundary conditions, it was found that the former is computationally more efficient as it does not require the inference of the initial internal temperature of the structure considered. The latter requires a computational time longer than 12 hours thus undoing the benefits of reducing the monitoring period. For this reason it is advisable to collect surface temperature measurements, as opposed to air temperature measurements and use the model with surface temperature boundary conditions.

## 5.4 Conclusions

The last two chapters presented a model based on the heat conduction equation that, coupled with a Bayesian inference algorithm, is able to calculate the $\mathcal{K}$-value of a building element using 24 hours of experimental data. This is an enormous improvement compared to the time required to calculate the U-value using the "Average Method": 3 days minimum according to the ISO 9869 but reaching up to two weeks [45]. In summary the main outcomes of the HDM are that it:

1. Is able to quantify the $\mathcal{K}$-value and thermal capacity of building element constructions in a very short period of time (1 day vs a week or more [45])
2. Is able to distinguish between different wall constructions, such as solid wall

and cavity wall, without prior knowledge

3. Offers the quantification of uncertainty associated with the value found, and considerably reduces the uncertainty associated with the current measurement standard, from 14%-28% suggested by the ISO 9869:2014 to 7%-10% as explained in section 5.3.
4. Offers a spatial representation of the heat transfer behaviour whitin a building element.

While the first three outcomes are very interesting for large scale monitoring, new build quality control and existing building performance assessment, the last point proves that this model offers a deeper understanding of the heat transfer through the building elements. This, therefore, opens the possibility to improve whole building energy simulations, which, as explained in the literature review section, currently hinge mostly on the U-value or the assumed values of thermal properties of the single construction layers.

Still the algorithm presented has high computational costs. There is value in exploring alternative approaches to enhance the prediction of the HDM as an analysis tool. The following chapter investigates the performance of a new computational algorithm, able to implement the HDM model with reduced computational costs.

# Chapter 6

# Ensemble Kalman filter

As mentioned in sections 5.3-5.4, the MCMC technique presents the drawback of high computational costs for the inference of U-value. This chapter describes an alternative method for the solution of the heat transfer problem within the Bayesian framework described in chapter 2. The algorithm chosen in the Ensemble Kalman Filter (EnKF) technique.

The new solution technique is based on particle filters that offer the possibility to approximate the posterior probability by a set of samples. This reduces the number of computations required by tackling several issues: i) in the application of MCMC to determine the thermal properties of walls there was shown in this work to be a need to compute 1 million iterations to ensure the convergence of the Markov chain, ii) for each iteration the heat equation has to simulate the whole data window considered (3 days, 1 day ...). The Kalman filter algorithm instead "self regulates" the number of iterations between one time step and the other thus not imposing a need to specify a fixed number of iterations a priori addressing issue (i), and for each of these iterations the heat equation has to simulate only a single time step, rather than the whole data window addressing issue (ii).

For these reasons, it is expected that the Ensemble Kalman Filter algorithm is able to produce significant reductions in computational cost, thus making the HDM a viable practical tool for the calculation of the thermal conductance.

Ensemble Kalman Filters have applications in various fields, such as the prediction of soil moisture content based on temperature measurements [90], and estimation of transient temperature field in oil pipelines, [76]. In the context of the built environment, Lin et Wang [91], proposed a method to forecast the dispersion of air contaminants using an Ensemble Kalman Filter methodology. Huchuk et al [92] used EnKF to train a simple RC network to be used as a foundation for a model-based predictive control (MPC) to regulate window shades to minimise energy consumption in an office room. In the context of this research, the Ensemble Kalman Filters will be used for the inference of effective thermal properties of building elements.

This chapter offers a brief introduction to the Ensemble Kalman Filter technique adopted, and displays the results obtained during the experimental validation.

In an analogous fashion to that adopted in chapter 4, the algorithm has been trialled on the same synthetic experiment used in the original verification of the HDM to verify that the EnKF technique maintains the same abilities to retrieve the profiles of thermal conductivity and volumetric heat capacity.

Later, the performance on different data sets has been investigated, in order to ascertain that, also the EnKF technique proposed is also able to distinguish different structures without prior knowledge.

## 6.1 Ensemble Kalman Filters

Ensemble Kalman filters, and in general particle filters, are mathematical techniques used to estimate the future state of a dynamical system from sensor measurements and knowledge of the previous state [93]. Particle filters are a different methodology to characterise the posterior distribution within the Bayesian framework.

The general concept behind particle filters, is that every probability distribution can be represented by a set of $N$ samples, also called particles. For instance, to represent the two humped probability distribution depicted in figure 6.1.1, one can draw more particles from the regions with higher probability and fewer particles from the region with lower probability, (figure 6.1.1, bottom), so that higher densities of particles represent the regions with higher probability. The advantage of this representation is that it is suitable for all kinds of probability distribution, thus offering an approximation of any arbitrary distribution.

This is particularly convenient for the case considered here as, as explained in the sections above, an explicit representation of the posterior $p(u|y)$ is not available, but, it is known, from Bayes' theorem, that

$$p(u|y) \propto p(y|u)p(u) \tag{6.1}$$

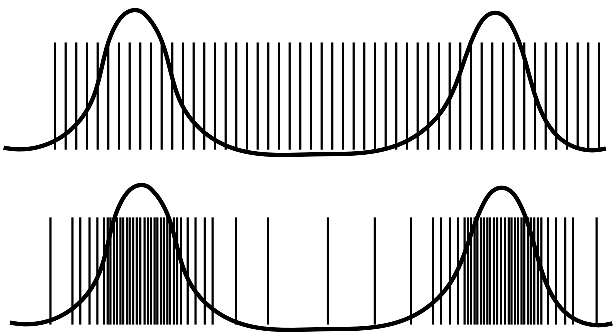

Figure 6.1.1: Diagram explaining the characterisation of probability distributions by sampling

and, therefore, it is still possible to evaluate if a sample belongs to a high probability region or a low probability region.

Consider the example shown in figure 6.1.1. Even if there is no prior information on the target distribution, it is still possible to draw samples from the uniform distribution (figure 6.1.1, top), evaluate the posterior probability of the samples via equation 6.1, and thus construct a new sample population that is representative of the posterior distribution.

In practice, the characterisation of the posterior is done by implementing a recursive feedback control system. In other words, the update step can be divided into two sub-steps: the time update, where a new prediction is made implementing the model based upon the knowledge of the previous state, and the measurements incorporated up to this point, and the feedback stage, where the value of the new prediction is adjusted when new measurements are available [94]. Figure 6.1.2, shows a diagram illustrating this concept.

At the first time step, the prior is given just by the a priori knowledge that the researcher can dispose of, and, for the heat transfer problem considered, this has been summarised in the distributions of thermal conductivity and volumetric heat capacity described in section 2.2.2. Sampling from this prior distribution can be obtained following the procedure described in appendix A, thus obtaining the first sample population.

The time update step consists of running the model for every particle i.e. making a prediction of the heat flux value for the first time step for each sample (or particle). Later, this is compared with the first measurement available, (feedback), and the likelihood of each particle is evaluated using equation 2.22. The particles that maximise the likelihood are selected while the particles that do not produce acceptable results are discarded. The subset of remaining particles form the posterior distribution, and will be used as prior distribution for the next time step.

As it can be seen, the particle filters approximate the posterior distribution “online”, i.e. as the data are being collected. This offers significant reduction in computational costs, as it doesn’t require the simulation of the full data set every time that the likelihood is evaluated. The algorithm incorporates the information contained in the data as it becomes available.

The creation of the posterior distribution by selecting only the particles that maximise the likelihood is called *importance sampling*. This is achieved by assigning a

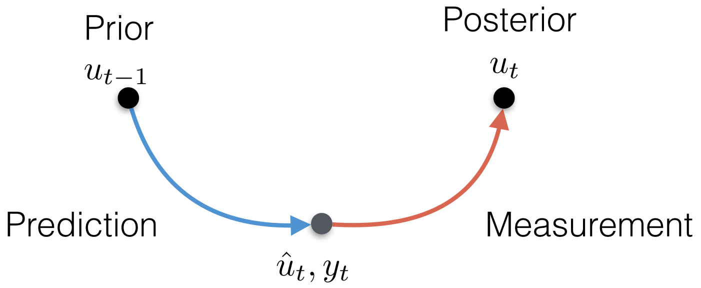

Figure 6.1.2: Diagram explaining the Kalman filtering algorithm

weight to each particle representing the probability distribution. Initially, all the particles are assigned identical weights. These weights are modified following the feedback step, and the newly assigned weights are proportional to the likelihood.

A well-known shortcoming of the importance sampling algorithm is the *weight degeneracy* problem. After a certain number of iterations, only a few samples will remain with non-negligible weights, and this is problematic for an accurate approximation of a probability distribution. Weight degeneracy is particularly pronounced when the posterior distribution is substantially different from the prior, as in the problem considered here, since the priors have been chosen to be wide and uninformative, and thus quite different from the sought posterior. A suitable measure of degeneracy is the effective sample size, $1 \leq ESS \leq N$: in the case of uniform weights $ESS =$ N and, in the case of only one particle with non-zero weight, $ESS = 1$ [94].

A common practice to solve the degeneracy problem is *resampling*. Resampling eliminates the particles with lowest weights and multiplies particles with higher weights. This, in turn, can lead to a sample composed only by identical particles, again an outcome that is detrimental for the appropriate characterisation of the probability distribution and the calculation of any estimate.

To solve this sample impoverishment issue, in this work, the procedure explained by Iglesias et al. [77] was adopted. The authors propose to smooth the transition between the prior and the posterior by introducing a number of intermediate artificial distributions, regulated by a tempering parameter. The methodology suggested by Iglesias et al.[77] is a subclass of particle filters, that provides an approximation of the moments of the target distribution (for the case considered here mean and variance). The mathematical description of the procedure can be found in [77], as a detailed outline of this algorithm is beyond the scope of this thesis.

For both the synthetic experiment and experimental data over which this algorithm has been validated, the ensemble size amounted to 300 particles, and, for better computational efficiency, at every iteration 15 measurements are assimilated at once, so that the total number of iterations can be reduced by a factor of 15.

## 6.2 Synthetic Experiments

The experiment proposed in this section, is the same as the experiment described in section 4.1. The situation examined corresponds to a wall construction with 5 layers. The profile of the "true" thermal conductivity and of the "true" specific heat capacity are displayed in figure 6.2.1. The thickness of the wall was considered to be 0.3 $m$ and it was discretised into 100 elements for the numerical solution of the heat equation.

With such profiles for thermal conductivity and volumetric heat capacity, the "true" $\mathcal{K}$-value and $\mathcal{C}$-value, calculated via equations (2.6), were

$$\mathcal{K}_{true} = 3.62\ [W/m^2K] \qquad \mathcal{C}_{true} = 3.19 \times 10^5\ [J/m^2K] \tag{6.2}$$

The boundary conditions are shown in the left panel of figure 4.1.2, the heat flux thus obtained is displayed in figure 4.1.2, right panel, which, for the purpose of the analysis, was corrupted with gaussian noise $\eta \sim N(0, 0.5)$.

The thermal conductance and heat capacity inferred from implementing the model with the Kalman filter were:

$$\mathcal{K}_{inferred} = 3.62 \pm 0.14\ [W/m^2K]$$
$$\mathcal{C}_{inferred} = 3.17 \times 10^5 \pm 2.68 \times 10^4\ [J/m^2K]$$

The parameters defining the prior of the thermal conductivity are $\lambda_k = 0.5$ and $\sigma_k = 0.25$ and, in a similar fashion, the parameters for the volumetric heat capacity are $\lambda_c = 0.1$ and $\sigma_c = 0.1$. Figure 4.1.4 displays the prior distributions of the conductance and heat capacity.

Figure 6.2.2 shows the reduction of the uncertainty in the determination of the thermal properties characterising the construction considered. The results are similar to the results obtained by implementing the MCMC described in section 4.1.1. The prior distribution is uninformative in the case of the thermal conductivity, and, in

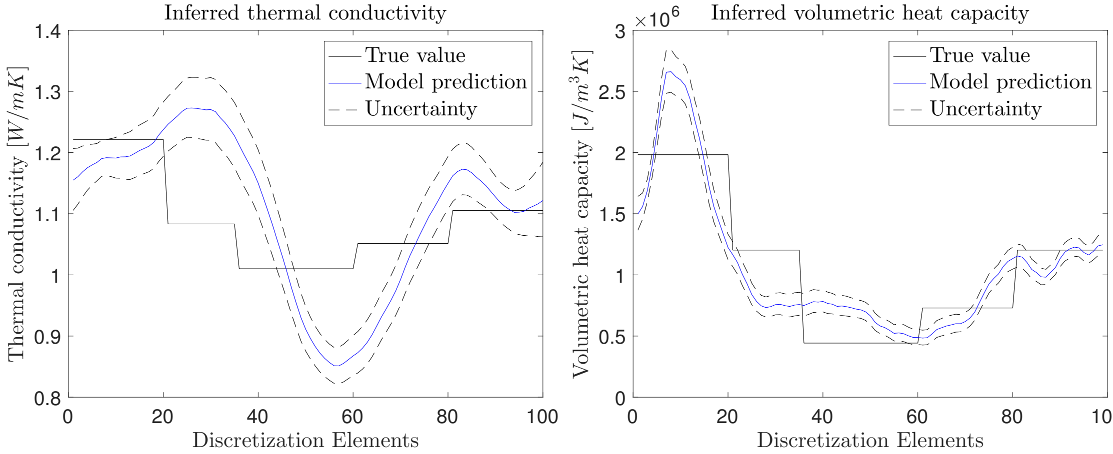

Figure 6.2.1: Synthetic experiment: true value of thermal conductivity and volumetric heat capacity and the profiles inferred by the HDM with the Kalman algorithm

the case of the volumetric heat capacity, it does not capture the “true capacity” at all.

After conditioning the model to the data, the uncertainty band is reduced in both cases and the mean of the posterior distributions follow the behaviour of the “true” thermal properties.

In both cases, both for the prior and the posterior distributions, the uncertainty represents three standard deviations from the mean value.

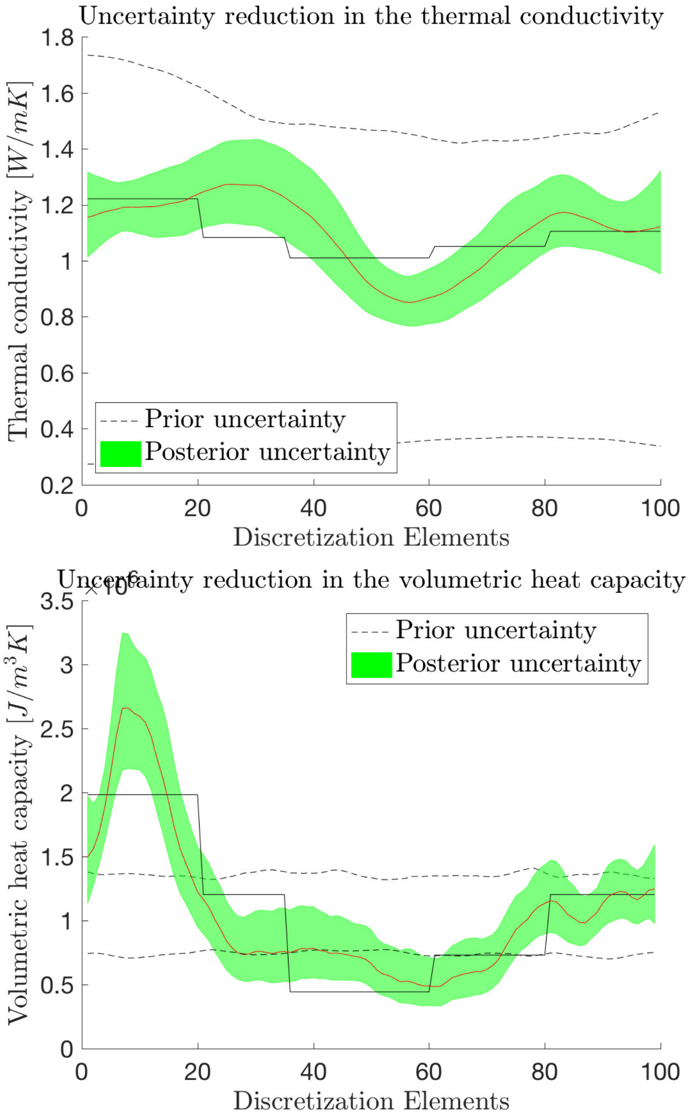

Figure 6.2.2: Synthetic experiment: Uncertainty reduction in the determination of the thermal conductivity and volumetric heat capacity

## 6.3 Validation experimental data

Following the investigation performed with the MCMC model, it was found that, with the model developed, it is possible to retrieve the thermal properties of a construction with just one day of experimental observations. As this is one of the most advantageous results guaranteed by the model developed, it was decided to trial the performance of the Ensemble Kalman filter on a single day data set, to ascertain whether this is still achievable with the new solution algorithm.

The results obtained are then compared with the output obtained by implementing the HDM with the MCMC algorithm.

Looking at figures 6.3.1 - 6.3.3, showing the heat flux predictions for the experimental data collected in the environmental chamber, the unoccupied solid wall property and the steel frame office, it can be seen that the predictions obtained in the validation windows are of good quality, as in the case of the model predictions obtained implementing the HDM model with the MCMC algorithm.

This is confirmed by the residuals calculated via equation (5.1), which, as may be seen from table 6.3.1, are similar to the residuals obtained with the MCMC algorithm. This suggests that Ensemble Kalman filters, even if they offer just an approximation of the posterior distribution, are effective in characterising the posterior of the thermal properties sought and are suitable for the solution of the inverse heat problem investigated in this study.

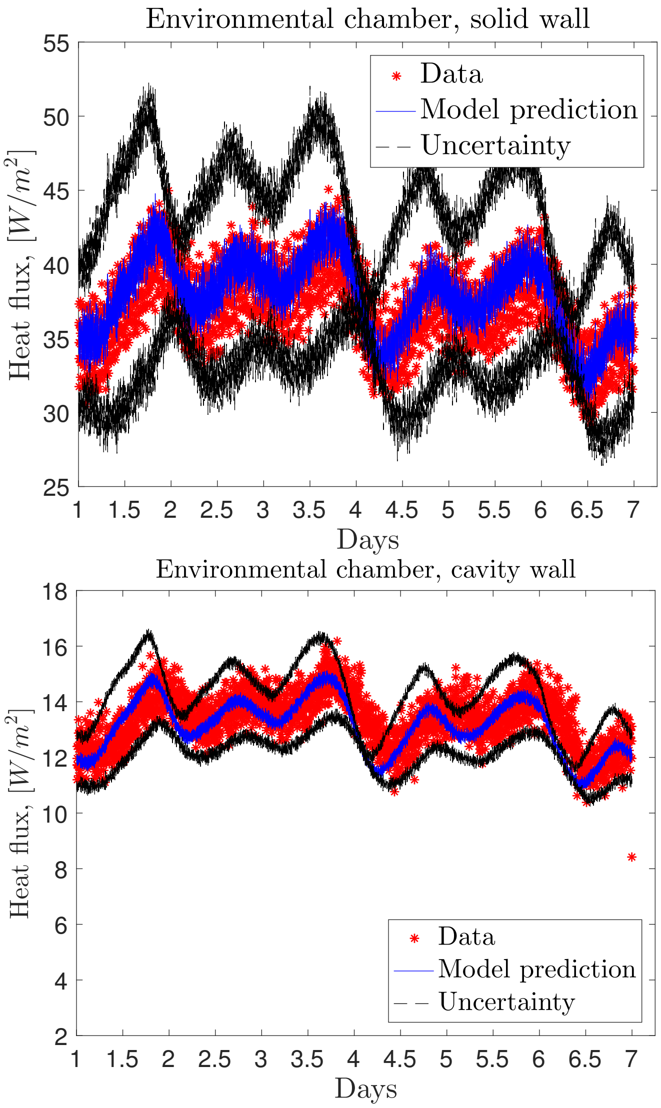

Figure 6.3.1: Environmental chamber, solid wall (top), cavity wall (bottom): heat flux predictions obtained with the Ensemble Kalman filter HDM

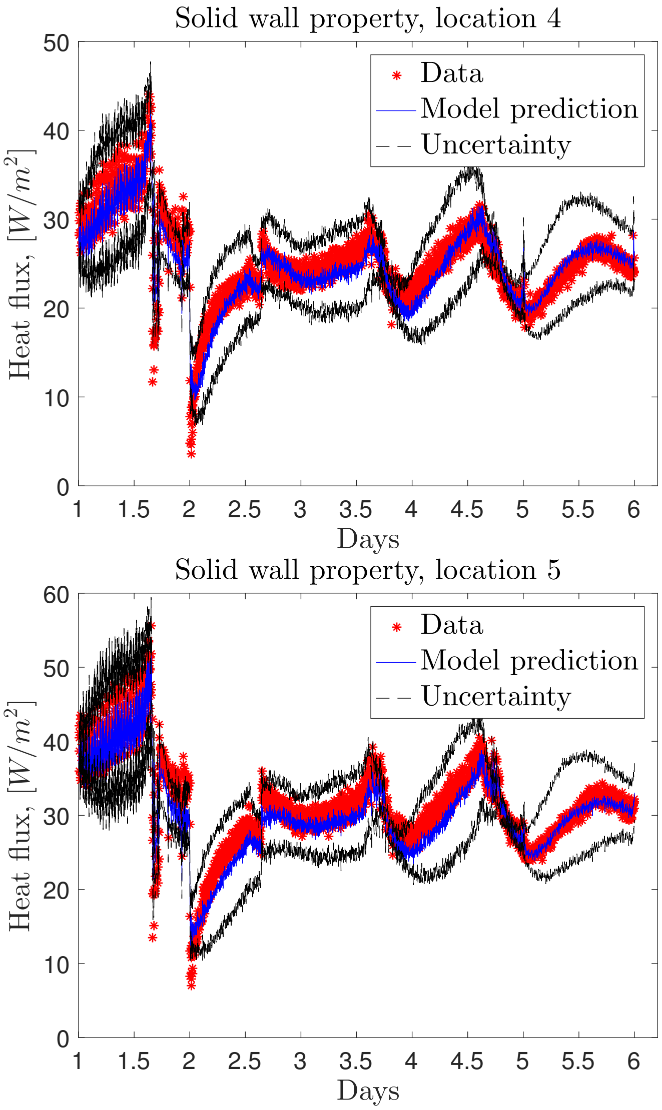

Figure 6.3.2: Unoccupied solid wall property, location 4 (top), location 5 (bottom): heat flux predictions obtained with the Ensemble Kalman filter HDM

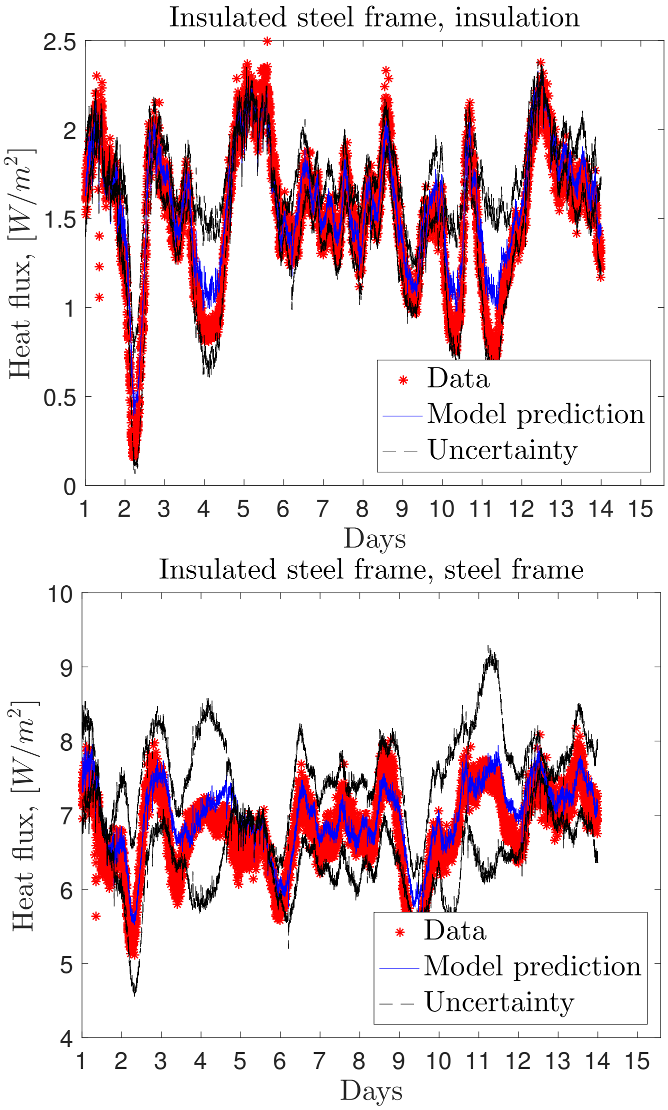

Figure 6.3.3: Insulated steel frame construction, insulation (top), steelframe (bottom): heat flux predictions obtained with the Ensemble Kalman filter HDM

Table 6.3.1: Residuals from experimental data for 1 day simulations for the Ensemble Kalman filter and MCMC algorithms.

| Experiment | Residual KF | Residual MCMC |
|---|---|---|
| Environmental chamber, solid | 1.47 | 1.40 |
| Environmental chamber, cavity | 0.75 | 1.79 |
| Office, Insulation | 0.13 | 0.13 |
| Office, Steel frame | 0.31 | 0.29 |
| Wortley, location 4 | 1.99 | 2.61 |
| Wortley, location 5 | 2.02 | 3.41 |

An interesting observation may be made in relation to the internal flux collected in the environmental chamber for the cavity wall. Looking at figure 4.4.1, it can be seen that the experimental data are affected by noise, and that the model predictions and uncertainty obtained with the MCMC model are also affected by the noise, making the picture difficult to interpret.

For the implementation of the model with the Ensemble Kalman filter, the experimental measurements have been previously smoothed with a gaussian low pass filter to reduce the noise present in the data. In this way, it is possible to obtain a clearer figure, as may be seen in Figure 6.3.1, bottom.

Looking at tables 6.3.2 - 6.3.4, comparing the values of the thermal conductance and heat capacity inferred with the Ensemble Kalman filtering technique, with the values obtained with the MCMC algorithm, it can be seen that the figures obtained with the two methods are in agreement, thus confirming that Ensemble Kalman filters, in the case considered, can provide a representation as good as the Markov Chain

Monte Carlo.

In most of the cases presented (environmental chamber experiments and insulated steel frame construction), the results inferred with the Ensemble Kalman filter algorithm and the values inferred with the MCMC are included in each other's error band.

The values inferred for the solid wall of the unoccupied property instead are not compatible as the error bands exclude each other. This was to be expected as, as mentioned in the previous analysis, the data collected on the solid wall property shows a step change in the temperature boundary conditions that might impact on the performance of the model.

Still, the values obtained fall within the expected range of thermal conductance and heat capacity for a solid wall construction.

Comparing the relative uncertainty obtained from both algorithms, displayed in tables 6.3.3 - 6.3.5, it can be seen that it is of similar magnitude, supporting the possibility that the distribution found by the Ensemble Kalman filter technique is a good approximation of the posterior defined from the Markov Chain Monte Carlo process.

Table 6.3.2: Values of the conductance obtained with the Ensemble Kalman filter and MCMC algorithm from 24 hours of experimental data.

| Experiment | Conductance KF [W/m$^2$K] | Conductance MCMC [W/m$^2$K] |
|---|---|---|
| Environmental chamber, solid | 3.15 ± 2.7 $\times 10^{-2}$ | 3.17 ± 9.5 $\times 10^{-3}$ |
| Environmental chamber, cavity | 0.76 ± 3.1 $\times 10^{-3}$ | 0.77 ± 9.7$\times 10^{-3}$ |
| Office, Insulation | 0.10 ± 5.5 $\times 10^{-4}$ | 0.11 ± 5.2$\times 10^{-4}$ |
| Office, Steel frame | 0.47 ± 2.0 $\times 10^{-3}$ | 0.47 ± 4.9$\times 10^{-4}$ |
| Wortley, location 4 | 2.31 ± 5.2 $\times 10^{-2}$ | 2.19 ± 3.2$\times 10^{-2}$ |
| Wortley, location 5 | 2.80 ± 1.1 $\times 10^{-1}$ | 2.65 ± 4.6$\times 10^{-2}$ |

Table 6.3.3: Relative uncertainty on the conductance obtained with the Ensemble Kalman filter and MCMC algorithm from 24 hours of experimental data.

| Experiment | Relative uncertainty, KF | Relative uncertainty, MCMC |
|---|---|---|
| Environmental chamber, solid | 0.9% | 0.3% |
| Environmental chamber, cavity | 0.4% | 1.3% |
| Office, Insulation | 0.6% | 0.5% |
| Office, Steel frame | 0.4% | 0.1% |
| Wortley, location 4 | 2.3% | 1.5% |
| Wortley, location 5 | 3.9% | 1.7% |

Table 6.3.4: Values of the Heat capacity obtained with the Ensemble Kalman filter and MCMC algorithm from 24 hours of experimental data.

| Experiment | Heat Capacity KF [J/m$^2$K] | Heat capacity MCMC [J/m$^2$K] |
|---|---|---|
| Environmental chamber, solid | $4.08\times10^5\pm 1.1\times10^5$ | $3.80\times10^5\pm 5.1\times10^4$ |
| Environmental chamber, cavity | $2.30\times10^5\pm 8.2\times10^4$ | $4.40\times10^5\pm 1.0\times10^5$ |
| Office, Insulation | $3.74\times10^4\pm 1.5\times10^3$ | $3.74\times10^4\pm 0.7\times10^3$ |
| Office, Steel frame | $7.62\times10^4\pm 4.1\times10^3$ | $7.94\times10^4\pm 1.9\times10^3$ |
| Wortley, location 4 | $2.60\times10^5\pm 2.0\times10^4$ | $3.84\times10^5\pm 2.5\times10^4$ |
| Wortley, location 5 | $3.33\times10^5\pm 2.8\times10^4$ | $5.47\times10^5\pm 4.7\times10^4$ |

Table 6.3.5: Relative uncertainty on the heat capacity obtained with the Ensemble Kalman filter and MCMC algorithm from 24 hours of experimental data. (* refers to 12 hours time window)

| Experiment | Relative uncertainty, KF | Relative uncertainty, MCMC |
|---|---|---|
| Environmental chamber, solid | 27.0 % | 13.4% |
| Environmental chamber, cavity | 35.7% | 22.7 % |
| Office, Insulation | 4.01% | 1.9 % |
| Office, Steel frame | 5.4% | 2.4% |
| Wortley, location 4 | 7.7% | 6.5% |
| Wortley, location 5 | 8.4% | 8.6% |

## 6.4 Computational cost reduction

As mentioned in section 6.1, Ensemble Kalman filters can provide a significant reduction in the computational costs associated with the implementation of the inference process. A representative quantification of the computational costs associated with each algorithm is offered by the number of times the forward map $\mathcal{G}(u)$ is evaluated.

In the implementation of the MCMC, $\mathcal{G}(u)$ is evaluated a million times for each of the unknowns plus one for the evaluation of the initial proposal, i.e. $2 \times 10^6 + 1$ times in the case of the problem with surface boundary conditions and $3 \times 10^6 + 1$ for the problem with convective boundary conditions. In each case, the output of $\mathcal{G}(u)$ has to be calculated for all the time steps of the simulation: 1008 time points (3.5 days with 5 minutes sampling).

The estimation of the computational cost associated with the Ensemble Kalman filter algorithm is not so accurate as in the MCMC case, due to the presence of the tempering parameter, which for every iteration, will prescribe a different number of intermediate artificial distributions to smooth the transition between the prior and posterior. None the less, it is possible to obtain a good estimation of evaluations of the model $\mathcal{G}(u)$. Monitoring the number of internal iterations necessary to create the artificial distribution chains at each assimilation step, it can be seen that the first step is the most expensive, and that the number of iterations drastically decreases for the following steps.

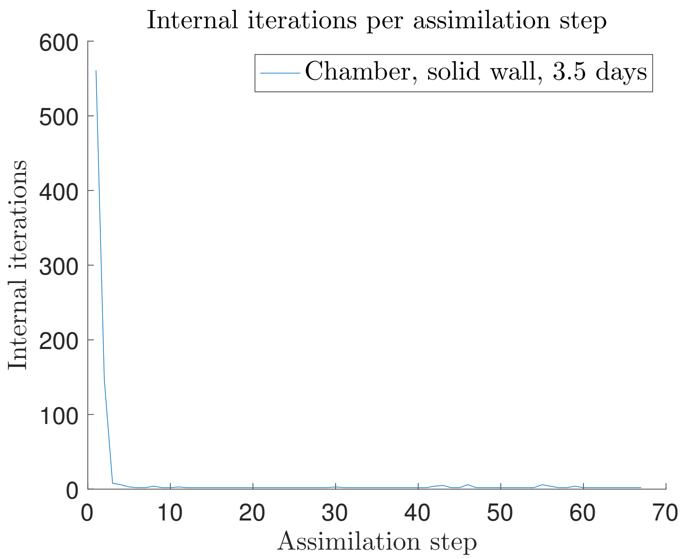

Figure 6.4.1: Internal iteration for each assimilation step, chamber data, solid wall

Figure 6.4.1 displays the number of internal iterations required to infer the thermal properties of the solid wall in the environmental chamber using 3.5 days of data. The first step requires 589 internal iterations but from the fifth step forward, the number of iterations required oscillates between 2 and 5. The average number of iterations over the total assimilation steps is $\sim 13$, therefore this has been chosen as a representative number of iterations per step.

In the solution algorithm with the Ensemble Kalman filters, $\mathcal{G}(u)$ is evaluated for every particle of the ensemble (300, in the case considered), and, for each particle, in each assimilation step, the algorithm evaluates $\mathcal{G}(u)$ at every internal iteration, therefore, in total, $\mathcal{G}(u)$ is evaluated 245.700 times $\sim 2.5 \times 10^5$, approximately 10 times less than with the Markov Chain Monte Carlo. Furthermore, instead of calculating the heat flux predictions for the whole time window considered, at each iteration $\mathcal{G}(u)$

evaluates the heat flux up to that point only, reducing the computational costs further.

The reduction in computational costs is clearly visible from the computational time requested to implement the 1 day simulations for the different data sets, summarised in table 6.4.1. From the table, it can be seen that the filtering tecnique offers a significant improvement on the computational times necessary for the convergence of the MCMC, displayed in table 5.3.1.

Table 6.4.1: Computational time required for the implementation of the HDM model with the Ensemble Kalman Filter on an Intel Core i3-4130 at 3.40 GHz

| Experiment | Length | Computational time |
|---|---|---|
| Environmental chamber, solid | 3.5 days | 215 sec |
| Environmental chamber, solid | 1 day | 50 sec |
| Office, Insulation | 1 day | 70 sec |
| Office, Steel frame | 1 day | 130 sec |
| Wortley, location 4 | 1 day | 42 sec |
| Wortley, location 5 | 1 day | 37 sec |

## 6.5 Conclusions

From the results presented in the sections above, it can be seen that the approximation method offered by the Ensemble Kalman filter is suitable for the application considered in this study as, with a small ensemble size of 300 particles, it is able to replicate the results obtained with the MCMC method.

The synthetic experiments show that the Ensemble Kalman filter algorithm is still able to reproduce the general trend of the “true” thermal properties, with the same limitations as in the case of the MCMC.

The validation made using the experimental data sets show that with one day of experimental data, the Ensemble Kalman filter algorithm is also able to infer the conductance and heat capacity of the construction investigated, with similar error margins to those retrieved with the MCMC.

The general agreement between the values and relative uncertainties inferred with the Ensemble Kalman filter and the MCMC suggest that, in this case, the Ensemble Kalman filter approximation is reliable in describing the posterior sought and that, considering the valuable computational costs reductions achievable with this method, it is a very promising tool for this application in the built environment.

# Chapter 7

# Research impact and conclusions

This chapter shows the impact of the accomplished work in the field of the built environment and draws the conclusions from the results obtained and described in chapters 4, 5 and 6.

Section 7.1 shows how the uncertainty in the U-value leads to a large variability on the predicted energy consumption and payback period, associated to energy retrofit interventions of a case study research building located at the University of Nottingham. Utilising the same case study, it is demonstrated how the reduced uncertainty obtainable with the model proposed in chapter 2 can lead to a reduced spread in the predictions of energy consumption and payback period.

Section 7.2 summarises the research results obtained, detailed in Chapter 4, 5 and 6 and draws the conclusions in relation to the aims and objectives outlined in the introduction.

Finally, section 7.3 indicates possible future research avenues for extending the work reported here.

## 7.1 Research Impact

This section demonstrates the relevance of the work carried out in the context of the built environment. In particular, it concentrates on the practical impact of U-value uncertainty on the final domestic energy consumption, dwelling carbon emissions and financial evaluation of retrofit intervention, showing why it is essential to consider the uncertainty on the thermal transmittance parameter rather than assuming just an absolute value.

For the purpose of this analysis, the software DesignBuilder v.5.0.3.007 was employed [29]. The dwelling studied is the Eon house, a retrofit research project, located at the University Park, Nottingham [25].

The dwelling was built within the CALEBRE research project (www.calebre.org.uk/) whitch aims to investigate the effectiveness of energy efficient retrofit in existing buildings. The E.on house was built in 2007 following a traditional 1930 design, including uninsulated cavity walls, second hand inefficient boiler and single glazing windows and doors. The dwelling was retrofitted in different stages, in order to assess the impact of each intervention on the reduction of energy consumption. Further information on the outcomes of this research project can be found in [22, 25, 95] and in the outputs section of the CALEBRE website.

In particular, Gillott et al. in [22] focus on the reduction of air permeability by conventional draft proofing interventions, such as silicon sealing of windows and door frames, and more targeted interventions such as floor sealing at skirting boards level and sealing at the junctions of walls and ceiling.

Even if the initial air permeability of the E.on house was 15.57 $m^3/hm^2$, their results show that the accurate application of conventional draught proofing interventions, such as the application of sealant to windows and door frames and fitting of covers on key locks, were found to be the most effective measures, providing reductions in air permeability by approximately 29%.

For the purpose of this demonstration, the building dimensions, openings, ventilation strategy and heating system have been modelled to replicate the E.on house at its Phase 2 retrofit stage indicated in [22]. The building fabric instead was set to a solid wall construction with an internal plaster layer. The U-value of the external walls, has been originally set to 1.92 $W/m^2K$ (as measured on the unisulated solid wall property described in section 3.3) and later, the uncertainty margin of 25% was applied to the thermal transmittance.

The building air permeability was set to 10 $m^3/hm^2$. This is consistent with a solid walled property that has had previous draught proofing interventions (such as double glazing and sealing of windows and door frames) and ceiling insulation, and it is consistent with the findings described by Gillott et al. [22] for the case study considered.

As mentioned earlier, the aim of this simulation is to quantify the impact of the

Table 7.1.1: Summary of the simulation options for Design Builder simulations

| **Simulation parameters** | |
|---|---|
| Simulation period | 1-Jan to 31-Dec |
| Time steps per hour | 6 |
| Weather data | Birmingham weather data |
| **Heating system** | |
| Bolier type | Condensing boiler |
| Boiler Efficiency | 0.75% |
| Heating fuel | Natural gas |
| **Fabric details** | |
| Glazing | Double glazing, U-value 2.66 $W/m^2K$ |
| Roof | Insulated at ceiling level, U-value 0.15 $W/m^2K$ |
| External walls | Solid brick with internal plaster, U-value see table 7.1.2 |
| Ground floor | Suspended ground floor, U-value 1.38 $W/m^2K$ |

uncertainty of the U-value on the final space heating energy consumption and, consequently, the carbon emissions related to this consumption.

Table 7.1.2 shows the energy consumption associated to different values of the thermal transmittance, keeping the rest of the simulation parameters unchanged, as detailed in the previous paragraph. The simulation results relate to a yearly simulation with a weather data file relative to Birmingham as provided by the DesignBuilder software package.

The simulation options are summarised in table 7.1.1. The internal gains due to occupants, lights and equipment were determined based on the standard occupancy and activity schedules for domestic buildings available in Design Builder.

As it can be seen from table 7.1.2, a 25% difference on the assumed U-value of the external walls leads to a large variability in the predicted space heating consumption, producing a shift of ±16% from the baseline prediction. In comparison, the same cal-

Table 7.1.2: Yearly energy consumption for space heating associated with different external wall U-values and % difference with baseline case.

| U-value [W/m$^2$K] | Space heating consumption [kWh/y] | Difference [%] |
|---|---|---|
| 1.92 | 17149 | Baseline |
| 2.40 (+25%) | 19884 | +15.9% |
| 1.44 (– 25%) | 14402 | – 16.0% |
| 2.11 (+10%) | 18223 | +6.3% |
| 1.73 (– 10%) | 16077 | – 6.3% |

culations have been performed applying an uncertainty margin of 10% on the external walls thermal transmittance, corresponding to the maximum U-value uncertainty obtained with the model developed in this thesis. Confronting the results displayed in table 7.1.2, it can be seen that the smaller uncertainty leads to a significantly reduced variability in fuel consumption, of approximately ±6.3%.

The corresponding carbon emissions, relative to the heating fuel consumption, are affected in the same measure, as the latter are obtained by multiplying the energy consumption by the relevant green house gas conversion factor. In the case of natural gas, the 2016 gross and net calorific value (CV) published by the Department for Business Energy & Industrial Strategy are 0.18 $kgCO_2/kWh$ and 0.20 $kgCO_2/kWh$ respectively [96]. These values lead to the $CO_2$ emissions displayed in table 7.1.3.

The same analysis has been performed in the case of an externally insulated solid wall construction, comparing the impact of the standard uncertainty (25%) and the smaller uncertainty (10%), achieved with the methodology investigated, on walls with a low U-value. An external layer of EPS with render finish has been applied to the ex-

Table 7.1.3: Yearly $CO_2$ emissions associated with space heating energy consumption

| U-value [W/m$^2$K] | Gross $CO_2$ Emissions [kg/y] | Net $CO_2$ Emissions [kg/y] | Difference [%] |
|---|---|---|---|
| 1.92 | 3087 | 3430 | Baseline |
| 2.40 (+25%) | 3579 | 3977 | +15.9% |
| 1.44 (– 25%) | 2592 | 2880 | – 16.0% |
| 2.11 (+10%) | 3280 | 3645 | +6.3% |
| 1.73 (– 10%) | 2894 | 3215 | – 6.3% |

Table 7.1.4: Yearly energy consumption for space heating associated with different external wall U-values and % difference with baseline case.

| U-value [W/m$^2$K] | Space heating consumption [kWh/y] | Difference [%] |
|---|---|---|
| 0.3 | 6912 | Baseline |
| 0.375 (+25%) | 7432 | +7.5% |
| 0.225 (– 25%) | 6388 | – 7.6% |
| 0.33 (+10%) | 7118 | +3% |
| 0.27 (– 10%) | 6702 | – 3% |

ternal solid wall construction, the thickness of the insulating layer has been adjusted to achieve the different U-values displayed in table 7.1.4. From this table, it can be seen that the same uncertainty levels on walls with better (smaller) U-values, lead to reduced uncertainty margins on the final energy predictions. This is reasonable because the space heating load will be less affected by the heat losses through the building fabric in a dwelling with lower U-values. Nevertheless, it is still evident that the smaller U-value uncertainty produces significantly more accurate results in the predicted fuel consumption, approximately halving the original uncertainty.

It is clear from the analysis presented that the uncertainty on the thermal transmittance leads to an important variability in the final dwelling energy prediction, especially in dwellings affected by external walls with larger U-values. In turn, this influences the payback period as the cost savings are based on the predicted fuel savings. For example, assuming an upfront cost for the installation of external wall insulation of £10,000, as suggested by the energy saving trust [97], and a standard natural gas price of 0.043£/kWh [98], the payback period in the worst case scenario (underestimated initial U-value and overestimated final U-value) and best case scenario (overestimated initial U-value and underestimated final U-value) are reported in table 7.1.5, under the assumption of 25% U-vlaue uncertainty. From the data displayed in this table, it can be seen that the energy savings associated with the same intervention have an extremely wide variability, as the savings in the best case scenario are nearly the double than in the worst case scenario.

Table 7.1.5: Payback period associated with different energy consumption scenarios, assuming 25% uncertainty on the external wall U-value

| | Pre-retrofit U-value [$W/m^2K$] | Post-retrofit U-value [$W/m^2K$] | Annual Savings [£/y] | Payback [y] |
|---|---|---|---|---|
| Worst case scenario | 1.44 | 0.375 | 300 | 33 |
| Best case scenario | 2.40 | 0.22 | 580 | 17 |

The U-value uncertainty reduction achievable with the model proposed, offers already significant diminution of the variability seen on the final energy consumption predictions, (as demonstrated in the previous paragraphs), thus ensuring fairer payback estimation as it can be seen in table 7.1.6.

Table 7.1.6: Payback period associated with different energy consumption scenarios, assuming 10% uncertainty on the external wall U-value

| | Pre-retrofit U-value [$W/m^2K$] | Post-retrofit U-value [$W/m^2K$] | Annual Savings [£/y] | Payback [y] |
|---|---|---|---|---|
| Worst case scenario | 1.73 | 0.33 | 385 | 26 |
| Best case scenario | 2.11 | 0.27 | 495 | 20 |

The simulations carried out in this section, clearly show the benefits associated with the U-value uncertainty reduction achieved with the inference methodology proposed, demonstrating the practical impacts of the research carried out in this study.

## 7.2 Conclusions

The aim of this study was to achieve a faster and more accurate process for the evaluation of the thermal transmittance in buildings from in situ measurements of temperature and surface heat flux. As discussed in chapters 4, 5 and 6, the HDM in combination with MCMC or EnKF sampling methods is able to obtain the thermal transmittance value within 24 hours. The investigation of the uncertainty associated with the thermal transmittance, calculated with the method proposed in chapter 2, is greatly reduced when compared with ISO9869:2014, decreasing from 28-14% to 10-7%.

Based on these figures it can be stated that the general aim of this thesis has been achieved.

Some of the objectives outlined in the introduction were functional to the construction of the model described in chapter 2 and do not present innovative aspects in the field of the built environment. These are discussed briefly here:

**Objective i:** Literature review. The literature survey shows that the U-value plays an important role in the performance of a dwelling and, due to the current pressure on improving dwelling efficiency and reducing carbon emissions, it is essential to obtain a quick and reliable U-value measurement procedure.

The current ISO9896:2014 standard requires a minimum monitoring period of 3 days (in ideal conditions) and the uncertainty associated with the calculation method adopted equates to 25% [48].

**Objective ii:** The numerical solution of the heat transfer equation has been obtained by means of a cell centred finite difference method.

**Objective vi:** The experimental data collection has been described in Chapter 3. The measurement procedure was carried out utilising standard equipment adopted in monitoring campaigns in the built environment. The data collected were of good quality and allowed the verification and the validation of the HDM.

The remaining objectives required the introduction of innovative methods in the field of the built environment. This lead, in some cases, to arbitrary choices made by the researcher, with consequences on the interpretation and validity of the results obtained. These are discussed here:

**Objectives iii - iv:** The introduction of spatially varying thermal properties required the introduction of a new Bayesian framework (as described in [82]) able to deal with the large number of parameters arising from the discretisation of the heat equation. The framework described in [82] has never been used before in the context of the inference of U-value. This choice allows the researcher to determine the nature of the functions describing the thermal properties sought. As discussed in section 2.2.2, in this study, continuous thermal properties subject to the Mattern correlation, equation (2.27), were assumed. Note that the choice of parameters characterising the covariance function lead to important differences in the appearance of the thermal properties sought, as discussed in sections 2.2.2 and 4.1. Furthermore the choice of the type of prior distribution is arbitrary as well. In this work, lognormal distributions were assumed for the distribution of $\kappa(x)$ and $c(x)$, but as discussed in section 2.2.2, these are at the discretion of the researcher.

**Objective v:** The characterisation of the posterior distribution is achieved following two different procedures: Markov Chain Monte Carlo (MCMC) and Ensemble Kalman Filters (EnKF). The MCMC algorithm, by construction, leads to the correct posterior distribution and, therefore, is an essential step in the implementation of the Bayesian framework. On the other side, this algorithm requires a large number of iterations to ensure that convergence is achieved, translating in high computational costs and long computation times.

The Ensemble Kalman filter instead is an approximation method and offers the benefit of a significant reduction in the computational costs (and times) associated with the inference of the thermal properties from the measured data sets. From the tests performed on synthetic and experimental data outlined in chapter 6, it can be seen that the EnKF is able to replicate the results obtained with the MCMC using only one day of experimental data. This may be seen from the heat flux predictions displayed in figures 6.3.1, 6.3.2, 6.3.3 and the figures obtained relative to the thermal conductance and heat capacity displayed in tables 6.3.2, 6.3.4. The uncertainty surrounding the values found is similar to the values found with the MCMC, as it may be seen from the data displayed in tables 6.3.3, 6.3.5.

This evidence suggests that, in the case considered, the EnKF is providing a good approximation of the posterior distribution sought and that, therefore, it is reasonable to use such an algorithm for the inference of the fabric thermal properties in future developments of the model proposed.

**Objective vii:** The practical impact of the uncertainty reduction provided by the model proposed is assessed by means of Design Builder simulations in section 7.1. This objective could be further pursued by monitoring pre and post retrofit energy consumption of a case study building in order to validate the results obtained by using a building simulation software.

In conclusion it can be stated that the aim and objectives outlined in the introduction have been achieved and it can be stated that the HDM with MCMC or EnKF algorithm is a promising tool for the inference of the U-value and heat capacity of building constructions. Still, further improvements can be made on its ability to infer the exact profile of the thermal properties across the building element thickness. As has been shown from the data on the synthetic experiments, the model developed is able to retrieve qualitative information regarding the construction of the wall considered, but as detailed in section 4.1, this feature cannot be used to retrieve the exact number of layers in a wall construction or the precise location of the interface. This, alongside other suggestions for future research are discussed in section 7.3.

## 7.3 Future work

### 7.3.1 Extension of the model performance

The methodology proposed in this thesis presents a great potential for the calculation of experimental uncertainty and reduction in monitoring times. Still, it requires further investigation before it can be safely promoted for the application in large monitoring campaigns as a standardised method.

Firstly the relationship between the definition of the prior probability distribution and the inferred thermal properties profiles has to be studied in more depth, as it is here where an essential assumption is being made by the researcher: the a priori determination of the "smoothness" of the thermal properties of the case considered, as discussed in sections 2.2.2 and 4.1.

Secondly it is essential to examine the impact of the discretisation level in the solution of the forward problem (the heat equation). This can be compared to a mesh refinement problem: discretising the heat equation in a small number of nodes (3-7 in the case of the most common RC network models) leads to a model that is not able to fully characterise the heat capacity of the element considered, but on the other hand, an over discretised model might lead to unnecessary computational costs, as might be the case for the models proposed in this work (100 nodes discretisation).

Finding the minimum number of nodes that guarantees results independent from the discretisation level is an essential step for the optimisation of the HDM in terms of the reduction of computational costs and times and finding a physically correct solution. This issue is addressed in a publication currently in progress during the writing of this thesis.

Still, the model proposed is flexible and could be further extended to overcome other restrictions that are currently a barrier to a quick and convenient U-value measurement procedure. It is possible to include a heat source term in the heat equation to model the impact of solar radiation in the building structure considered. This can be used to extend the monitoring periods of the building fabric to the summer season, as the impact of radiation on the energy stored in the wall is currently the main reason for reducing the monitoring periods to the winter season.

The Bayesian framework developed, would allow the estimation of the solar radiation as a new unknown parameter of the model, without the necessity of including other experimental equipment during the monitoring period (such as a pyranometer).

In a similar way, it could be possible to include the estimate of the convective heat transfer coefficients in the inference process, for the cases where the standard values are not applicable.

### 7.3.2 Other applications in the built environment

Possibly, the most pressing future research avenue based on the work carried out in this thesis is the investigation of the uncertainty on the predicted final figures of building energy consumption.

In the case study described in section 7.1, it has been shown that the uncertainty currently accepted on the thermal transmittance parameter can lead to ±15.4% uncertainty in the final space heating energy consumption figures.

This number is extremely large when considering that it is generated by the uncertainty in a single parameter, without considering the error margin associated with other important variables that impact the energy performance of a building, such as air infiltration, roof U-value, glazing characteristics and heating system efficiency.

The author believes that the framework developed during this research project could be extended to other areas in the built environment, such as the measurement of air tightness or whole building heat loss coefficient, as these are essentially inverse problems where, from measured data, the researchers are inferring building envelope properties.

Better characterisation of the uncertainty of the most influential building parameters will, in turn, lead to a better reformulation of the performance gap problem, introducing a margin of uncertainty on the predictions obtained and on the experimental data collected.

# References

[1] Randall Munroe. 4.5 degrees. `https://xkcd.com/1379/`. Accessed: February 2017.

[2] Amanda Penistone. 2015 uk greenhouse gas emissions, final figures. Technical report, Department for Business, Energy and Industrial Strategy, February 2017.

[3] Energy flow chart. `https://www.gov.uk/government/statistics/energy-flow-chart-2015`, 2016. Accessed: 10 April 2017.

[4] Energy consumption in the uk. Technical report, Department for Business, Energy and Industrial Strategy, 2016.

[5] Hukseflux. User manual hfp01 and hfp03. `http://www.hukseflux.com/sites/default/files/product_manual/HFP01_HFP03_manual_v1620.pdf`. Accessed: 20 April 2017.

[6] Campbell Scientific. Cs215 temperature and relative humidity probe. `https://s.campbellsci.com/documents/us/manuals/cs215.pdf`. Accessed: 15 July 2015.

[7] Conservation of fuel and power, building regulations part l, April 2016.

[8] CIBSE. Guide a environmental design. *The Chartered Institution of Building Services Engineers, London*, 2015.

[9] Susan Solomon. *Climate change 2007-the physical science basis: Working group I contribution to the fourth assessment report of the IPCC*, volume 4. Cambridge University Press, 2007.

[10] United Nations. Status of ratification of the kyoto protocol. "`http://unfccc.int/kyoto_protocol/status_of_ratification/items/2613.php`", October 2014. Accessed: 6 October 2014.

[11] Questions and answers on eu ratification of the second commitment period of the kyoto protocol. `http://europa.eu/rapid/press-release_MEMO-13-956_en.htm`, March 2017. Accessed: March 2017. URL: `http://europa.eu/rapid/press-release_MEMO-13-956_en.htm`.

[12] HM Government. Climate change act 2008. Technical report, HM Government, 2008.

[13] Committee on climate change. `https://www.theccc.org.uk`. Accessed: 10 April 2017.

[14] Digest of united kingdom energy statistics 2016. Technical report, Department for Business, Energy and Industrial Strategy, 2016.

[15] National insulation association. `http://www.nia-uk.org/consumer/`. 11 April 2017.

[16] Retrofit: Domestic buildings. `http://www.ukgbc.org/resources/key-topics/new-build-and-retrofit/retrofit-domestic-buildings`, March 2017. Accessed: 7 March 2017.

[17] Energy company obligation: Help to heat april 2017 to september 2018. `https://www.gov.uk/government/uploads/system/uploads/attachment_data/file/586260/ECO_Help_to_Heat_Government_response_FINAL_26_Jan_17.pdf`. Accessed: 20 April 2017.

[18] Private rented sector energy efficiency regulations (domestic). `https://www.gov.uk/government/uploads/system/uploads/attachment_data/file/401381/Dom_PRS_Energy_Efficiency_Regulations_-_Gov_Response_FINAL__04_02_15_.pdf`, 2015. Accessed: 20 April 2017.

[19] Future energy efficiency policy. `http://researchbriefings.parliament.uk/ResearchBriefing/Summary/POST-PN-0550`, February 2017. Accessed: February 2017.

[20] CA Yunus and JG Afshin. *Heat and Mass Transfer: Fundamentals and Applications*. Tata McGraw-Hill, New Delhi, India, 2011.

[21] Jason Palmer and Ian Cooper. United kingdom housing energy fact file 2013. *Department of Energy and Climate Change*, 2013.

[22] MC Gillott, Dennis L Loveday, J White, CJ Wood, Ksenia Chmutina, and Keyur Vadodaria. Improving the airtightness in an existing uk dwelling: The challenges,

the measures and their effectiveness. *Building and Environment*, 95:227–239, 2016.

[23] Andrea Gasparella, Giovanni Pernigotto, Francesca Cappelletti, Piercarlo Romagnoni, and Paolo Baggio. Analysis and modelling of window and glazing systems energy performance for a well insulated residential building. *Energy and Buildings*, 43(4):1030–1037, 2011.

[24] Geert Bauwens and Staf Roels. Co-heating test: A state-of-the-art. *Energy and Buildings*, 82:163–172, 2014.

[25] Matthew R Hall, Sean P Casey, Dennis L Loveday, and Mark Gillott. Analysis of uk domestic building retrofit scenarios based on the e. on retrofit research house using energetic hygrothermics simulation–energy efficiency, indoor air quality, occupant comfort, and mould growth potential. *Building and Environment*, 70:48–59, 2013.

[26] Octávio Alves, Eliseu Monteiro, Paulo Brito, and Pedro Romano. Measurement and classification of energy efficiency in hvac systems. *Energy and Buildings*, 130:408–419, 2016.

[27] Ofgem. Overview of previous schemes. `https://www.ofgem.gov.uk/environmental-programmes/eco/overview-previous-schemes`. Accessed: 20 April 2017.

[28] Chris Watson and Paul Bolton. Warm front scheme. `http://researchbriefings.parliament.uk/ResearchBriefing/Summary/SN06231#fullreport`, 2013. Accessed: 20 April 2017.

[29] Design builder software ltd. `https://designbuilder.co.uk`. Accessed: 20 April 2017.

[30] Energyplus. `https://energyplus.net`. Accessed: 20 April 2017.

[31] Tas environmental design solutions limited. `http://www.edsl.net/main/`. Accessed: 10 April 2017.

[32] The government s standard assessment procedure for energy rating of dwellings. Technical report, Building Research Establishment (BRE), 2014.

[33] Francis GN Li, AZP Smith, Phillip Biddulph, Ian G Hamilton, Robert Lowe, Anna Mavrogianni, Eleni Oikonomou, Rokia Raslan, Samuel Stamp, Andrew Stone, et al. Solid-wall u-values: heat flux measurements compared with standard assumptions. *Building Research &amp; Information*, (ahead-of-print):1–15, 2014.

[34] AT Booth and R Choudhary. Decision making under uncertainty in the retrofit analysis of the uk housing stock: Implications for the green deal. *Energy and Buildings*, 64:292–308, 2013.

[35] Sung H Hong, Tadj Oreszczyn, and Ian Ridley. The impact of energy efficient refurbishment on the space heating fuel consumption in english dwellings. *Energy and Buildings*, 38(10):1171–1181, 2006.

[36] S Hong, Ian Ridley, and Tadj Oreszczyn. The impact of energy efficient refurbishment on the airtightness in english dwellings. 2004.

[37] Elie Azar and Carol C Menassa. A comprehensive analysis of the impact of occupancy parameters in energy simulation of office buildings. *Energy and Buildings*, 55:841–853, 2012.

[38] Rajat Gupta and Matt Gregg. Do deep low carbon domestic retrofits actually work? *Energy and Buildings*, 129:330–343, 2016.

[39] M Hughes, J Palmer, and P Pope. A guide to the cambridge housing model. *London: DECC. Available here: www. tinyurl. com/HousingFactFile (last accessed 5 September 2012)*, 2011.

[40] Pier Giorgio Cesaratto and Michele De Carli. A measuring campaign of thermal conductance in situ and possible impacts on net energy demand in buildings. *Energy and Buildings*, 59:29–36, 2013.

[41] Olaf Gutschker. Parameter identification with the software package lord. *Building and Environment*, 43(2):163–169, 2008.

[42] Transient system simulation tool. `http://www.trnsys.com`. Accessed: 10 April 2017.

[43] S Doran. Detr framework project report: Field investigations of the thermal performance of construction elements as built. *Building Research Establishment Client Report*, (78132), 2000.

[44] Francesco Asdrubali, Francesco D'Alessandro, Giorgio Baldinelli, and Francesco Bianchi. Evaluating in situ thermal transmittance of green buildings masonries—a case study. *Case Studies in Construction Materials*, 1:53–59, 2014.

[45] P Baker. U–values and traditional buildings: in situ measurements and their comparisons to calculated values. *Historic Scotland Technical Paper*, 10, 2011.

[46] BS ISO 6946:2007. Building components and building elements — thermal resistance and thermal transmittance — calculation method. Technical report, The British Standsrds Institution, 2007.

[47] DataTaker. Dt80 range user's manual. `http://www.datataker.com/documents/manuals/UM-0085-B7%20-%20DT8x%20Users%20Manual.pdf`. Accessed: 20 April 2017.

[48] BS ISO 9869-1:2014. Thermal insulation - building elements - in-situ thermal resistance and thermal transmittance. Technical report, The British Standsrds Institution, 2014.

[49] Xi Meng, Biao Yan, Yanna Gao, Jun Wang, Wei Zhang, and Enshen Long. Factors affecting the in situ measurement accuracy of the wall heat transfer coefficient using the heat flow meter method. *Energy and Buildings*, 86:754–765, 2015.

[50] M Cucumo, A De Rosa, V Ferraro, D Kaliakatsos, and V Marinelli. A method for the experimental evaluation in situ of the wall conductance. *Energy and Buildings*, 38(3):238–244, 2006.

[51] Angeliki Kylili, Paris A Fokaides, Petros Christou, and Soteris A Kalogirou. Infrared thermography (irt) applications for building diagnostics: A review. *Applied Energy*, 134:531–549, 2014.

[52] Matthew Fox, David Coley, Steve Goodhew, and Pieter de Wilde. Thermography methodologies for detecting energy related building defects. *Renewable and Sustainable Energy Reviews*, 40:296–310, 2014.

[53] Matthew Fox, Steve Goodhew, and Pieter De Wilde. Building defect detection: External versus internal thermography. *Building and Environment*, 2016.

[54] Rossano Albatici and Arnaldo M Tonelli. Infrared thermovision technique for the assessment of thermal transmittance value of opaque building elements on site. *Energy and Buildings*, 42(11):2177–2183, 2010.

[55] Rossano Albatici, Arnaldo M Tonelli, and Michela Chiogna. A comprehensive experimental approach for the validation of quantitative infrared thermography in the evaluation of building thermal transmittance. *Applied Energy*, 141:218–228, 2015.

[56] Paris A Fokaides and Soteris A Kalogirou. Application of infrared thermography for the determination of the overall heat transfer coefficient (u-value) in building envelopes. *Applied Energy*, 88(12):4358–4365, 2011.

[57] Giuliano Dall'O, Luca Sarto, Angela Panza, et al. Infrared screening of residential buildings for energy audit purposes: results of a field test. *Energies*, 6(8):3859–3878, 2013.

[58] Waldemar Minkina and Sebastian Dudzik. *Infrared Thermography, Errors and Uncertainties*. Wiley Online Library, 2009.

[59] Rick Kramer, Jos van Schijndel, and Henk Schellen. Simplified thermal and hygric building models: a literature review. *Frontiers of Architectural Research*, 1(4):318–325, 2012.

[60] GJ Ríos-Moreno, M Trejo-Perea, R Castaneda-Miranda, VM Hernández-Guzmán, and G Herrera-Ruiz. Modelling temperature in intelligent buildings by means of autoregressive models. *Automation in Construction*, 16(5):713–722, 2007.

[61] O Gutschker. Lord–modelling and identification software for thermal systems, user manual. *BTU Cottbus*, 2004.

[62] Paslink. `http://dynastee.info/data-analysis/standardisation/`, March 2017. Accessed: 10 March 2017.

[63] K Ghazi Wakili, B Binder, M Zimmermann, and Ch Tanner. Efficiency verification of a combination of high performance and conventional insulation layers in retrofitting a 130-year old building. *Energy and Buildings*, 82:237–242, 2014.

[64] Xinhua Xu and Shengwei Wang. Optimal simplified thermal models of building envelope based on frequency domain regression using genetic algorithm. *Energy and Buildings*, 39(5):525–536, 2007.

[65] Kevin J Kircher and K Max Zhang. On the lumped capacitance approximation accuracy in rc network building models. *Energy and Buildings*, 2015.

[66] Gilles Fraisse, Christelle Viardot, Olivier Lafabrie, and Gilbert Achard. Development of a simplified and accurate building model based on electrical analogy. *Energy and buildings*, 34(10):1017–1031, 2002.

[67] Alfonso P Ramallo-González, Matthew E Eames, and David A Coley. Lumped parameter models for building thermal modelling: An analytic approach to simplifying complex multi-layered constructions. *Energy and Buildings*, 60:174–184, 2013.

[68] Philippe Lauret, Harry Boyer, Carine Riviere, and Alain Bastide. A genetic algorithm applied to the validation of building thermal models. *Energy and buildings*, 37(8):858–866, 2005.

[69] Shengwei Wang and Xinhua Xu. Simplified building model for transient thermal performance estimation using ga-based parameter identification. *International Journal of Thermal Sciences*, 45(4):419–432, 2006.

[70] Yeonsook Heo, Ruchi Choudhary, and GA Augenbroe. Calibration of building energy models for retrofit analysis under uncertainty. *Energy and Buildings*, 47:550–560, 2012.

[71] David JC MacKay. Probable networks and plausible predictions—a review of practical bayesian methods for supervised neural networks. *Network: Computation in Neural Systems*, 6(3):469–505, 1995.

[72] Phillip Biddulph, Virginia Gori, Clifford A Elwell, Cameron Scott, Caroline Rye, Robert Lowe, and Tadj Oreszczyn. Inferring the thermal resistance and effective

thermal mass of a wall using frequent temperature and heat flux measurements. *Energy and Buildings*, 78:10–16, 2014.

[73] Virginia Gori, Valentina Marincioni, Phillip Biddulph, and Clifford A Elwell. Inferring the thermal resistance and effective thermal mass distribution of a wall from in situ measurements to characterise heat transfer at both the interior and exterior surfaces. *Energy and Buildings*, 135:398–409, 2017.

[74] Julien Berger, Helcio RB Orlande, Nathan Mendes, and Sihem Guernouti. Bayesian inference for estimating thermal properties of a historic building wall. *Building and Environment*, 106:327–339, 2016.

[75] Jingbo Wang and Nicholas Zabaras. A bayesian inference approach to the inverse heat conduction problem. *International Journal of Heat and Mass Transfer*, 47(17):3927–3941, 2004.

[76] Helcio RB Orlande. Inverse problems in heat transfer: new trends on solution methodologies and applications. *Journal of Heat Transfer*, 134(3):031011, 2012.

[77] Marco Iglesias, Minho Park, and M.V Tretyakov. Bayesian inversion in rasin transfer molding. *[In Progress]*, 2017.

[78] Sergey I Kabanikhin. *Inverse and ill-posed problems: theory and applications*, volume 55. Walter De Gruyter, 2011.

[79] Peter M Lee. *Bayesian statistics: an introduction*. John Wiley & Sons, 2012.

[80] S.L. Cotter, G.O. Roberts, A.M. Stuart, and D. White. MCMC methods for functions: modifying old algorithms to make them faster. *Submitted*, page arXiv:1202.0709, 2012.

[81] Andrew Gelman, John B Carlin, Hal S Stern, and Donald B Rubin. *Bayesian data analysis*, volume 2. Chapman & Hall/CRC Boca Raton, FL, USA, 2014.

[82] A.M. Stuart. Inverse problems: a Bayesian perspective. In *Acta Numerica*, volume 19. 2010.

[83] Dani Gamerman and Hedibert F Lopes. *Markov chain Monte Carlo: stochastic simulation for Bayesian inference*. CRC Press, 2006.

[84] Mary Kathryn Cowles and Bradley P Carlin. Markov chain monte carlo convergence diagnostics: a comparative review. *Journal of the American Statistical Association*, 91(434):883–904, 1996.

[85] Sensirion. Digital humidity sensor sht7x. `https://www.sensirion.com/en/environmental-sensors/humidity-sensors/pintype-digital-humidity-sensors`. Accessed: 20 April 2017.

[86] Stanley. Stanley st-02-230-e / st-02-240-e / st-03-230-e / st-03-240-e / st-033-230-e / st-033-240-e / st-05-400-e / st-09-400-e st-02-230-e / st-02-240-e / st-03-230-e / st-03-240-e / st-033-230-e / st-033-240-e / st-05-400-e / st-09-400-e. `http://www.free-instruction-manuals.com/pdf/pa_475063.pdf`. Accessed: 10 March 2015.

[87] SR Delaforce, ER Hitchin, and DMT Watson. Convective heat transfer at internal surfaces. *Building and Environment*, 28(2):211–220, 1993.

[88] C Luo, B Moghtaderi, S Hands, and A Page. Determining the thermal capacitance, conductivity and the convective heat transfer coefficient of a brick wall by annually monitored temperatures and total heat fluxes. *Energy and Buildings*, 43(2):379–385, 2011.

[89] Petter Wallentén. Convective heat transfer coefficients in a full-scale room with and without furniture. *Building and Environment*, 36(6):743–751, 2001.

[90] Jianzhi Dong, Susan C Steele-Dunne, Tyson E Ochsner, and Nick van de Giesen. Determining soil moisture by assimilating soil temperature measurements using the ensemble kalman filter. *Advances in Water Resources*, 86:340–353, 2015.

[91] Cheng-Chun Lin and Liangzhu Leon Wang. Forecasting simulations of indoor environment using data assimilation via an ensemble kalman filter. *Building and Environment*, 64:169–176, 2013.

[92] Brent Huchuk, H Burak Gunay, William O'Brien, and Cynthia A Cruickshank. Model-based predictive control of office window shades. *Building Research & Information*, 44(4):445–455, 2016.

[93] Lorenz Biegler, George Biros, Omar Ghattas, Matthias Heinkenschloss, David Keyes, Bani Mallick, Luis Tenorio, Bart van Bloemen Waanders, Karen Willcox, and Youssef Marzouk. *Large-scale inverse problems and quantification of uncertainty*, volume 712. John Wiley & Sons, 2011.

[94] Branko Ristic, Sanjeev Arulampalam, and Neil James Gordon. *Beyond the Kalman filter: Particle filters for tracking applications*. Artech house, 2004.

[95] J White, MC Gillott, CJ Wood, Dennis L Loveday, and Keyur Vadodaria. Performance evaluation of a mechanically ventilated heat recovery (mvhr) system as part of a series of uk residential energy retrofit measures. *Energy and Buildings*, 110:220–228, 2016.

[96] Greenhouse gas reporting - conversion factors 2016. `https://www.gov.uk/government/publications/greenhouse-gas-reporting-conversion-factors-2016`, October 2016. Accessed: 15 May 2017.

[97] Home insulation, energy saving trust. `http://www.energysavingtrust.org.uk/home-insulation/solid-wall`, 2017. Accessed: 10 May 2017.

[98] Quarterly energy prices. Technical report, Department for Business Energy and Industrial Strategy, March 2017.

# Appendix A

# MCMC scheme

The algorithm below illustrates the steps to implement the MCMC scheme defined in chapter 2, considering the heat transfer problem with surface temperature boundary conditions. Algorithm 1, describes how to generate samples from the prior distributions as described in section . Algorithm 2 explains how to implement the Metropolis within Gibbs scheme inside the Markov Chain Monte Carlo.

**Algorithm 1 (Sampling from the prior)**

(1) *Define the values of* $\sigma_\kappa$ *and* $\lambda_\kappa$ *defining the variance of the correlation length of the Gaussian random field* $\psi_\kappa$*, as per equations* (2.26)-(2.27)*.*

(2) *Calculate the covariance function, equation* (2.27)*.*

(3) *Perform the single value decomposition of the covariance matrix* ($C_\kappa$) *obtained, so that*

$$C_\kappa = VDV^T, \tag{A.1}$$

*(4) Generate a random sample with covariance* $C_\kappa$

$$\nu_\kappa = V\sqrt{D}\xi_k \tag{A.2}$$

*Where* $\xi_k$ *is a random vector drawn from a normal distribution* $\sim N(0,1)$

*(5) Define the mean of the prior distribution as* $m_\kappa$

*(6) A random sample of the thermal conductivity prior distribution* $\mathbb{P}(\kappa)$ *is given by*

$$\mu_\kappa = exp(m_\kappa + \nu_\kappa) \tag{A.3}$$

*(7) Repeat operations (1)-(6) for the generation of samples belonging to the prior of the volumetric heat capacity* $\mathbb{P}(c)$.

**Algorithm 2 (MCMC: Metropolis-within-Gibbs)**

*Draw the initial proposal:* $u^{(0)} = (\kappa^{(0)}, c^{(0)}) \sim \mathbb{P}(u)$.

*For* $m = 0, \ldots$

*(1) Generate a new proposal* $v_r$ *defined by*

$$v_\kappa = \mathbf{E}(\kappa) + \sqrt{1-\beta_r^2}(\kappa^{(m)} - \mathbf{E}(\kappa)) + \beta_\kappa \xi, \quad \xi \sim N(0, C_\kappa),\ \beta_r \in [0,1], \tag{A.4}$$

*(2) Accept or reject* $v = (v_r, u_c^{(m)})$

$$(u_r^{(m+1)}, u_c^{(m)}, u_I^{(m)}) = \begin{cases} v & \text{with probability } a(u^{(m)}, v) \\ u^{(m)} & \text{otherwise} \end{cases} .$$

*where* $u^{(m)} \equiv (u_r^{(m)}, u_c^{(m)})$ *with* $a(u,v)$ *defined by (2.38).*

*(3) Let* $v_c$ *defined by*

$$v_c = \mathbf{E}(c) + \sqrt{1-\beta_c^2}(u_c^{(m)} - \mathbf{E}(c)) + \beta_c\xi, \quad \xi \sim N(0, C_c),\ \beta_c \in [0,1], \tag{A.5}$$

*(4) Accept or reject* $v = (u_\kappa^{(m+1)}, v_c)$

$$(u_\kappa^{(m+1)}, u_c^{(m+1)}) = \begin{cases} v & \text{with probability } a(\hat{u}^{(m)}, v) \\ \hat{u}^{(m)} & \text{otherwise} \end{cases}.$$

*where* $\hat{u}^{(m)} \equiv (u_\kappa^{(m+1)}, u_c^{(m)})$ *with* $a(u,v)$ *defined by (2.38).*